

# Understanding Intermolecular Interactions in Organic Heterojunction Devices with the Use of Density Functional Theory

by

©Sarah Abdulmajeed Ayoub

M. Sc. (Physics) Memorial University

B. Sc. (Physics) King Abdulaziz University

A thesis submitted to the School of Graduate Studies in partial fulfillment of the requirements for the degree of Doctor of Philosophy

Department of Physics and Physical Oceanography

Memorial University of Newfoundland

May 14, 2018

ST. JOHN'S

NEWFOUNDLAND

# Abstract

In the past two decades, the field of organic semiconductors has gathered immense attention and development due to their remarkable advantages in the applications in devices such as organic light emitting diodes (OLEDs) and organic solar cells (OSCs). The performance of these devices has significantly improved after the introduction of heterojunction structures which combine donor and acceptor type conjugated materials. Experimental studies suggest that, in addition to electronic and optical material properties, intermolecular interactions are critical for determining the efficiency of such devices. However, a detailed understanding of the impact of these intermolecular interactions is still lacking. In this thesis, I employ dispersion corrected density functional theory (D-DFT) methods to investigate the properties of these interfacial regions in the various promising (monomer/monomer and monomer/fullerene) combinations that are used in OLEDs and OSCs. I analyze binding energies and employ DFT (B3LYP) to obtain the electronic offsets of gas phase and interacting D-DFT monomers and fullerenes combinations. For the various pairings used in OSCs, I first assess the accuracy of D-DFT methods and then I investigate their properties and the effect of alkyl side chains on their interfacial interactions. My study shows that B97-D3 and B3LYP-D3 methods yield the most accurate electronic and absorption results. My results highlight useful (general) trends in electronic, structural, and intermolecular properties and side chains effect of these combinations that are well correlated with the experimentally determined efficiencies. In particular, I determine common factors that lead to achieving the best device performance

for combinations of fluorene-based polymers in OLEDs and the highest experimental efficiency (over 10%) for combinations of quaterthiophene-based polymers and fullerenes in OSCs. For example, monomer/fullerene pairings that have some of the highest OSC efficiencies exhibit the lowest interfacial LUMO offset and largest ratio of open-circuit voltage (as determined by interfacial band gap) to monomer's energy gap. For fluorene-based dimers used in OLEDs, I found monomers that have well-matched chain-lengths and HOMO-LUMO energy gaps exhibit the best device performance. I hope this thesis (which connects theory with the experimental data) will expedite the process of finding promising materials for organic heterojunction devices to improve their efficiencies.

# Co-Authorship

The thesis author (Sarah A. Ayoub) was the main contributor to all of the proceeding manuscripts, sharing authorship with Dr. Jolanta B. Lagowski, the supervisor for this graduate project. This work resulted in three manuscripts and an on-going work: first work entitled *Optimizing the performance of multilayered organic polymer devices using computational dimer approach-a case study* published in the Journal of Physical Chemistry C, second work entitled *Optimizing the Performance of the Bulk Heterojunction Organic Solar Cells Based on DFT Simulations of their Interfacial Properties* recently published in the Materials & Design, third work entitled *Assessment of the performance of four dispersion-corrected DFT methods using optoelectronic properties and binding energies of organic monomer/fullerene pairs* recently published in Computational & Theoretical Chemistry, and final work entitled *A DFT investigation of conjugated polymers and fullerenes interactions - side chain effect* is being prepared for a publication. In all four works, Dr. Jolanta B. Lagowski assisted with directing the research, analyzing the data and writing the manuscripts in her role as a supervisor.

# Acknowledgements

First, I would like to thank my supervisor Dr. Jolanta B. Lagowski for giving me her full support in making my PhD research both possible and successful. I had the privilege to learn so much from her knowledge and have gained so many research skills from her guidance. She was not only an amazing supervisor in directing my research but also very thoughtful, kind, and appreciative in different matters, which have made my journey more enjoyable. Being a mother of two toddlers while a PhD student, my research would not have been possible without her constant care and understanding. I'll never forget the time she provided me the lab office that gave me a private area that let me have my newborn infant with me during his first couple of months. It made research and work much easier for me. From the bottom of my heart I say to Dr. Jolanta, thank you for everything. I've been most fortunate to be your student!

Second, thanks and appreciations go to the supervisory committee of my PhD, Dr. Martin Plumer and Dr. Kris Poduska, for their encouraging comments and beneficial suggestions during annual meetings. Thanks to the professors who taught me courses and impacted my research, Dr. Martin Plumer, Dr. Anand Yethiraj, Dr. John Whitehead, Dr. Raymond Poirier, Dr. John Lewis, and Dr. Luc Beaulieu. Thanks to Donna Coombs and Maureen Wade for always offering me excellent assistance and making me smile in the department. Many thanks go to everyone (faculty, staff, and students) in the Physics Department at Memorial University (MUN) for the great time I had during my studies.

Third, sincere thanks and gratitude go to Oliver Stueker at ACENET, Gregory Shamov at WestGrid, Fred Perry at MUN, and my dear friend Shahrazad Malek for all the time and support to make my computations easier and accessible. Because of them, my computation skills have greatly improved. I also would like to thank ACENET, WestGrid, SHARKNET, Compute Canada, and MUN for the computational resources and facilities

and Natural Sciences and Engineering Research Council of Canada (NSERC) for partial research funding.

Fourth, much appreciation goes to King Abdulaziz University (KAU) in Saudi Arabia and the Saudi Cultural Bureau in Ottawa for the full scholarship and financial support given to me and my family during my studies in Canada. I also appreciate my teachers Dr. Thuriya Baeraky, Dr. Hala Al-Jawhari, Dr. Reem Altuwirqi, and the head office at the Physics Department of KAU for their continuous help and support prior to and during my scholarship. I would like to thank Dr. Zain Yamani at King Fahad University for his efforts with me in reviewing different courses in physics to prepare me for my studies in Canada.

Fifth, I am forever grateful to all my family in Saudi Arabia and in Canada. I am so thankful to my parents and my husband for being behind every success I made through the years and supporting me from the beginning. Thanks to my mom Hayat and my dad Abdulmajeed for everything they did to improve my education from grade one until coming to Canada to pursue my PhD degree. Thanks to my husband, soulmate, and best friend Alan Hillier for working hard with me, taking care of our kids (Maria and Malik), and fulfilling all my needs to accomplish the achievements presented in this thesis. I am also thankful to all my siblings (Samer, Maha, Abdulrahman, Ayah, Ghada, Abdullah, Reema, and Mohammad) for their constant support and encouragement, and special thanks go to my dear brother Abdulrahman for accompanying me to Canada. Sincere thanks go to my mother in law Linda and sister in law Katherine for always providing a great helping hand and assistance. Thanks to my friend Dr. Zeina Hashim for her loving support and constantly checking on my PhD progress.

Last, but not least, thanks to my teacher and dear friend Dr. Reem Altuwirqi who inspired me and made me fall in love with physics when she taught me my first-year undergraduate course. Since then, I wanted to follow her path and inspire others.

# Table of Contents

<b>Abstract</b> .....	<b>ii</b>
<b>Co-Authorship</b> .....	<b>iv</b>
<b>Acknowledgements</b> .....	<b>v</b>
<b>List of Tables</b> .....	<b>xi</b>
<b>List of Figures</b> .....	<b>xii</b>
<b>List of Abbreviations</b> .....	<b>xvi</b>
<b>1 Introduction</b> .....	<b>1</b>
1.1 Renewable Energy and Energy Consumption.....	1
1.2 Electronic Structure of Organic Semiconductors.....	3
1.3 Multilayer OLEDs.....	5
1.4 Bulk Heterojunction OSCs.....	7
1.4.1 Fundamentals of OSCs .....	9
1.4.2 Materials Development in OSCs.....	12
1.4.2.1 Early OSC Polymers.....	13
1.4.2.2 D-A Copolymers.....	14
1.4.2.3 Side Chains .....	15
1.4.3 What Limits the State-of-Art OSCs? .....	17
1.5 Density Functional Theory in OSCs and OLEDs .....	20
1.6 Outline.....	22
Bibliography.....	24
<b>2 Theoretical Approach</b> .....	<b>27</b>

2.1	The Schrödinger Equation.....	27
2.2	Hartree-Fock Method .....	29
2.3	Moving Beyond HF Method .....	31
2.4	Density Functional Theory .....	31
2.4.1	Hohenberg-Kohn Theorems.....	32
2.4.2	Kohn-Sham Formalism.....	33
2.5	Classification of Exchange-Correlation Functionals.....	35
2.5.1	LDA Functionals.....	35
2.5.2	GGA Functionals .....	37
2.5.3	Hybrid Functionals.....	37
2.6	Corrections Beyond Ground State Conventional DFT .....	40
2.6.1	Long-Range Correction .....	40
2.6.2	Dispersion Correction .....	41
2.7	The D-DFT Approach .....	42
2.7.1	The DFT-D2 Correction .....	43
2.7.2	The DFT-D3 Correction .....	45
2.7.3	Comparison between DFT-D2 and -D3.....	46
2.7.4	Selection of a D-DFT Method .....	47
2.8	Time-Dependent DFT .....	48
	Bibliography.....	50
<b>3</b>	<b>Optimizing the Performance of Multilayered Organic Polymer Devices Using Computational Dimer Approach – A Case Study .....</b>	<b>52</b>
3.1	Abstract .....	52
3.2	Introduction .....	53
3.3	Theoretical/Computational Details.....	57
3.3.1	Computational Approach .....	57
3.3.2	The Configuration of OxFn and TPAFn Pairings.....	58
3.3.3	Analysis of Computational Results.....	60
3.4	Results and Discussion.....	68
3.4.1	The Heterogeneous Pairs .....	68
3.4.1.1	The Electronic Structure of the Heterojunction.....	68

3.4.1.2	The Effect of Chain Length Mismatch on the Energy Gap Difference.....	70
3.4.1.3	The Effect of Chain Length Mismatch on the Binding Energy.....	75
3.4.1.4	Correlation of Energy Gap Differences with the Binding Energies ....	78
3.4.2	Homogeneous OxFn-OxFn and TPAFn-TPAFn (n=1-3) Pairs .....	80
3.5	Conclusions .....	82
	Bibliography.....	85
<b>4</b>	<b>Assessment of the Performance of Four Dispersion-Corrected DFT Methods Using Optoelectronic Properties and Binding Energies of Organic Monomer/Fullerene Pairs .....</b>	<b>89</b>
4.1	Abstract .....	89
4.2	Introduction .....	90
4.3	Materials and Methods .....	93
4.4	Results and Discussions .....	96
4.4.1	Binding Energies Comparison .....	96
4.4.2	Electronic Levels and Band Gaps Comparison.....	100
4.4.3	Side Chains Effect.....	108
4.4.4	The Absorption Spectra Comparison .....	112
4.5	Conclusions .....	119
	Bibliography.....	121
<b>5</b>	<b>Optimizing the Performance of the Bulk Heterojunction Organic Solar Cells Based on DFT Simulations of their Interfacial Properties</b>	<b>123</b>
5.1	Abstract .....	123
5.2	Introduction .....	124
5.3	Theoretical/Computational Details.....	128
5.3.1	Computational Methodology .....	128
5.3.2	Definitions of the Computed Interfacial Quantities.....	129
5.4	Results and Discussions .....	131
5.4.1	Conformational Analysis .....	131

5.4.1.1	Homogeneous Pairs .....	132
5.4.1.2	Heterogeneous Pairs .....	135
5.4.2	Electronic Properties of the Interacting Monomers and Fullerenes at the Interface. ....	138
5.4.3	Electronic Properties of the Isolated Monomers and Fullerenes .....	144
5.4.4	Binding Energies of Homogeneous and Heterogeneous Pairs.....	144
5.4.5	Further Verification of our Conclusions .....	149
5.5	Conclusions .....	150
	Acknowledgments .....	152
	Bibliography.....	153
<b>6</b>	<b>A DFT Investigation of Conjugated Polymers and Fullerenes Interactions - Side Chain Effect .....</b>	<b>156</b>
6.1	Abstract .....	156
6.2	Introduction .....	157
6.2	Computational Details.....	163
6.2.1	Computational Approach .....	163
6.2.2	The Preferred Configurations of Monomers and Fullerenes Pairings .....	164
6.2.3	Side Chain Studies .....	165
6.2.4	Computed Parameters .....	167
6.3	Results and Discussion.....	168
6.3.1	Various Pairs with High PCEs .....	168
6.3.2	Varying the Length of Side Chains.....	170
6.3.3	Varying the Type of Side Chains .....	181
6.3.4	Branching Positions of Branched Side Chains .....	190
6.3.5	Energy Levels of Monomers with Side Chains .....	194
6.4	Conclusions .....	200
	Bibliography.....	202
<b>7</b>	<b>Summary and Future Work.....</b>	<b>205</b>
	Bibliography.....	211
	<b>Appendices.....</b>	<b>212</b>

# List of Tables

Table 3.1: Chain length difference, intermolecular distance, energy gap difference, and binding energy per unit average chain length for various pairings of OxFm-TPAFn .....	74
Table 3.2: Chain length difference intermolecular distance, energy gap difference, and binding energy per unit average chain length for various pairings of OxFm-TPAFn that require an addition of monomer(s).....	75
Table 4.1: MADs of the SP B3LYP electronic parameters.....	111

# List of Figures

Figure 1.1: The illustration of $sp^2$ -hybridization of two carbon atoms and energy levels ..	4
Figure 1.2: Bilayer configuration of OLEDs and OSCs. ....	5
Figure 1.3: Energy level diagram of a multilayer OLED. ....	6
Figure 1.4: BHJ configurations of OSCs. ....	9
Figure 1.5: The major five processes of OSCs. ....	11
Figure 1.6: Chemical Structures of P3HT and PCBM.....	13
Figure 1.7: Structures of PBDTTPD polymers.....	15
Figure 1.8: Types of alkyl side chains. ....	16
Figure 3.1: Molecular structures of OxFn and TPAFn.....	59
Figure 3.2: Illustration of the chain length matching.....	60
Figure 3.3: Energy-level diagram of a bilayered OLED.....	62
Figure 3.4: Illustration of the determination of the chain lengths.....	62
Figure 3.5: Example of the determination of the chain length shift .....	63
Figure 3.6: Energy gaps versus the reciprocal of chain lengths.....	65
Figure 3.7: The energy gap difference of heterogenous dimers .....	65
Figure 3.8: The binding energy of homogenous and heterogenous pairs .....	67
Figure 3.9: Example of the determination of the average perpendicular distance.....	68
Figure 3.10: The energy levels of the OxFn-TPAFn .....	70
Figure 3.11: The energy gap difference and the binding energy .....	73

Figure 3.12: The optimized geometry of OxF3-TPAF2 .....	73
Figure 3.13: The binding energy of well-matched OxFm-TPAFn .....	79
Figure 3.14: The binding energy of OxFn-OxFn and TPAFn-TPAFn .....	81
Figure 4.1: The binding energies of fourteen monomer/fullerene pairs.....	99
Figure 4.2: The SP B3LYP of electronic parameters.....	102
Figure 4.3: MADs in electronic parameters.....	107
Figure 4.4: The percentage deviations and the energy gaps of nP3HT .....	108
Figure 4.5: Binding energies of monomer/fullerene .....	110
Figure 4.6: The maximum absorption wavelengths of isolated and interacting monomers .....	115
Figure 4.7: The percentage deviations in maximum absorption wavelengths.....	117
Figure 4.8: The maximum absorption wavelengths of interacting monomers with long side chains .....	118
Figure 4.9: MADs of maximum absorption wavelengths.....	119
Figure 5.1: Schematic illustration of the energy levels of polymer/fullerene.....	131
Figure 5.2: The binding energy versus configurations of monomer/monomer .....	133
Figure 5.3: The optimized configurations of PCBM/PCBM .....	134
Figure 5.4: The relative conformational and binding energies of fullerenes .....	134
Figure 5.5: Three type of configurations for monomer/fullerene .....	136
Figure 5.6: The relative conformational and binding energies for the three types of configurations .....	137
Figure 5.7: The energy levels of the interacting monomers .....	141

Figure 5.8: Interfacial bandgaps versus PCEs .....	142
Figure 5.9: LUMO offset and HOMO offset versus energy gap .....	142
Figure 5.10: Interfacial bandgaps versus monomers' energy gaps.....	143
Figure 5.11: The ratio of interfacial band gap versus monomer's energy gap .....	143
Figure 5.12: Binding energies of heterogeneous and homogenous pairs .....	147
Figure 5.13: Binding energy versus monomer's chain length .....	147
Figure 5.14: The binding energy of homogenous pairs versus the ratio of interfacial band gap per monomer's energy gap.....	148
Figure 5.15: (a) LUMO offsets versus monomers' energy gaps and (b) binding energy versus the ratio of interfacial band gap per monomer's energy gap .....	150
Figure 6.1: Illustrations of the preferred configurations.....	165
Figure 6.2: Total binding energies and binding energies per average chain lengths .....	169
Figure 6.3: B97-D3 binding energies versus monomers' chain lengths.....	170
Figure 6.4: Binding energies versus the lengths of side chains .....	176
Figure 6.5: The optimized geometries of pairs containing P3HT.....	177
Figure 6.6: The optimized geometries of pairs containing PCDTBT .....	178
Figure 6.7: The optimized geometries of pairs containing PBDTTPD.....	179
Figure 6.8: The optimized geometries of pairs containing PNT4T, Pff4TBT, and PBTff4T .....	180
Figure 6.9: Binding energies versus the number of branched side chains .....	186
Figure 6.10: The optimized geometries of pairs containing P3HT with branched side chains .....	187

Figure 6.11: The optimized geometries of PBDTTPD with branched side chains.....	188
Figure 6.12: The optimized geometries of pairs containing PTB with branched side chains .....	189
Figure 6.13: Binding energies versus the branching positions of branched side chains	192
Figure 6.14: The optimized geometries of pairs containing PNT4T and PBTff4T with three different branching poisions .....	193
Figure 6.15: Energy levels of gas phase monomers with and without side chains.....	197
Figure 6.16: The energy levels of interacting monomers with various side chains.....	199
Figure 6.17: The ratio of interfacial bandgap per energy gap versus monomer's energy gap .....	200

# List of Abbreviations

- **1ON** 1-Octylnonyl
- **2DT** 2-Decyltetradecyl
- **2OD** 2-Octyldodecyl
- **3OT** 3-Octyltridecyl
- **BDT** Benzodithiophene
- **BHJ** Bulk Heterojunction
- **B.O** Born-Oppenheimer
- **BT** Benzothiadiazole
- **CC** Coupled Cluster Theory
- **CI** Configuration Interactions
- **D-A** Donor-Acceptor
- **D-DFT** Dispersion Corrected Density Functional Theory
- **DFBT** Difluorobenzothiadiazole
- **DFT** Density Functional Theory
- **EA** Electron Affinity
- **EH** 2-Ethylhexyl
- **EML** Emitting Layer
- **ETL** Electron Transport Layer
- **GGA** Generalized Gradient Approximation

- **HF** Hartree-Fock
- **HOMO** Highest Occupied Molecular Orbital
- **HOMOs** Highest Occupied Molecular Orbitals
- **HTL** Hole Transport Layer
- **IP** Ionization Potential
- **KS** Kohn-Sham
- **LDA** Local Density Approximation
- **LCAO** Linear Combination of Atomic Orbitals
- **LBG** Low Band Gap
- **LEDs** Light Emitting Diodes
- **LR** Long-Range
- **LSDA** Local Spin Density Approximation
- **LUMO** Lowest Occupied Molecular Orbital
- **LUMOs** Lowest Occupied Molecular Orbitals
- **MAD** Mean Average Deviation
- **MADs** Mean Average Deviations
- **MEH-PPV** 2-Methoxy-5-(2-ethylhexyloxy)-polyphenylenevinylene
- **MO** Molecular Orbital
- **MOs** Molecular Orbitals
- **MP** Moller-Plesset Perturbation Theory
- **OLED** Organic Light Emitting Diode
- **OLEDs** Organic Light Emitting Diodes

- **OPVCs** Organic Photovoltaic Cells
- **OSC** Organic Solar Cell
- **OSCs** Organic Solar Cells
- **OxF** Oxadiazole-fluorene copolymer
- **P3BT** Poly(3-butylthiophene)
- **P3EHT** Poly(3-(2-ethylhexyl)thiophene)
- **P3HT** Poly(3-hexylthiophene)
- **P3HTs** Poly(3-hexylthiophene)s
- **P3HT-co-EHT** Poly(3-hexylthiophene-co-3-(2-ethylhexyl)thiophene)
- **P3PT** Poly(3-pentylthiophene)
- **PBDTTPD** Poly(benzo[1,2-b:4,5-b']-dithiophene-thieno[3,4-c]pyrrole-4,6-dione)
- **PBTff4T-2OD** Poly[(2,1,3-benzothiadiazol-4,7-diyl)-alt-(4',3''-difluoro-3,3'''-di(2-octyldodecyl)-2,2';5',2'';5'',2'''-quaterthiophen-5,5'''-diyl)]
- **PC<sub>71</sub>BM** [6,6]-Phenyl C<sub>71</sub> butyric acid methyl ester
- **PCBM** [6,6]-Phenyl-C<sub>61</sub> butyric acid methyl ester
- **PCDTBT** Poly[N-9'-heptadecanyl-2,7-carbazole-alt-5,5-(4',7'-di-2-thienyl-2',1',3'-benzothiadiazole)]
- **PCE** Power Conversion Efficiency
- **PCEs** Power Conversion Efficiencies
- **PeSCs** Perovskite Solar Cells
- **Pff4TBT-2OD** Poly[(5,6-difluoro-2,1,3-benzothiadiazol-4,7-diyl)-alt-(3,3'''-di(2-octyldodecyl)-2,2';5',2'';5'',2'''-quaterthiophen-5,5'''-diyl)]

- **PLED** Polymeric Light-Emitting Diode
- **PNT4T-2OD** Poly[(naphtho[1,2-c:5,6-c']bis[1,2,5]thiadiazol-5,10-diyl)-alt-(3,3''-di(2-octyldodecyl)-2,2';5',2'';5'',2'''-quaterthiophen-5,5'''-diyl)]
- **PTB** Thieno[3,4-B]thiophene/benzodithiophene
- **PTB7** Poly[[4,8-bis[(2-ethylhexyl)oxy]benzo[1,2-b:4,5-b']dithiophene-2,6-diyl][3-fluoro-2-[(2-ethylhexyl)carbonyl]thieno[3,4-b]thiophenediyl]]
- **SC** Side Chains
- **SCs** Solar Cells
- **SCF** Self-Consistent Field
- **SP** Single Point
- **SR** Short-Range
- **TD-DFT** Time Dependent Density Functional Theory
- **TPAF** Triphenylamine-fluorene copolymer
- **TPD** Thienopyrroledione

# Chapter 1

## 1 Introduction

### 1.1 Renewable Energy and Energy Consumption

Energy consumption plays an essential role in our daily life. However, we often do not notice our reliance on energy until its absence due to a temporary blackout. In many regions of the world, millions of people still do not have consistent access to electricity. Research for renewable energy is necessary not only to fulfill the current global demands but also to help the environment from harmful long-term effects of pollution resulting from fossil fuel-based energy sources. [1] Solar energy is the largest secure sustainable energy source that can provide efficiently all the energy needs of the world. Hence, solar cells (SCs), which convert solar light directly into electricity, have been recognized as essential devices for production of future global energy. In addition to providing renewable energy, consuming less energy to generate light is another challenge that drives the development of light emitting diodes (LEDs). SCs and LEDs are promising candidates that offer environmental solutions and cost saving benefits for next generation electronics. The majority of conventional SCs and LEDs are based on inorganic semiconducting materials which are still limited globally by their high costs and related environmental issues. [1]

In 1977, Alan G. MacDiarmid, Hideki Shirakawa, and Alan J. Heeger discovered that polyacetylene can conduct. This has changed the concept of organic polymers as being predominately insulators. [2] This discovery, which was awarded the Nobel Prize in 2000, opened the door to new research and industrial applications that involve the use of synthesized organic semiconducting hydrocarbon-based materials. It has turned the attention of scientists' community from the use of inorganic to organic semiconductors in optoelectronic devices such as organic light emitting diodes (OLEDs) and organic solar cells (OSCs). Organic semiconductors pose unique advantages such as low cost, flexibility in synthesis, and ease of manufacturing. Another benefit of these materials, particularly polymers, is that they are solution processable (as ink) which allows for high-volume and low-cost manufacturing of optoelectronic devices on a wide range of flexible substrates (e.g. paper and cloth). These advantages are not found in manufacturing the traditional inorganic semiconductor devices which involve the use of hazardous materials, and very expensive and complicated methods of production. [3]

Remarkable progress has been made in the development of organic semiconductors due to their most interesting properties in terms of manufacturing SCs and LEDs that fulfill the urgent need of renewable energy and energy consumption, respectively. Interest in organic semiconducting devices has risen strongly after the demonstration of heterojunction structure including p- and n- conducting organic materials. In recent years, it has been widely recognized that the heterojunction, which is an interface between two different semiconducting materials, is the key to the success of organic semiconducting devices. However, efficiencies of OSCs, that have reached 11%, are still much less than

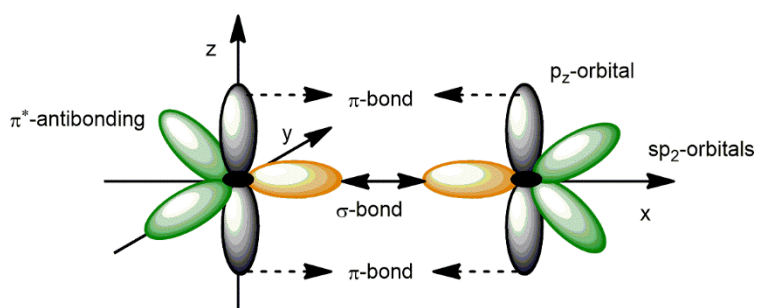
inorganic solar cell devices (about 26%). [4] The physics of organic semiconductors is still not well understood, not only for the applications of OSCs but, also for OLEDs which are now available in industry. Therefore, further improvements and deeper understanding of organic materials and their heterojunctions are necessary to maximize efficiencies and move into a competitive position in industry.

## 1.2 Electronic Structure of Organic Semiconductors

All organic conjugated materials depend on conjugated  $\pi$ -electron systems for conduction. The molecular framework of conjugated small molecules or polymers composes of alternating single and double carbon-carbon bonds. From the quantum mechanical point of view, within a molecule or polymer, each carbon atom has three  $sp^2$  hybridized orbitals (i.e. making three  $\sigma$ -bonds to the surrounding atoms). The leftover non-hybridized  $p_z$  orbitals, which is perpendicular to the plane of the chain, overlap to form  $\pi$ -bonding and  $\pi^*$  anti-bonding molecular orbitals (MOs) (see Figure 1.1 (a)). Electrons in these  $\pi$  orbitals are delocalized along the conjugated chains. Because each MO is capable of containing two spin-paired electrons, the lowest energy (quantum) states that correspond to the  $\pi$ -bonding MOs are occupied while the higher energy  $\pi^*$  anti-bonding MOs are empty. For these systems, the top  $\pi$ -orbital is the highest occupied molecular orbital (HOMO) and the bottom  $\pi^*$ -orbital is the lowest unoccupied molecular orbital (LUMO) in their ground states. Figure 1.1 (b) illustrates a simple energy level diagram for the formation of HOMO and LUMO energy levels from the  $2p_z$  orbitals of carbons in ethene. The alternating bond

lengths (between single (longer) and double (shorter) bonds), which are formed along the conjugated chains, stabilize the  $\pi$  orbitals and destabilize the  $\pi^*$  orbitals. This distortion opens up an energy gap ( $E_g$ ), between HOMO and LUMO, that ranges from 1 to 3 eV, thus giving the conjugated molecular chains a semiconducting property. The electronic properties of organic semiconductors make them to be very useful materials for SCs and LEDs. [5]

(a)



(b)

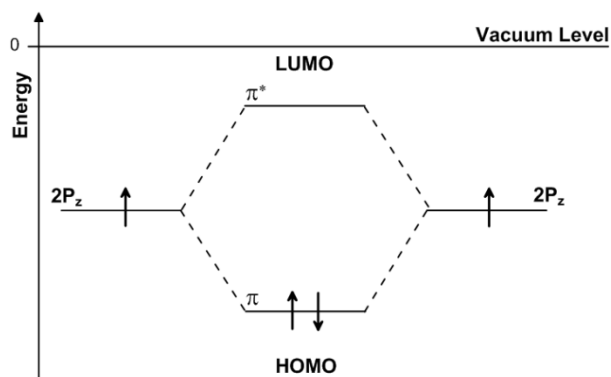


Figure 1.1: The illustration of (a)  $sp^2$ -hybridization of two carbon atoms and (b) the formation of HOMO and LUMO energy levels from the atomic orbitals of ethene.

## 1.3 Multilayer OLEDs

In 1987, C. W. Tang introduced the first organic light-emitting diode (OLED) with a double organic layer structure: electron transport layer (ETL) and hole transport layer (HTL), which are equivalent to n- and p-type semiconductors, respectively. [6] This novel structure achieved a higher efficiency compared to the early OLED devices that consisted of a single organic layer sandwiched between two electrodes. Since then, the bilayer configuration has become the basic structure of OLEDs (see Figure 1.2).

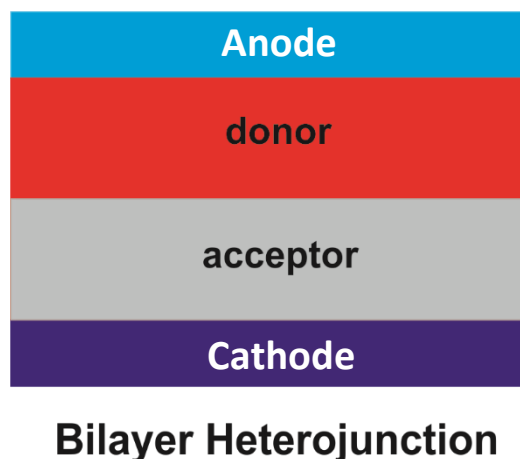


Figure 1.2: Bilayer configuration of OLEDs and OSCs.

In an OLED, light is produced by the recombination of holes and electrons, which are injected from the electrodes. When the voltage is applied between the electrodes, holes and electrons are injected (from the anode and cathode, respectively) into the organic material. Then, the charges are transported inside the material, and recombine at the heterojunction sites to form excitons and thus emit light. To obtain highly efficient OLEDs,

the charge injection and transport must have good balance. To do so, it is recommended that a multilayer organic structure is designed so that each layer has a specialized function. Figure 1.3 illustrates the energy level diagram of a multilayer OLEDs containing of the hole transporting layer (HTL), electron transport layer (ETL), and emitting layer (EML). Thus, multiple interfaces between organic layers are created in multilayer OLED devices. It has been shown that the performance of OLED devices is highly dependent on the interfacial organic/organic interactions, as they control the charge transport and recombination. Consequently, huge efforts have been made to optimize these interfaces in order to enhance the device performances. Despite the great progress in developing OLEDs, which have led to the advanced flat panel displays, controlling the interfaces of multilayer organic structures remains a challenge. [7]

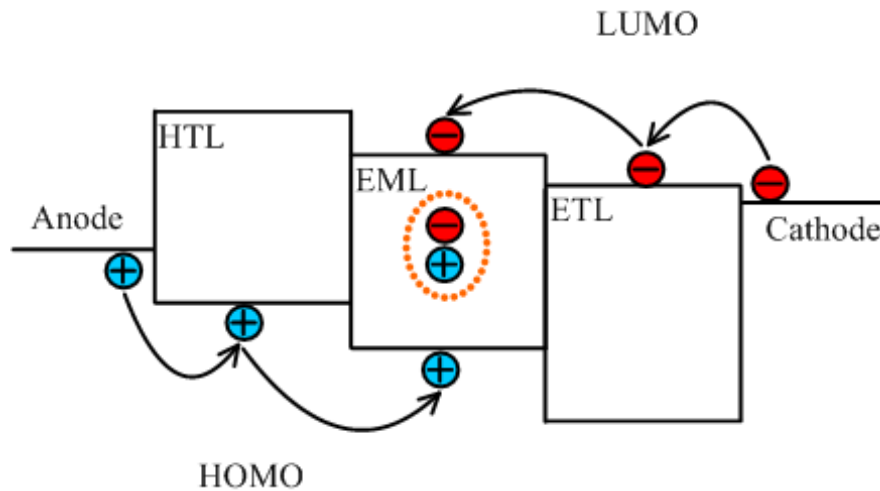


Figure 1.3: Energy level diagram of a multilayer OLED.

## 1.4 Bulk Heterojunction OSCs

Similar to OLEDs, the device structure of the early OSCs was based on one single (or homogeneous) organic layer sandwiched between two electrodes of different work functions. Upon the absorption of light, excitons are formed and dissociate into free charges to generate power. Excitons are electron-hole pairs bound by the Coulombic attraction forces. That is, it is necessary to break an exciton to obtain electric current. Excitons tend not to dissociate easily into free charges because of the low dielectric constant in organic materials. Sufficient extra energy is required to separate an electron and a hole of an exciton which exhibits a short lifetime. [8] This is difficult to achieve with a single organic layer. Consequently, the single-layer OSCs exhibited very low efficiency of far below 1% [9] which make them undesirable for any application. This problem was solved by introducing a second organic semiconducting layer into OSC. In 1986, C. W. Tang used a double layer structure as an active layer in the OSC and reported an increase in the power conversion efficiency of about or above 1%. [10] This indicated that, in a bilayer OSC, a certain percentage of the absorbed photons has reached the interface between the two layers and thus dissociated into charge carriers. The typical configuration of the bilayer structure of OSC is shown in Figure 1.2. However, the efficiency of bilayer OSCs is still very low due to the very small exciton diffusion-length which is much smaller than the required thickness of absorbing layer (80-200 nm). [1] As a result, the majority of excitons decay before reaching the bilayer heterojunction, hence, identifying methods to maximize interfaces, and thus charge separations, became a major focus of OSC research.

In 1995, Heeger and Wudl groups obtained a power conversion efficiency of 2.9% in OSC made of a blended system of polymer (MEH-PPV) and fullerene ( $C_{60}$ ). [11] This system suggests the use of conjugated polymers (p-type semiconductor) as electron donors and fullerene derivatives (n-type semiconductor) as electron acceptors in a new configuration called bulk heterojunction (BHJ) OSC (see Figure 1.4). In this configuration, the donor and acceptor materials are mixed together forming a bicontinuous interpenetrated system. In BHJ OSCs, no chemical doping is applied and the charges are created at the heterojunction from the photo-excited donor to the acceptor or vice versa. Hence, the donor term is referred to a molecule that can readily lose an electron and the acceptor term is referred to a molecule that can readily accept an electron. The advantage of the BHJ configuration is that it accommodates the required thickness for sufficient absorption of light, as well as the low exciton diffusion length in disordered organic materials. Excitons are dissociated efficiently in BHJ OSCs due to the distributed heterojunctions between the donor and acceptor materials (i.e. the number of interfaces are increased), hence, the chance of exciton decay before reaching the interface is significantly reduced. Since then, the BHJ configuration has become the state-of-art for OSCs. [8]

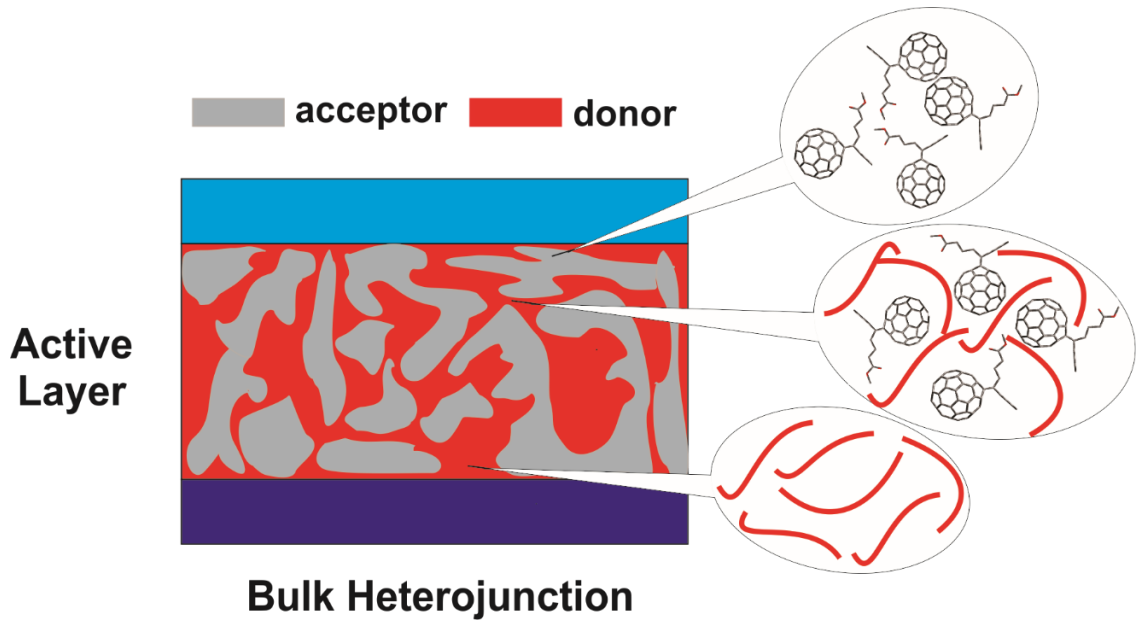


Figure 1.4: BHJ configurations of OSCs.

### 1.4.1 Fundamentals of OSCs

As indicated in the previous section, the device performance of OSCs is described by the power conversion efficiency (PCE). It is based on three parameters: the short-circuit current density ( $J_{SC}$ ), the open-circuit voltage  $V_{OC}$ , and the fill factor  $FF$ . All these parameters depend highly on the materials used in OSC. The total power conversion efficiency is given by,

$$PCE = \frac{J_{sc}V_{oc}FF}{P_{Solar}} \quad (1.1)$$

where  $P_{Solar}$  is the incident power from solar light. The value of  $FF$  is the ratio of the measured maximum power ( $J_{max}V_{max}$ ) to the product of  $J_{SC}$  and  $V_{OC}$ . To extract power

from an OSC consisting of (polymer) donor and (fullerene) acceptor materials, five major processes must occur (see Figure 1.5). The management of these processes should be efficiently controlled to optimize the efficiency of OSC devices [12]:

**(1) Exciton generation:** When photons are absorbed, excitons are generated. To maximize the absorption efficiency, the organic material should capture a large fraction of the incoming sunlight. To do so, the bandgaps, which determine the absorption limit for a material, must be optimized when designing new molecules and polymers.

**(2) Exciton diffusion:** Excitons, that are generated upon absorption, will diffuse within the material to the donor/acceptor interface. To achieve this process efficiently, and since excitons are short-lived species, the donor/acceptor phase separation must be as small as possible to exploit the full exciton diffusion length (i.e. losing no excitons) prior to the subsequent step of charge separation at the interface.

**(3) Exciton dissociation:** The exciton dissociation occurs as the excitons reach the heterojunction interface. Favorable conditions for exciton dissociation takes place at the interface when the energy difference between the LUMOs of the donor and acceptor exceeds the exciton binding energy, resulting in the generation of free electrons and holes.

**(4) Charge transport:** The generated charges will be transported to the electrodes under the driving force of the built-in electric field between the two electrodes. The migration of charges occurs through their respective phases (i.e. electrons through acceptor and holes through donor).

**(5) Charge collection:** The migrated charges must cross the active layer/electrodes interfaces to reach the external circuit. To optimize the charge collection efficiency, the work function of the hole or electron collection electrode must match well with the corresponding HOMO or the LUMO level of the active layers.

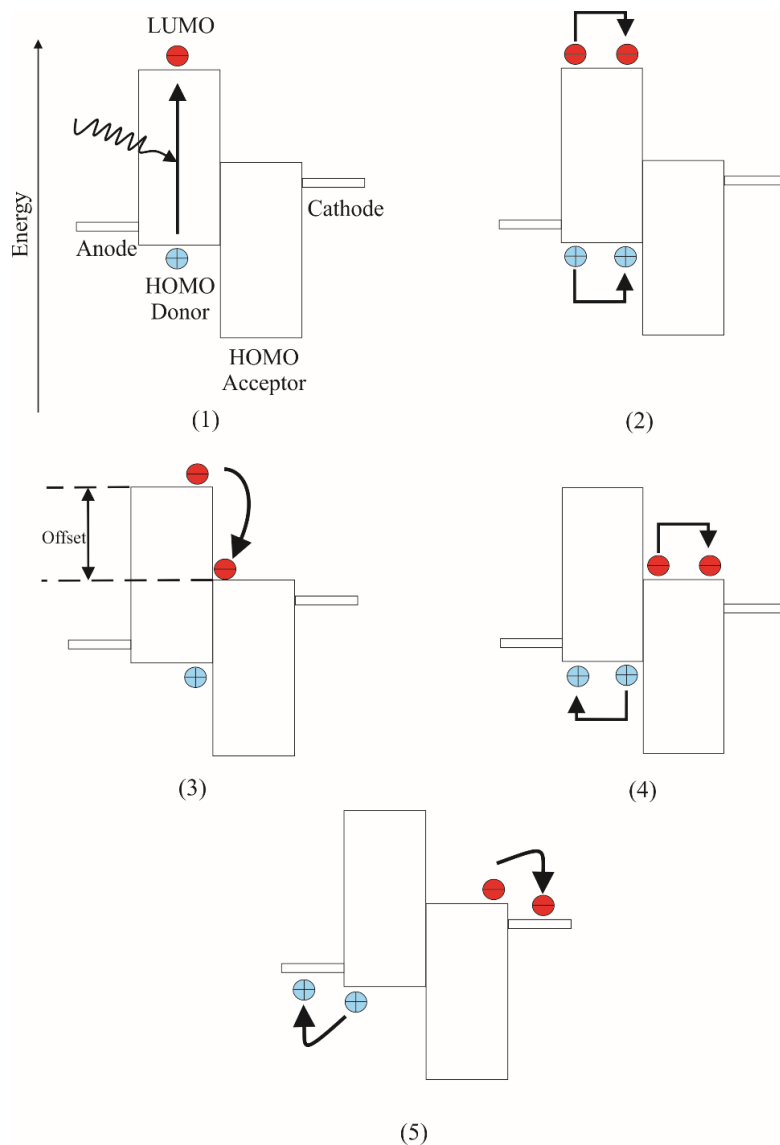


Figure 1.5: The major five processes responsible for photocurrent within the donor/acceptor composites of OSCs. Note this illustration is made for the case of excitons that are generated in the donor phase.

## 1.4.2 Materials Development in OSCs

For high performance OSCs, the development of donor materials includes primarily polymers. The fullerene derivatives have dominated the development of acceptor materials due to their high electron affinity and superior ability to transport electrons. Some n-type conjugated polymers with stronger visible absorption have been used as acceptors in OSCs, however, fullerene derivatives are still preferable acceptors in OSCs due to their higher efficiencies. [13] In fact, the success of BHJ OSCs is attributed to the good compatibility between semiconducting polymers and fullerenes. The acceptor fullerenes that are commonly used in the fabrication of BHJ OSCs are PCBM and PC<sub>71</sub>BM. Due to the stronger absorption of PC<sub>71</sub>BM, it has been widely used more often than PCBM in OSCs. The PCE values of polymer/PC<sub>71</sub>BM devices are either better or comparable to those of polymer/PCBM devices. [1]

Since the acceptor fullerenes (PCBM or PC<sub>71</sub>BM) remain the same for most polymer/fullerene OSC devices, research efforts have been focused more on the design of donor polymers. In fact, one of the most important issues in literature for enhancing the development of OSCs is the rational design of donor polymers. [14] This is because the backbone of conjugated polymers can determine the fundamental optoelectronic properties, such as band gap, position of energy levels, and charge carrier mobilities. Hence, careful selection of proper polymers is essential to obtain the desired properties. In addition, incorporating the appropriate side chains can highly modify the properties of polymers. In general, the desired features for an ideal donor polymer material in an OSC device include: (1) a low band gap value to maximize light absorption (~ range of 1-2 eV),

(2) appropriate energy level alignments (HOMO level around -5.4 eV and LUMO level around -3.9 eV)[15] with those of fullerenes, (3) high hole mobility to improve charge transport, and (5) excellent interfaces with fullerenes to optimize exciton diffusion, exciton dissociation, and charge transport. [14]

### 1.4.2.1 Early OSC Polymers

The progress of designing donor polymers has gone through many phases. The early class of polymers used in OSCs is the poly(3-hexylthiophene) (P3HT) with a bandgap of about 1.9 eV. P3HT OSCs exhibit PCEs up to 5% after modifications on the morphology (that involved thermal annealing). [16] P3HT/PCBM are the most benchmarked combinations for OSC studies which help in revealing the structure-property correlations and modifying the design of other high-performance polymers (see Figure 1.6). [17] Due to the relatively large band gap and small difference between the HOMO energy level of P3HT and LUMO energy level of fullerene, the PCEs of P3HT/fullerene solar cells are limited.

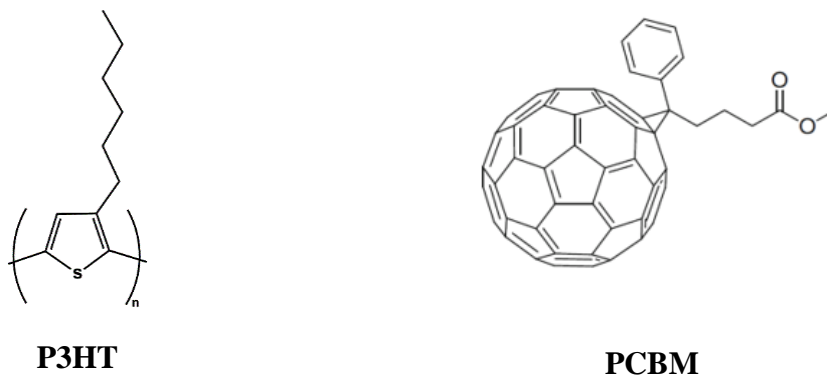


Figure 1.6: Chemical Structures of P3HT and PCBM.

### 1.4.2.2 D-A Copolymers

A major advancement in the designing of OSCs was made by the introduction of donor-acceptor (D-A) copolymers which lead to a significant improvement in PCEs. In contrast to homopolymer P3HT, a D-A copolymer consist of one electron-rich unit (donor) and one electron-deficient unit (acceptor). The D-A approach is mainly used to construct low band gap polymers with tunable energy levels. The band gap of D-A copolymers is lowered by the internal charge transfer between the donor and acceptor units. The unique advantage of these types of polymers is that the HOMO and LUMO energies can be tuned separately by adjusting the electron donating ability of the donor and electron affinity of the acceptor. The D-A copolymers are considered the most successful class of polymer photovoltaic materials. Over the years, a variety of D-A polymers have been developed such as oligothiophene-, benzodithiophene (BDT)-, benzothiadiazole (BT)-, and thienopyrroledione (TPD)-based polymers. Figure 1.7 illustrates an example of a D-A copolymer (PBDTTPD) which consists of alternating BDT (donor) and TPD (acceptor) units. [14]

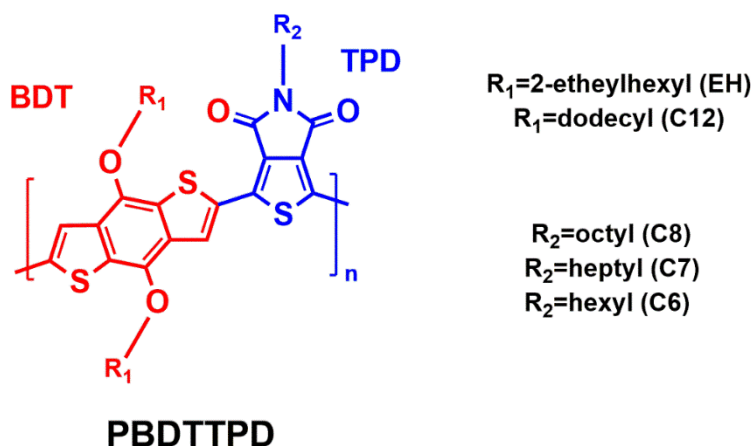


Figure 1.7: Structures of PBDTTPD polymers.

### 1.4.2.3 Side Chains

Compared to simple P3HT, D-A copolymers can be more amenable to structural modifications due to the many sites along the backbones that are available for side chains and chemical functionalization. Side chains attached to the polymer backbones can strongly affect the intermolecular interactions between different polymer chains and between polymers and fullerenes as well as the solubility of polymers. It has been reported that alkyl side chains can exert a considerable influence on the properties of low band gap (LBG) copolymers and can lead to higher PCEs in OSCs. [18, 19] The role of side chains is apparent on the  $\pi - \pi$  stacking and lamellar distances between polymers. Both factors are crucial for the charge transport and thus the device performance. [20-22] The length (number of carbon atoms), type (linear or branched), and branching position of side chains are important as well (see Figure 1.8). For example, long and branched side chains can improve the solubility of polymers, however the oversized side chains can cause too much

steric hindrance that enlarges the intermolecular  $\pi$  distance, and hence lowers the charge transport and device performance. [14] Over the years, many of different side chains have been tested when designing polymers with desired properties. An example of the D-A copolymers that were examined with different side chains while leading to higher PCEs are PTB7 (with all-branched side chains and PCE of 9.2%)[23], PBDTTPD (with linear (C12)-and-branched (C7) side chains and PCE of 8.5%)[18], and Pff4TBT-2OD (with 2-position branched side chains and PCE of 10.5%) [24] (see Scheme 4.1 in Chapter 4 and Scheme 5.1 in Chapter 5 for their chemical structures).

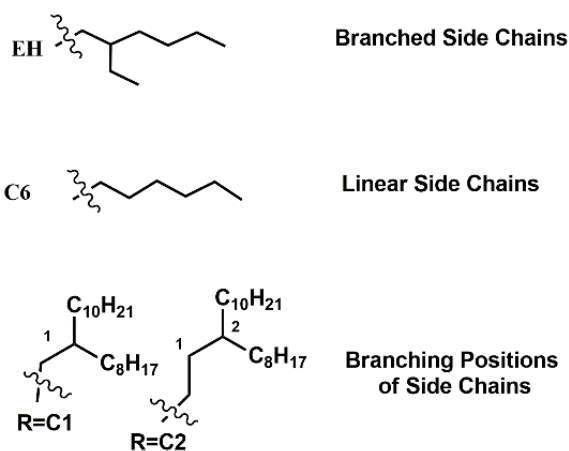


Figure 1.8: Types of alkyl side chains.

### 1.4.3 What Limits the State-of-Art OSCs?

Considering that the operation of OSCs relies on several steps starting from light absorption to extracting charges, which are discussed in subsection 1.4.1, it is obvious that not all these processes have a high efficiency. These mechanisms are limited by a number of factors such as too large a band gap of organic semiconductors, low charge mobility, large exciton binding energy, and others. [25] While research efforts are ongoing to minimize these limitations, the structure and properties of heterojunction region should also be studied. It is widely accepted that the processes of exciton dissociation, charge separation, and charge recombination are controlled by the polymer/fullerene interfaces. [22] Even though a huge effort was made on synthesizing hundreds of materials for OSCs to increase the PCE, which currently reached 11 % [24], no clear strategy is known for optimizing the polymer/fullerene interfaces. Many systems that include some promising material properties (such as the strong absorption and high hole mobility) yield low or moderate PCEs. [26-29] The potential problem of not obtaining the expected high PCEs for these systems is the fact that it is still poorly understood how the polymer/fullerene interactions and arrangements can influence the charge separation and transport in OSCs. It is known that the better the arrangements of intermolecular interfaces between donor and acceptor materials, the better the device performance. For example, it was reported that vertically aligned and ordered layered BHJ morphology can significantly improve the efficiencies of OSCs. [15] However, it is difficult to anticipate experimentally how intermolecular interactions of polymer/fullerene will affect the device performance. Moreover, identifying the factors that control the final structure of a thin film which arises

from a complex of contributions (interactions between donor polymers, between donor polymers and fullerene acceptors, and between fullerene acceptors) poses great challenges (see Figure 1.4). Controlling each one of these three interactions is of great importance for overall device performance. For example, strong interchain  $\pi$ - $\pi$  stacking among conjugated polymers due to highly planar structures with the extended  $\pi$  systems leads to higher hole mobilities and PCEs. [14]

In addition to the interfacial arrangements of the molecular pairings, the electronic structures of polymers and fullerenes may also be affected by these interfacial interactions. [30] For example, it is known that the  $V_{OC}$  of OSCs is currently very low (less than half of the incident photon energy) which limits the efficiencies of OSCs. [31] In general, under the condition of illumination,  $V_{OC}$  is defined as the quasi-Fermi level splitting within the polymer and fullerene phase-separated domains. Based on this observation, the expression of  $V_{OC}$  was obtained as,

$$qV_{OC} = (\Delta\epsilon_{H_D-L_A} - \Delta) - k_B T \ln \frac{n_e n_h}{N_c^2}, \quad (1.2)$$

where  $q$  is the elementary charge,  $\Delta\epsilon_{H_D-L_A}$  is the interfacial energy gap between the HOMO of the donor and the LUMO of the acceptor,  $k_B$  is the Boltzmann constant,  $T$  is the temperature,  $n_e$  and  $n_h$  are the electron and hole densities in the fullerene and polymer domains at open circuit, and  $N_c$  is the density of states at the conduction band edge of the polymer and fullerene. The energy shift,  $\Delta$ , originates from the disorder within the phase separated domains. The  $V_{OC} = \Delta\epsilon_{H_D-L_A} - \Delta$  is generally an accepted value that is obtained at  $T = 0$  K. At  $T \neq 0$  K, many experimental reports have confirmed that  $V_{OC}$ , for given

BHJ OSC containing polymers with band gap,  $E_g$ , is linearly correlated with the difference between the HOMO energy of the donor and the LUMO energy of the acceptor, but with its actual value being reduced by 0.3 V. [31] This approximate linear correlation between the  $V_{OC}$  and  $E_g$  can be clearly seen from  $\Delta\epsilon_{H_D-L_A}$ , since this difference can be rewritten as,

$$\begin{aligned}\Delta\epsilon_{H_D-L_A} &= (\epsilon_{LUMO(polymer)} - \epsilon_{HOMO(polymer)}) \\ &\quad - (\epsilon_{LUMO(polymer)} - \epsilon_{LUMO(fullerene)}) \\ &= E_{g(polymer)} - \Delta\epsilon_{LUMO}.\end{aligned}\tag{1.3}$$

At finite  $T$ , the quasi Fermi levels are shifted into the gap between the HOMO and LUMO levels (i.e. above the HOMO and below the LUMO levels) resulting in a reduction of  $V_{OC}$ . Many reports estimated that the observed reduction in  $V_{OC}$  is approximately 0.3 V which results from the temperature dependence of the quasi-Fermi levels in the polymer and fullerene domains (that is given by the second term of equation (1.2)). [32] Therefore, the common phenomenologically determined expression of  $V_{OC}$  used in designing new materials for OSCs is defined by the following equation,

$$V_{OC} = \frac{1}{q} \{ \Delta\epsilon_{H_D-L_A} \} - 0.3.\tag{1.4}$$

Up to now, most progress in maximizing the  $V_{OC}$  has been made by controlling the energy levels of polymers and fullerenes by increasing the energetic distance between the HOMO of the donor and the LUMO of the acceptor (i.e. by increasing  $\Delta\epsilon_{H_D-L_A}$ ). It has been reported that higher  $V_{OC}$  is obtained with low HOMO levels of donor polymers. [33] However, the HOMO level cannot be greatly reduced because that would increase the band

gap of the donor, and hence the light absorbing ability would be diminished. The above discussion and equation (1.3) illustrate that in addition to  $E_{g(\text{polymer})}$ , other interfacial factors such as  $\Delta\epsilon_{LUMO}$  must be taken into account when maximizing the  $V_{OC}$ . This indicates that understanding and controlling interfacial and electronic properties of OSCs materials in the active layer is not always straightforward. Therefore, one needs to introduce some new insights to push OSC PCEs beyond 12%.

## 1.5 Density Functional Theory in OSCs and OLEDs

Computational investigations play a critical role in determining the best material candidates for OSCs and OLEDs. They can assist researchers in identifying promising organic materials as well as providing explanations to the experimental observations. The most efficient quantum mechanical approach for simulating properties of conjugated materials is the density functional theory (DFT). It is known that the trends in the calculated DFT results on conjugated systems are almost always similar to the corresponding experimental trends. [34-36] In general, many computational studies, that have applied DFT to the polymers/fullerene systems (using for example the well-known B3LYP approximation [37]), produced electronic properties of (isolated) polymers and fullerenes and their absorption spectra (using the time dependent DFT [38, 39]) in the gas phase. The application of these conventional DFT approximations on the polymer/fullerene complexes is not possible due to the well-known DFT failure in describing the van der Waal interactions. Recently, the dispersion-corrected DFT (D-DFT)

methods have been developed to include the effect of intermolecular interactions in molecular systems. However, due to the large size of polymer/fullerene and polymer/polymer combinations, OSCs and OLEDs using D-DFT methods are lacking as opposed to the conventional DFT methods (such as DFT/B3LYP [37] and TD-DFT/B3LYP [38, 39]). In addition, the majority of the studies that have applied D-DFT methods on small combinations such as (P3HT/PCBM) have mainly focused on understanding the mechanism of the interfacial charge transfer excitons. [40-42]

Most computational studies take into account the size of the molecular systems by using approximate approaches that are still relatively accurate but are not prohibitively computationally intensive. For example, one common approach is to employ monomers of polymers or short oligomers in the simulations. It has been shown that this approach provides very accurate results relative to corresponding experimental data (see for example [43, 44]). In this thesis, we employ the D-DFT approximation(s) to investigate the intermolecular interactions between conjugated materials using: 1- a dimer approach (which consists of pairing of two (possibly different) monomers that are not covalently bonded) and 2- a monomer/fullerene approach (which consists of pairing of monomer and fullerene). Hence, this thesis is primarily concerned with the studying of molecular properties of interfacial regions of organic semiconducting materials. Moreover, we apply both approaches to identify common interfacial, structural, and electronic properties of highly efficient devices by seeking correlations between these properties and the (experimentally determined) performance of OSCs and OLEDs. In the analysis of the computed interfacial-property results, good (linear) correlations between computational

and experimental data have little data-point scatter around the fitted line while bad correlations have unclear trends with large data-point scatter.

To the best of our knowledge, no computational studies were found in the literature that employed D-DFT approximations providing an extensive investigation on various monomer/monomer or monomer/fullerene combinations at the interfacial regions of OSCs and OLEDs. In addition, we believe that the work presented in this thesis is successful and provide unique results due to the following reasons: 1- we focus on the interfacial properties of organic molecular combinations instead of the intrinsic properties of isolated organic molecules, 2- we investigate various types of monomers and fullerenes instead of a specific type of polymers/molecules, 3- our results are mainly based on the D-DFT methods instead of conventional DFT and TD-DFT methods, and 4- we search for an answer to a different kind of question such as “what makes certain combinations give higher efficiency than others” whereas most computational studies search for gaining an insight into “what is the interfacial charge-transfer mechanism for a specific type of materials used in organic devices”.

## 1.6 Outline

The remainder of this thesis is organized as follows. In Chapter 2, we give a brief description of the basic theories underlying DFT methods. In Chapter 3, we apply the dimer approach to analyze the intermolecular interactions between bound monomer pairs of different fluorene-based conjugated polymers using D-DFT (B97D) method. We

illustrate how the heterogeneous properties that can be used to determine the best matching between polymers and hence to optimize performance in OLEDs. This computational work is considered as a test case of study of monomers used in organic devices. Since we found the results to be promising, we carried out full assessment of D-DFT methods employed on various monomers and fullerenes used in OSCs in Chapter 4. In Chapter 4, we employ four D-DFT methods to assess their accuracy by computing binding energies, electronic parameters, and optimal properties of the various promising molecular pairings of organic monomers and fullerenes used in OSCs. We select the D-DFT methods that give the consistent binding energies relative to the other D-DFT methods and yield (relative to experimental values) the most accurate electronic and absorption results. In Chapter 5, we analyze the conformations, electronic structures, and binding energies at the interfacial region of various promising homogeneous and heterogeneous pairings of monomers and fullerenes using the D-DFT (B97D3) and the hybrid B3LYP DFT methods. We further test our conclusions on another independent set of monomers and fullerenes to confirm that the common interfacial and electronic properties are present in conjugated materials in OSCs with high PCEs. In Chapter 6, we investigate the influence of alkyl side chains on the binding energies and electronic structures of various molecular pairings of fullerenes and monomers optimized at the D-DFT methods. We also identify favorable side chain arrangements that could be used to optimize the device performance of OSCs. Finally, in Chapter 7, we summarize our results and discuss future work.

# Bibliography

- [1] J.F. Yan, B.R. Saunders, *Third-Generation Solar Cells: A Review and Comparison of Polymer: Fullerene, Hybrid Polymer and Perovskite Solar Cells*, RSC Advances 4 (2014) 43286-43314.
- [2] H. Shirakawa, E.J. Louis, A.G. Macdiarmid, C.K. Chiang, A.J. Heeger, *Synthesis of Electrically Conducting Organic Polymers - Halogen Derivatives of Polyacetylene, (Ch)X*, Journal of the Chemical Society-Chemical Communications 16 (1977) 578-580.
- [3] K.A. Mazzio, C.K. Luscombe, *The Future of Organic Photovoltaics*, Chemical Society Reviews 44 (2015) 78-90.
- [4] M.A. Green, Y. Hishikawa, E.D. Dunlop, D.H. Levi, J. Hohl-Ebinger, A.W.Y. Ho-Baillie, *Solar Cell Efficiency Tables (Version 51)*, Progress in Photovoltaics 26 (2018) 3-12.
- [5] P. Stallinga, *Electrical Characterization of Organic Electronic Materials and Devices* (Wiley, UK, 2009).
- [6] C.W. Tang, S.A. Vanslyke, *Organic Electroluminescent Diodes*, Applied Physics Letters 51 (1987) 913-915.
- [7] H. Ma, H.L. Yip, F. Huang, A.K.Y. Jen, *Interface Engineering for Organic Electronics*, Advanced Functional Materials 20 (2010) 1371-1388.
- [8] C.J. Brabec, S. Gowrisanker, J.J.M. Halls, D. Laird, S.J. Jia, S.P. Williams, *Polymer-Fullerene Bulk-Heterojunction Solar Cells*, Advanced Materials 22 (2010) 3839-3856.
- [9] G.A. Chamberlain, *Organic Solar-Cells - A Review*, Solar Cells 8 (1983) 47-83.
- [10] C.W. Tang, *2-Layer Organic Photovoltaic Cell*, Applied Physics Letters 48 (1986) 183-185.
- [11] G. Yu, J. Gao, J.C. Hummelen, F. Wudl, A.J. Heeger, *Polymer Photovoltaic Cells - Enhanced Efficiencies Via a Network of Internal Donor-Acceptor Heterojunctions*, Science 270 (1995) 1789-1791.
- [12] J.D. Myers, J.G. Xue, *Organic Semiconductors and Their Applications in Photovoltaic Devices*, Polymer Reviews 52 (2012) 1-37.
- [13] C.R. McNeill, N.C. Greenham, *Conjugated-Polymer Blends for Optoelectronics*, Advanced Materials 21 (2009) 3840-3850.
- [14] L.Y. Lu, T.Y. Zheng, Q.H. Wu, A.M. Schneider, D.L. Zhao, L.P. Yu, *Recent Advances in Bulk Heterojunction Polymer Solar Cells*, Chemical Reviews 115 (2015) 12666-12731.
- [15] H.X. Zhou, L.Q. Yang, W. You, *Rational Design of High Performance Conjugated Polymers for Organic Solar Cells*, Macromolecules 45 (2012) 607-632.
- [16] W.L. Ma, C.Y. Yang, X. Gong, K. Lee, A.J. Heeger, *Thermally Stable, Efficient Polymer Solar Cells with Nanoscale Control of the Interpenetrating Network Morphology*, Advanced Functional Materials 15 (2005) 1617-1622.
- [17] M.T. Dang, L. Hirsch, G. Wantz, J.D. Wuest, *Controlling the Morphology and Performance of Bulk Heterojunctions in Solar Cells. Lessons Learned from the Benchmark Poly(3-Hexylthiophene): 6,6 -Phenyl-C-61-Butyric Acid Methyl Ester System*, Chemical Reviews 113 (2013) 3734-3765.

- [18] C. Cabanetos, A. El Labban, J.A. Bartelt, J.D. Douglas, W.R. Mateker, J.M.J. Frechet, M.D. McGehee, P.M. Beaujuge, *Linear Side Chains in Benzo 1,2-B:4,5-B' Dithiophene-Thieno 3,4-C Pyrrole-4,6-Dione Polymers Direct Self-Assembly and Solar Cell Performance*, Journal of the American Chemical Society 135 (2013) 4656-4659.
- [19] Y.Y. Liang, D.Q. Feng, Y. Wu, S.T. Tsai, G. Li, C. Ray, L.P. Yu, *Highly Efficient Solar Cell Polymers Developed Via Fine-Tuning of Structural and Electronic Properties*, Journal of the American Chemical Society 131 (2009) 7792-7799.
- [20] C. Piliago, T.W. Holcombe, J.D. Douglas, C.H. Woo, P.M. Beaujuge, J.M.J. Frechet, *Synthetic Control of Structural Order in N-Alkylthieno 3,4-C Pyrrole-4,6-Dione-Based Polymers for Efficient Solar Cells*, Journal of the American Chemical Society 132 (2010) 7595-7597.
- [21] P.M. Beaujuge, H.N. Tsao, M.R. Hansen, C.M. Amb, C. Risko, J. Subbiah, K.R. Choudhury, A. Mavrinskiy, W. Pisula, J.L. Bredas, F. So, K. Mullen, J.R. Reynolds, *Synthetic Principles Directing Charge Transport in Low-Band-Gap Dithienosilole-Benzothiadiazole Copolymers*, Journal of the American Chemical Society 134 (2012) 8944-8957.
- [22] K.R. Graham, C. Cabanetos, J.P. Jahnke, M.N. Idso, A. El Labban, G.O.N. Ndjawa, T. Heumueller, K. Vandewal, A. Salleo, B.F. Chmelka, A. Amassian, P.M. Beaujuge, M.D. McGehee, *Importance of the Donor:Fullerene Intermolecular Arrangement for High-Efficiency Organic Photovoltaics*, Journal of the American Chemical Society 136 (2014) 9608-9618.
- [23] Z.C. He, C.M. Zhong, S.J. Su, M. Xu, H.B. Wu, Y. Cao, *Enhanced Power-Conversion Efficiency in Polymer Solar Cells Using an Inverted Device Structure*, Nature Photonics 6 (2012) 591-595.
- [24] Y.H. Liu, J.B. Zhao, Z.K. Li, C. Mu, W. Ma, H.W. Hu, K. Jiang, H.R. Lin, H. Ade, H. Yan, *Aggregation and Morphology Control Enables Multiple Cases of High-Efficiency Polymer Solar Cells*, Nature Communications 5 (2014) 5293.
- [25] R.A.J. Janssen, J. Nelson, *Factors Limiting Device Efficiency in Organic Photovoltaics*, Advanced Materials 25 (2013) 1847-1858.
- [26] B. Carsten, J.M. Szarko, H.J. Son, W. Wang, L.Y. Lu, F. He, B.S. Rolczynski, S.J. Lou, L.X. Chen, L.P. Yu, *Examining the Effect of the Dipole Moment on Charge Separation in Donor-Acceptor Polymers for Organic Photovoltaic Applications*, Journal of the American Chemical Society 133 (2011) 20468-20475.
- [27] B. Carsten, J.M. Szarko, L.Y. Lu, H.J. Son, F. He, Y.Y. Botros, L.X. Chen, L.P. Yu, *Mediating Solar Cell Performance by Controlling the Internal Dipole Change in Organic Photovoltaic Polymers*, Macromolecules 45 (2012) 6390-6395.
- [28] Y.X. Li, J.Y. Zou, H.L. Yip, C.Z. Li, Y. Zhang, C.C. Chueh, J. Intemann, Y.X. Xu, P.W. Liang, Y. Chen, A.K.Y. Jen, *Side-Chain Effect on Cyclopentadithiophene/Fluorobenzothiadiazole-Based Low Band Gap Polymers and Their Applications for Polymer Solar Cells*, Macromolecules 46 (2013) 5497-5503.
- [29] X.G. Guo, N.J. Zhou, S.J. Lou, J.W. Hennek, R.P. Ortiz, M.R. Butler, P.L.T. Boudreault, J. Strzalka, P.O. Morin, M. Leclerc, J.T.L. Navarrete, M.A. Ratner, L.X. Chen, R.P.H. Chang, A. Facchetti, T.J. Marks, *Bithiopheneimide-Dithienosilole/Dithienogermole Copolymers for Efficient Solar Cells: Information from Structure-Property-Device Performance Correlations and Comparison to Thieno 3,4-C*

- Pyrrole-4,6-Dione Analogues*, Journal of the American Chemical Society 134 (2012) 18427-18439.
- [30] X. Chen, F.Q. Bai, H.T. Wang, H.X. Zhang, Y.A. Tang, *The Impact of Molecular Stacking Interactions on the Electronic Structure and Charge Transport Properties in Distyrylbenzene (DSB-) Based D-A Complexes: A Theoretical Study*, RSC Advances 5 (2015) 47681-47691.
- [31] N.K. Elumalai, A. Uddin, *Open Circuit Voltage of Organic Solar Cells: An in-Depth Review*, Energy & Environmental Science 9 (2016) 391-410.
- [32] B.Y. Qi, J.Z. Wang, *Open-Circuit Voltage in Organic Solar Cells*, Journal of Materials Chemistry 22 (2012) 24315-24325.
- [33] H. Zhou, L. Yang, W. You, *Rational Design of High Performance Conjugated Polymers for Organic Solar Cells*, Macromolecules 45 (2012) 607-632.
- [34] C. Risko, M.D. McGehee, J.L. Bredas, *A Quantum-Chemical Perspective into Low Optical-Gap Polymers for Highly-Efficient Organic Solar Cells*, Chemical Science 2 (2011) 1200-1218.
- [35] L. Ling, J.B. Lagowski, *DFT Study of Electronic Band Structure of Alternating Triphenylamine-Fluorene Copolymers*, Polymer 54 (2013) 2535-2543.
- [36] L. Ling, J.B. Lagowski, *Electronic Band Structure of Alternating Fluorene-Oxadiazole Conjugated Copolymer - A 1D Solid-State DFT Study*, Journal of Molecular Structure-Theochem 944 (2010) 146-155.
- [37] G. Boschetto, H.T. Xue, J. Dziedzic, M. Krompiec, C.K. Skylaris, *Effect of Polymerization Statistics on the Electronic Properties of Copolymers for Organic Photovoltaics*, Journal of Physical Chemistry C 121 (2017) 2529-2538.
- [38] T.L.D. Tam, T.T. Lin, *Tuning Energy Levels and Film Morphology in Benzodithiophene-Thienopyrrolodione Copolymers Via Nitrogen Substitutions*, Macromolecules 49 (2016) 1648-1654.
- [39] N. Van den Brande, G. Van Lier, F. Da Pieve, G. Van Assche, B. Van Mele, F. De Proft, P. Geerlings, *A Time Dependent DFT Study of the Efficiency of Polymers for Organic Photovoltaics at the Interface with PCBM*, RSC Advances 4 (2014) 52658-52667.
- [40] Y. Kanai, J.C. Grossman, *Insights on Interfacial Charge Transfer across P3HT/Fullerene Photovoltaic Heterojunction from Ab Initio Calculations*, Nano Letters 7 (2007) 1967-1972.
- [41] K. Sen, R. Crespo-Otero, O. Weingart, W. Thiel, M. Barbatti, *Interfacial States in Donor-Acceptor Organic Heterojunctions: Computational Insights into Thiophene-Oligomer/Fullerene Junctions*, Journal of Chemical Theory and Computation 9 (2013) 533-542.
- [42] A.R.S. Kandada, G. Grancini, A. Petrozza, S. Perissinotto, D. Fazzi, S.S.K. Raavi, G. Lanzani, *Ultrafast Energy Transfer in Ultrathin Organic Donor/Acceptor Blend*, Scientific Reports 3 (2013).
- [43] J. Gierschner, J. Cornil, H.J. Egelhaaf, *Optical Bandgaps of Pi-Conjugated Organic Materials at the Polymer Limit: Experiment and Theory*, Advanced Materials 19 (2007) 173-191.
- [44] S.J. Yang, P. Olishovski, M. Kertesz, *Bandgap Calculations for Conjugated Polymers*, Synthetic Metals 141 (2004) 171-177.

# Chapter 2

## 2 Theoretical Approach

In this Chapter, we introduce the theoretical approaches used in this thesis to describe the electronic and interfacial properties of molecular combinations. The main focus of this Chapter is on the density functional theory (DFT) whose main goal is to solve the well-known time-independent Schrödinger equation. This Chapter presents the basic theories underlying DFT methods. This is followed by a description of the dispersion-corrected DFT used to study the intermolecular interactions and a brief explanation of time-dependent DFT to study the absorption properties of the systems of interest.

### 2.1 The Schrödinger Equation

In 1926, Schrödinger [1] developed a time-independent equation that determines precisely the electronic structures of matter. For a system consisting of  $M$  nuclei and  $N$  electrons, this equation is described by,

$$\hat{H}\Psi = E\Psi \tag{2.1}$$

where  $\hat{H}$  is an operator that represents the total Hamiltonian,  $\Psi$  is the total wave function, and  $E$  is the total energy of the molecular system. The Hamiltonian includes the kinetic and potential energies of the many electron system as follows,

$$\hat{H} = -\frac{\hbar}{2m_e} \sum_i^N \nabla_i^2 - \frac{\hbar}{2} \sum_A^M \frac{1}{M_A} \nabla_A^2 - \frac{e^2}{4\pi\epsilon_0} \sum_i^N \sum_A^M \frac{Z_A}{r_{iA}} + \frac{e^2}{4\pi\epsilon_0} \sum_i^N \sum_j^N \frac{1}{r_{ij}} + \frac{e^2}{4\pi\epsilon_0} \sum_A^M \sum_B^M \frac{Z_A Z_B}{R_{AB}}, \quad (2.2)$$

where  $m_e$  is the mass of the electron,  $M_A$  is the mass of the nucleus,  $\nabla_i^2$  is the Laplacian,  $Z_A$  is the nuclear charge of the atom  $A$ ,  $r_{iA}$  is the distance between nucleus  $A$  and electron  $i$ ,  $r_{ij}$  is the distance between electrons  $i$  and  $j$ ,  $R_{AB}$  is the distance between nuclei  $A$  and  $B$ ,  $\epsilon_0$  is the permittivity of free space, and  $\hbar$  is the Plank constant divided by  $2\pi$ . Equation (2.2) can be re-written as,

$$\hat{H} = \hat{T}_e + \hat{T}_n + \hat{V}_{n-e} + \hat{V}_{e-e} + \hat{V}_{n-n}, \quad (2.3)$$

where  $\hat{T}_e$  and  $\hat{T}_n$  represent the electronic and nuclear kinetic energies respectively,  $\hat{V}_{n-e}$  represents the attractive potential energy of nucleus-electron, and  $\hat{V}_{e-e}$  and  $\hat{V}_{n-n}$  represent the repulsive potential energies of electron-electron and nucleus-nucleus respectively.

In order to solve the Schrödinger equation that involves a problem with  $(3N + 3M)$  degrees of freedom, approximations are required. The most popular approximation that took advantage of the fact that nuclei move much more slowly than do electrons is known as Born-Oppenheimer (B.O) approximation. [2] With the assumption that the nuclei are stationary relative to the electrons, the second and last terms of equation (2.3)

are zero and constant respectively, resulting into the following electronic Schrödinger equation,

$$\hat{H}^{elec}\Psi^{elec} = E^{elec}\Psi^{elec}, \quad (2.4)$$

where

$$\hat{H} = -\frac{\hbar}{2m_e}\sum_i^N \nabla_i^2 - \frac{e^2}{4\pi\epsilon_0}\sum_i^N \sum_A^M \frac{Z_A}{r_{iA}} + \frac{e^2}{4\pi\epsilon_0}\sum_i^N \sum_j^M \frac{1}{r_{ij}}. \quad (2.5)$$

Although the approximation made by B.O was successful in reducing the complexity of solving the many-body Schrödinger equation, equation (2.4) is still insolvable for the many-electron systems and further approximations are needed.

## 2.2 Hartree-Fock Method

Hartree-Fock (HF)[3, 4] method is the second approximation that is made to solve the Schrödinger equation by assuming that electrons move independently of each other and can only interact with the average field of other electrons. This assumption requires that the individual electrons are described by functions called spin orbitals  $\psi_i$ . For fermions, the total (multiple-electron) wave function must be anti-symmetric upon interchange of electron coordinates to satisfy Pauli-Exclusion principle. In the HF approximation, the total wave function is often written in the form of a single determinant called the Slater determinant,

$$\Psi = \frac{1}{\sqrt{n!}} \begin{vmatrix} \psi_1(1) & \psi_2(1) & \dots & \psi_n(1) \\ \psi_1(2) & \psi_2(2) & \dots & \psi_n(2) \\ \dots & \dots & \dots & \dots \\ \psi_1(n) & \psi_2(n) & \dots & \psi_n(n) \end{vmatrix}, \quad (2.6)$$

where  $\frac{1}{\sqrt{n!}}$  is the normalization factor for an n-electron determinant. To describe the motional states that electrons have in molecules, linear combination of atomic orbitals (LCAO) approximation was introduced to HF method. Based on the LCAO approximation[5], molecular orbitals ( $\psi_i$ ) are represented in terms of the atomic orbitals ( $\phi$ ):

$$\psi_i = \sum_{\mu} c_{\mu i} \phi_{\mu}, \quad (2.7)$$

where  $c_{\mu i}$  are the molecular orbital coefficients. Applying both HF and LCAO approximations to the electronic Schrödinger equation lead to the HF operator equation:

$$\hat{f}\psi_i = \epsilon_i \psi_i, \quad (2.8)$$

where  $\epsilon_i$  are the orbital energies and  $\hat{f}$  is the HF operator given by,

$$\hat{f} = \hat{h} + \sum_j^N (2\hat{J}_j - \hat{K}_j), \quad (2.9)$$

where  $\hat{h}$  represents the energy of a single electron including the kinetic and nucleus-electron potential energies,  $\sum_j^N (2\hat{J}_j - \hat{K}_j)$  represents the electron-electron repulsion energy of a single electron with all other electrons,  $\hat{J}_j$  and  $\hat{K}_j$  are called the Coulomb and exchange operators, respectively. The HF equation (2.8) can be solved iteratively using the self-consistent field (SCF) method. [6]

## 2.3 Moving Beyond HF Method

The main problem of HF method is that it is inadequate for calculating many observables due to an exclusion of the electron correlation in the HF approximation. The difference between the exact and HF energies is defined as electron correlation energy ( $E_{corr} = E_{exact} - E_{HF}$ ). This correlation energy is due to the fact that the interaction of electrons with different spins is not included in the HF approximation. The major approaches (so called post HF methods) that include correlation energy are the configuration interactions (CI), Moller-Plesset perturbation theory (MP), and the coupled cluster theory (CC). [7] However, these methods are extremely computationally intensive for large molecular systems. Hence, there is a great need for an efficient and less computationally intensive method that can describe their intermolecular properties accurately.

## 2.4 Density Functional Theory

Density functional theory (DFT) is amongst the most widely used and computationally accessible post HF method that includes electron correlations. DFT employs the electron density,  $\rho(x, y, z)$ , instead of the many-electron wavefunction as the main variable. Using the B.O approximation, the DFT electronic energy is written as,

$$E_{elec}[\rho(r)] = T_e[\rho(r)] + V_{n-e}[\rho(r)] + V_{e-e}[\rho(r)] + Q_{e-e}[\rho(r)], \quad (2.10)$$

where the terms represent the kinetic energy of the electrons, the nuclear-electron attractive energy, the electron-electron repulsive energy, and the non-classical electron-electron

repulsive energy respectively. The latter term is a correction to the self-repulsion included in the classical  $V_{e-e}[\rho(r)]$ . The middle terms in equation (2.10) are known and are given as follows,

$$V_{n-e}[\rho(r)] = \sum_A \int \frac{Z_A}{|r-r_A|} \rho(r) dr , \quad (2.11)$$

$$V_{e-e}[\rho(r)] = \frac{1}{2} \int \int \frac{\rho(r_1)\rho(r_2)}{r_{12}} dr_1 dr_2. \quad (2.12)$$

Exact mathematical expressions for  $T_e[\rho(r)]$  and  $Q_{e-e}[\rho(r)]$  are not known and approximations must be used for them. Circa 1930, Thomas and Fermi [8, 9] developed a simple approximation to  $T_e[\rho(r)]$  which is exact for a uniform electron gas. However, Thomas-Fermi method failed in many ways (e.g. it could not reproduce chemical bonds), and therefore, this method had been abandoned until the middle of 1960. The concept of Thomas-Fermi method was revived to motivate the DFT formalism. [10, 11]

## 2.4.1 Hohenberg-Kohn Theorems

In 1964, Hohenberg and Kohn [12] formulated two fundamental theorems of DFT. The first theorem (after called the existence theorem) states that all the ground state electron properties of a system are determined uniquely by the ground state electron density function  $\rho_0(x, y, z)$  as obtained in the presence of an external potential,  $v$ , and the ground state energy of a molecule is a functional of the  $\rho_0(x, y, z)$  i.e.,

$$E_0 = E_0[\rho_0]. \quad (2.13)$$

The exact ground state energy functional is not known. The second theorem uses the energy variational principle that states that any trial electron density function ( $\rho_t$ ) will give energy higher than or equal to the true ground state energy calculated with  $\rho_0$ , that is,

$$E_v[\rho_t] \geq E_0[\rho_0], \quad (2.14)$$

where  $E_v$  is the electronic energy of the system.

## 2.4.2 Kohn-Sham Formalism

In 1965, Kohn and Sham [13] proposed a practical approach that employed Hohenberg and Kohn theorems to obtain the electronic properties of molecular systems. They solved the hindrance of not having accurate kinetic energy functionals by assuming that the kinetic energy describes a fictitious system of non-interacting electrons that has the same density as the original set of interacting electrons. The kinetic energy of the non-interacting electrons can be approximated by a single Slater determinant of Kohn-Sham orbitals ( $\psi_i^{KS}$ ), and it is given by,

$$T_s[\{\psi_i^{KS}\}] = -\frac{1}{2} \sum_i \int \psi_i^{KS}(r) \nabla^2 \psi_i^{KS}(r) dr. \quad (2.15)$$

The Kohn-Sham orbitals give the electron density as follows,

$$\rho(r_1) = \sum_i^N |\psi_i^{KS}(r_1)|^2. \quad (2.16)$$

To obtain the Kohn-Sham orbitals, the variational principle, that requires the energy to be minimum with respect to  $\psi_i^{KS}$ , was used to obtain Kohn-Sham equations,

$$\hat{h}^{KS}\psi_i^{KS} = \epsilon_i\psi_i^{KS}, \quad (2.17)$$

where  $\hat{h}^{KS}$  is the Kohn-Sham operator and it is represented as,

$$\hat{h}^{KS} = \hat{h} + \sum_j^N 2\hat{f}_j + v_{xc}, \quad (2.18)$$

where  $\hat{h}$  is the energy of a single electron including the kinetic and nucleus-electron potential energies,  $\hat{f}_j$  is the Coulomb operator, and  $v_{xc}$  is the exchange-correlation potential functional. The difference between Kohn-Sham operator in equation (2.18) and HF operator in equation (2.8) is  $v_{xc}$  which replaces the HF exchange operator. The exchange-correlation potential functional is given as the functional derivative of the exchange-correlation energy functional with respect to the electron density,

$$v_{xc} = \frac{\delta E_{xc}}{\delta \rho}, \quad (2.19)$$

where  $E_{xc}[\rho]$  is the exchange-correlation energy functional (see below). Similar to HF equations, Kohn-Sham equations are solved iteratively using the SCF method.

Since the kinetic energy of the non-interacting system in equation (2.15) is not equal to  $T_e[\rho(r)]$ , the difference between both terms is added to the non-classical electronic repulsive energy  $Q_{e-e}[\rho(r)]$  to define the exchange-correlation functional ( $E_{xc}[\rho]$ ),

$$E_{xc}[\rho(r)] \equiv T_e[\rho(r)] - T_s[\{\psi_i^{KS}\}] + Q_{e-e}[\rho(r)]. \quad (2.20)$$

Therefore, based on Kohn-Sham DFT approach, equation (2.10) for the electronic energy of an N-electron system can be expressed as,

$$E_{elec} = -\frac{1}{2}\sum_i \int \psi_i^{KS}(r)\nabla^2\psi_i^{KS}(r)dr + \sum_A \int \frac{Z_A}{|r-r_A|}\rho(r)dr + \frac{1}{2}\int\int\frac{\rho(r_1)\rho(r_2)}{r_{12}}dr_1dr_2 + E_{XC}[\rho]. \quad (2.21)$$

The only unknown term in equation (2.21) is the exchange-correlation functional, hence, approximations are required. In the past 30 years, many accurate approximations to  $E_{XC}[\rho]$  have been proposed, leading to a great accumulation of knowledge of electronic and structural properties in several areas in molecular and solid state physics. [11] In this thesis, the main approach for investigating the intermolecular interactions of monomers and fullerenes used in OLEDs and OSCs is the dispersion corrected-DFT methods. Since this approach is built on the conventional DFT approximations, we describe in the following section the DFT functionals that are developed prior to the addition of the dispersion correction.

## 2.5 Classification of Exchange-Correlation Functionals

### 2.5.1 LDA Functionals

The local density approximation (LDA) forms the foundation for most of the other (more advanced) exchange-correlation functionals. The original LDA uses only the local density of a uniform electron gas in  $E_{XC}$ . In this model, the local exchange-correlation energy functional is often expressed as,

$$E_{xc}[\rho(r)] = \int \rho(r)\epsilon_{xc}[\rho(r)]dr , \quad (2.22)$$

where  $\epsilon_{xc}[\rho(r)]$  is the energy density of a uniform electron gas and it is often represented as a sum of exchange and correlation energies,

$$\epsilon_{xc} = \epsilon_x + \epsilon_c . \quad (2.23)$$

The exact form of LDA exchange functional part for this model is given by,

$$E_x^{LDA}[\rho(r)] = -\frac{3}{4}\left(\frac{3}{\pi}\right)^{1/3} \int [\rho(r)]^{4/3} dr . \quad (2.24)$$

The LDA correlation functional part has been approximated by Vosko, Wilk and Nusair (VWN) [14] (it has a very complicated function many parameters functional form). For open shell systems, the electronic density is replaced by the spin electronic densities ( $\rho_\alpha$  and  $\rho_\beta$ ), and the method is often referred to as the local spin density approximation (LSDA). However, because most real systems have inhomogeneous density distributions, these functionals lead to inaccurate molecular properties. [11]

Many different DFT approximations of the exchange-correlation functionals treat the individual exchange and correlation contributions separately. The various exchange-correlation functionals are classified based on their formulations.

## 2.5.2 GGA Functionals

The best-known approximation after LDA is the generalized gradient approximation (GGA). It uses both the local electron density ( $\rho$ ) and the gradient of the electron density ( $\nabla\rho$ ) which accounts for the inhomogeneities in the density. Thus,

$$E_{xc}^{GGA}[\rho(r)] = \int \rho(r) \varepsilon_{xc}[\rho(r), \nabla\rho(r)] dr . \quad (2.25)$$

The general form of most GGA functionals, which includes the LDA functional, is given by,

$$\varepsilon_{xc}^{GGA}[\rho(r)] = \varepsilon_{xc}^{LDA}[\rho(r)] + \Delta\varepsilon_{xc}\left[\frac{\nabla\rho(r)}{\rho^{4/3}(r)}\right] . \quad (2.26)$$

Some of the most common GGA exchange functionals are PBE [15], B [16], and PW91 [17], while some of the most popular GGA correlation functionals are LYP [18], PBE [15], and PW91 [17]. These functionals can be combined to obtain GGA exchange-correlation functionals. Although GGA functionals include more information than LDA functionals, they are not always accurate, hence additional factors need to be considered for the exchange-correlation functional in order to improve the accuracy of DFT.

## 2.5.3 Hybrid Functionals

Today, the most commonly used DFT functionals are the hybrid functionals which mix the GGA functionals with a fraction of the HF exchange term. The general form of a hybrid density functional is given by,

$$E_{XC} = c_X E_X^{HF} + E_{XC}^{DFT}, \quad (2.27)$$

where  $c_X$  is a small fractional number. The main distinguishing characteristic of the hybrid functionals is the percentage of HF exchange energy used. Some of the most popular hybrid functionals that have shown remarkable accuracy for many molecular systems are:

- **B3LYP** [19] is the first hybrid functional and most widely used method in all DFT calculations. Using Becke's three parameters, this functional connects between the HF exchange integral and the LSDA exchange functional and between the Lee, Yang, and Parr's (LYP) GGA correlation functional and the LSDA correlation functional, and adds the GGA term of Becke (B) exchange functional as follows,

$$E_{XC}^{B3LYP} = (1 - a)E_X^{LSDA} + aE_X^{HF} + b\Delta E_X^B + (1 - c)E_C^{LSDA} + cE_C^{LYP}, \quad (2.28)$$

where a, b, and c are the three parameters (i.e. "3" in "B3LYP" indicates the number of parameters).

- **PBE0** [20] is another important hybrid functional that was developed by Adamo and Barone. It uses the PBE GGA exchange-correlation functional as a reference and combines 75% of PBE GGA exchange functional and 25% of HF exchange integral as follows,

$$E_{XC}^{PBE0} = E_{XC}^{PBE} + \frac{1}{4}(E_X^{HF} - E_X^{PBE}), \quad (2.29)$$

The simplicity of the PBE0 hybrid functional form and the lack of parameters in the functional made it a widely applicable method for quantum chemistry. Note that the PBE0 functional is labeled as PBE1PBE in Gaussian software.

- **B97** [21] was developed by Becke in 1997 (i.e. B97) who proposed to expand the GGA exchange-correlation functional using power series expansions that include the local spin density and its first derivative, in combination with a small fraction of the HF exchange as follows,

$$E_{XC}^{B97} = E_X^{B97} + E_C^{B97} + c_X E_X^{HF}, \quad (2.30)$$

$$E_X^{B97} = \sum_{\sigma}^{\alpha,\beta} \int \varepsilon_{X,\sigma}^{LSDA}(\rho_{\sigma}) g_{X,\sigma}^{B97}(s_{\sigma}^2) dr, \quad (2.31)$$

$$g_{X,\sigma}^{B97}(s_{\sigma}^2) = \sum_{i=0}^N c_{X\sigma,i} u_{X\sigma}^i, \quad (2.32)$$

$$u_{X\sigma} = \gamma_{X\sigma} s_{\sigma}^2 (1 + \gamma_{X\sigma} s_{\sigma}^2)^{-1}, \quad (2.33)$$

$$s_{\sigma} = \frac{|\nabla\rho(r)|}{\rho^{4/3}(r)}, \quad (2.34)$$

$$\gamma_{X\sigma} = 0.004, \quad (2.35)$$

where  $\sigma$  denotes  $\alpha$  or  $\beta$  spin,  $g$  denote gradient correction factors that depend on the reduced gradient density ( $s_{\sigma}$ ),  $u_{X\sigma}$  is the expansion function, and the linear coefficients ( $c_{X\sigma,i}$ ) of the expansions are optimized using a systematic fitting procedure to a set of experimental data. A similar format is used for the B97 correlation functional. The resulting B97 exchange-correlation functional lead to the development of many accurate functionals such as  $\omega$ B97x which will be mentioned in the following section.

## 2.6 Corrections Beyond Ground State Conventional DFT

Remarkable success has been observed in the last twenty years for DFT in obtaining the most accurate and fastest approaches for the electronic structure calculations for various molecular systems. However, it is known that the conventional DFT functionals neglected certain physical properties such as the long-range electron-electron exchange interaction and dispersion interaction which is a pure electron-electron correlation, which are important in determining properties of noncovalently bonded systems. Hence, various types of corrections were developed to incorporate these particular physical properties.

### 2.6.1 Long-Range Correction

The long-Range correction was made to the conventional exchange functionals since they do not include explicitly electron-electron interactions at large distances (as  $r \rightarrow \infty$ ). To formulate the long-range correction, the electron-electron interaction can be divided into two parts, short and long, as follows,

$$\frac{1}{r} = \frac{1-g(r)}{r} + \frac{g(r)}{r}, \quad (2.36)$$

where  $g(r)$  is a function that is assumed to be the error function  $erf(\omega r)$ , and  $\omega$  is a parameter. The first term in equation (2.36) represents the short-range operator, and the second term represents the long-range operator. The basic idea of this approach is to use a

DFT exchange functional for the short-range (SR) term and a 100% HF exchange for the long-range (LR) term. This lead to the following form of the long-range corrected functional,

$$E_{XC} = E_X^{HF,LR} + E_X^{DFT,SR} + E_C^{DFT}. \quad (2.37)$$

- **$\omega$ B97x** [22], which is one of the most popular long-range corrected functionals, includes a long-range correction to the B97 hybrid functional. That is, it includes 100% long-range HF exchange, a small fraction of short-range HF exchange, short-range B97 exchange functional, and B97 correlation functional as follows,

$$E_{XC}^{\omega B97x} = E_X^{HF,LR} + c_X E_X^{HF,SR} + E_X^{B97,SR} + E_C^{B97}, \quad (2.38)$$

where  $c_X$  is a fractional number.

## 2.6.2 Dispersion Correction

Dispersion interaction (van der Waals type of interactions) has been neglected in DFT correlation functionals even though it is a significant contribution to the correlation energy, especially for the noncovalently bonded systems. Dispersion can be described as an attractive interaction that originates between instantaneous dipole moments within the electron distributions of two distant atoms or molecules. As a classical expression, the London-dispersion interaction is governed by the well-known relationship,

$$E_{disp} \propto \frac{C_6}{R^6}, \quad (2.39)$$

where  $C_6$  is the dispersion coefficient and  $R^6$  is the distance between two molecular or atomic fragments. Equation (2.39) shows that the dispersion energy depends on the sixth power of the distance between these fragments, indicating that it is naturally a non-local term. Since DFT calculations contain only short-range contributions to the electron correlations, this long-range regime of the dispersion energy cannot be incorporated in conventional correlation DFT functionals. Therefore, conventional DFT calculations always fail to describe the long-range dispersion interactions. So far, many approaches have been suggested to include the dispersion corrections. Of these approaches, the so called D-DFT (dispersion-corrected DFT) is the most promising. It is very well-tested, and accurate technique which is described in the following section.

## 2.7 The D-DFT Approach

The D-DFT approach includes the dispersion correction by simply adding the empirical dispersion term to the Kohn-Sham energy obtained using the DFT KS method ( $E_{KS-DFT}$ ). Hence, the total energy is given by,

$$E_{D-DFT} = E_{KS-DFT} + E_{disp}. \quad (2.40)$$

The dispersion correction is computed separately after the conventional DFT computation is performed. The small effect of the dispersion interaction on the electron densities allows the correction to be calculated separately. Therefore, the D-DFT approach is performed at

negligible computational cost which in turn makes it an attractive technique for large molecular systems. Grimme adopted this approach and developed two versions of corrections (DFT-D2 [23] and DFT-D3 [24]) that refined his original version DFT-D1. Grimme’s DFT-D2 and -D3 can be combined with any DFT functional. For example, the B97-D functional that utilize DFT-D2 was the first successful attempt for Grimme’s dispersion correction. Also, it was reported that the addition of dispersion corrections provide a notable improvement over the uncorrected functionals (such as B3LYP and PBE0). [24] The same is also applied for long-range hybrid functionals that benefit from Grimme’s dispersion corrections. For example, the  $\omega$ B97x-D and  $\omega$ B97x-D3 are long-range hybrid functionals that utilise the DFT-D2 and -D3 corrections, respectively. The following subsections focus on describing both corrections.

### 2.7.1 The DFT-D2 Correction

The DFT-D2 correction considers the dispersion contributions of all atom pairs in a given molecular system that will be then summed up to obtain the following dispersion formula,

$$E_{\text{disp}}^{\text{DFT-D2}} = -s_6 \sum_{A \neq B} \frac{C_6^{AB}}{R_{AB}^6} f_{\text{damp}}^{\text{DFT-D2}}(R_{AB}), \quad (2.41)$$

where  $R_{AB}$  is the distance between atom  $A$  and  $B$ ,  $C_6^{AB}$  is a dispersion coefficient for atom  $A$  and  $B$ ,  $f_{\text{damp}}^{\text{DFT-D2}}$  is a damping function, and  $s_6$  is a global scaling parameter that depends on the DFT used. [25] When equation (2.41) is substituted in equation (2.40), the electron correlations of the long-range region are treated equally well as that of the short-range

region. To obtain a smooth connection between the short and long-region parts, the damping function is determined as follows,

$$f_{\text{damp}}^{\text{DFT-D2}}(R_{AB}) = \frac{1}{1 + e^{-20(\frac{R_{AB}}{R_r} - 1)}}, \quad (2.42)$$

where  $R_r$  is the sum of van der Waals radii. Equation (2.42) indicates that  $f_{\text{damp}}^{\text{DFT-D2}}$  is reduced to 1 at large  $R_{AB}$ , and vanished at small  $R_{AB}$ . The dispersion coefficients are determined from element-specific dispersion coefficients using,

$$C_6^{AB} = \sqrt{C_6^A C_6^B}, \quad (2.43)$$

$$C_6^A = 0.05N \times \text{IP}^A \times \alpha^A, \quad (2.44)$$

where  $\text{IP}^A$  and  $\alpha^A$  (that are given in atomic units) are the respective atomic ionization potential and dipole polarizability for an atom  $A$ , and  $N$  can be 2, 10, 18, 36, or 54 depending on the respective element's row in the periodic table.

The DFT-D2 corrections have been combined with various DFT functionals such as B97-D and  $\omega$ B97x-D functionals. [26] We note that for the B97-D, Grimme modified the Becke's B97 functional to re-determine the linear parameters in equation (2.32) by a least squares fit in order to account better for the inclusion of the dispersion correction. [23] It has been shown that DFT-D2 provided a good description of dispersion interactions in many molecular systems. This approximation also shows the importance of including the London dispersion in general thermochemistry. However, the shortcomings of this approach (such as, for example, the Van der Waals radii and dispersion coefficients were

only obtained for elements up to xenon) motivated the development of DFT-D3 correction. [27]

## 2.7.2 The DFT-D3 Correction

The DFT-D3 dispersion correction can be described as,

$$E_{\text{disp}}^{\text{DFT-D3}} = -\frac{1}{2} \sum_{A \neq B} \sum_{n=6,8} s_n \frac{C_n^{AB}}{R_{AB}^n} f_{\text{damp},n}^{\text{DFT-D3}}(R_{AB}). \quad (2.45)$$

Equation (2.45) shows that the DFT-D3 depends on two multipole terms: the sixth-order with dispersion coefficient  $C_6^{AB}$ , and the eighth-order with dispersion coefficient  $C_8^{AB}$ . The latter multipole term, which decays to zero at shorter distances, is designed to take into account the medium interatomic distances. Similar to DFT-D2, the DFT-D3 damping functions are used to avoid near singularities and double-counting effect of correlations at the medium-range. The DFT-D3 damping functions for the sixth-order and eighth-order terms are expressed as,

$$f_{\text{damp},n}^{\text{DFT-D3}}(R_{AB}) = \frac{1}{1 + e^{-\gamma(R_{AB}/s_{r,n}R_0^{AB})^{-1}}}, \quad (2.46)$$

where  $s_{r,6}$  is a scale factor that depends on the DFT functional,  $s_{r,8}$  is fixed to unity,  $R_0^{AB}$  is the cut-off radius for the AB atom pair, and  $\gamma$  (which is set to 14 and 16 for the  $R^{-6}$  and  $R^{-8}$  terms, respectively) is a global constant that determines the steepness of the damping function.

### 2.7.3 Comparison between DFT-D2 and -D3

As mentioned in section 2.7.1, the DFT-D2 correction is applied for elements up to xenon. In contrast, the DFT-D3 correction can be applied for the first 94 elements of the periodic table. The significant difference between the two approaches is that DFT-D3 features flexible  $C_n^{AB}$  which depends on the coordination sphere of each atom within a molecule. Hence, the dispersion coefficients  $C_n^{AB}$  in DFT-D3 are system dependent while the  $C_6^{AB}$  in DFT-D2 are fixed for each element. DFT-D3 is therefore more accurate and flexible than DFT-D2 method.

It is clear from subsections 2.6.1 and 2.6.2 that the DFT-D2 and -D3 differ also by the number of parameters in the dispersion corrections that can be adjusted. In fact, the DFT-D2 requires, for each DFT functional, one fit parameter ( $s_6$ ), whereas DFT-D3 requires two fit parameters ( $s_{r,6}$  and  $s_8$ ). These parameters are determined using a least-squares fit of 130 noncovalent interaction energies. [25] In the DFT-D2 correction, the global scaling parameters ( $s_6$ ) are fitted empirically, for each DFT method, to take into account the different behavior of DFT functionals in the short- and medium-range regimes. For instance, they are found to be 1.05 for B3LYP and 1.25 for B97-D functionals. [23] In contrast,  $s_6$  are kept fixed at unity in the DFT-D3 correction whereas  $s_8$  are needed to be adjusted empirically for each DFT method.

The above comparison between DFT-D2 and -D3 show that the DFT-D3 without doubt is the best of choice for the dispersion corrected DFT calculations. However, both DFT-D2 and -D3 corrections have been extensively benchmarked when combined with

DFT functionals, and they both lead to improvements such as increased accuracy in the computational chemistry which involves noncovalently bonded molecular systems. [27]

## 2.7.4 Selection of a D-DFT Method

Many of DFT methods that are devoted to approximating the exchange-correlation functionals are available and useful in describing molecular geometry, electronic properties, and others. However, the excess of the proposed methods makes selecting the appropriate DFT functional challenging. Since the D-DFT methods include similar dispersion terms and various KS DFT functionals, the choice of a D-DFT method is based on the exchange-correlation functionals (which are described in section 2.5). In this thesis, we limit our selection of the D-DFT approaches to the most popular methods that include different flavors of exchange-correlation functionals. We consider the following set of D-DFT methods: B3LYP-D3, PBE0-D3, B97-D(3), and  $\omega$ B97x-D. The first two functionals have been successfully applied (without the dispersion corrections) to a wide range of sizes and geometries of molecular systems, and have performed well for many important properties (except for the noncovalent interactions). Since the PBE0 approximation is not a parametrized method for any certain chemistry, it generally provides consistent results for different molecular systems. The excellent performance of B3LYP, particularly for organic molecular systems, has been numerous reported in literature, which in turn have made it the most widely used DFT method in the past two decades. However, hybrid functionals are known to provide inaccurate description of the conjugation, planarity, bond

length alternation, and HOMO energies with growing chain length in conjugated polymers. [28-30] Anyhow, it is expected that the addition of Grimme's dispersion correction to the PBE0 and B3LYP will not only provide an improvement to the description of noncovalent interactions but also an improvement to the basic properties of molecular systems. Currently, the B97-D(3) and  $\omega$ B97x-D approximations are the most recommendable D-DFT methods for non-covalent interactions. In particular, the  $\omega$ B97x-D method is suitable for conjugated systems at all chain lengths. In addition, the B97-D(3) method provides a good balance between the computational expediency and the accuracy. Although both D-DFT methods are capable to produce reliable orbital energies, their drawback is that they produce HOMO–LUMO energy gaps that deviate by one or more eVs from the experimental data. [30] In this case, the single point B3LYP calculations performed on the optimized geometries of D-DFT methods work best for the electronic structures of organic systems as they deviate by less than 0.2 eV with respect to the experimental data. [31]

## 2.8 Time-Dependent DFT

DFT as described thus far is limited only to the calculation of the electronic ground states. To calculate many of the properties of molecules associated with either excited states or time-dependent external fields, time-dependent density-functional theory (TD-DFT) is required. TD-DFT is based on the time-dependent Schrodinger equation for the many-electron wavefunction  $\Psi(t)$ . It is given by:

$$i \frac{\partial}{\partial t} \Psi(t) = \hat{H}(t) \Psi(t), \quad (2.47)$$

$$\hat{H}(t) = \hat{T} + \hat{V}_{e-e} + \hat{V}_{ext}(t), \quad (2.48)$$

where  $\hat{T}$  is the kinetic energy,  $\hat{V}_{e-e}$  is the electron-electron repulsion, and  $\hat{V}_{ext}(t)$  is the external potential that includes the nuclear attraction and any field applied to the system. Runge and Gross [32] developed the central theorem of TD-DFT that states that there is a one-to-one correspondence between the time dependent external potential  $v_{ext}(r, t)$  and the time-dependent electron density  $\rho(r, t)$ . This theorem implies that TD-DFT is an extension of Hohenberg-Kohn theorem to the time-dependent systems by showing that all observable properties of many-electron system, starting from a given initial state  $\Psi(0)$ , can be extracted from the time-dependent density. Thus, the density of the interacting many electron system is obtained as the density of the non-interacting system using the time-dependent KS equations:

$$i \frac{\partial}{\partial t} \psi_i(r, t) = \left( -\frac{\nabla^2}{2} + v_{KS}[\rho](r, t) \right) \psi_i(r, t) \quad (2.49)$$

The time-dependent Kohn-Sham potential again includes the exchange-correlation energy which is unknown, hence, it is required to be approximated. The most popular application of TD-DFT is the calculation of the excitations and (absorption and emission) spectra using the B3LYP functional. [33] It is also possible to use the D-DFT functionals in the TD-DFT calculations.

# Bibliography

- [1] E. Schrodinger, *An Undulatory Theory of the Mechanics of Atoms and Molecules*, Physical Review 28 (1926) 1049-1070.
- [2] M. Born, R. Oppenheimer, *Quantum Theory of Molecules*, Annalen Der Physik 84 (1927) 0457-0484.
- [3] V. Fock, *Approximation Method for the Solution of the Quantum Mechanical Multibody Problems*, Zeitschrift Fur Physik 61 (1930) 126-148.
- [4] J.C. Slater, *Note on Hartree's Method*, Physical Review 35 (1930) 0210-0211.
- [5] J.E. Lennard-Jones, *The Electronic Structure of Some Diatomic Molecules*, Transactions of the Faraday Society 25 (1929) 0668-0685.
- [6] A. Szabo, N.S. Ostlund, *Modern Quantum Chemistry: Introduction to Advanced Electronic Structure Theory* (McGRAW-HILL Publishing Company, 1989).
- [7] T. Engel, *Quantum Chemistry & Spectroscopy* (Pearson Education, USA, 2013).
- [8] L.H. Thomas, *The Calculation of Atomic Fields*, Proceedings of the Cambridge Philosophical Society 23 (1927) 542-548.
- [9] E. Fermi, *A Statistical Method for Determining Some Properties of the Atoms and Its Application to the Theory of the Periodic Table of Elements*, Zeitschrift Fur Physik 48 (1928) 73-79.
- [10] T. Tsuneda, *Density Functional Theory in Quantum Chemistry* (Springer, Japan, 2014).
- [11] N. Mardirossian, M. Head-Gordon, *Thirty Years of Density Functional Theory in Computational Chemistry: An Overview and Extensive Assessment of 200 Density Functionals*, Molecular Physics 115 (2017) 2315-2372.
- [12] P. Hohenberg, W. Kohn, *Inhomogeneous Electron Gas*, Physical Review B 136 (1964) B864-B871.
- [13] W. Kohn, L.J. Sham, *Self-Consistent Equations Including Exchange and Correlation Effects*, Physical Review 140 (1965) A1133-A1138.
- [14] S.H. Vosko, L. Wilk, M. Nusair, *Accurate Spin-Dependent Electron Liquid Correlation Energies for Local Spin-Density Calculations - a Critical Analysis*, Canadian Journal of Physics 58 (1980) 1200-1211.
- [15] J.P. Perdew, K. Burke, M. Ernzerhof, *Generalized Gradient Approximation Made Simple*, Physical Review Letters 77 (1996) 3865-3868.
- [16] A.D. Becke, *Density-Functional Exchange-Energy Approximation with Correct Asymptotic-Behavior*, Physical Review A 38 (1988) 3098-3100.
- [17] J.P. Perdew, J.A. Chevary, S.H. Vosko, K.A. Jackson, M.R. Pederson, D.J. Singh, C. Fiolhais, *Atoms, Molecules, Solids, and Surfaces - Applications of the Generalized Gradient Approximation for Exchange and Correlation*, Physical Review B 46 (1992) 6671-6687.

- [18] C.T. Lee, W.T. Yang, R.G. Parr, *Development of the Colle-Salvetti Correlation-Energy Formula into a Functional of the Electron-Density*, Physical Review B 37 (1988) 785-789.
- [19] A.D. Becke, *Density-Functional Thermochemistry .3. The Role of Exact Exchange*, Journal of Chemical Physics 98 (1993) 5648-5652.
- [20] C. Adamo, V. Barone, *Toward Reliable Density Functional Methods without Adjustable Parameters: The PBE0 Model*, Journal of Chemical Physics 110 (1999) 6158-6170.
- [21] A.D. Becke, *Density-Functional Thermochemistry .5. Systematic Optimization of Exchange-Correlation Functionals*, Journal of Chemical Physics 107 (1997) 8554-8560.
- [22] J.-D. Chai, M. Head-Gordon, *Systematic Optimization of Long-Range Corrected Hybrid Density Functionals*, Journal of Chemical Physics 128 (2008) 084106.
- [23] S. Grimme, *Semiempirical GGA-Type Density Functional Constructed with a Long-Range Dispersion Correction*, Journal of Computational Chemistry 27 (2006) 1787-1799.
- [24] L. Goerigk, S. Grimme, *A Thorough Benchmark of Density Functional Methods for General Main Group Thermochemistry, Kinetics, and Noncovalent Interactions*, Physical Chemistry Chemical Physics 13 (2011) 6670-6688.
- [25] S. Grimme, J. Antony, S. Ehrlich, H. Krieg, *A Consistent and Accurate Ab Initio Parametrization of Density Functional Dispersion Correction (DFT-D) for the 94 Elements H-Pu*, Journal of Chemical Physics 132 (2010) 154104.
- [26] J.D. Chai, M. Head-Gordon, *Long-Range Corrected Hybrid Density Functionals with Damped Atom-Atom Dispersion Corrections*, Physical Chemistry Chemical Physics 10 (2008) 6615-6620.
- [27] A.O. de la Roza, G.A. DiLabio, *Non-Covalent Interactions in Quantum Chemistry and Physics* (Elsevier, Amsterdam, Netherlands, 2017).
- [28] M. Wykes, B. Milian-Medina, J. Gierschner, *Computational Engineering of Low Bandgap Copolymers*, Frontiers in Chemistry 1 (2013).
- [29] M. Niskanen, T.I. Hukka, *Modeling of Photoactive Conjugated Donor-Acceptor Copolymers: The Effect of the Exact Hf Exchange in DFT Functionals on Geometries and Gap Energies of Oligomer and Periodic Models*, Physical Chemistry Chemical Physics 16 (2014) 13294-13305.
- [30] U. Salzner, A. Aydin, *Improved Prediction of Properties of Pi-Conjugated Oligomers with Range-Separated Hybrid Density Functionals*, Journal of Chemical Theory and Computation 7 (2011) 2568-2583.
- [31] M.J. Eslamibidgoli, J.B. Lagowski, *The Effect of Side-Chain Length on the Solid-State Structure and Optoelectronic Properties of Fluorene-Alt-Benzothiadiazole Based Conjugated Polymers-A DFT Study*, Journal of Physical Chemistry A 116 (2012) 10597-10606.
- [32] E. Runge, E.K.U. Gross, *Density-Functional Theory for Time-Dependent Systems*, Physical Review Letters 52 (1984) 997-1000.
- [33] N.T.M. Miguel A.L. Marques, Fernando M.S. Nogueira, E.K.U. Gross, *Fundamentals of Time-Dependent Density Functional Theory* (Springer, Berlin, Heidelberg, 2012).

# Chapter 3

## 3 Optimizing the Performance of Multilayered Organic Polymer Devices Using Computational Dimer Approach – A Case Study

Reproduced with permission from Sarah A. Ayoub and Jolanta B. Lagowski, *Journal of Physical Chemistry C*, 2016, 120, 496–507.

### 3.1 Abstract

The construction of multilayered organic polymer devices often involves long experimental searches for the combinations of polymers that give the optimum device performance. Combinations of different fluorene-based conjugated polymers such as alternating triphenylamine-fluorene (TPAF)- and oxadiazole-fluorene (OxF)-based conjugated copolymers were considered as components of multilayered organic light-emitting diodes (OLEDs). It was found that OxF3-TPAF2 combination gave the best OLED performance. Theoretical/experimental investigations of the properties of single (isolated) polymer chains did not yield conclusive evidence for choosing OxF3-TPAF2

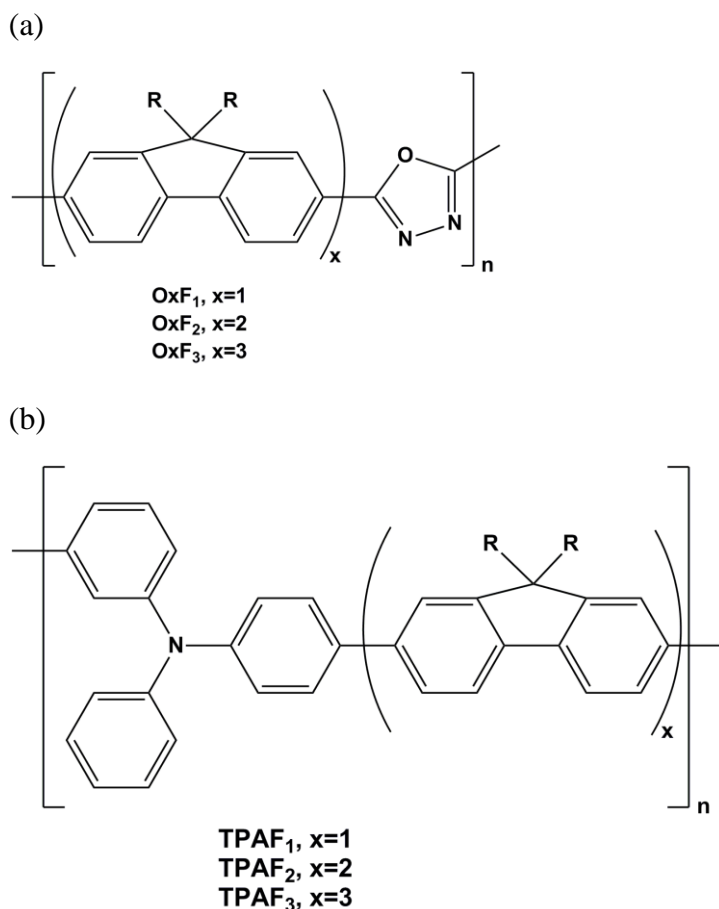
over other similar combinations. For multilayered OLEDs, the interfacial region is critical to the performance of a device. Hence, in this work, we focus on studying the properties of the various pairs of monomers of OxFn and TPAFn (n=1-3) copolymers. We analyze their electronic structures and binding energies using the dispersion-corrected density functional theory (DFT/B97D) method. Our results illustrate that the (empirically favourable) combination of OxF3 and TPAF2 monomers, with their chain lengths and HOMO-LUMO energy gaps well matched, has the closest intermolecular distance and the highest binding energy of all the combinations of OxFn and TPAFn (n=1-3) monomers. This study illustrates that (heterogeneous) dimer properties can be used to determine the best matching between polymers and hence optimal performance in multilayered devices.

## 3.2 Introduction

Organic conjugated polymers have been and are attracting much attention in material science due to their promising potential in optoelectronic devices such as organic light-emitting diodes (OLEDs) and organic photovoltaic cells (OPVCs). OLED or OPVC can be made simply by sandwiching one or more layers of organic thin film between two electrodes. In each case, charge transport is the key property that determines the device performance. [1-3] Today, heterogeneous structures (such as multilayered OLEDs or bulk heterojunction OPVCs) are essential for the improved performance of these devices. [4-8] The initial selection of polymers, used in multilayered applications, is based on the individual polymer properties such as its highest occupied and lowest unoccupied

molecular orbital (HOMO and LUMO) eigenvalues, HOMO-LUMO energy gap ( $E_g$ ) absorption spectrum, charge mobility, and others. [9-12] In addition, for the multilayered OLEDs or OPVCs, the interfacial (heterogeneous) region plays a critical role in the charge transport and, hence, in the device performance.

Fluorene-based polymers have been employed in heterogeneous structures due to their excellent chemical stability and high photoluminescence efficiency both in solution and solid films, with emitted wavelengths in the blue spectral region. [5] In the case study we consider, alternating triphenylamine-fluorene (TPAF) copolymers constitute a hole transport layer (HTL) while alternating oxadiazole-fluorene (OxF) copolymers constitute an electron transport (ETL) and an emitting layer (EML). [13] In order to prevent the next layer from dissolving into it, [14, 15] the TPAF-based polymers were cross-linked. The cross-linked TPAF (referred to as X-TPAF) exhibits better electron-blocking properties than the widely used PEDOT-PSS. [13] Using these polymers, the multilayered polymeric blue light-emitting diode (PLED) [13] exhibited the best device performance when OxF3 was combined with X-TPAF2 (see Scheme 3.1).



Scheme 3.1: Chemical composition of (a) OxFn (n=1-3) and (b) TPAFn (n=1-3). R is an alkyl side chain (R=C<sub>8</sub>H<sub>17</sub> and R=C<sub>2</sub>H<sub>5</sub> for the long and short side chains respectively).

The main motivation behind this work was to find a clear explanation as to why among the other combinations studied in the work of Lu et al. [13] the combination OxF<sub>3</sub>-TPAF<sub>2</sub> exhibited the best device performance. Previous DFT and experimental investigations, [5, 13, 16] showed that copolymer types (OxFs or TPAFs) have small differences between their respective energy levels and band gaps. For example, all TPAFn polymers with n=1-3 have LUMO eigenvalues close to 2.3 eV, HOMOs close to 5.2 eV and band gaps close to 2.9 eV, [5] and similarly OxF<sub>2</sub> and OxF<sub>3</sub> have the corresponding

values of 2.7 eV, 5.7 eV and 3 eV, (the values for OxF1 are 2.9, 6.1 and 3.2 eV [16]). Hence, for example, matching the individual polymer levels at the heterojunction did not lead to an insight as to why OxF3-TPAF2 gave the highest device performance (see Table A1 in Appendix A).

In this work, as another possible way for understanding the experimental findings of Lu et al., [13] we investigate the structural and electronic properties of (heterogeneous) dimers (not single isolated monomers or polymers) consisting of nine possible combinations of monomers of OxF<sub>n</sub> and TPAF<sub>n</sub> (n=1-3). In general, the intermolecular interaction between two, the same or different, conjugated polymers and monomers is affected by factors such as their respective chemical compositions, degree of backbone planarizations, [17-19] the structure, length, and position of (alkyl) side chains, [20-22] and the ability of their chain backbones to form co-facial ( $\pi$ - $\pi$  stacking) configurations. [23, 24] All of these and many more factors contribute to the binding energies (per unit length) of heterogeneous and homogeneous pairs. In order to simplify our analysis, for the heterogeneous dimers, we calculate the binding energies of nine monomer pairs (with monomer lengths,  $L_1$  and  $L_2$ , and  $L_1 \neq L_2$  in the co-facial initial configuration) and consider the dependence of their binding energies on their average ( $L_{avg} = \frac{L_1+L_2}{2}$ ) and mismatched ( $\Delta L = |L_1 - L_2|$ ) lengths. Equally important is the electronic structure of the heterojunction in multilayered devices. Hence we also determine the energy level and gap differences at junctions in heterogeneous dimers (see discussion below) and study their dependence on  $L_{avg}$  and  $\Delta L$ . The trends in binding energies and electronic structure energy

differences will be, then, compared with the device performance (for example, we will check if the pair with highest binding energy will give the best OLED performance).

Bound (stable) monomer pairs require that we include the effect of the (non-covalent) intermolecular interactions in our computations. Hence the binding energy calculations are carried out using the dispersion-corrected density functional theory DFT (B97D). It is hoped that this work will provide an insight and a computational tool that can be used when choosing the appropriate organic conjugated polymers for the purpose of producing high performance multilayered or heterogeneous optoelectronic devices.

## 3.3 Theoretical/Computational Details

### 3.3.1 Computational Approach

All geometries of non-covalently bonded pairs of OxFn and TPAFn (n=1-3) monomers were optimized using the DFT/B97D/6-31G(d) as implemented in Gaussian 09. [25] B97D [26] is a reparameterization of the B97[27] hybrid exchange-correlation functional. It includes (semiempirical) dispersion (D) corrections that account for the long range, non-covalent intermolecular (van der Waals) interactions. B97D provides a good balance between the computational expediency and the accuracy. [28-32] One drawback of B97D approximation is that it produces the HOMO-LUMO energy gaps that deviate by one or more eVs from the experimental data. [33] Hence, using the optimized B97D geometries in single point calculations, we regenerated the HOMO and LUMO energies and their

differences with B3LYP functional which combines Becke's three-parameter [34] hybrid exchange functional with Lee and Yang's [35] gradient corrected correlation functional. In general, the DFT/B3LYP gives a good agreement (deviations are less than 0.2 eV) with the experimental electronic structure data [36-38] (previous works [5, 16] show that this is also true for OxFn and TPAFn, n=1-3, see Table A3 in Appendix A in addition). The visualization of molecular structures was carried out using GaussView. [39]

### 3.3.2 The Configuration of OxFn and TPAFn Pairings

To simulate the interfacial interactions between and within the layers of conjugated polymers such as OxFn and TPAFn (n=1-3), we considered two types of pairings: a heterogeneous (consisting of one OxFn and one TPAFn monomer, i.e. OxFn-TPAFn pairs with m,n=1-3) and a homogeneous one (two monomers of the same type, OxFn-OxFn, or TPAFn-TPAFn pairs with n=1-3). Typically, to facilitate the solubility, polymers have long alkyl side chains attached to fluorenes (see Scheme 3.1 and Figure 3.1). Side chains' lengths can also affect molecular packing and bulk structures of polymers. [33] To assess the effect of the side chain lengths on dimer structures, monomers with two types of side chains were studied: ethyl (C<sub>2</sub>H<sub>5</sub>) and octyl (C<sub>8</sub>H<sub>17</sub>) chains (referred as short and long side chains respectively).

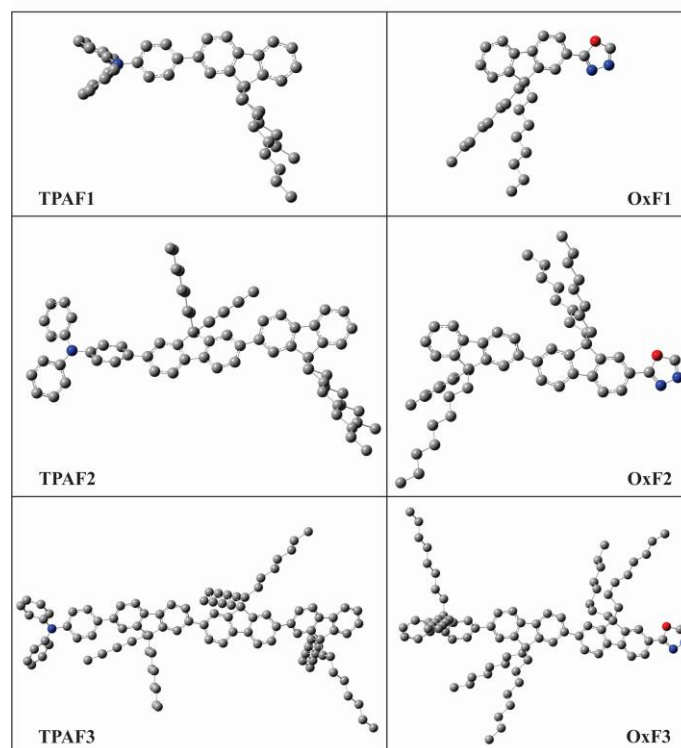


Figure 3.1: Molecular structures (optimized with B97D) of OxFn and TPAFn ( $n=1-3$ ) with long alkyl side chains. Hydrogen atoms are not shown for clarity.

The  $\pi$ - $\pi$  (non-covalent) intermolecular interactions in organic semiconductors can significantly affect charge transport and stability of the organic devices. Hence, in the initial configurations (before optimization), the monomers were arranged in a co-facial  $\pi$ -stacking orientations with approximate 4-5 Å separations. For the heterogeneous pairs of OxFn with TPAFn ( $n=1-3$ ), the preferred orientation (which corresponded to a lower energy) was one with the oxadizole ring in OxFn and the phenyl rings in TPAFn at the opposite ends of the dimers (see for example, Figure 3.2). In some cases (when heterogeneous dimers had the chain length differences exceeding  $\sim 6$  Å), extra monomers were added to either OxFn or TPAFn monomer to better match the lengths of the two

compounds in a given pair (see subsections 3.3.3 and 3.4.1 for more discussion). For example, in the case of OxF1-TPAF2 pair, the 2OxF1-TPAF2 pair had its chain length difference reduced from 13.46 Å to 2.35 Å (see Figure 3.2).

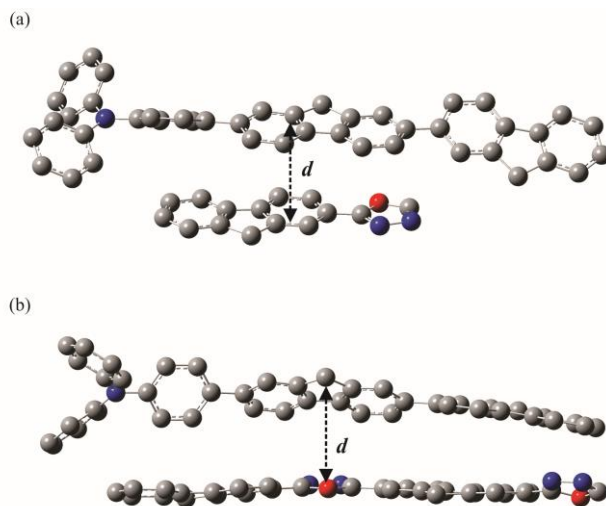


Figure 3.2: Illustration of the chain length matching with the use of the optimized structures of (a) OxF1-TPAF2 and (b) 2OxF1-TPAF2. Part (a) also gives an example of how the intermolecular distance  $d$  is determined and shows the preferred co-facial orientation. Hydrogens and side chains are omitted for clarity and when calculating the intermolecular distances.

### 3.3.3 Analysis of Computational Results

The details of the electronic structures of organic layers are important in the characterization of the charge transport of OLEDs. In particular, the respective electrode contacts to the HTL and ETL/EML control the balance of the injection of holes and electrons into their respective energy levels. In addition, to further enhance the probability of exciton recombination in the EML, the heterojunction must be designed to facilitate the

hole transport from the HTL into the EML and to block electrons in the opposite direction [40] (in most materials electrons have higher mobility than holes). Both the balancing of charges at the injection sites and through the heterojunction is critical to the maximization of the OLED efficiency.

Figure 3.3 shows the typical energy level diagram of a bilayered OLED. The energy barrier for the electron injection ( $\Delta E_e$ ) is determined by the difference between the electron affinity ( $EA_2$ ) or the LUMO level of the EML and the work function ( $\Phi_c$ ) of the cathode. Similarly, the energy barrier for the hole injection ( $\Delta E_h$ ) is determined by the difference between the ionization potential ( $IP_1$ ) or the HOMO level of the HTL and the work function ( $\Phi_a$ ) of the anode. At the injection sites, the energy levels in Lu et al.'s [13] work showed that the best matching between  $\Delta E_e$  and  $\Delta E_h$  (0.32 and 0.36 eV respectively, see Table A1 in Appendix A) was obtained for the OxF3-TPAF2 pair. However, at the heterojunction, the (polymer) energy level offsets,  $\Delta LUMO$  and  $\Delta HOMO$  or  $\Delta EA$  and  $\Delta IP$  (see Figure 3.3), were not very useful in picking the OxF3-TPAF2 as the preferred pair. In this work, we find that the quantities that correlate best with the device performance are the relative magnitudes of  $\Delta LUMOs$  and  $\Delta HOMOs$  of the monomers of OxFn and TPAFm in OxFm-TPAFn (m,n=1-3) dimers. It should be noted that the difference between  $\Delta LUMO$  and  $\Delta HOMO$  is equivalent to the difference between the HOMO-LUMO energy gaps, that is  $\Delta E_g = (\Delta LUMO - \Delta HOMO) = E_{g1} - E_{g2}$ , (where  $E_{g1}$  and  $E_{g2}$  are  $E_g$ 's of monomer 1 and 2 respectively).

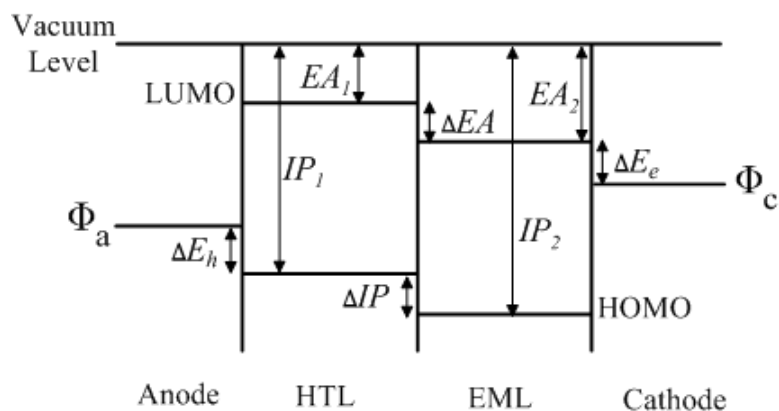


Figure 3.3: Energy-level diagram of a bilayered (HTL and EML/ETL) OLED.

The simplest structural characteristic of a given monomer is its length,  $L$ . The chain length of a monomer (which is defined as the end-to-end distance ( $L$ ) along its chain backbone) was determined by projecting the end-carbon atoms onto the, say  $x$ -axis and taking the difference between these  $x$ -coordinates (see Figure 3.4 for an illustration). For homogeneous pairs, instead of calculating the chain length difference, the chain length shift,  $L_{shift} = |x'_1 - x'_2|$ , was calculated (see Figure 3.5 for an illustration).

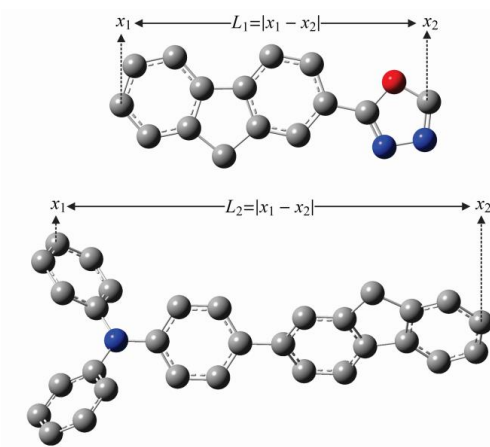


Figure 3.4: Illustration of the determination of the chain lengths ( $L_1$  and  $L_2$ ) of OxF1 and TPAF1 monomers in a heterogeneous OxF1-TPAF1 pair. Hydrogens and side chains are omitted for clarity.

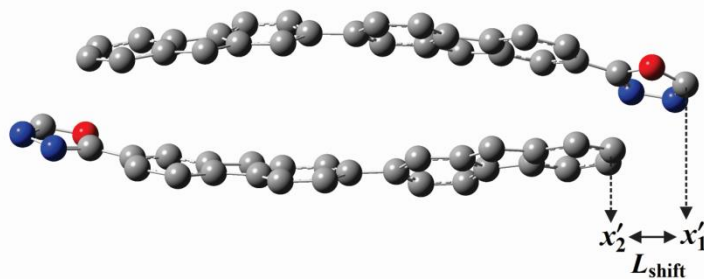


Figure 3.5: Example of the determination of the chain length shift in a homogeneous pair. Hydrogens and side chains are omitted for clarity.

It is well established that, for oligomers, their HOMO-LUMO energy gaps are inversely proportional to their lengths [41-43] (with  $(\text{HOMO} - \text{LUMO})(\text{oligomer}) \rightarrow E_g(\text{polymer})$  as  $L \rightarrow \infty$ , see also Figure A1 in Appendix A for the corresponding OxFn and TPAFn plots). Hence it is not unexpected that as the number of fluorenes in OxFn (from OxF1 to OxF3) or in TPAFn (from TPAF1 to TPAF3) increases, the corresponding energy gaps will decrease. Figure 3.6 clearly shows that this relationship is linear. We will show that, for heterogeneous pairs of monomers, the important property is the band gap difference ( $\Delta E_g$ ) and its dependence on monomer chain length mismatch ( $\Delta L$ ). In the short derivation below (with more details in Appendix A) we obtain the functional dependence of  $\Delta E_g$  on  $\Delta L$  and  $L_{avg}$ . Since,  $E_g$  is nearly linearly proportional to  $1/L$  for a given monomer type (see Figure 3.6),  $\Delta E_g$  can be expressed as the difference of their respective straight lines, that is,

$$\begin{aligned} \Delta E_g &= E_g - E'_g \\ &= \frac{m}{L} + b - \frac{m'}{L'} - b' \end{aligned} \tag{3.1}$$

where  $m$  and  $m'$  are the slopes, and  $b$  and  $b'$  are the intercepts of the straight lines that correspond to the two monomer types, respectively. Since,  $L=L_{avg} + \Delta L/2$  and  $L'=L_{avg} - \Delta L/2$  and using the binomial expansion to first order in  $\Delta$  we obtain

$$\Delta E_g = -\frac{\Delta L}{L_{avg}^2} m_{avg} + \frac{\Delta m}{L_{avg}} + \Delta b + O(\Delta^2) \quad (3.2)$$

where  $m_{avg} = \frac{m+m'}{2}$  and  $\Delta m = m - m'$  are the average and the difference of the slopes, and  $\Delta b = b - b'$  is the difference of the intercepts. Given that  $\Delta m$  and  $\Delta b$  terms are, in most cases, smaller relative to the first term for a given  $\Delta L$  in equation (3.2) (see Table A2 in Appendix A) we can approximate  $\Delta E_g$  by

$$|\Delta E_g| = \frac{|\Delta L|}{L_{avg}^2} m_{avg} + O(\Delta^2). \quad (3.3)$$

To test the above equation, we plot  $|\Delta E_g|$  as function of  $1/L_{avg}^2$  for some (fixed)  $\Delta L$ 's (see Figure 3.7). Figure 3.7 clearly shows that  $|\Delta E_g|$  varies nearly linearly with  $1/L_{avg}^2$  for a given  $\Delta L$ . In section 3.4, we determine  $L_{avg}$ ,  $\Delta L$  and  $|\Delta E_g|$  for all monomer pairs (OxFm-TPAFn (m,n=1-3)), plot  $|\Delta E_g|L_{avg}^2$  as a function of  $\Delta L$  (since  $|\Delta E_g|L_{avg}^2 \propto \Delta L$  from equation (3.3)), and investigate how this relationship can be used in selecting the best materials for multilayered devices.

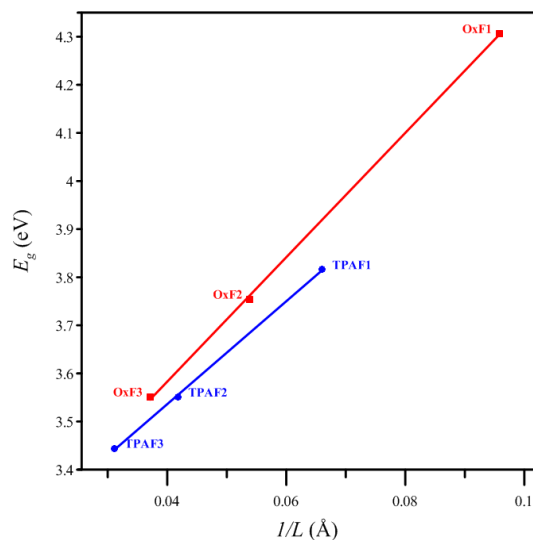


Figure 3.6: Energy gaps versus the reciprocal of chain lengths for the various monomers as indicated.

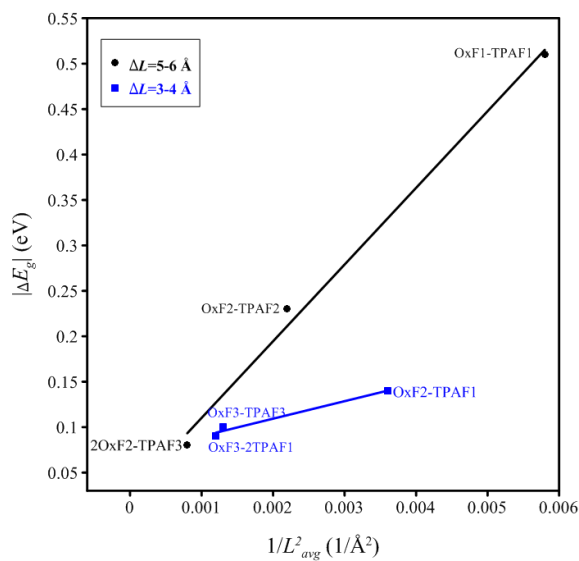


Figure 3.7: The energy gap difference of heterogenous dimers with long side chains as a function of their reciprocal square average chain length for some representative  $\Delta L$ 's.

The magnitudes of the binding energies of homogeneous or heterogeneous pairs are also used in the analysis of the B97D geometry optimization results to determine the relative stability and intermolecular distance of the interacting monomers. The binding energy ( $\Delta E_b$ ) is given by:

$$\Delta E_b = \sum_{i=1}^2 E_i - E_{pair} \quad (3.4)$$

where  $E_{pair}$  is the total energy of the pair, and  $E_1$  and  $E_2$  are the total energies of individual monomers. Similar to the obtaining of the relationship between  $\Delta E_g$  and  $L_{avg}^2$  and  $\Delta L$  above, the binding energy dependence on  $L_{avg}$  and  $\Delta L$  is also determined. This dependence is evaluated by carrying out four (empirically based) calibrations. Binding energies of two different homogenous pairs and heterogeneous pairs (with  $\Delta L = 5-6 \text{ \AA}$  as a function of their average chain lengths) are plotted in Figure 3.8. Figure 3.8 shows that  $\Delta E_b$  of the homogenous and heterogeneous pairs increases almost linearly with their respective average chain length for a given  $\Delta L$  ( $\Delta L = 0$  for a homogeneous dimers). Hence, in our result analysis (section 3.4) in order to remove binding energy dependence on length, we plot  $\Delta E_b/L_{avg}$  (for brevity we often refer to it simply as binding energy) as a function of  $\Delta L$  and again study how this relationship can be used in selecting the best materials for multilayered devices.

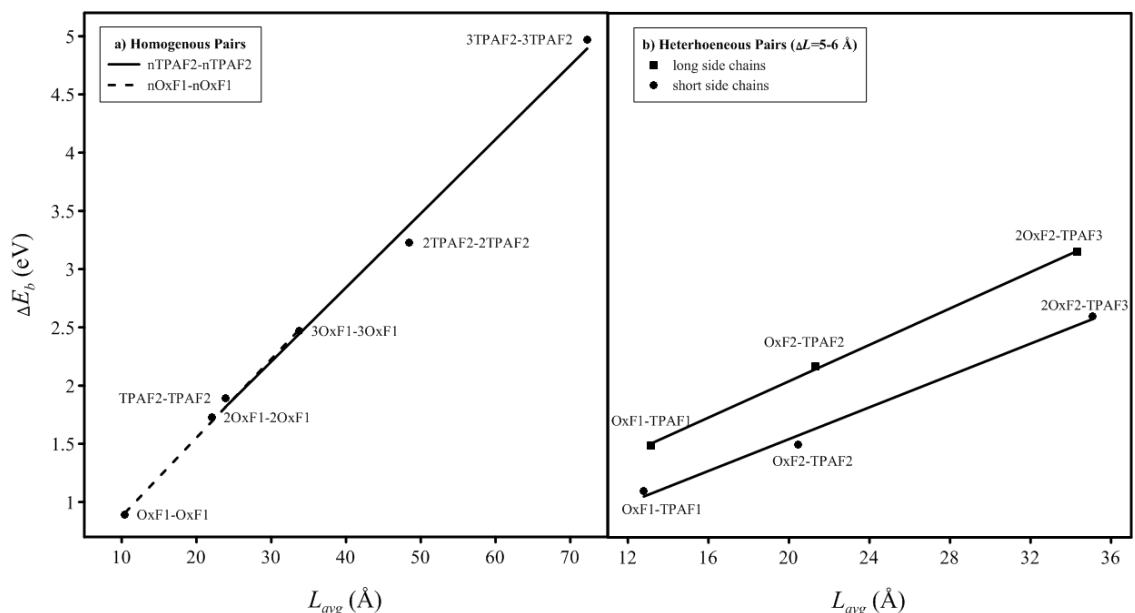


Figure 3.8: The binding energy of a) homogenous pairs with short side chains and b) heterogeneous pairs with short and long side chains as a function of their average chain lengths for a given  $\Delta L$ .

The trends in binding energies are indicative of the relative intermolecular strengths in the respective heterogeneous and/or homogeneous pairs. This can be quantitatively assessed by the magnitudes of intermolecular distances ( $d$ ) between monomers. It is expected that the smaller  $d$ , the stronger is the interaction and the larger the binding energy. Hence, roughly,  $d$  is inversely proportional to the binding energy. The determination of  $d$  between the backbone planes of OxFn and TPAFn monomers is not straightforward due to the nonplanarity of the monomer backbones. Therefore, we estimated  $d$  as the distance between the two centers of mass of the co-facial monomers in a given pair (see Figure 3.2). For the poorly matched monomers that are significantly shifted relative to each other, the average perpendicular distance  $d_{\perp}$  between monomers in a given pair was also calculated (see Figure 3.9).

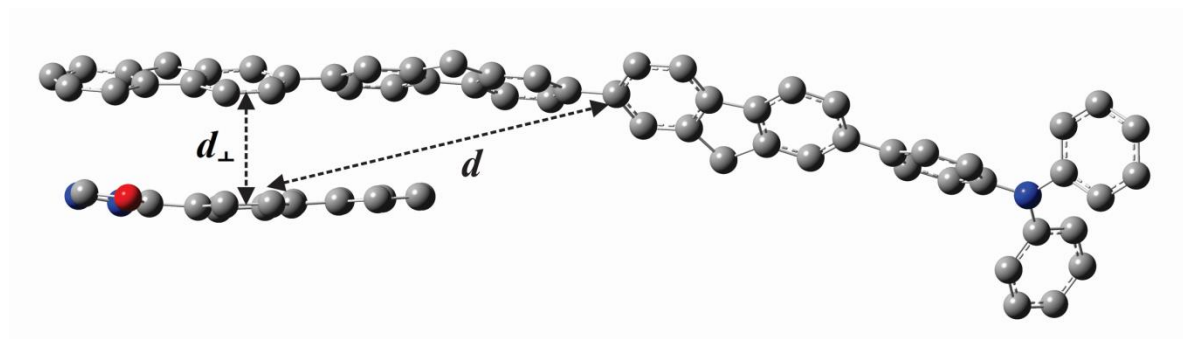


Figure 3.9: Example of the determination of the average perpendicular distance ( $d_{\perp}$ ) in the case of the poorly matched monomers that are significantly shifted relative to each other (and  $d$  is unusually large). Hydrogens and side chains are omitted for clarity.

## 3.4 Results and Discussion

### 3.4.1 The Heterogeneous Pairs

#### 3.4.1.1 The Electronic Structure of the Heterojunction

To deduce the effect of the heterojunction on charge transport, the energy levels of nine combinations of OxFn-TPAFn ( $m,n=1-3$ ) are illustrated in Figure 3.10. Since OxFn is used as an ETL and an EML, we search for a TPAFn that has a HOMO level comparable to an OxFn (i.e.  $\Delta\text{HOMO}$  should be small) and a shallow LUMO level (i.e. moderate  $\Delta\text{LUMO}$ ) in order to confine the excitons within the EML. With these criteria in mind, the results of Figure 3.10 show that the OxF1-TPAFn and OxF2-TPAFn ( $n=1-3$ ) pairs are not desirable for enhancing the device performance due to the large  $\Delta\text{HOMOs}$  ( $> 0.5$  eV) that can significantly lower the hole transport from TPAFn to OxF1 or OxF2. In contrast, the OxF3-TPAFn ( $n=1-3$ ) pairs exhibit lower  $\Delta\text{HOMOs}$  (0.3-0.44 eV) and moderate  $\Delta\text{LUMOs}$

(0.35-0.63 eV), thus, they have good potential for optimal hole transport and electron blocking capability. Of the two, OxF3-TPAF2 and OxF3-TPAF3 pairs (that were extensively tested experimentally [13]), both have similar  $\Delta$ LUMOs, while a lower  $\Delta$ HOMO is observed in the OxF3-TPAF2 pair (hence it has a smaller barrier to transport of holes) relative to the OxF3-TPAF3 pair. In fact, the OxF3-TPAF2 pair displays similar values for  $\Delta$ LUMO and  $\Delta$ HOMO (0.34 and 0.32 eV respectively, giving a difference of 0.02 eV which is smallest amongst all pairs). This result leads us to suggest that the best device performance that was exhibited by the OxF3-TPAF2 pair is in large part due to optimal (relative) locations of the energy levels at the interface and the fact that  $\Delta$ LUMO  $\approx$   $\Delta$ HOMO (or  $\Delta$ LUMO -  $\Delta$ HOMO  $\approx$  0) resulting in a balanced hole and electron transport at (or near) the heterojunction. This analysis shows that the differences ( $[\Delta$ LUMO -  $\Delta$ HOMO]s) as well as the magnitudes of  $\Delta$ LUMOs and  $\Delta$ HOMOs are important parameters that can be used to select the best materials for the device performance. In addition, it shows that the best way to carry out this analysis is with monomer (not polymer) dimers since the differences between monomer energy levels are more pronounced and clearly display trends that are useful for the material selection.

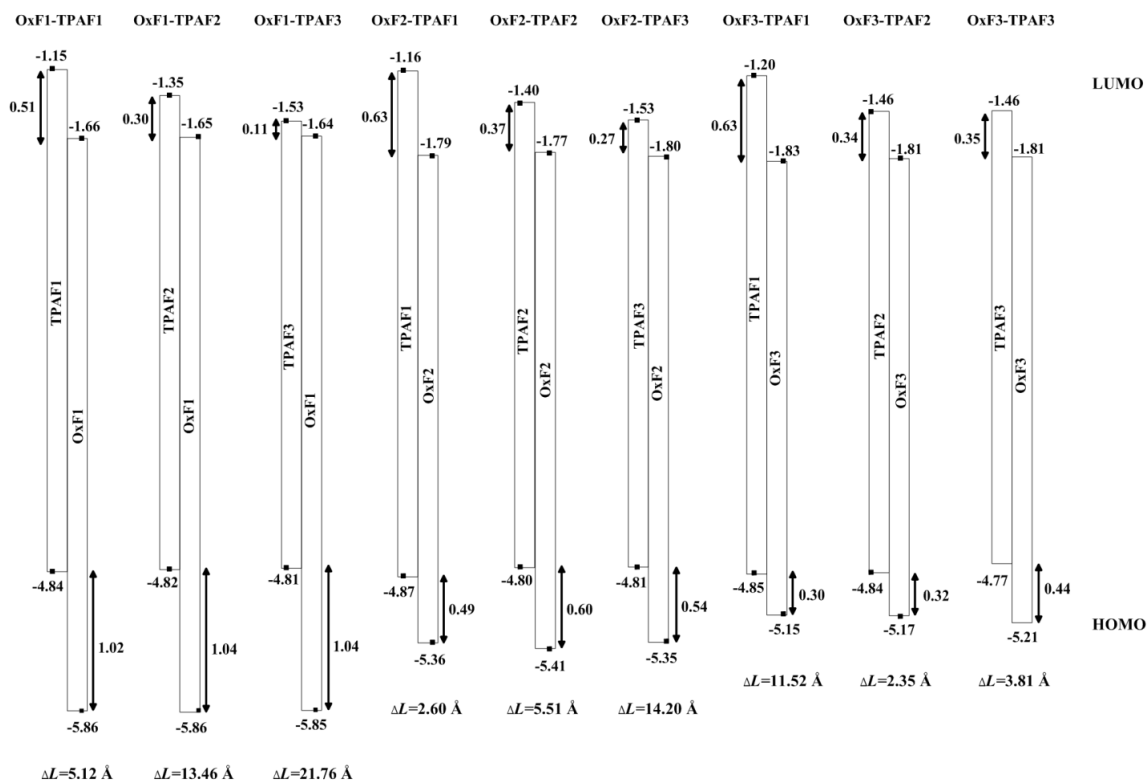


Figure 3.10: The energy levels of the OxFm-TPAFn (m,n=1-3) pairs at the heterojunction.  $\Delta$ HOMOs and  $\Delta$ LUMOs are represented on the side of energy levels.

### 3.4.1.2 The Effect of Chain Length Mismatch on the Energy Gap Difference

We can analyze our systems with the help of  $\Delta E_g$ 's since as discussed in subsection 3.3.3  $(\Delta \text{LUMO} - \Delta \text{HOMO}) = \Delta E_g$ . In subsection 3.3.3, we showed that  $|\Delta E_g| L_{avg}^2 \propto \Delta L$ . In this subsection, we investigate the dependence of  $|\Delta E_g| L_{avg}^2$  on  $\Delta L$  for the monomer OxFm-TPAFn (m,n=1-3) pairs with short and long side chains. Figure 3.11 (a) and b)) shows that  $|\Delta E_g| L_{avg}^2$  increases almost linearly with  $\Delta L$  (i.e. the larger  $\Delta L$ , the higher the energy gap difference) and the length of side chains has a relatively small effect on this linear relationship. Other works [44-46] also showed that the electronic structure of polymers

and macromolecules is nearly independent of the length of alkyl side chains (see also Table A4 in Appendix A).

In addition, the OxF3-TPAF2 pair has the best matched monomer lengths (i.e. it has the smallest  $\Delta L$ ) and the lowest energy gap difference of all OxF<sub>m</sub>-TPAF<sub>n</sub> (m,n=1-3) pairs (with either short and long side chains, see Figure 3.11 and Table 3.1). In fact, the OxF3-TPAF2 pair is well matched without the need of adding other monomers (see Figure 3.12). This is a significant result since, as stated in the Introduction, the best OLED performance was obtained with the OxF3-TPAF2 combination. [13] These results indicate that the near equality of  $\Delta LUMO$  and  $\Delta HOMO$  (or equivalently vanishing  $\Delta E_g$ ) as discussed above (see Figure 3.10) is primarily due to the well matching of monomer chain lengths in a given dimer. Based on these results, it seems that, for monomers, the magnitude of  $\Delta L$  correlates well with energy gap difference (and corresponding energy-level offsets) and is an important factor that can be used to select the best polymers for the enhanced device performance.

However, in general, in real systems we are dealing with long chain polymers, not isolated monomers, and it could be argued that we can decrease  $\Delta L$  by matching segments (that are longer than one monomer) of polymers. Hence, we further study the effect of matching the monomer lengths on the energy gap difference (in pairs that display large mismatch in monomer lengths) by adding extra monomer(s) to the shorter one in a given pair (see Table 3.2). The results of the well-matched pairs (with additional monomer(s)) show again that the energy gap difference decreases when the monomers are better matched in length. For example, when  $\Delta L$  decreases from the mismatched OxF1-TPAF2

pair (with long side chains) to the well-matched 2OxF1-TPAF2 pair (from 13.46 to 2.35 Å), the energy gap difference decreases (from 0.73 to 0.09 eV). However, once again the lowest energy gap difference is obtained for the OxF3-TPAF2 pair (without any additional monomer(s)) even when this did not correspond to the smallest  $\Delta L$ . This indicates that, in addition to  $\Delta L$ , there must be another parameter that should be considered when determining optimal charge transport (which involves hopping of charge between chains) and device performance. This other parameter is the intermolecular distance ( $d$ ) between monomers and will be discussed below in the context of binding energies of dimers.

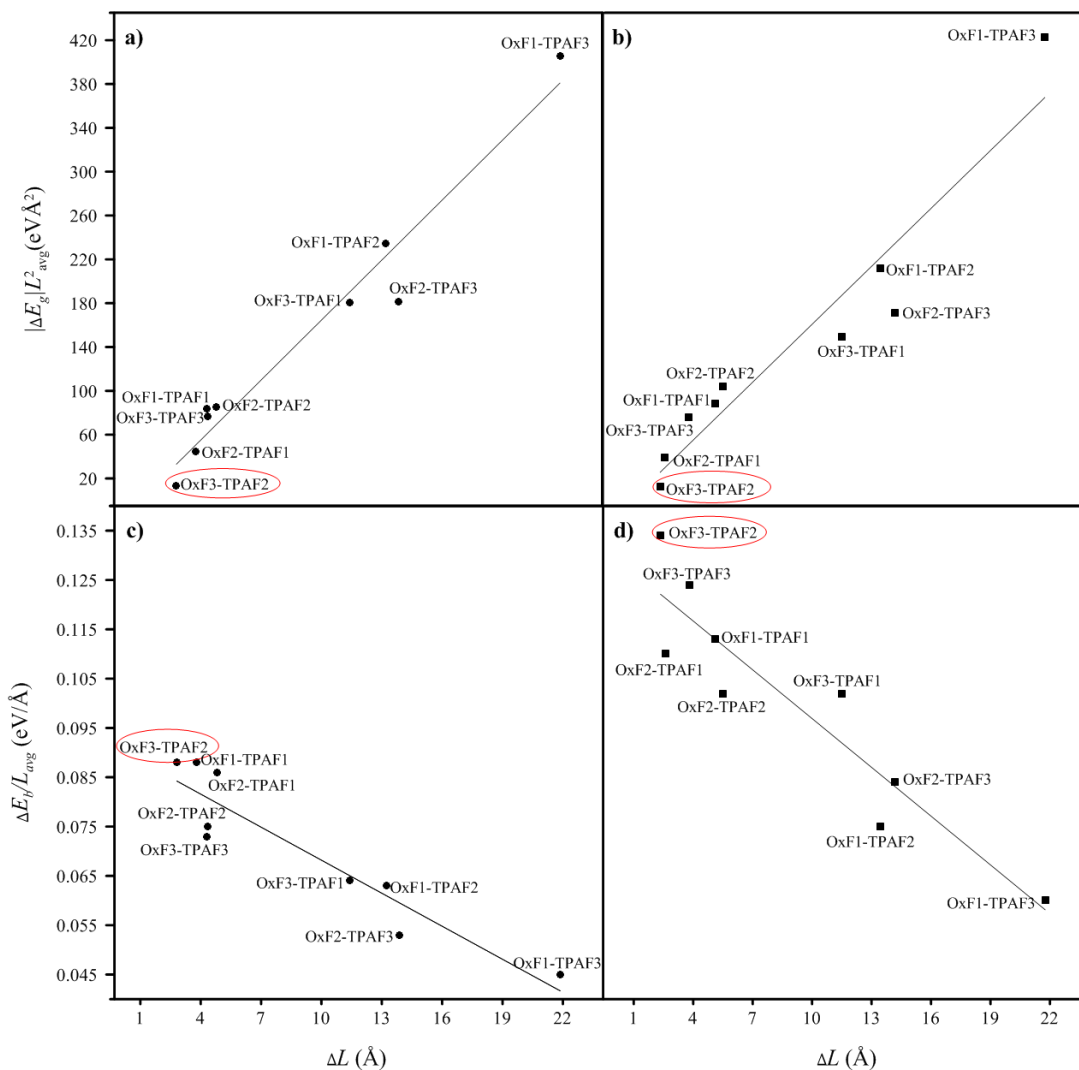


Figure 3.11: The energy gap difference of OxFm-TPAFn (m,n=1-3) with a) short (●) and b) long (■) side chains and the binding energy of the pairs with c) short (●) and d) long (■) side chains as a function of chain length difference.

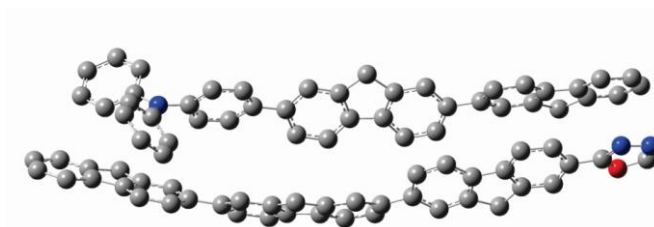


Figure 3.12: The optimized geometry of OxF3-TPAF2 that gives the best matched of all heterogeneous pairs (without the need of adding extra monomer(s)).

Table 3.1: Chain length difference ( $\Delta L$ ), intermolecular distance ( $d$ ), energy gap difference ( $|\Delta E_g|$ ), and binding energy per unit average chain length ( $\Delta E_b/L_{avg}$ ) for various pairings of OxFm-TPAFn (m,n=1-3) with monomers containing (a) short and (b) long side chains. Each pair was optimized using B97D/6-31G(d) ( $\Delta E_g$  was obtained using B3LYP, see text). In some case, the average perpendicular distance ( $d_{\perp}$ ) is given in brackets for the poorly matched monomers due to shifting (see Figure 3.9).

	Pair	$\Delta L$ (Å)	$d$ (Å)	$ \Delta E_g $ (eV)	$\Delta E_b/L_{avg}$ (eV/Å)
(a) Short Side Chains	OxF1-TPAF1	4.81	4.2	0.52	0.086
	OxF1-TPAF2	13.22	3.7	0.82	0.063
	OxF1-TPAF3	21.65	4.8	0.9	0.045
	OxF2-TPAF1	3.79	3.9	0.16	0.088
	OxF2-TPAF2	4.32	3.6	0.2	0.073
	OxF2-TPAF3	13.86	9.7 (5.1)	0.29	0.053
	OxF3-TPAF1	11.41	6.0 (4.1)	0.4	0.064
	OxF3-TPAF2	2.81	3.5	0.02	0.088
	OxF3-TPAF3	4.36	5.3 (4.2)	0.09	0.075
(b) Long Side Chains	OxF1-TPAF1	5.12	4.1	0.51	0.106
	OxF1-TPAF2	13.46	4.1	0.73	0.075
	OxF1-TPAF3	21.76	11.7 (3.9)	0.93	0.061
	OxF2-TPAF1	2.60	4.2	0.14	0.116
	OxF2-TPAF2	5.51	6.7 (4.6)	0.23	0.105
	OxF2-TPAF3	14.20	5.4	0.27	0.084
	OxF3-TPAF1	11.52	4.9	0.33	0.102
	OxF3-TPAF2	2.35	3.6	0.02	0.134
	OxF3-TPAF3	3.81	5.6 (4.1)	0.09	0.124

Table 3.2: Chain length difference ( $\Delta L$ ), intermolecular distance ( $d$ ), energy gap difference ( $|\Delta E_g|$ ), and binding energy per unit average chain length ( $\Delta E_b/L_{avg}$ ) of OxFm-TPAFn ( $m,n=1-3$ ) pairings that require an addition of monomer(s) to better match their chain lengths, with monomers containing (a) short and (b) long side chains. Each pair was optimized using B97D/6-31G(d) ( $\Delta E_g$  was obtained using B3LYP, see text). In some cases, the average perpendicular distance ( $d_{\perp}$ ) is given in brackets for the poorly matched monomers due to shifting (see Figure 3.9).

	Pair	$\Delta L$ (Å)	$d$ (Å)	$ \Delta E_g $ (eV)	$\Delta E_b/L_{avg}$ (eV/Å)
(a) Short Side Chains	2OxF1-TPAF2	2.59	4.7	0.07	0.080
	3OxF1-TPAF3	0.27	4.7	0.03	0.074
	2OxF2-TPAF3	7.24	4.1	0.06	0.074
	OxF3-2TPAF1	5.8	5.3	0.08	0.073
(b) Long Side Chains	2OxF1-TPAF2	2.35	5.3 (4.2)	0.09	0.112
	3OxF1-TPAF3	3.59	4.4	0.15	0.107
	2OxF2-TPAF3	5.65	4.5	0.08	0.092
	OxF3-2TPAF1	3.74	4.5	0.1	0.111

### 3.4.1.3 The Effect of Chain Length Mismatch on the Binding Energy

The previous two subsections focused on the electronic structure of heterogeneous dimers. In this subsection, we consider the effect of  $\Delta L$  on the binding energies of dimers. The binding energies of all pairs with short and long side chains as a function of  $\Delta L$  are displayed in Figure 3.11 c) and d). The results show that the binding energy per unit length

increases as  $\Delta L$  decreases. In contrast to the electronic structure, the side chains have an effect on both the slope and the intercept of these (fitted) binding energy straight lines. The binding energy of pairs with long side chains increases more steeply than the corresponding values for dimers with short side chains (see Figure A2 in Appendix A for an example of an optimized structure of a dimer with short and long side chains). However, the results of all OxF<sub>m</sub>-TPAF<sub>n</sub> (m,n=1-3) pairs with short and long side chains (see Figure 3.11 and Table 3.1) show that the OxF<sub>3</sub>-TPAF<sub>2</sub> pair (which has the smallest  $\Delta L$ ) exhibits the highest binding energy. This significant increase in the binding energy appears to be due to the very good overlap between the well-matched OxF<sub>3</sub> and TPAF<sub>2</sub> monomers (see Figure 3.12).

To be consistent with real systems that include long-chain polymers with matched segments (i.e. lower  $\Delta L$ ), we further study the correlation between the binding energy and  $\Delta L$  in poorly-matched pairs relative to their well-matched ones (with additional monomers, see Table 3.2). The results show again that the binding energy increases when the monomers are better matched in length. For example, when  $\Delta L$  decreases from the mismatched OxF<sub>1</sub>-TPAF<sub>2</sub> pair to the well-matched 2OxF<sub>1</sub>-TPAF<sub>2</sub> pair (from 13.46 to 2.35 Å) with long side chains, the binding energy increases (from 0.075 to 0.112 eV), respectively. However, once again the highest binding energy is obtained for the OxF<sub>3</sub>-TPAF<sub>2</sub> pair (without additional monomer(s)) even when this did not correspond to the smallest  $\Delta L$ . That is, while in some pairs  $\Delta L$  can be decreased further by adding extra monomer(s), this addition decreases the overlap region (as can be seen from the increased intermolecular distance) between monomers resulting in a binding energy which is not as

high as that for the OxF3-TPAF2 pair. This means that matching the monomer lengths of the interfacial polymers in multilayered devices is not only important for matching  $\Delta$ LUMOs with  $\Delta$ HOMOs and hence lowering the energy gap difference, but also for increasing the binding energy and ultimately device performance. This analysis illustrates that the important factor to consider while determining the optimal device performance is  $\Delta L$  of monomers (not oligomers of any length) in heterogeneous pairs.

As noted above, in addition to  $\Delta L$ , the intermolecular distance (as determined by binding energy calculations) is an important structural parameter of heterogeneous dimers (see Tables 3.1 and 3.2). The results reveal that both  $d$  and  $\Delta L$  between OxFm-TPAFn (m,n=1,3) monomers must be known in order to determine which pair has the best potential for multilayered devices. Table 3.1 shows that among all OxFm-TPAFn (m,n=1-3) pairs, the best matched OxF3-TPAF2 pair (having the smallest  $\Delta L$ ) exhibits the shortest  $d$  (3.5-3.6 Å) which is near the optimal distance (3.4 to 4 Å) needed for a good charge transport in organic conjugated crystals and thin films. [47, 48] In contrast, Table 3.2 shows that  $d$  of the other well-matched (also having small  $\Delta L$ ) pairs (with the additional monomer(s)) is above this range with  $d$  closer to 4.1 Å or higher. These results indicate that in well-matched pairs (with small  $\Delta L$  and without any additions)  $d$  is reduced and the monomer chain backbones overlap more fully enhancing charge transport.

### 3.4.1.4 Correlation of Energy Gap Differences with the Binding Energies

In the previous two subsections, the dependence of the energy gap difference and of the binding energy on the  $\Delta L$  was discussed extensively for the heterogeneous dimers. In this subsection we show that the above results can be displayed even more succinctly by putting energy gap difference and binding energy on the same plot for the pairs with well-matched monomers (with  $\Delta L < 6 \text{ \AA}$ ). Since the energy gap difference is proportional to  $\Delta L$  and the binding energy is inversely proportional to  $\Delta L$ , that is,

since

$$|\Delta E_g| L_{avg}^2 \propto \Delta L$$

and

$$\frac{\Delta E_b}{L_{avg}} \propto 1/\Delta L$$

then

$$\frac{\Delta E_b}{L_{avg}} \propto 1/|\Delta E_g| L_{avg}^2. \quad (3.5)$$

In other words, binding energy and energy gap difference are approximately inversely proportional to each other for a given  $\Delta L$ . This relationship is illustrated on Figure 3.13 for  $\Delta L < 6 \text{ \AA}$  (where in most cases, the dimers with lower energy gap difference exhibit higher binding energy and vice versa even if we include pairs with the additional monomers as given in Table 3.2). Once again the OxF3-TPAF2 pair exhibits the lowest energy gap difference and the highest binding energy.

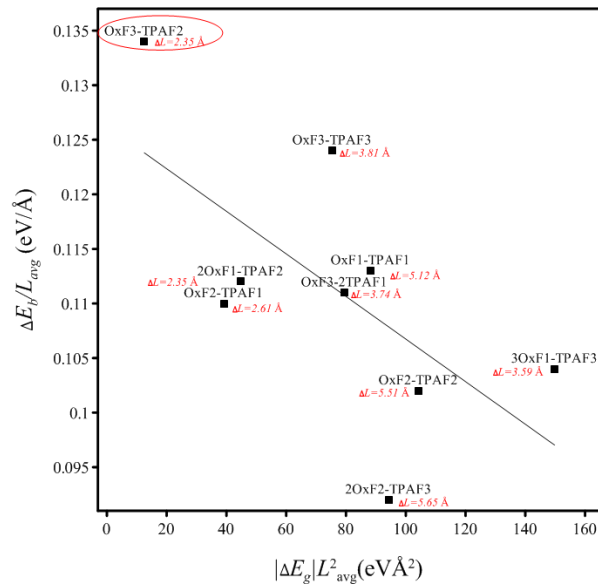


Figure 3.13: The binding energy of well-matched OxFm-TPAFn (m,n=1-3) pairs with long side chains as a function of energy gap difference.

All of the above subsections (3.4.1.1-3.4.1.4) illustrate that the most effective way to obtain a good match for polymer layers in a multilayered device is to select polymers whose monomers have the smallest chain length and HOMO-LUMO gap differences, and highest binding energies. Figure 3.11 c) and d) also shows that the best (unambiguous) agreement with experiment is obtained when monomers with long side chains are used in these calculations.

### 3.4.2 Homogeneous OxFn-OxFn and TPAFn-TPAFn (n=1-3) Pairs

In order to analyze the effect of structural-features of the homogeneous pairs on their intermolecular interactions, the binding energies of OxFn-OxFn and TPAFn-TPAFn (n=1-3) dimers with long side chains are plotted as a function of  $L_{shift}$  and  $d$  in Figure 3.14. The results of all homogeneous pairs show that the highest binding energy corresponds to the case when both parameters  $L_{shift}$  and  $d$  are (simultaneously) small. Figure 3.14 shows that this corresponds to the OxF2-OxF2 and TPAF2-TPAF2 dimers. Similar to the heterogeneous-pairs results, the binding energy of pairs with long side chains is significantly larger than the corresponding energy of those with short side chains (see Table A5 in Appendix A).

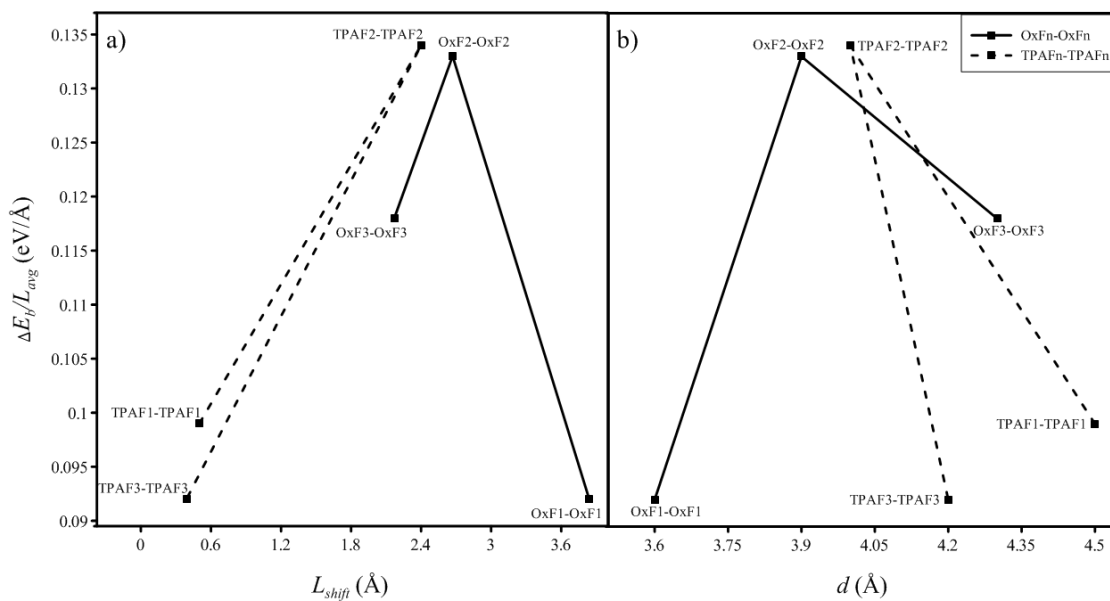


Figure 3.14: The binding energy of OxFn-OxFn and TPAFn-TPAFn ( $n=1-3$ ) homogeneous pairs with long side chains as a function of a) length shift and b) intermolecular distance.

With everything else being equal, it is expected that polymers whose monomer pairs have the highest binding energies will result in organic devices with improved performance. Our calculations indicate that OxF2 or TPAF2 polymers (with long side chains) would be the best choice for maximizing the efficiency of single-layered organic devices. However, for optimizing the performance of multilayered devices, other factors (such as the binding energy and energy gap difference of heterogeneous dimers) must be considered. Based on the above analysis in subsection 3.4.1.3, the OxF3-TPAF2 pairing has the largest binding energy which is consistent with the best device performance. The OxF3-OxF3 homogeneous dimer does not have the highest binding energy (it is second highest for dimers with long side chains) but OxF3 is an optimal match to TPAF2 in a multilayered device. These results highlight the important role of the heterogeneous

monomer pairs, in comparison to the homogenous pairs, in maximizing the multilayered devices efficiencies.

### 3.5 Conclusions

In this work, we have analyzed the  $\pi$ - $\pi$  intermolecular interaction between various pairings of monomers of OxFn and TPAFm (m,n=1-3) copolymers using the dispersion-corrected DFT (B97D) method. Our results indicate that the binding energies (and intermolecular distances) of the heterogeneous dimers are affected by matching monomers' chain lengths and the lengths of alkyl side chains. Given the analysis carried out in this work, the fact that the OxF3-TPAF2 pair of copolymers exhibited the best OLED performance can be attributed to the following factors:

1. having the best matching of OxF3 and TPAF2 monomers' chain lengths (without any additional monomer(s));
2. having the best matching between  $\Delta$ LUMO and  $\Delta$ HOMO (or correspondingly having very small  $|\Delta E_g|$ ) of OxF3-TPAF2 monomer pair;
3. having the highest binding energy which leads to having the closest average intermolecular distance among the pairs of OxFm-TPAFn (m,n=1-3) monomers with and without the side chains;
4. having relative high binding energies for the homogeneous monomer pairs of OxF3 and TPAF2 especially when long side chains are present.

Based on the above case study, we recommend the following computational approach when deciding on the polymers to be used in the multilayered devices:

1. select number of polymers with the appropriate electronic structure (HOMO, LUMO eigenvalues and energy gaps) that can match well the respective work functions of the electrodes;
2. for the respective heterogeneous monomer pairs, calculate the gas phase monomers' lengths and their differences;
3. determine the gas phase energy gaps of the monomers and their differences as well as  $\Delta$ LUMOs and  $\Delta$ HOMOs for the pairs;
4. calculate binding energies (and intermolecular distances) only for heterogeneous pairs with small differences in length and energy gap;
5. carry out experiments with the pair with the highest binding energy (and smallest average (perpendicular) intermolecular distance) that have the best match in length and energy gap.

In all the above study, the binding energies should be computed with one of the dispersion corrected DFT methods (such as B97D) and the electronic structure should be calculated using hybrid exchange-correlation functional such as B3LYP (either on gas phase or dispersion corrected DFT optimized monomers). To conclude, we have determined the factors that lead to maximizing the binding energy of monomers and thus, to enhancing the performance of optoelectronic devices. This work gives insight into the connection between the intermolecular interactions and device performance.

## Acknowledgments

We would like to thank the following for making this research possible: WestGrid ([www.westgrid.ca](http://www.westgrid.ca)), Compute Canada, and ACENET ([www.acceleratediscovery.ca](http://www.acceleratediscovery.ca)) for providing the computational facilities. ACENET is the regional high performance computing consortium for universities in Atlantic Canada, and it is funded by the Canada Foundation for Innovation (CFI), the Atlantic Canada Opportunities Agency (ACOA), and the provinces of Newfoundland and Labrador, Nova Scotia, and New Brunswick. We would also like to thank King Abdulaziz University in Saudi Arabia and the Saudi Cultural Bureau in Canada for the full scholarship given to Sarah Ayoub.

# Bibliography

- [1] J. Cornil, D. Beljonne, J.P. Calbert, J.L. Bredas, *Interchain Interactions in Organic Pi-Conjugated Materials: Impact on Electronic Structure, Optical Response, and Charge Transport*, *Advanced Materials* 13 (2001) 1053-1067.
- [2] C. Li, M.Y. Liu, N.G. Pschirer, M. Baumgarten, K. Mullen, *Polyphenylene-Based Materials for Organic Photovoltaics*, *Chemical Reviews* 110 (2010) 6817-6855.
- [3] J.G.C. Veinot, T.J. Marks, *Toward the Ideal Organic Light-Emitting Diode. The Versatility and Utility of Interfacial Tailoring by Cross-Linked Siloxane Interlayers*, *Accounts of Chemical Research* 38 (2005) 632-643.
- [4] H. Zhou, L. Yang, W. You, *Rational Design of High Performance Conjugated Polymers for Organic Solar Cells*, *Macromolecules* 45 (2012) 607-632.
- [5] L. Ling, J.B. Lagowski, *DFT Study of Electronic Band Structure of Alternating Triphenylamine-Fluorene Copolymers*, *Polymer* 54 (2013) 2535-2543.
- [6] G. Yu, J. Gao, J.C. Hummelen, F. Wudl, A.J. Heeger, *Polymer Photovoltaic Cells - Enhanced Efficiencies Via a Network of Internal Donor-Acceptor Heterojunctions*, *Science* 270 (1995) 1789-1791.
- [7] M.C. Gather, A. Koehnen, K. Meerholz, *White Organic Light-Emitting Diodes*, *Advanced Materials* 23 (2011) 233-248.
- [8] J.R. Sheats, H. Antoniadis, M. Hueschen, W. Leonard, J. Miller, R. Moon, D. Roitman, A. Stocking, *Organic Electroluminescent Devices*, *Science* 273 (1996) 884-888.
- [9] A.P. Kulkarni, C.J. Tonzola, A. Babel, S.A. Jenekhe, *Electron Transport Materials for Organic Light-Emitting Diodes*, *Chemistry of Materials* 16 (2004) 4556-4573.
- [10] S. Braun, W.R. Salaneck, M. Fahlman, *Energy-Level Alignment at Organic/Metal and Organic/Organic Interfaces*, *Advanced Materials* 21 (2009) 1450-1472.
- [11] E. Bundgaard, F.C. Krebs, *Low Band Gap Polymers for Organic Photovoltaics*, *Solar Energy Materials and Solar Cells* 91 (2007) 954-985.
- [12] S.W. Ko, R. Mondal, C. Risko, J.K. Lee, S.H. Hong, M.D. McGehee, J.L. Bredas, Z.A. Bao, *Tuning the Optoelectronic Properties of Vinylene-Linked Donor-Acceptor Copolymers for Organic Photovoltaics*, *Macromolecules* 43 (2010) 6685-6698.
- [13] J.P. Lu, Y.N. Jin, J.F. Ding, Y. Tao, M. Day, *High-Efficiency Multilayer Polymeric Blue Light-Emitting Diodes Using Boronate Esters as Cross-Linking Linkages*, *Journal of Materials Chemistry* 16 (2006) 593-601.
- [14] H. Yan, B.J. Scott, Q.L. Huang, T.J. Marks, *Enhanced Polymer Light-Emitting Diode Performance Using a Crosslinked-Network Electron-Blocking Interlayer*, *Advanced Materials* 16 (2004) 1948-1953.
- [15] A. Charas, H. Alves, L. Alcacer, J. Morgado, *Use of Cross-Linkable Polyfluorene in the Fabrication of Multilayer Polyfluorene-Based Light-Emitting Diodes with Improved Efficiency*, *Applied Physics Letters* 89 (2006) 143519.
- [16] L. Ling, J.B. Lagowski, *Electronic Band Structure of Alternating Fluorene-Oxadiazole Conjugated Copolymer - a 1D Solid-State DFT Study*, *Journal of Molecular Structure-Theochem* 944 (2010) 146-155.
- [17] M.T. Dang, L. Hirsch, G. Wantz, J.D. Wuest, *Controlling the Morphology and Performance of Bulk Heterojunctions in Solar Cells. Lessons Learned from the Benchmark*

*Poly(3-Hexylthiophene): 6,6 -Phenyl-C-6l-Butyric Acid Methyl Ester System*, Chemical Reviews 113 (2013) 3734-3765.

[18] C.L. Chochos, S.A. Choulis, *How the Structural Deviations on the Backbone of Conjugated Polymers Influence Their Optoelectronic Properties and Photovoltaic Performance*, Progress in Polymer Science 36 (2011) 1326-1414.

[19] A.C. Grimsdale, K.L. Chan, R.E. Martin, P.G. Jokisz, A.B. Holmes, *Synthesis of Light-Emitting Conjugated Polymers for Applications in Electroluminescent Devices*, Chemical Reviews 109 (2009) 897-1091.

[20] G.Z. Yang, W.Z. Wang, M. Wang, T.X. Liu, *Side-Chain Effect on the Structural Evolution and Properties of Poly(9,9-Dihexylfluorene-Alt-2,5-Dialkoxybenzene) Copolymers*, Journal of Physical Chemistry B 111 (2007) 7747-7755.

[21] J.M. Granadino-Roldan, A. Garzon, G. Garcia, M. Moral, A. Navarro, M.P. Fernandez-Liencre, T. Pena-Ruiz, M. Fernandez-Gomez, *Theoretical Study of the Effect of Alkyl and Alkoxy Lateral Chains on the Structural and Electronic Properties of Pi-Conjugated Polymers Consisting of Phenylethynyl-1,3,4-Thiadiazole*, Journal of Physical Chemistry C 115 (2011) 2865-2873.

[22] E. Cho, C. Risko, D. Kim, R. Gysel, N.C. Miller, D.W. Breiby, M.D. McGehee, M.F. Toney, R.J. Kline, J.L. Bredas, *Three-Dimensional Packing Structure and Electronic Properties of Biaxially Oriented Poly(2,5-Bis(3-Alkylthiophene-2-Yl)Thieno- 3,2-B Thiophene) Films*, Journal of the American Chemical Society 134 (2012) 6177-6190.

[23] J. Guo, Y. Liang, J. Szarko, B. Lee, H.J. Son, B.S. Rolczynski, L. Yu, L.X. Chen, *Structure, Dynamics, and Power Conversion Efficiency Correlations in a New Low Bandgap Polymer: PCBM Solar Cell*, Journal of Physical Chemistry B 114 (2010) 742-748.

[24] J.M. Szarko, J.C. Guo, Y.Y. Liang, B. Lee, B.S. Rolczynski, J. Strzalka, T. Xu, S. Loser, T.J. Marks, L.P. Yu, L.X. Chen, *When Function Follows Form: Effects of Donor Copolymer Side Chains on Film Morphology and BHJ Solar Cell Performance*, Advanced Materials 22 (2010) 5468-5472.

[25] M.J. Frisch, G.W. Trucks, H.B. Schlegel, G.E. Scuseria, M.A. Robb, J.R. Cheeseman, G. Scalmani, V. Barone, B. Mennucci, G.A. Petersson, H. Nakatsuji, M. Caricato, X. Li, H.P. Hratchian, A.F. Izmaylov, J. Bloino, G. Zheng, J.L. Sonnenberg, M. Hada, M. Ehara, K. Toyota, R. Fukuda, J. Hasegawa, M. Ishida, T. Nakajima, Y. Honda, O. Kitao, H. Nakai, T. Vreven, J.A. Montgomery, Jr., J.E. Peralta, F. Ogliaro, M. Bearpark, J.J. Heyd, E. Brothers, K.N. Kudin, V.N. Staroverov, R. Kobayashi, J. Normand, K. Raghavachari, A. Rendell, J.C. Burant, S.S. Iyengar, J. Tomasi, M. Cossi, N. Rega, J.M. Millam, M. Klene, J.E. Knox, J.B. Cross, V. Bakken, C. Adamo, J. Jaramillo, R. Gomperts, O.Y. R. E. Stratmann, A.J. Austin, R. Cammi, C. Pomelli, J.W. Ochterski, R.L. Martin, K. Morokuma, V.G. Zakrzewski, G.A. Voth, P. Salvador, J.J. Dannenberg, S. Dapprich, A.D. Daniels, Ö. Farkas, J.B. Foresman, J.V. Ortiz, J. Cioslowski, D.J. Fox, in: Gaussian, Inc., Wallingford, CT, (2009).

[26] S. Grimme, *Semiempirical GGA-Type Density Functional Constructed with a Long-Range Dispersion Correction*, Journal of Computational Chemistry 27 (2006) 1787-1799.

[27] A.D. Becke, *Density-Functional Thermochemistry .5. Systematic Optimization of Exchange-Correlation Functionals*, Journal of Chemical Physics 107 (1997) 8554-8560.

- [28] D.V. Dudenko, J.R. Yates, K.D.M. Harris, S.P. Brown, *An NMR Crystallography DFT-D Approach to Analyse the Role of Intermolecular Hydrogen Bonding and Pi-Pi Interactions in Driving Cococrystallisation of Indomethacin and Nicotinamide*, *Crystengcomm* 15 (2013) 8797-8807.
- [29] P. Lazar, F. Karlicky, P. Jurecka, M. Kocman, E. Otyepkova, K. Safarova, M. Otyepka, *Adsorption of Small Organic Molecules on Graphene*, *Journal of the American Chemical Society* 135 (2013) 6372-6377.
- [30] Y.-A. Duan, Y. Geng, H.-B. Li, X.-D. Tang, J.-L. Jin, Z.-M. Su, *Theoretical Study on Charge Transport Properties of Cyanovinyl-Substituted Oligothiophenes*, *Organic Electronics* 13 (2012) 1213-1222.
- [31] Y. Minenkov, A. Singstad, G. Occhipinti, V.R. Jensen, *The Accuracy of DFT-Optimized Geometries of Functional Transition Metal Compounds: A Validation Study of Catalysts for Olefin Metathesis and Other Reactions in the Homogeneous Phase*, *Dalton Transactions* 41 (2012) 5526-5541.
- [32] S. Yesilot, B. Cosut, H.A. Alidagi, F. Hacivelioglu, G.A. Ozpinar, A. Kilic, *Intramolecular Excimer Formation in Hexakis(Pyrenyloxy)Cyclotriphosphazene: Photophysical Properties, Crystal Structure, and Theoretical Investigation*, *Dalton Transactions* 43 (2014) 3428-3433.
- [33] M.J. Eslamibidgoli, J.B. Lagowski, *The Effect of Side-Chain Length on the Solid-State Structure and Optoelectronic Properties of Fluorene-Alt-Benzothiadiazole Based Conjugated Polymers-a DFT Study*, *Journal of Physical Chemistry A* 116 (2012) 10597-10606.
- [34] A.D. Becke, *Density-Functional Thermochemistry .3. The Role of Exact Exchange*, *Journal of Chemical Physics* 98 (1993) 5648-5652.
- [35] C.T. Lee, W.T. Yang, R.G. Parr, *Development of the Colle-Salvetti Correlation-Energy Formula into a Functional of the Electron-Density*, *Physical Review B* 37 (1988) 785-789.
- [36] X.B. Feng, N.M. Harrison, *Electronic Structure of CaCuO<sub>2</sub> from the B3LYP Hybrid Density Functional*, *Physical Review B* 69 (2004) 155107.
- [37] A. Irfan, A.G. Al-Sehemi, *DFT Study of the Electronic and Charge Transfer Properties of Perfluoroarene-Thiophene Oligomers*, *Journal of Saudi Chemical Society* 18 (2014) 574-580.
- [38] S.Q. Niu, X.B. Wang, J.A. Nichols, L.S. Wang, T. Ichiye, *Combined Quantum Chemistry and Photoelectron Spectroscopy Study of the Electronic Structure and Reduction Potentials of Rubredoxin Redox Site Analogues*, *Journal of Physical Chemistry A* 107 (2003) 2898-2907.
- [39] (Semichem Inc.:Shawnee Mission, Wallingford, CT, 2000-2008).
- [40] A. Rajagopal, C.I. Wu, A. Kahn, *Energy Level Offset at Organic Semiconductor Heterojunctions*, *J. App. Phys.* 83 (1998) 2649-2655.
- [41] C.Y. Chi, G. Wegner, *Chain-Length Dependence of the Electrochemical Properties of Conjugated Oligofluorenes*, *Macromolecular Rapid Communications* 26 (2005) 1532-1537.
- [42] S.S. Zade, N. Zamoshchik, M. Bendikov, *From Short Conjugated Oligomers to Conjugated Polymers. Lessons from Studies on Long Conjugated Oligomers*, *Accounts of Chemical Research* 44 (2011) 14-24.

- [43] U. Salzner, P.G. Pickup, R.A. Poirier, J.B. Lagowski, *Accurate Method for Obtaining Band Gaps in Conducting Polymers Using a DFT/Hybrid Approach*, Journal of Physical Chemistry A 102 (1998) 2572-2578.
- [44] E.F. Oliveira, F.C. Lavarda, *Effect of the Length of Alkyl Side Chains in the Electronic Structure of Conjugated Polymers*, Materials Research 17 (2014) 1369-1374.
- [45] X.-Y. Wang, F.-D. Zhuang, X. Zhou, Y. Dong-Chu, W. Jie-Yu, J. Pei, *Influence of Alkyl Chain Length on the Solid-State Properties and Transistor Performance of Bn-Substituted Tetrathienonaphthalenes*, Journal of Materials Chemistry C 2 (2014) 8152-8161.
- [46] J.M. Granadino-Roldan, A. Garzon, G. Garcia, M. Moral, A. Navarro, F.-L. Paz, M., T. Pena-Ruiz, M. Fernandez-Gomez, *Theoretical Study of the Effect of Alkyl and Alkoxy Lateral Chains on the Structural and Electronic Properties of Pi-Conjugated Polymers Consisting of Phenylethynyl-1,3,4-Thiadiazole*, Journal of Physical Chemistry C 115 (2011) 2865-2873.
- [47] V. Coropceanu, J. Cornil, D.A. da Silva Filho, Y. Olivier, R. Silbey, J.-L. Bredas, *Charge Transport in Organic Semiconductors*, Chemical Reviews 107 (2007) 926-952.
- [48] J.L. Bredas, J.P. Calbert, D.A. da Silva, J. Cornil, *Organic Semiconductors: A Theoretical Characterization of the Basic Parameters Governing Charge Transport*, Proceedings of the National Academy of Sciences of the United States of America 99 (2002) 5804-5809.

# Chapter 4

## 4 Assessment of the Performance of Four Dispersion-Corrected DFT Methods Using Optoelectronic Properties and Binding Energies of Organic Monomer/Fullerene Pairs

A slightly revised version of Chapter 4 has been published with (Sarah A. Ayoub and Jolanta B. Lagowski, *Computational and Theoretical Chemistry*, 2018, 1139, 15-26).

### 4.1 Abstract

With the aid of different polymer materials, their properties can be adjusted so as to enhance the efficiencies of heterogeneous organic solar cells. It is known that computational investigations involving density functional theory (DFT) can play an important role in identifying polymers with favourable properties and hence in speeding up the process of designing organic solar cells with higher efficiencies. However, what is

often not known is which one of the dispersion-corrected DFT (D-DFT) methods gives the most accurate results (relative to the experimental data) for the various properties of conjugated systems such as are found in heterogeneous organic solar cells. In this study, we employ  $\omega$ B97x-D, B97-D3, B3LYP-D3, and PBE1PBE-D3 and assess their accuracy by computing binding energies and electronic parameters (such as HOMO and LUMO eigenvalues) of the various (promising) molecular pairings of organic monomers and fullerenes. In addition, we employ time dependent DFT (TD-DFT) to determine optical properties of monomers such as their maximum absorption wavelengths and compare them with the experimental findings. Our results show that B97-D3 and B3LYP-D3 computations give the largest binding energies relative to the other D-DFT methods and they yield (relative to experimental values) the most accurate electronic and absorption results.

## 4.2 Introduction

Since the discovery of organic conjugated polymers, there has been a great interest in their use in organic solar cells (OSC). The best devices that have shown high power conversion efficiencies (PCEs), that recently reached above 10%, [1] consist of a mixture of conjugated polymers and fullerenes in the bulk heterojunction active layer. The interest in OSCs can be attributed to their unique characteristics, such as low cost and easy processing, compared to inorganic materials. However relatively high PCEs of inorganic

solar cells, reaching 25%, [2] means that many theoretical and experimental studies will continue to focus on improving the performance of OSCs.

It is known that, amongst many factors, the knowledge of intermolecular interactions, HOMO and LUMO levels, and optical absorptions of polymers and fullerenes is critical in designing of efficient OSCs. Carrying out experiments for the numerous organic materials that could be considered as possible candidates for OSCs is both expensive and very time consuming. Instead computational investigations are often carried out to determine the best material candidates for OSCs. However, an accurate simulation of the properties of these materials remains a major challenge due to the large molecular size of conjugated systems involved and the heterogeneous nature of the most efficient OSCs. For this reason, most computational studies tend to use approximate approaches that are still relatively accurate but are not prohibitively computationally intensive. For example, one common approach is to employ monomers of polymers or short oligomers in the simulations. It has been shown that this approach provides very accurate results relative to corresponding experimental data (see for example [3, 4]). Recently, we used a dimer approach (which consists of two (possibly different) conjugated monomers that are not covalently bonded) that employed dispersion-corrected density functional theory (D-DFT) B97D approximation to take into account the intermolecular interactions that play a major role in the multi-layered organic light emitting diodes. [5] Our results highlighted some very useful (general) trends in electronic, structural and intermolecular properties of these dimers that can be used as a guide when selecting promising heterogeneous polymer pairs for these multi-layered diodes. In addition, in order to reduce the computation time

even further, the long side chains of monomers are often replaced with either shorter or no side chains.

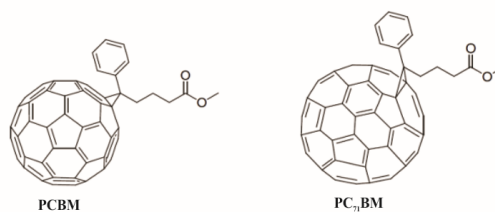
Undoubtedly, DFT is the most efficient quantum mechanical approach for simulating properties of monomers and oligomers of conjugated polymers. It is known that the calculated DFT data of conjugated systems display some deviations from the corresponding experimental values, however, the trends in DFT values are almost always similar to the respective experimental trends. [6-8] An important extension of DFT is the time dependent DFT (TD-DFT) which is a popular method of obtaining optical absorption and emission spectra for the systems of interest. Both DFT and TD-DFT methods have played a significant role in providing the understanding of the electronic and optical properties of isolated conjugated molecules at a reasonable computational cost. [5, 9] The D-DFT is very important for describing the intermolecular interactions between, say, monomers and fullerenes in the active layer of OSCs. However, due to the large size of monomer/fullerene combinations, D-DFT methods are rarely used in the studies of organic solar cells as opposed to the conventional DFT methods (such as DFT/B3LYP [10] and TD-DFT/B3LYP [11, 12]). To our knowledge, no computational studies, that provide a comparison of D-DFT methods as applied to organic monomers and fullerenes in OSCs, are available as yet. It is our belief that determining the most accurate D-DFT method(s), that exhibits consistent trends in comparison to the corresponding experimental ones, is an essential step in the computational effort whose main goal is to improve the efficiency of OSCs.

In this study, we assess the performance of the four D-DFT methods:  $\omega$ B97x-D, B97-D3, B3LYP-D3, and PBE1PBE-D3 and determine the most favorable D-DFT method for polymer and fullerene combinations used in OSCs. The assessment is carried out by comparing the computational results with the respective experimental values for materials that have been found to exhibit high PCEs such as P3HT (3.1-5.2%) [13, 14], PCDTBT (5-7.5%) [15], PBDTTPD (6.8-8.5%) [16, 17], PTB7 (8.2 %) [18], PNT4T (10.1%) [1], PBTff4T (9.6-10.4%) [1], and PffBT4T (10.4-10.5%) [1] in combination with PCBM or PC<sub>71</sub>BM. Using the four D-DFT methods, we examine the trends of the binding energies of monomer/fullerene combinations and compare the electronic structures data and (TD-DFT) maximum absorption wavelengths with the corresponding experimental values. We also briefly comment on the effect of side chains on the monomer and fullerene interactions.

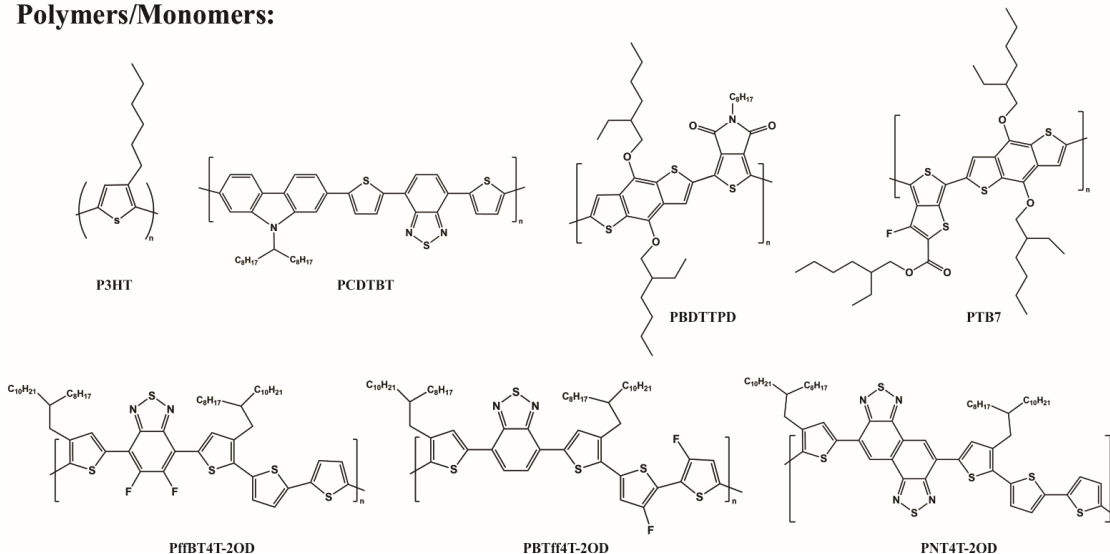
### 4.3 Materials and Methods

The chemical structures of P3HT, PTB7, PCDTBT, PBDTTPD, PNT4T-2OD, PffBT4T-2OD, and PBTff4T-2OD polymers and PCBM and PC<sub>71</sub>BM fullerenes are shown in Scheme 4.1. As mentioned in the Introduction, one approach to reducing the computational cost is to shorten the side chains of polymers. In this work, most monomers used in computations have their side chains shortened to C<sub>2</sub>H<sub>5</sub> or have no side chains. In few cases, we perform calculations for monomers with long side chains to assess if monomers with short and long side chains give similar property trends.

## Fullerene:



## Polymers/Monomers:



Scheme 4. 1: Chemical composition of PCBM, PC<sub>71</sub>BM, P3HT, PTB7, PCDTBT, PBDTTPD, PNT4T-2OD, PffBT4T-2OD, and PBTff4T-2OD.

All calculations are carried out with Gaussian 09. [19] All geometries of the isolated seven monomers and two fullerenes and the fourteen molecular pairs of monomer/fullerene are geometry optimized using the B97-D3, B3LYP-D3,  $\omega$ B97x-D, and PBE1PBE-D3 methods at the 6-31G(d) basis set level. The B3LYP-D3 and the PBE1PBE-D3 (also known as PBE0-D3) is a hybrid generalized gradient approximations (GGA) functional, [20-22] the B97-D3 is a semi-empirical Grimme's modified GGA functional, [23] and the  $\omega$ B97x-D is a long-range corrected hybrid density functional. [24] All four of these functionals are augmented with Grimme's dispersion term to overcome the well-known failure of DFT in describing the van der Waal interactions. Three functionals: B97-

D3, B3LYP-D3, and PBE1PBE-D3 include the latest D3 version of Grimme's dispersion term [25] and the  $\omega$ B97x-D method includes the D2 version [24] of this term (only available in Gaussian 09). Using the D-DFT methods, for each pair, we calculate the binding energy ( $\Delta E_b$ ) which is defined as the difference between the total energies of monomers and fullerenes, and the total energy of the monomer/fullerene pair,

$$\Delta E_b = \sum_{i=1}^2 E_i - E_{pair}. \quad (4.1)$$

Also, the B3LYP method is used to geometry optimize the isolated monomers and fullerenes to obtain their electronic structures in the gas phase.

Because the DFT/B3LYP/6-31G(d) results are known to be in good agreement with the respective experimental values and trends, we carry out B3LYP single point (SP) calculations on the D-DFT geometries of the monomers and fullerenes (referred to as interacting, instead of isolated, monomers and fullerenes) to generate their HOMO ( $\epsilon_{HOMO}$ ) and LUMO ( $\epsilon_{LUMO}$ ) eigenvalues and energy gaps ( $E_g$ 's). Similarly, the absorption spectra and maximum absorption wavelengths ( $\lambda_{max}$ 's) of monomers are computed with SP TD-DFT/B3LYP using their optimized isolated D-DFT and B3LYP, and interacting D-DFT geometries.

We estimate the accuracy of D-DFT methods by computing the mean absolute deviation (MAD) and percentage deviation (% dev) defined respectively as follows

$$MAD = \frac{\sum_{i=1}^n |x_i - c|}{n}, \quad (4.2)$$

$$\% \text{ dev} = \frac{|x_i - c|}{c} \times 100, \quad (4.3)$$

where  $x_i$  denotes the computed data such as  $\epsilon_{HOMO}$ ,  $\epsilon_{LUMO}$ ,  $E_g$ , or  $\lambda_{max}$  of monomers and fullerenes,  $c$  denotes the corresponding B3LYP gas phase or experimental values, and  $n$  is the number of data points.

## 4.4 Results and Discussions

In this section, we use the results of our computations and identify the optimal D-DFT method(s) that can be employed to carry out future calculations on the molecular combinations that may include conjugated monomers (with and without side chains) and fullerenes.

### 4.4.1 Binding Energies Comparison

First we examine the magnitudes of binding energies,  $\Delta E_b$ 's (see equation 4.1), of the fourteen monomer/fullerene pairs (see Scheme 4.1) as obtained using B3LYP-D3, B97-D3,  $\omega$ B97x-D, and PBE1PBE-D3 methods (see Figure 4.1 and Table B1 in Appendix B).

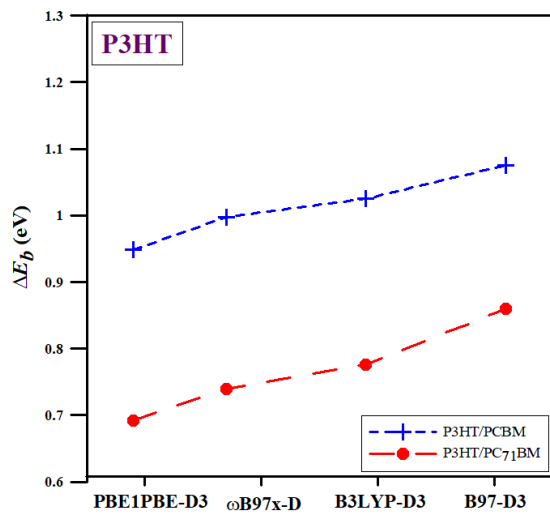
The results of the four D-DFT methods binding energy computations show that the stabilities of most pairs are inversely proportional to the size of the fullerene. That is, with one exception, the  $\Delta E_b$ 's of monomer/fullerene pairs with a fewer number of heavy atoms ( $N_h$ ), i.e. those containing PCBM, are larger (by approximately 0.2 eV) than those with larger  $N_h$  (containing PC<sub>71</sub>BM). The one exception is the combination that includes PBDTPD as can be seen from Figure 4.1 (d) (where two values are fairly close to each

other). Our results also show that the largest magnitudes of  $\Delta E_b$  are those calculated using the B97-D3 method while the smallest ones are those calculated using the PBE1PBE1-D3 method. The B3LYP-D3 and  $\omega$ B97x-D3 magnitudes of binding energies have intermediate values that are relatively close to each other for most pairs. This trend for the magnitudes of  $\Delta E_b$ 's (PBE1PBE-D3 <  $\omega$ B97x-D3  $\leq$  B3LYP-D3 < B97-D3) is clearly seen for all the pairs (see Figure 4.1 (a) to (g)).

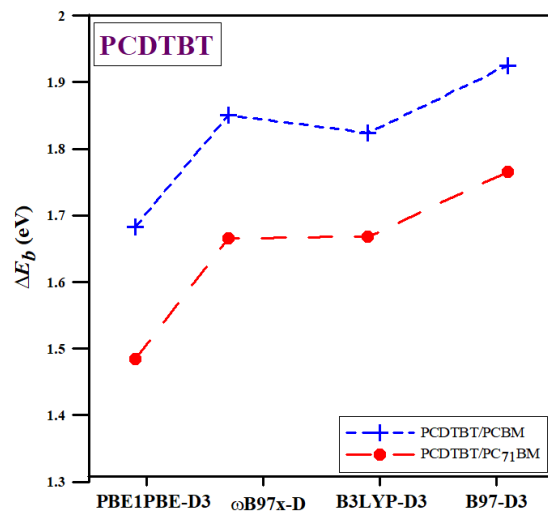
The above results indicate that consistent trends (rankings from the smallest to the largest) of the magnitudes of  $\Delta E_b$ 's for the various monomer/fullerene pairs are produced by all four of the D-DFT approximations (see Table B1 in Appendix B). Therefore, we can select the preferred method(s) for computing  $\Delta E_b$ 's for similar molecular systems based on which one of them is the least computationally intensive. B97-D3 computations take the least amount of time to complete relative to the other methods. We also briefly discuss the differences in the spread of the  $\Delta E_b$ 's as obtained from different D-DFT methods in Appendix B (see section B2). The results show that the spread in the  $\Delta E_b$  values is larger for longer monomers (>18 Å) and it tends to level off as the monomers get even longer.

In order to further assess the accuracy of these four D-DFT approaches we compare the computed electronic structure data with the corresponding experimental values. This comparison is carried out in the next subsection.

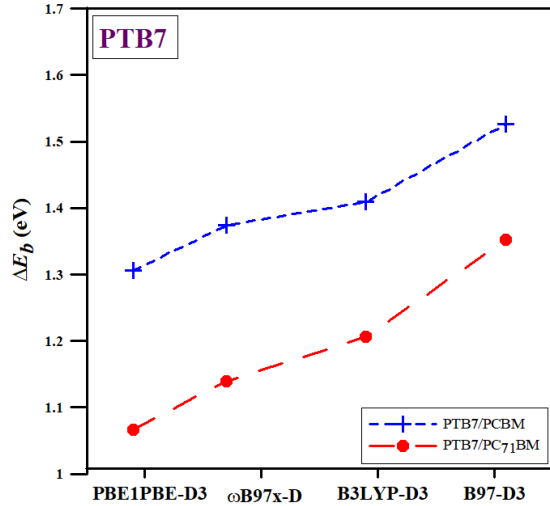
(a)



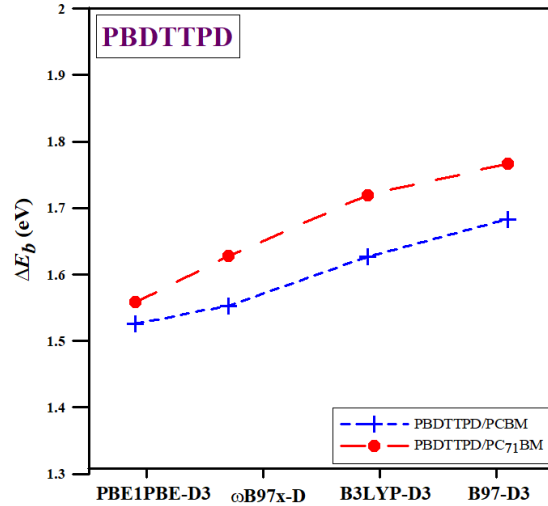
(b)



(c)



(d)



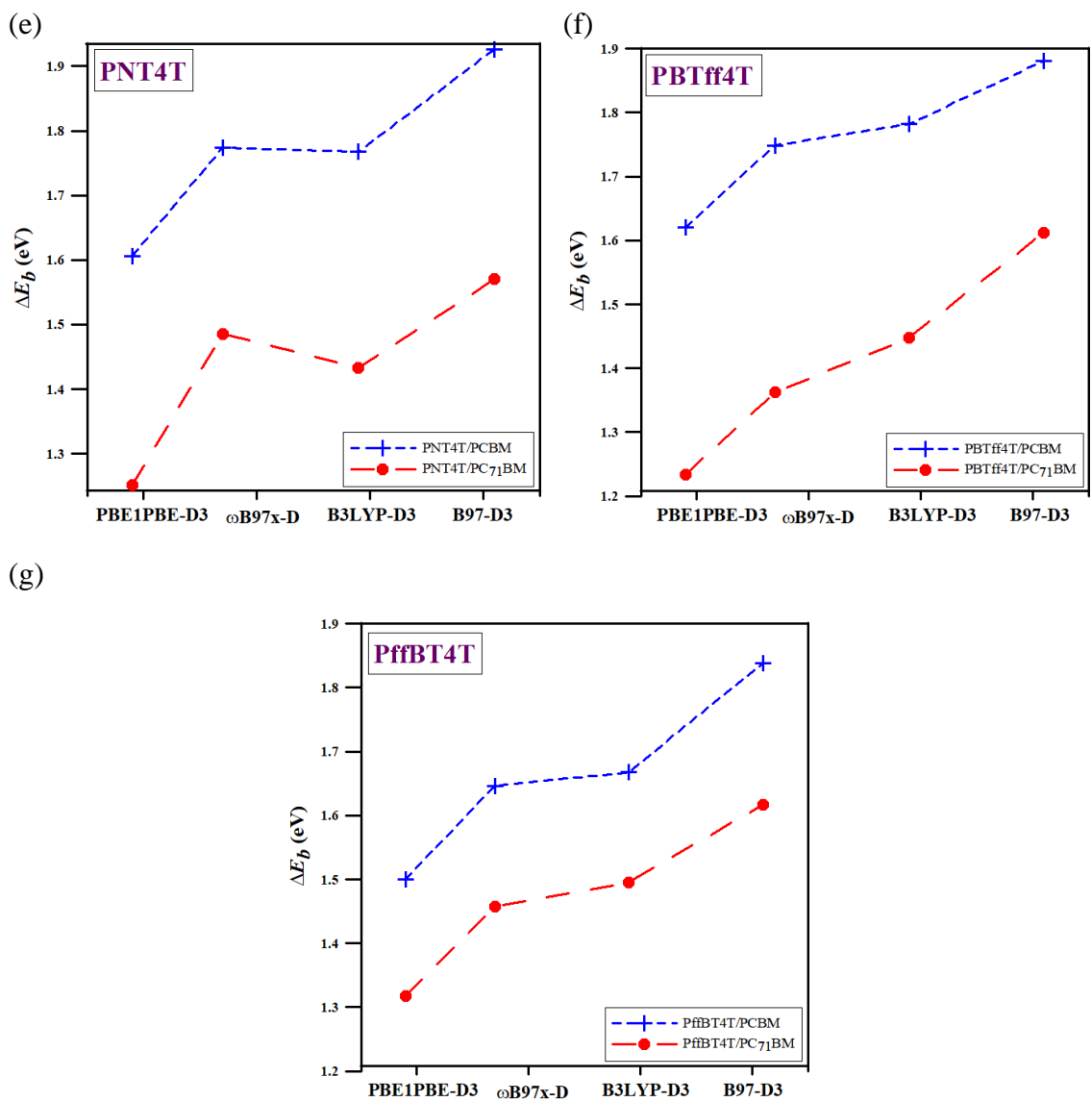


Figure 4.1: The binding energies of fourteen monomer/fullerene pairs optimized with the four D-DFT methods. For comparison purposes, all the y-axes are of the same length (0.7 eV).

## 4.4.2 Electronic Levels and Band Gaps Comparison

The  $\epsilon_{HOMO}$ ,  $\epsilon_{LUMO}$ , and  $E_g$  values (calculated with the SP B3LYP method using the D-DFT optimized geometries) for the seven interacting monomers with both types of fullerenes (PCBM and PC<sub>71</sub>BM) are displayed in Figure 4.2 and are given in Table B2 in Appendix B. In most cases (with the exception of PBTff4T), the  $\epsilon_{LUMO}$ 's of monomers interacting with PCBM are lowered relative to those interacting with PC<sub>71</sub>BM. In contrast, the  $\epsilon_{HOMO}$ 's of the monomers interacting with PCBM are raised relative to those interacting with PC<sub>71</sub>BM. As a result of these lowerings and raisings, the  $E_g$ 's of most monomers (such as P3HT, PTB7, PNT4T, and Pff4TBT) interacting with PCBM are smaller than those interacting with PC<sub>71</sub>BM. In the case of PCDTBT and PBDTTPD monomers, their values for  $\epsilon_{LUMO}$ 's,  $\epsilon_{HOMO}$ 's and  $E_g$ 's are nearly the same irrespective of which fullerene they are interacting with.

Moreover, our SP B3LYP results indicate that for a given interacting monomer (in most cases), the lowest  $\epsilon_{LUMO}$ , the highest  $\epsilon_{HOMO}$  and the smallest  $E_g$  are found for those using the (optimized) B97-D3 geometries while the highest  $\epsilon_{LUMO}$ , the lowest  $\epsilon_{HOMO}$  and the largest  $E_g$  are exhibited for those using the (optimized)  $\omega$ B97x-D geometries. The electronic parameters corresponding to the B3LYP-D3 geometries have intermediate values between those employing the  $\omega$ B97x-D and B97-D3 geometries. In general, it is clear from Figure 4.2 that the electronic data of the interacting monomers follow the order of  $\omega$ B97x-D < B3LYP-D3 < B97-D3 for the  $\epsilon_{HOMO}$ 's and the order of  $\omega$ B97x-D > B3LYP-D3 > B97-D3 for the  $\epsilon_{LUMO}$ 's and the  $E_g$ 's. We find that the electronic parameters obtained

using the PBE1PBE-D3 geometries do not show consistent trends (in some cases, they are close to B3LYP-D3 results (see P3HT and PNT4T), in others they are closer to B97-D3 (see PCDTBT, PBTff4T) and yet in others they are closer to either B3LYP-D3 or B97-D3 depending on which fullerene they are interacting with (see PffBT4T, PBDTTPD). These inconsistencies indicate that PBE1PBE-D3 should probably not be used to study the dispersion effect in conjugated molecular systems.

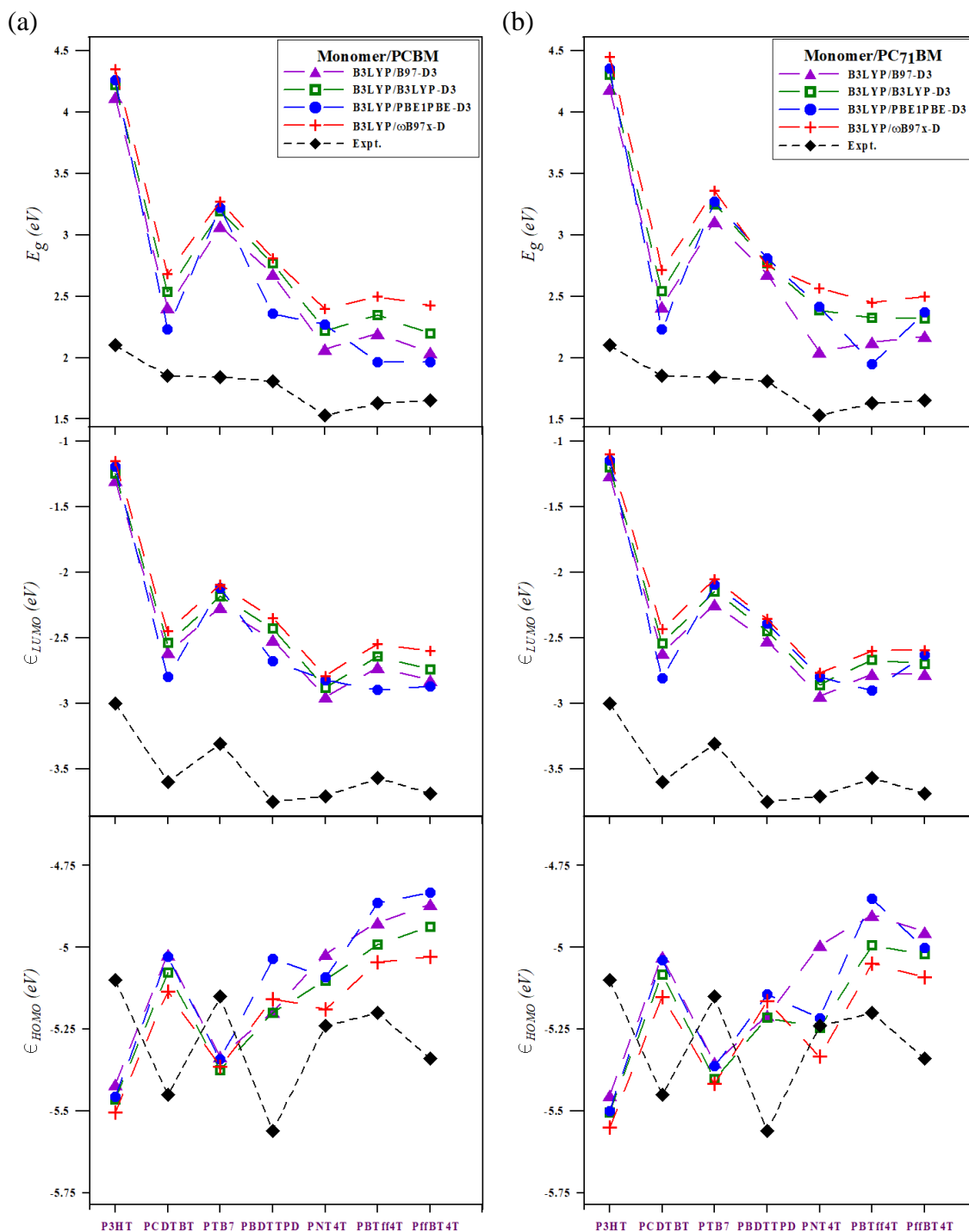


Figure 4.2: The SP B3LYP of  $\epsilon_{HOMO}$ 's,  $\epsilon_{LUMO}$ 's, and  $E_g$ 's obtained using the four D-DFT optimized geometries of the interacting monomers with (a) PCBM and (b) PC<sub>71</sub>BM. Monomers, along the x-axis, are ordered (from the lowest to the highest) according to the PCEs of their respective OSCs.

To further assess the accuracy of the four D-DFT methods, we calculate the MADs of the  $\epsilon_{HOMO}$ ,  $\epsilon_{LUMO}$ , and  $E_g$  values by: (1) comparing the respective electronic parameters as obtained by applying SP B3LYP to the D-DFT geometries of the isolated (gas phase) monomers and fullerene to the corresponding (optimized) B3LYP gas phase values, and (2) comparing the respective electronic parameters as obtained by applying SP B3LYP to the D-DFT geometries of the interacting monomers and fullerenes to the corresponding experimental data (see Table B3 and Appendix B). In the first case, as expected, the electronic data of the B3LYP and B3LYP-D3 isolated monomers and fullerenes are very similar (with an MAD of 0.01, 0.00, and 0.02 eV for  $\epsilon_{HOMO}$ ,  $\epsilon_{LUMO}$ , and  $E_g$  respectively) since the structural corrections due to the dispersion are small for the isolated monomers and fullerenes. Deviations due to other D-DFT methods relative to B3LYP are also relatively small (less than 0.1 eV in most cases). Table B3 and Figure 4.3 (a) show that the MADs of the SP B3LYP  $\epsilon_{HOMO}$ ,  $\epsilon_{LUMO}$ , and  $E_g$  values (using the four D-DFT isolated monomer and fullerene geometries) relative to the (optimized) B3LYP gas phase values follow the order of B3LYP-D3 < PBE1PBE-D3 < B97-D3 <  $\omega$ B97x-D.

The results of the MADs relative to the experimental values are also given in Table B3 in Appendix B and are shown in Figure 4.3 (b). In this second case, our results show that the highest MADs (close to 1.15 eV) are for the  $\epsilon_{LUMO}$ 's while the lowest MADs (close to 0.3 eV) are for the  $\epsilon_{HOMO}$ 's. The MAD values of  $E_g$ 's are of the order of 1 eV. These types of deviations are typical of B3LYP DFT calculations (giving good agreement with experimental data for HOMO but not for LUMO eigenvalues). [26] It should also be noted that the large values of MADs for  $E_g$ 's is due to the fact that we are comparing (computed)

monomer  $E_g$ 's to (experimental) polymer  $E_g$ 's which are typically quite a bit smaller than the  $E_g$ 's of the monomers (since, up to a point,  $E_g$ 's decrease linearly with the length of the oligomer [27]). Moreover, even for monomers, we can see that the accuracy of  $E_g$ 's is dependent on the monomer's lengths. This is clearly illustrated in Figure 4.4 which shows an example of the percentage deviation from the experimental values (see equation 4.3) for  $E_g$ 's of the interacting monomers with PC<sub>71</sub>BM using the B97-D3 geometries as a function of the monomer's length. This is also confirmed in Figure 4.4 (b) that illustrates the  $E_g$ 's of nP3HT as function of 1/n, where n=1, 2, and 3, indicating that the  $E_g$  of 3P3HT obtained using the B97-D3 geometry is very close to the experimental value. Hence, it is expected that the MAD values computed with  $E_g$ 's, HOMOs and LUMOs of only long chain-length monomers (above 18 Å) will be reduced for all D-DFT geometries in comparison to MAD values obtained using all electronic data that includes short and long monomers (see Figure 4.3 (c) and (b) respectively where this comparison is made).

Since B3LYP often gives good electronic results, it is expected, that the B3LYP-D3 would produce the smallest deviations from experimental data. Somewhat unexpectedly, the PBE1PBE-D3 and B97-D3 methods give somewhat smaller deviations from the experimental data than B3LYP-D3 indicating the solid-state effect (due to dispersion) is better represented in PBE1PBE-D3 and B97-D3 relative to B3LYP-D3 method. The highest MAD values are found for the  $\omega$ B97x-D method. Therefore, based on the MAD results of Table B3 in Appendix B and Figure 4.3, the accuracy of the D-DFT methods (from highest to lowest) as used in the SP B3LYP electronic structure calculations can be ranked as follows B97-D3 $\geq$ PBE1PBE-D3>B3LYP-D3> $\omega$ B97x-D.

Even though the above MAD results show that the PBE1PBE-D3 gives relatively high accuracy for the electronic parameters when compared to the respective gas phase and experimental values, the fact that this method does not show consistent trend for the individual  $\epsilon_{HOMO}$ 's,  $\epsilon_{LUMO}$ 's, and  $E_g$ 's of the interacting monomers and fullerenes as seen in Figure 4.2, makes it somewhat unreliable. In order to gain further insight as to why some of the D-DFT methods (such as the B97-D3) exhibit smaller deviations in the SP B3LYP electronic parameters than others (such as the  $\omega$ B97x-D), we compute the MADs using optimized electronic structure values as obtained from the four D-DFT methods for the interacting monomers and fullerenes (without the use of the SP B3LYP calculations) and compare them to the corresponding experimental values (see Figure 4.3 (d) and Table B4 in Appendix B). The results show a large increase in the MADs for the  $\omega$ B97x-D electronic parameters. Relatively large MADs are also observed in the  $\epsilon_{LUMO}$  and  $E_g$  calculated with the PBE1PBE-D3 method and the  $\epsilon_{HOMO}$  calculated at the B97-D3 method. On the other hand, the MADs calculated with B97-D3 method are significantly decreased for the  $\epsilon_{LUMO}$  and  $E_g$ , confirming the relative accuracy of the B97-D3 when determining electronic structures with and without performing the SP B3LYP calculations (see Figure 4.3 (b) and (d)). However, the significant increase in most of the MAD values leads us to highlight the importance of performing the SP B3LYP method on the D-DFT geometries to obtain more accurate electronic parameters. We analyze the chain length dependence on MAD values in greater details in Appendix B (see Figures B4 and B5).

In conclusion, based on the discussion in subsections 4.4.1 and 4.4.2, we recommend the B97-D3 and B3LYP-D3 methods as preferable D-DFT methods for the

monomer/fullerene computations because they provide consistent trends for the electronic parameters and binding energies (in addition to giving small MAD values). We also note (as in subsection 4.4.1) that the B97-D3 approximation is less computationally intensive compared to the other D-DFT methods. We use both (B97-D3 and B3LYP-D3) methods in further studies involving pairs with monomers with long side chains.

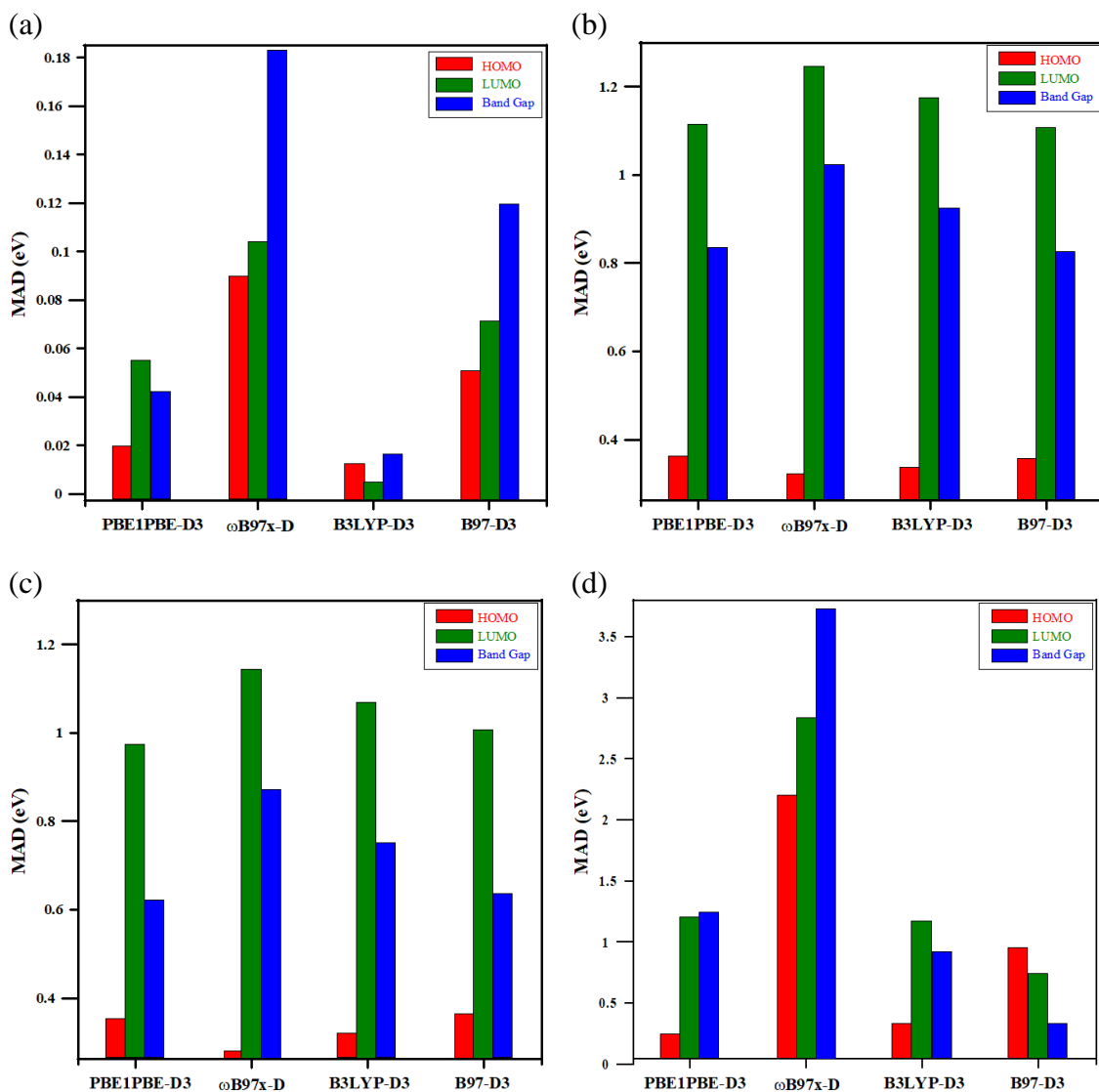


Figure 4.3: MADs in  $\epsilon_{HOMO}$ 's,  $\epsilon_{LUMO}$ 's, and  $E_g$ 's calculated (a) with the SP B3LYP using the four D-DFT isolated monomers and fullerenes relative to the B3LYP gas phase, and (b) with the SP B3LYP and (d) without SP B3LYP using the four D-DFT interacting monomers and fullerenes relative to experimental values. (c) is the same as (b) but excluding the values corresponding to short monomers (with chain lengths smaller than  $18 \text{ \AA}$ ).

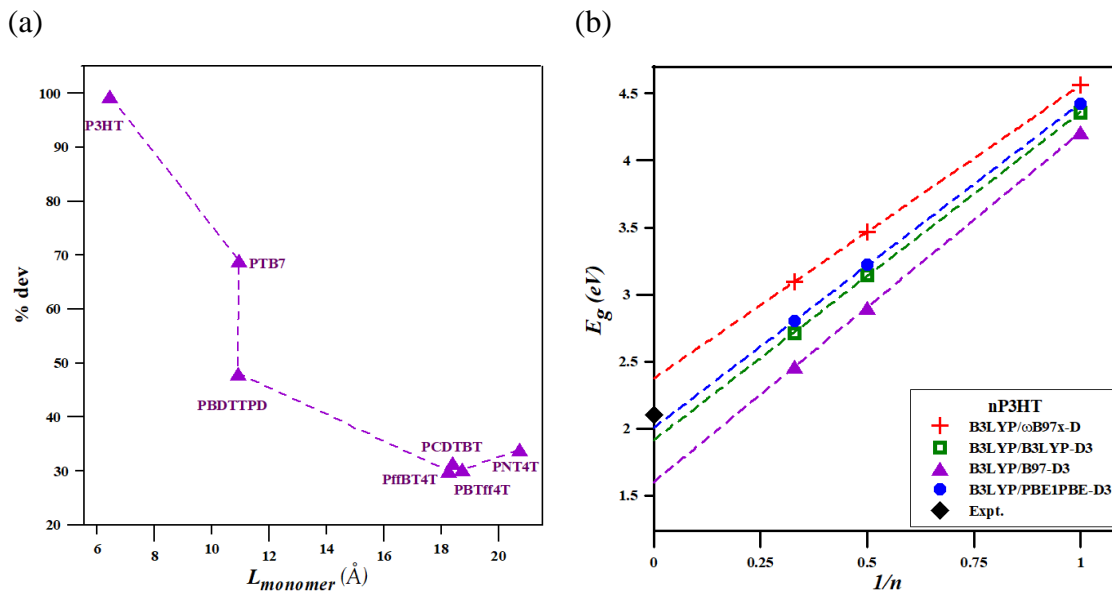


Figure 4.4: (a) The percentage deviations of nP3HT from the experimental values for  $E_g$ 's of the interacting monomers with PC<sub>71</sub>BM using the B97-D3 geometries versus the monomers' lengths, and (b) the  $E_g$ 's of nP3HT using the four D-DFT geometries versus  $1/n$  (where  $n=1,2,3$ ).

### 4.4.3 Side Chains Effect

We further test the performance of the D-DFT methods by considering monomers with long side chains in the monomer/fullerene pairs. It is known that monomer/polymers used in the BHJ solar cells have long side chains attached to the backbones to enhance their solubility during the thin-film formation (spin-coating) process. In this subsection, we focus on the results obtained from the two D-DFT methods: the B3LYP-D3 and the B97-D3. First, we compare the  $\Delta E_b$ 's of combinations that include monomers with long side chains to those that include monomers with short side chains (see subsection 4.4.1) for both types of fullerenes (see Figure 4.5 and Table B1 in Appendix B). In all cases, as

expected, the results show that  $\Delta E_b$ 's are larger for pairs with long side chains than for those with short side chains. Also, as in the case of short side chains, the B97-D3 binding energies are higher in comparison to the corresponding B3LYP-D3 values (by approximately 0.09 eV for the long side chain monomers which is comparable to approximately 0.07 eV for short side chains) (see Figure 4.5). The few exceptions for the monomers with long side chains that have B97-D3  $\Delta E_b$ 's smaller or nearly the same as B3LYP-D3  $\Delta E_b$ 's are PTB7 and PBDTTPD with both fullerenes. In general, similar trends of the relative magnitudes of  $\Delta E_b$ 's are observed for the B97-D3 and B3LYP-D3 methods for both the short and long side chain monomers. The one prominent difference is that among all pairs containing monomers with short side chains, PCDTBT/fullerene exhibits the largest  $\Delta E_b$  (and the variations in the magnitudes of  $\Delta E_b$ 's are relatively small in the case of short chain monomers), in contrast, among pairs containing monomers with long side chains, PNT4T/fullerene clearly has the largest  $\Delta E_b$  (see Figure 4.5). These results show that the (two) selected D-DFT methods provide consistent results for  $\Delta E_b$ 's for different combinations that include different lengths of side chains. We plan to investigate the effect of side chains on binding energies more thoroughly in future work.

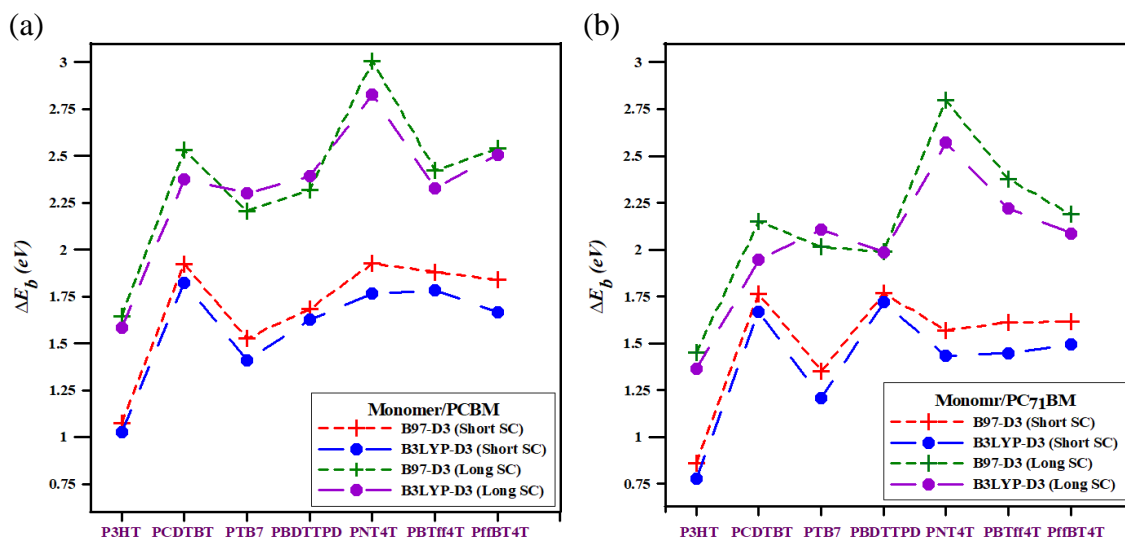


Figure 4.5: Binding energies of (a) monomer/PCBM and (b) monomer/PC<sub>71</sub>BM with short and long side chains (SC) optimized at the B97-D3 and the B3LYP-D3 methods.

We also assess further the performance of the two selected D-DFT methods by comparing the SP B3LYP electronic structures of the interacting monomers with short side chains to those with long side-chains (see Figure B1 in Appendix B). Similar to the short side chains results in subsection 4.4.2,  $\epsilon_{LUMO}$ 's (and  $\epsilon_{HOMO}$ 's) obtained using the B97-D3 interacting monomers are lower (and higher) than those using the B3LYP-D3 interacting monomers. In other words, the trend B3LYP-D3 > B97-D3 for  $\epsilon_{LUMO}$ 's and  $E_g$ 's and B3LYP-D3 < B97-D3 for  $\epsilon_{HOMO}$ 's is clearly seen for all the interacting monomers with long side chains. Our results also agree with previous observations which show that the length of side chains has a small effect on the electronic properties [26] of molecular systems (see Table B5 in Appendix B where the respective HOMO, LUMO and energy gap differences are given). Therefore, it is expected the MAD electronic structure results for monomers with short and long side chains will be similar. This is confirmed in Table 4.1 where it is

shown that the results of the B3LYP-D3 and B97-D3 MAD computations for the isolated and interacting monomers with long side chains show that they are very similar to the corresponding MAD values for monomers with short side chains. In summary, the results of this subsection confirm that, for the most part, the trends (but not magnitudes) in the  $\Delta E_b$ 's and in the electronic structures for the monomers with long side chains are similar to those obtained for monomers with short side chains and can be equally well reproduced with either the B3LYP-D3 or B97-D3 method.

Table 4.1: MADs of the SP B3LYP ( $\epsilon_{HOMO}$ ,  $\epsilon_{LUMO}$ , and  $E_g$ ) obtained using the D-DFT isolated and interacting fullerenes and monomers with short and long side chains (SC).

MAD			B3LYP-D3			B97-D3		
			$\epsilon_{HOMO}$ (eV)	$\epsilon_{LUMO}$ (eV)	$E_g$ (eV)	$\epsilon_{HOMO}$ (eV)	$\epsilon_{LUMO}$ (eV)	$E_g$ (eV)
relative to B3LYP gas phase values	isolated fullerenes and monomers	with short SC	0.01	0.00	0.02	0.05	0.07	0.12
		with long SC	0.05	0.02	0.06	0.05	0.07	0.08
relative to experimental values	interacting fullerenes and monomers	with short SC	0.34	1.17	0.92	0.36	1.11	0.82
		with long SC	0.28	1.21	0.96	0.31	1.14	0.86

#### 4.4.4 The Absorption Spectra Comparison

In this subsection, we present the results of TD-DFT calculations for the seven monomers using two (non-optimized SP) approaches: (1) by carrying out SP TD-DFT/B3LYP computations on the four D-DFT optimized geometries of the isolated monomers, and (2) by performing the SP TD-DFT/B3LYP computations on the four D-DFT geometries of the interacting monomers. We examine the accuracy of the results of these TD-DFT/D-DFT calculations by comparing the computed maximum absorption wavelengths ( $\lambda_{max}$ 's) of the monomers to the corresponding gas phase and experimental values (see Figure 4.6 and Table B6 in Appendix B) in the first and second approach respectively.

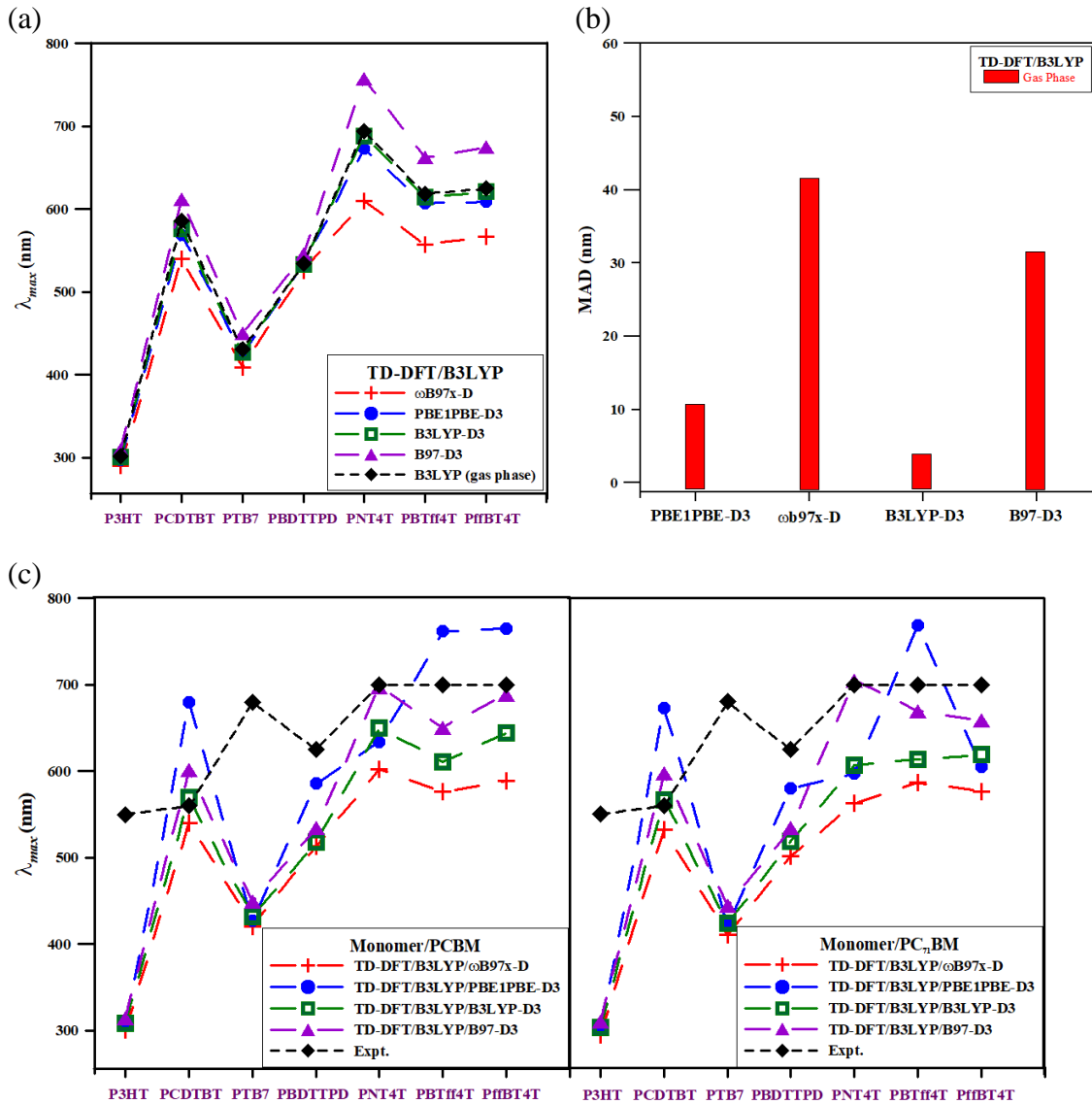
The absorption results of the first approach, as presented in Figure 4.6 (a) and Table B6 in Appendix B (see also examples of the TD-DFT/B3LYP absorption spectra in Figure B2 in Appendix B), show that the TD-DFT/B3LYP  $\lambda_{max}$ 's of isolated monomers obtained using  $\omega$ B97x-D and B97-D3 geometries exhibit the lowest and highest values respectively compared to those obtained using B3LYP-D3 and PBE1PBE-D3 geometries which display intermediate values that are very close to the B3LYP  $\lambda_{max}$ 's. In order to illustrate these trends more succinctly we display in Figure 4.6 (b) the MADs of  $\lambda_{max}$ 's relative to the TD-DFT/B3LYP gas phase values. This figure clearly shows that the  $\lambda_{max}$ 's obtained using B3LYP-D3 and PBE1PBE-D3 geometries are more accurate than those obtained using  $\omega$ B97x-D and B97-D3 geometries. In particular, B3LYP-D3 and PBE1PBE-D3 give MAD values of 3.9 and 10.8 nm respectively and  $\omega$ B97x-D and B97-D3 of 41.4 and 31.6 nm respectively. Hence, it can be said, that the accuracy of the TD-DFT/B3LYP/D-DFT,

from the highest to lowest can be ranked as follow: B3LYP-D3>PBE1PBE-D3>B97-D3> $\omega$ B97x-D.

The absorption results of the second approach are presented in Figure 4.6 (c) and Table B7 in Appendix B. The results show that the TD-DFT/B3LYP/D-DFT  $\lambda_{max}$ 's of monomers interacting with the smaller fullerenes are generally larger than those interacting with the larger fullerenes. Similar to the TD-DFT results of the first approach, the calculated data obtained using the second approach show that the  $\lambda_{max}$ 's of interacting monomers obtained using  $\omega$ B97x-D and B97-D3 geometries exhibit the lowest and highest values respectively compared to those obtained using B3LYP-D3 geometries which exhibit intermediate values. In addition, similarly to the electronic structure results as discussed in subsection 4.4.2, the results of TD-DFT/B3LYP  $\lambda_{max}$ 's obtained using PBE1PBE-D3 interacting monomers do not show consistent trends relative to other D-DFT methods. For example, the  $\lambda_{max}$  of PCDTBT obtained using the PBE1PBE-D3 geometries gives the highest value among the other D-DFT methods, while the  $\lambda_{max}$  of PNT4T obtained using the PBE1PBE-D3 geometries has a lower value compared to B3LYP-D3 and B97-D3 values (it does not have the highest value). Therefore, we do not recommend using PBE1PBE-D3 geometries in TD-DFT/B3LYP computations. Figure 4.6 (d) shows the MAD of the (interacting)  $\lambda_{max}$ 's relative to experimental values. These results indicate that, once again, TD-DFT/B3LYP/B97-D3 is the most accurate method. We also note that performing the SP TD-DFT/B3LYP on the B97-D3 (and other D-DFT) geometries is a critical step in these studies since MADs increase significantly (see Table B7 in Appendix B) when the TD-DFT calculations are carried out directly on B97-D3 (and

other D-DFT) geometries. The results of the second approach indicate that the accuracy order (from highest to lowest) for the TD-DFT/B3LYP/D-DFT methods is as follows:

B97-D3 > B3LYP-D3 ≥ PBE1PBE-D3 > ωB97x-D.



(d)

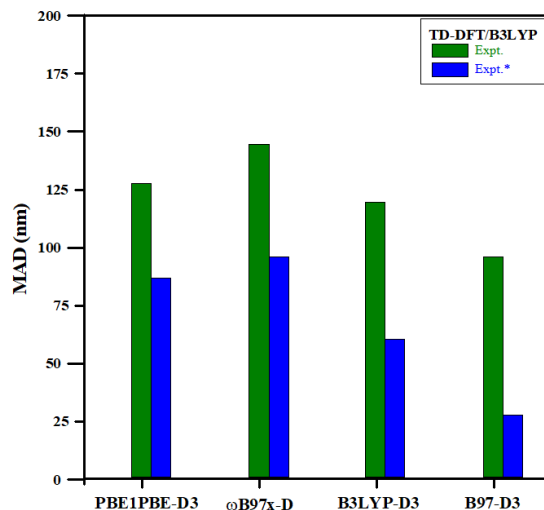


Figure 4.6: The maximum absorption wavelengths obtained using TD-DFT/B3LYP on the four D-DFT optimized geometries (a) for the isolated monomers and their (b) MADs from gas phase values, and (c) for the interacting monomers with both types of fullerenes and their (d) MADs from experimental values.

From Figure 4.6 (c), we note that there appears to be a correlation between the deviations in the  $\lambda_{max}$ 's and the monomer's chain-lengths. To assess the validity of this correlation, we determine the percentage deviations of TD-DFT/B3LYP/B97-D3  $\lambda_{max}$ 's from their experimental values (see equation (4.3)) for all interacting monomers with PCBM, and plot them versus the monomer's chain-length in Figure 4.7 (a). The results show that as the monomer's chain-length increases from approximately 6 to 20 Å, the percentage deviation decreases from 43.5 to 0.4 % for the interacting monomers, respectively. Similar results were also obtained for the other D-DFT methods, indicating that the TD-DFT results are more accurate for monomers with longer backbone chain-lengths. To verify this point, we plot the  $\lambda_{max}$ 's of nP3HT as function of n, where n=1, 2, and 3, corresponding to chain-lengths of about 6, 14, and 22 Å respectively (see Figure 4.7

(b)). For the four D-DFT nP3HT (where n=1,2,3) geometries, the results show that as the number of monomers increases from P3HT to 3P3HT, the  $\lambda_{max}$ 's are increased bringing them closer to the corresponding (bulk) experimental value. In fact, the  $\lambda_{max}$  of 3P3HT obtained using the B97-D3 geometry is in very good agreement with the experimental value. Figure 4.7 (b) also illustrates that the accuracy order for the D-DFT methods (from the highest to the lowest) is again B97-D3>B3LYP-D3 $\geq$ PBE1PBE-D3> $\omega$ B97xD3. We also exclude the data of monomers with chain-lengths shorter than 18 Å in our MADs of  $\lambda_{max}$ 's relative to the experimental data (i.e. we include only PCDTBT, PNT4T, PBTff4T, and Pff4TBT monomers in these calculations). These MAD results are shown as blue bars (marked as MAD from Expt.\*) in Figure 4.6 (d) and Table B7 in Appendix B. The TD-DFT/B3LYP/D-DFT results show that the MADs calculated using only  $\lambda_{max}$ 's of monomers with long backbone chain-lengths are considerably smaller than those calculated using all  $\lambda_{max}$ 's (of monomers with short and long backbone lengths). However, in all cases (short or long chain-lengths), the relative accuracy of methods for the  $\lambda_{max}$ 's has the same order (from highest to lowest): B97-D3>B3LYP-D3>PBE1PBE-D3> $\omega$ B97xD3

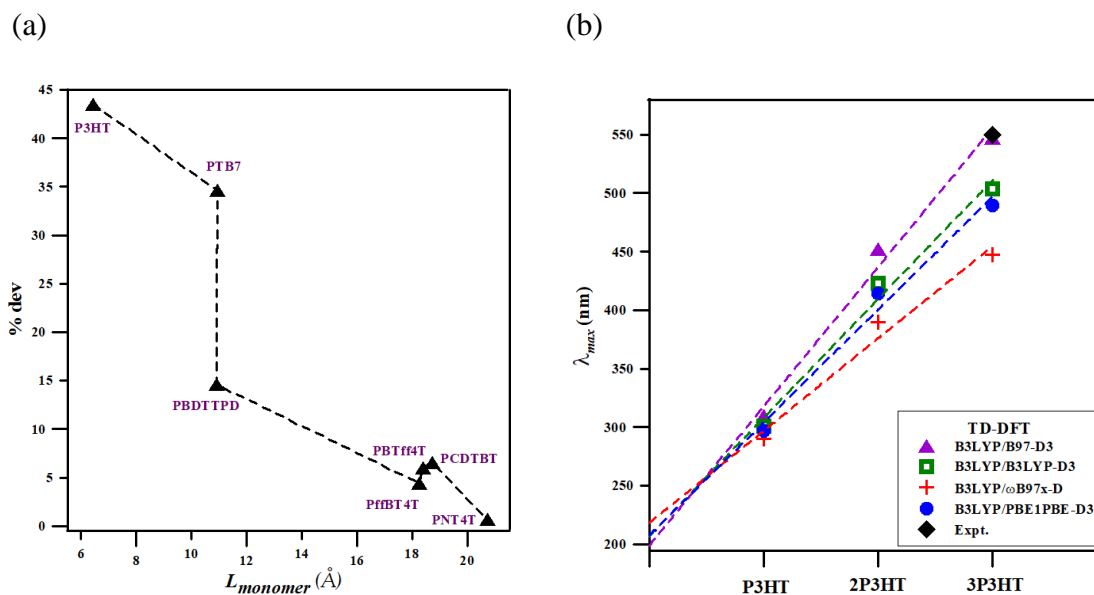


Figure 4.7: (a) The percentage deviations in TD-DFT/B3LYP/B97-D3  $\lambda_{max}$ 's of the interacting monomers with PCBM versus the chain-lengths of isolated monomers, and (b) the  $\lambda_{max}$ 's of nP3HT using the four D-DFT geometries versus n (where n=1,2,3).

Based on the above results, it is clear that B3LYP-D3 and B97-D3 are the best (most consistent in trends and accuracy) methods for performing TD-DFT on monomers with short side chains to obtain the absorption results. To further confirm this conclusion, we calculate the TD-DFT/B3LYP  $\lambda_{max}$ 's using the B97-D3 and B3LYP-D3 geometries of the (fourteen) interacting monomers with long side chains (see Figure 4.8 and Table B7 in Appendix B). The results show that, unlike the short side chains results (see Figure 4.6 (c)), the  $\lambda_{max}$ 's of monomers interacting with smaller fullerenes are not always larger than those interacting with larger fullerenes. For example, the  $\lambda_{max}$ 's of PBDTTPD, PNT4T, and PBTff4T interacting with PC<sub>71</sub>BM are larger than those interacting with PCBM. However, the  $\lambda_{max}$ 's obtained using the B3LYP-D3 and B97-D3 monomers with both types of fullerenes follow a similar trend as was obtained with the short side chain in that the B97-D3  $\lambda_{max}$ 's are higher than B3LYP-D3  $\lambda_{max}$ 's (see Figure 4.8). Overall the

accuracy of the  $\lambda_{max}$ 's as determined by MAD values is higher for short side chains compared to long side chains results (see Figure 4.9), (i.e. the presence of long side chains increases MADs of  $\lambda_{max}$ 's from experimental data from 119.9 to 130.1 nm for the B3LYP-D3 monomers, and from 95.8 to 119.0 nm for the B97-D3 monomers). However, for both short and long side chains, the lowest MADs  $\lambda_{max}$ 's from the experimental values are found for the B97-D3 method, indicating once again that B97-D3 is one of the more accurate method for studying the TD-DFT/B3LYP absorption spectra.

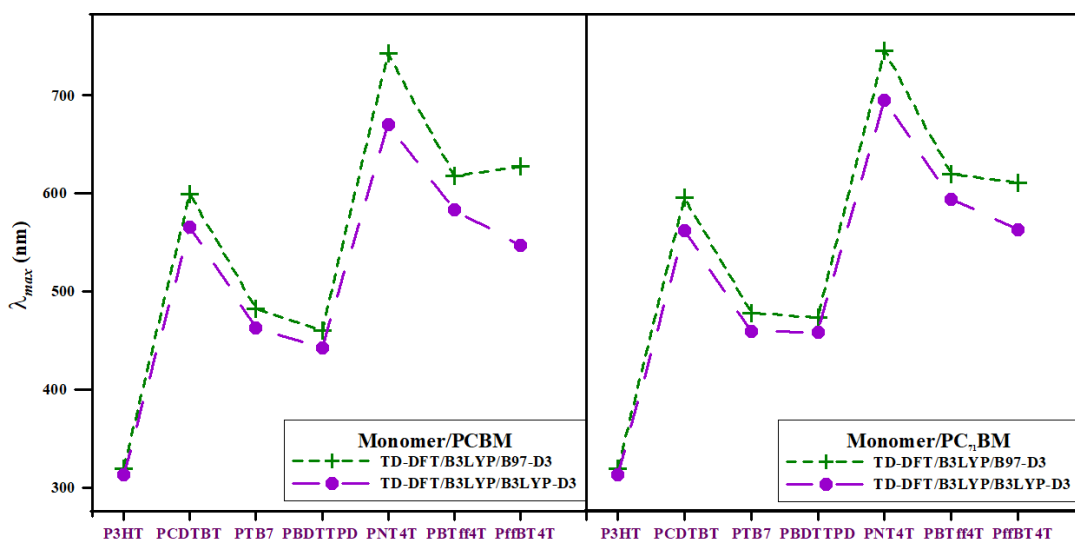


Figure 4.8: The maximum absorption wavelengths of interacting monomers with long side chains and with PCBM and PC<sub>71</sub>BM.

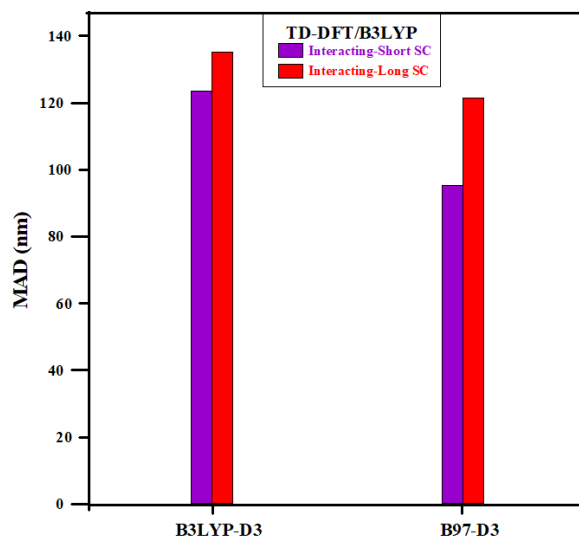


Figure 4.9: MADs of B3LYP-D3 and B97-D3  $\lambda_{max}$ 's of interacting monomers with short and long side chains relative to experimental data.

## 4.5 Conclusions

We have compared the performance of the four D-DFT methods (B97-D3, B3LYP-D3,  $\omega$ B97x-D, and PBE1PBE-D3) on various monomers and fullerenes that exhibited high PCE in organic solar cells. We have carried out D-DFT computations and analyzed the binding energies of monomer/fullerene pairs. We have used the D-DFT geometries to perform SP B3LYP and TD-DFT calculations to obtain the electronic structures and the absorptions of isolated and interacting monomers. For  $\Delta E_b$ 's,  $\epsilon_{LUMO}$ 's,  $\epsilon_{HOMO}$ 's  $E_g$ 's, and  $\lambda_{max}$ 's, we have found that the method accuracy order (from the highest to lowest) is B97-D3>B3LYP-D3> $\omega$ B97x-D. We also found that PBE1PBE-D3 exhibits the lowest binding energies compared to other methods and provides inconsistent trends for the electronic and absorption parameters. In addition, our results showed that performing single point B3LYP calculations on the D-DFT geometries is essential to obtain the most accurate electronic

and absorption properties. Moreover, we found that the electronic and optical accuracy between computed and bulk experimental data can be increased further if only monomers and oligomers (longer than 18 Å) were used in the computations. Based on our results that employ the monomer/fullerene approach, we find that B97-D3 and B3LYP-D3 methods are reliable for investigating intermolecular interactions and electronic and optical properties for various types of monomers (isolated or interacting) and with various lengths of side chains. We recommend either of the methods for conducting future computational studies on materials employed in organic solar cells.

## Acknowledgments

We would like to thank the following for making this research possible: WestGrid ([www.westgrid.ca](http://www.westgrid.ca)), SHARCNET ([www.sharcnet.ca](http://www.sharcnet.ca)), ACENET ([www.ace-net.ca](http://www.ace-net.ca)), and Compute Canada *Calcul Canada* ([www.computecanada.ca](http://www.computecanada.ca)) for providing the computational facilities. ACENET is the regional high performance computing consortium for universities in Atlantic Canada, and it is funded by the Canada Foundation for Innovation (CFI), the Atlantic Canada Opportunities Agency (ACOA), and the provinces of Newfoundland and Labrador, Nova Scotia, and New Brunswick. SHARCNET ([www.sharcnet.ca](http://www.sharcnet.ca)) is a consortium of 18 colleges, universities and research institutes operating a network of high-performance computer clusters across south western, central and northern Ontario. We would also like to thank King Abdulaziz University in Saudi Arabia and the Saudi Cultural Bureau in Canada for the full scholarship given to S.A.A.

# Bibliography

- [1] Y.H. Liu, J.B. Zhao, Z.K. Li, C. Mu, W. Ma, H.W. Hu, K. Jiang, H.R. Lin, H. Ade, H. Yan, *Aggregation and Morphology Control Enables Multiple Cases of High-Efficiency Polymer Solar Cells*, Nature Communications 5 (2014) 5293.
- [2] J.W. Jung, J.W. Jo, E.H. Jung, W.H. Jo, *Recent Progress in High Efficiency Polymer Solar Cells by Rational Design and Energy Level Tuning of Low Bandgap Copolymers with Various Electron-Withdrawing Units*, Organic Electronics 31 (2016) 149-170.
- [3] J. Gierschner, J. Cornil, H.J. Egelhaaf, *Optical Bandgaps of Pi-Conjugated Organic Materials at the Polymer Limit: Experiment and Theory*, Advanced Materials 19 (2007) 173-191.
- [4] S.J. Yang, P. Olishevski, M. Kertesz, *Bandgap Calculations for Conjugated Polymers*, Synthetic Metals 141 (2004) 171-177.
- [5] S.A. Ayoub, J.B. Lagowski, *Optimizing the Performance of Multilayered Organic Polymer Devices Using Computational Dimer Approach-A Case Study*, Journal of Physical Chemistry C 120 (2016) 496-507.
- [6] C. Risko, M.D. McGehee, J.L. Bredas, *A Quantum-Chemical Perspective into Low Optical-Gap Polymers for Highly-Efficient Organic Solar Cells*, Chemical Science 2 (2011) 1200-1218.
- [7] L. Ling, J.B. Lagowski, *DFT Study of Electronic Band Structure of Alternating Triphenylamine-Fluorene Copolymers*, Polymer 54 (2013) 2535-2543.
- [8] L. Ling, J.B. Lagowski, *Electronic Band Structure of Alternating Fluorene-Oxadiazole Conjugated Copolymer - A 1D Solid-State DFT Study*, Journal of Molecular Structure-Theochem 944 (2010) 146-155.
- [9] M.J. Eslamibidgoli, J.B. Lagowski, *The Effect of Side-Chain Length on the Solid-State Structure and Optoelectronic Properties of Fluorene-Alt-Benzothiadiazole Based Conjugated Polymers-A DFT Study*, Journal of Physical Chemistry A 116 (2012) 10597-10606.
- [10] G. Boschetto, H.T. Xue, J. Dzedzic, M. Krompiec, C.K. Skylaris, *Effect of Polymerization Statistics on the Electronic Properties of Copolymers for Organic Photovoltaics*, Journal of Physical Chemistry C 121 (2017) 2529-2538.
- [11] T.L.D. Tam, T.T. Lin, *Tuning Energy Levels and Film Morphology in Benzodithiophene-Thienopyrrolodione Copolymers Via Nitrogen Substitutions*, Macromolecules 49 (2016) 1648-1654.
- [12] N. Van den Brande, G. Van Lier, F. Da Pieve, G. Van Assche, B. Van Mele, F. De Proft, P. Geerlings, *A Time Dependent DFT Study of the Efficiency of Polymers for Organic Photovoltaics at the Interface with PCBM*, RSC Advances 4 (2014) 52658-52667.
- [13] M.D. Irwin, B. Buchholz, A.W. Hains, R.P.H. Chang, T.J. Marks, *P-Type Semiconducting Nickel Oxide as an Efficiency-Enhancing Anode Interfacial Layer in Polymer Bulk-Heterojunction Solar Cells*, Proceedings of the National Academy of Sciences of the United States of America 105 (2008) 2783-2787.
- [14] H.Y. Wang, X. Wang, P. Fan, X. Yang, J.S. Yu, *Enhanced Power Conversion Efficiency of P3HT:PC71BM Bulk Heterojunction Polymer Solar Cells by Doping a High-Mobility Small Organic Molecule*, International Journal of Photoenergy (2015).

- [15] S. Beaupre, M. Leclerc, *PCDTBT: En Route for Low Cost Plastic Solar Cells*, Journal of Materials Chemistry A 1 (2013) 11097-11105.
- [16] C. Cabanetos, A. El Labban, J.A. Bartelt, J.D. Douglas, W.R. Mateker, J.M.J. Frechet, M.D. McGehee, P.M. Beaujuge, *Linear Side Chains in Benzo 1,2-B:4,5-B' Dithiophene-Thieno 3,4-C Pyrrole-4,6-Dione Polymers Direct Self-Assembly and Solar Cell Performance*, Journal of the American Chemical Society 135 (2013) 4656-4659.
- [17] C. Piliago, T.W. Holcombe, J.D. Douglas, C.H. Woo, P.M. Beaujuge, J.M.J. Frechet, *Synthetic Control of Structural Order in N-Alkylthieno 3,4-C Pyrrole-4,6-Dione-Based Polymers for Efficient Solar Cells*, Journal of the American Chemical Society 132 (2010) 7595-7597.
- [18] Z.C. He, C.M. Zhong, S.J. Su, M. Xu, H.B. Wu, Y. Cao, *Enhanced Power-Conversion Efficiency in Polymer Solar Cells Using an Inverted Device Structure*, Nature Photonics 6 (2012) 591-595.
- [19] G.W.T. M. J. Frisch, H. B. Schlegel, G. E. Scuseria, M. A. Robb, J. R. Cheeseman, G. Scalmani, V. Barone, G. A. Petersson, H. Nakatsuji, X. Li, M. Caricato, A. Marenich, J. Bloino, B. G. Janesko, R. Gomperts, et al., (2016).
- [20] A.D. Becke, *Density-Functional Thermochemistry .3. The Role of Exact Exchange*, Journal of Chemical Physics 98 (1993) 5648-5652.
- [21] C.T. Lee, W.T. Yang, R.G. Parr, *Development of the Colle-Salvetti Correlation-Energy Formula into a Functional of the Electron-Density*, Physical Review B 37 (1988) 785-789.
- [22] C. Adamo, V. Barone, *Toward Reliable Density Functional Methods without Adjustable Parameters: The PBE0 Model*, Journal of Chemical Physics 110 (1999) 6158-6170.
- [23] S. Grimme, *Semiempirical GGA-Type Density Functional Constructed with a Long-Range Dispersion Correction*, Journal of Computational Chemistry 27 (2006) 1787-1799.
- [24] J.D. Chai, M. Head-Gordon, *Long-Range Corrected Hybrid Density Functionals with Damped Atom-Atom Dispersion Corrections*, Physical Chemistry Chemical Physics 10 (2008) 6615-6620.
- [25] S. Grimme, J. Antony, S. Ehrlich, H. Krieg, *A Consistent and Accurate Ab Initio Parametrization of Density Functional Dispersion Correction (DFT-D) for the 94 Elements H-Pu*, Journal of Chemical Physics 132 (2010) 154104.
- [26] E.F. Oliveira, F.C. Lavarda, *Effect of the Length of Alkyl Side Chains in the Electronic Structure of Conjugated Polymers*, Materials Research-Ibero-American Journal of Materials 17 (2014) 1369-1374.
- [27] U. Salzner, P.G. Pickup, R.A. Poirier, J.B. Lagowski, *Accurate Method for Obtaining Band Gaps in Conducting Polymers Using a DFT/Hybrid Approach*, Journal of Physical Chemistry A 102 (1998) 2572-2578.

# Chapter 5

## 5 Optimizing the Performance of the Bulk Heterojunction Organic Solar Cells Based on DFT Simulations of their Interfacial Properties

A slightly revised version of Chapter 5 has been published with (Sarah A. Ayoub and Jolanta B. Lagowski, *Materials and Design*, 2018, in press, doi: 10.1016/j.matdes.2018.07.016).

### 5.1 Abstract

Experimental studies suggest that the intermolecular interactions between polymers and fullerenes are critical to the design of efficient bulk heterojunction organic photovoltaic cells. However, a detailed understanding of these intermolecular interactions is still lacking. In this work, by correlating simulation data with experimentally determined efficiencies, we identify interfacial factors that can be used to enhance the performance of BHJ organic solar cells. We employ dispersion corrected density functional theory method

(B97D3) to investigate the properties of the interfacial region in various promising combinations of monomers (P3HT, PTB7, PCDTBT, PBDTTPD, PNT4T, PffBT4T, and PBTff4T) and fullerenes (PCBM and PC<sub>71</sub>BM) used in OSCs. We analyze the conformational structures and binding energies of these combinations, and obtain the electronic offsets of gas phase and interacting monomers and fullerenes. Our findings indicate that monomer/fullerene pairs that exhibit the highest experimentally determined PCEs (i.e. those containing PNT4T, Pff4TBT, and PBTff4T) have the following common characteristics: the lowest interfacial LUMO offset, the largest ratio of  $V_{oc}$  (as determined by interfacial band gap) to monomer's energy gap,  $E_g$ , and relatively high binding energy. We believe that materials that display these interfacial characteristics will produce more efficient organic solar cells.

## 5.2 Introduction

The new generation of power sources such as organic solar cells (OSCs) and organic/inorganic perovskite solar cells (PeSCs) have attracted tremendous attention primarily due to flexible device fabrication, lightweight, and low cost. [1, 2] To date, power conversion efficiencies (PCEs) of over 20% have been achieved by PeSCs due to their remarkable advantages such as high optical absorptions across a wide range of the solar spectrum. [3] However, the inhomogeneity of film (surface) morphology used in PeSCs has led to the poor device reproducibility and delayed their practical applications. [4, 5] Recently, for OSCs, a bulk-heterojunction (BHJ) devices that contained conjugated polymers (electron-donors) and fullerenes (electron-acceptors) mixed together gave the

highest PCEs of the order of 10%. Poly(3-hexylthiophene)s (P3HTs) were widely used electron-donors in the fabrication of BHJ solar cells. However, P3HTs are known to exhibit a limited PCE value of 3-5% [6, 7] due to their restricted absorption (<600nm) when they are combined with fullerenes. A new generation of semiconducting copolymers (called donor-acceptor (D-A) copolymers) were synthesized with low energy gaps in the range of 1.3-1.6 eV to maximize light harvesting. The development of D-A copolymers enabled the tuning of energy levels and optical band gaps to improve the device performance. The most widely studied D-A copolymers are PCDTBT (based on 2,7-carbazole/dithienyl-2,1,3-benzothiazole) [8], PBDTTPD (based on thieno[3,4-c]pyrrole-4,6-dione) [9], and PTB7 (based on thieno[3,4-b]thiophene/benzodithiophene) [10]. Efficiencies of conventional OSCs were improved using PCDTBT to 7.5%, PTB7 to 8.25%, and PBDTTPD to 8.5%. [2] Recently, record-efficiencies (exceeding 10%) were achieved with a new successful family of quaterthiophene-based polymers such as PffBT4T-2OD, PBTff4T-2OD, and PNT4T-2OD. [11]

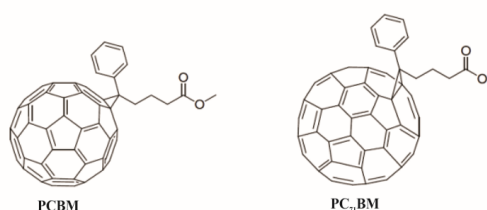
Despite the substantial improvements of OSCs, their PCEs are still low compared to the PCEs of inorganic solar cells or of PeSCs. One major reason for these differences is that the interfacial region in OSCs that contains polymers and fullerenes in close contact, is still not well understood or controlled. For example, the preferred orientation of polymers relative to the fullerenes at the polymer/fullerene interface is still not known in most cases. [1, 9] The electronic structures of polymers and fullerenes may also be affected by these interfacial interactions. [12] Understanding and controlling these factors is not always straightforward. For example, it is known that the open-circuit voltage,  $V_{OC}$ , of

OSCs is currently very low (less than half of the incident photon energy) which limits the efficiencies of OSCs. [13] The PCE of OSC can be improved by increasing its  $V_{OC}$ , which, for a given BHJ OSC containing polymer with a band gap,  $E_g$ , is known to be proportional to the interfacial energy gap  $\epsilon_{HOMO(polymer)} - \epsilon_{HOMO(fullerene)}$  (where HOMO and LUMO stand for the highest and lowest molecular orbital respectively, and  $\epsilon_{HOMO(polymer)}$  and  $\epsilon_{HOMO(fullerene)}$  are the corresponding HOMO and LUMO eigenvalues of the polymer and fullerene respectively). It is also known that  $V_{OC}$  increases with increasing  $E_g$  of polymers [2] but a large  $E_g$  is not conducive to an optimal absorption across the broad range of solar spectrum. Hence, in practice, maximizing  $V_{OC}$  by simply increasing  $E_g$  of the polymers and/or the interfacial energy gap is not recommended since this procedure is not compatible with producing other desirable properties of OSCs. Using computational means, the purpose of this Chapter is to provide a new insight as to how the intermolecular interactions in the interfacial region affect the properties of polymer/fullerene systems and to seek useful correlations between these properties and the experimentally determined efficiencies of OSCs.

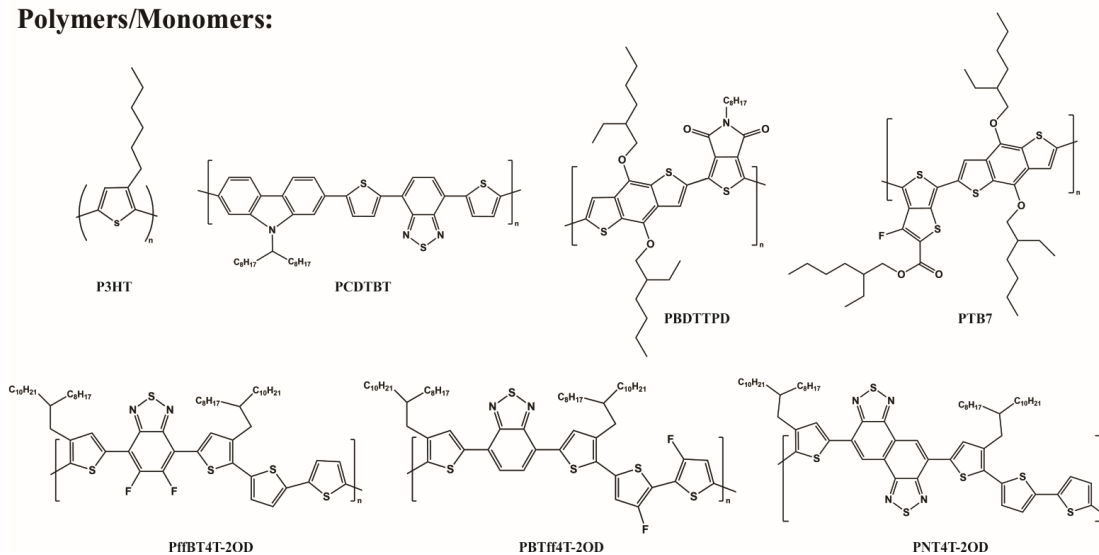
In general, many computational studies that have applied density functional theory (DFT) to the polymers/fullerene systems (using for example the well known B3LYP approximation [14]) produced the electronic properties of (isolated) polymers and fullerenes and their absorption spectra (using the time dependent DFT [15, 16]) in the gas phase. However, as mentioned above, understanding the effect of intermolecular interactions on the structural, optical and electronic properties of materials used in OSCs is critical to the device performance. With the help of the dispersion-corrected DFT (D-

DFT) methods, it is possible to include the intermolecular interactions in our computations. For the system studied, we have determined [17] that B97D is a reliable method for investigating their interfacial properties at a reasonable computational cost. We employ the D-DFT/B97D3 approximation to investigate the binding energies and the electronic properties of various molecular pairings of seven monomers of copolymers: P3HT, PCDTBT, PBDTTPD, PTB7, PffBT4T, PBTff4T, PNT4T, and two types of PCBM and PC<sub>71</sub>BM fullerenes (see Scheme 5.1). Using the experimental PCE data, we identify practical trends in their material properties that we hope will expedite the process of finding/predicting promising materials for OSCs in the future and eventually lead to a design of OSCs with greater efficiencies.

#### Fullerene:



#### Polymers/Monomers:



Scheme 5.1: Chemical composition of PCBM, PC<sub>71</sub>BM, P3HT, PTB7, PCDTBT, PBDTTPD, PNT4T-2OD, PffBT4T-2OD, and PBTff4T-2OD monomers.

## 5.3 Theoretical/Computational Details

### 5.3.1 Computational Methodology

All geometries of non-covalently bonded pairs of monomers and fullerenes are optimized using the B97D3/6-31G(d) as implemented in Gaussian 09. The B97D3 functional is a modified B97 hybrid functional, which is a mixture of a re-parameterized generalized-gradient approximation (GGA) functional and a fraction of the Hartree-Fock exchange term. [18] The B97D3 also includes the latest D3 version of Grimme's (empirical) dispersion-correction term, which accounts for the van der Waals interactions. In addition to the B97D3 method, the B3LYP functional [19, 20], which is the most widely used DFT functional, is also employed to our computations. It combines Becke's three-parameter hybrid exchange functional with Lee and Yang's gradient corrected correlation functional. [21] B3LYP electronic structure data are in good agreement with the corresponding experimental data. [14] In contrast, the D-DFT methods give electronic structure results that are widely different from the experimental values. [22] We employ B3LYP in the geometry optimization of isolated monomers and fullerenes as well as on the B97D3 optimized geometries of monomers and fullerenes (which we refer to as the interacting geometries of monomers and fullerenes). In both cases, we generate B3LYP HOMO and LUMO eigenvalues and energy gaps.

### 5.3.2 Definitions of the Computed Interfacial Quantities

In this subsection, we define the quantities, such as binding energies, LUMO offsets, HOMO offsets, and the interfacial energy gaps, that are used to characterize the interfacial-region of monomer/fullerene combinations. Binding energy ( $\Delta E_b$ ) is used to estimate the stabilities of monomer/monomer, monomer/fullerene, and fullerene/fullerene pairs.  $\Delta E_b$  is defined as,

$$\Delta E_b = \sum_{i=1}^2 E_i - E_{pair} \quad (5.1)$$

where  $E_{pair}$  is the total energy of the pair, and  $E_1$  and  $E_2$  are the total energies of individual monomers, fullerenes or monomers and fullerenes depending whether we are considering homogeneous or heterogeneous pairs.

An optimal energy level alignment at the interface of polymer/fullerene heterojunction is very important for the enhanced performance of OSCs. A simple schematic illustration of the energy levels and the offsets are shown in Figure 5.1. Appropriate LUMO offset (given by  $\Delta\epsilon_{LUMO} = \epsilon_{LUMO(monomer)} - \epsilon_{LUMO(fullerene)}$ ) and HOMO offset (given by  $\Delta\epsilon_{HOMO} = \epsilon_{HOMO(monomer)} - \epsilon_{HOMO(fullerene)}$ ) are essential for good charge transport in OSCs. Typically, a small  $\Delta\epsilon_{LUMO}$  is required for a good electron transfer from the photo-excited acceptor to the donor and good charge separation, while at the same time a larger  $\Delta\epsilon_{HOMO}$  is required for a poor hole transfer and for the prevention of charge recombination (due to mobilities mismatch between the electrons and holes). In general, very large energetic offsets are not preferred for the better charge separations since they contribute to additional waste of the photon's energy. [23] Interfacial energy gap

$(\Delta\epsilon_{H_D-L_A})$  is another significant energetic-offset (between monomer (donor) HOMO and fullerene (acceptor) LUMO) that is related to  $V_{OC}$  (as discussed in section 5.2) which can be approximated by,

$$V_{OC} = \frac{1}{q} \{ \Delta\epsilon_{H_D-L_A} \} - 0.3, \quad (5.2)$$

where  $q$  is the electron charge, the value 0.3 is an empirical factor [2], and  $\Delta\epsilon_{H_D-L_A}$  is the interfacial energy gap given by,

$$\Delta\epsilon_{H_D-L_A} = | \epsilon_{HOMO(monomer)} | - | \epsilon_{LUMO(fullerene)} |. \quad (5.3)$$

Many groups have focused on improving the PCE by the strategy of lowering the polymer HOMO level to maximize  $V_{OC}$ . However, polymer HOMO levels that are too deep may lead to diminishing of the charge separation, resulting in lowering of the PCE. [23] In this work, we calculated the above interfacial energetic offsets for the heterogenous monomer/fullerene pairs to gain a greater insight into their effect on the performance of polymer/fullerene solar cells.

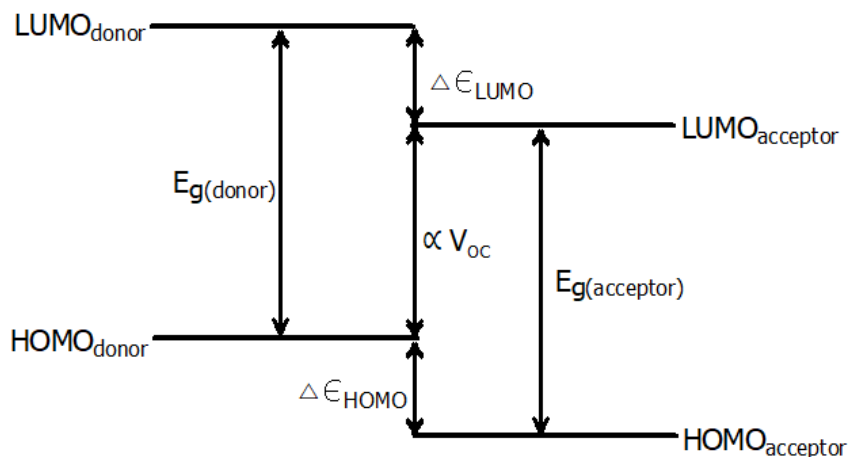


Figure 5.1: Schematic illustration of the energy levels at the interface of polymer/fullerene pair in OSCs.

## 5.4 Results and Discussions

### 5.4.1 Conformational Analysis

Within the active heterogeneous layer of OSCs consisting of conjugated polymers and fullerenes, there are three types of interfacial interactions present: interactions between monomers, between monomers and fullerenes, and between fullerenes. Their (many) orientations relative to each other define their possible conformations. The calculations of the interfacial and electronic quantities require that we identify the most stable conformations of these pairings. The procedure for carrying out the initial conformational energy search is described in Appendix C. In all cases (for the homogeneous and heterogeneous pairs) the chosen (few) conformations are selected for further analysis that involves D-DFT/B97D3 optimizations. The results of these optimizations are discussed below.

### 5.4.1.1 Homogeneous Pairs

For monomer/monomer pairs, we consider four different configurations. These configurations include different mirrored and/or rotated orientations of monomers relative to each other (see for example the configurations of PBDTTPD dimer in Figure C1 in Appendix C). The results of the relative conformational energies,  $(E - E_0)$ 's, and  $\Delta E_b$ 's of the four configurations are represented in Figure C2 in Appendix C and Figure 5.2 respectively. The various oriented configurations exhibited similar values of  $\Delta E_b$  for each dimer. In particular, the difference between the lowest and the highest  $\Delta E_b$  for all dimers is relatively small (it ranges from 0.06 to 0.27 eV). That is, these four configurations are nearly degenerate. The lowest energy conformational state corresponding to the highest  $\Delta E_b$  varies from dimer to dimer. For the purpose of this work we list the highest  $\Delta E_b$  and  $\Delta E_b / L_{monomer}$  (where  $L_{monomer}$  is the chain length of isolated monomers) for each homogeneous dimer (indicating conformation to which it belongs to) in Table C1 Appendix C.

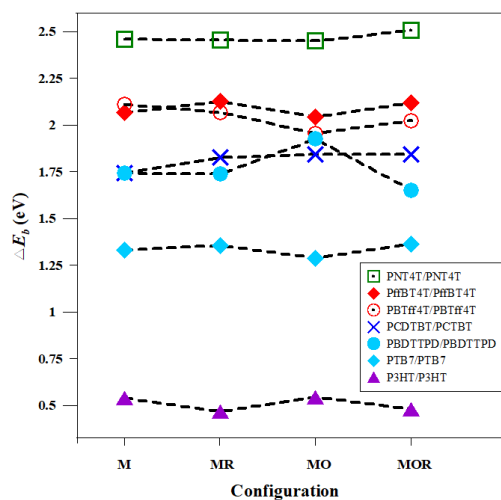


Figure 5.2: The binding energy versus configurations of monomer/monomer pairs using the B97D3 method (see Appendix C for the definitions of M, MR, MO and MOR).

For fullerene/fullerene pairs, six possible configurations are optimized using the B97D3 method (see an example for PCBM/PCBM pair in Figure 5.3). The corresponding relative conformational and binding energies of PCBM/PCBM and PC<sub>71</sub>BM/PC<sub>71</sub>BM pairs are shown in Figure 5.4. Contrary to the results of monomer/monomer pairs, the orientations of fullerenes in a pair are of a great importance. For example, the bottom/bottom configuration of PC<sub>71</sub>BM/PC<sub>71</sub>BM pair exhibited higher  $E - E_0$  and lower  $\Delta E_b$  (by 0.74 eV) compared to those of the top/side configuration. For both types of fullerenes, the lowest conformational energies and highest  $\Delta E_b$  are found for the side/side configurations (the side groups are in opposite direction for the case of PC<sub>71</sub>BM/PC<sub>71</sub>BM, and the side groups are in the same direction for the case of PCBM/PCBM).

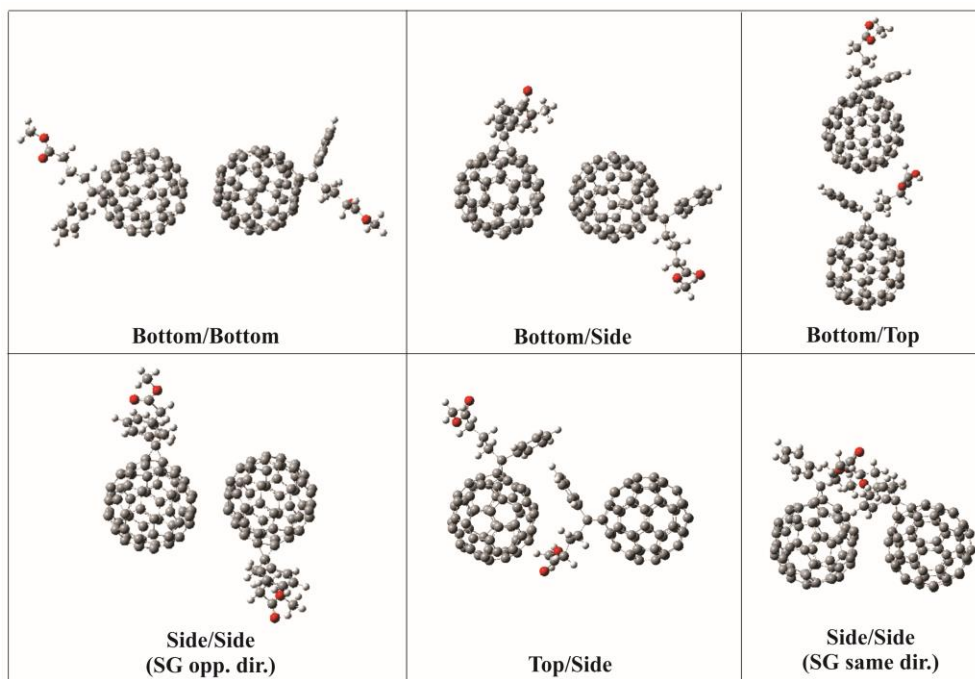


Figure 5.3: The optimized configurations of PCBM/PCBM pairs using the B97D3 method.

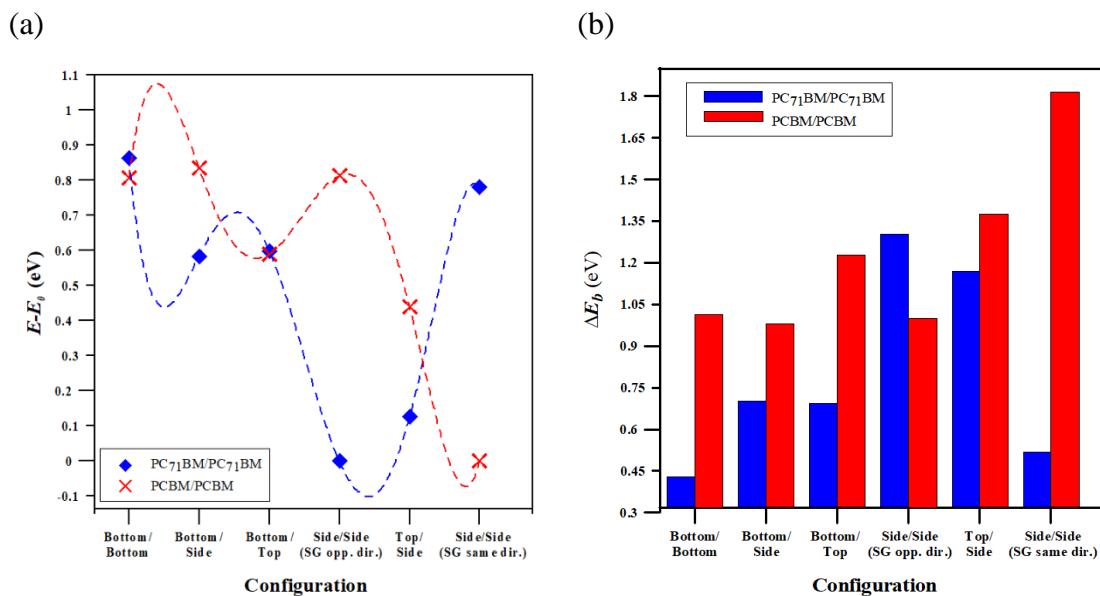


Figure 5.4: The relative conformational and binding energies of PCBM/PCBM and PC<sub>71</sub>BM/PC<sub>71</sub>BM pairs calculated at the B97D3 method.

### 5.4.1.2 Heterogeneous Pairs

For each heterogeneous pair, three types of conformations (where the monomer is located at the bottom, side, or top of the fullerene) are selected (see Figure 5.5 for examples and Figures C3 and C4 in Appendix C for the remaining combinations). In Figure 5.6, the relative conformational and binding energies for all of the heterogeneous pairs are plotted versus the three types of configurations. Typically, the  $\Delta E_b$ 's for monomers located at the top and bottom of fullerenes are smaller than those located at the sides of fullerenes by 0.2 to 0.8 eV. Hence, the lowest energy (most stable) conformations are obtained for monomers located at the sides of fullerenes. These findings imply that polymers must be placed on the sides of fullerenes to increase the stability of the active layer. This result highlights the importance of ordered BHJ structures that may contribute to improved performance of OSCs. In fact, it was reported that vertically aligned and ordered layered BHJ morphology can significantly improve the efficiencies of OSCs. [24] For instance, the efficiency of P3HT/PCBM OSCs was greatly enhanced to 7.3% with the incorporation of vertically aligned fullerenes. [25] In the following subsections, we use the side configurations of the heterogeneous pairs to further investigate their electronic and interfacial properties.

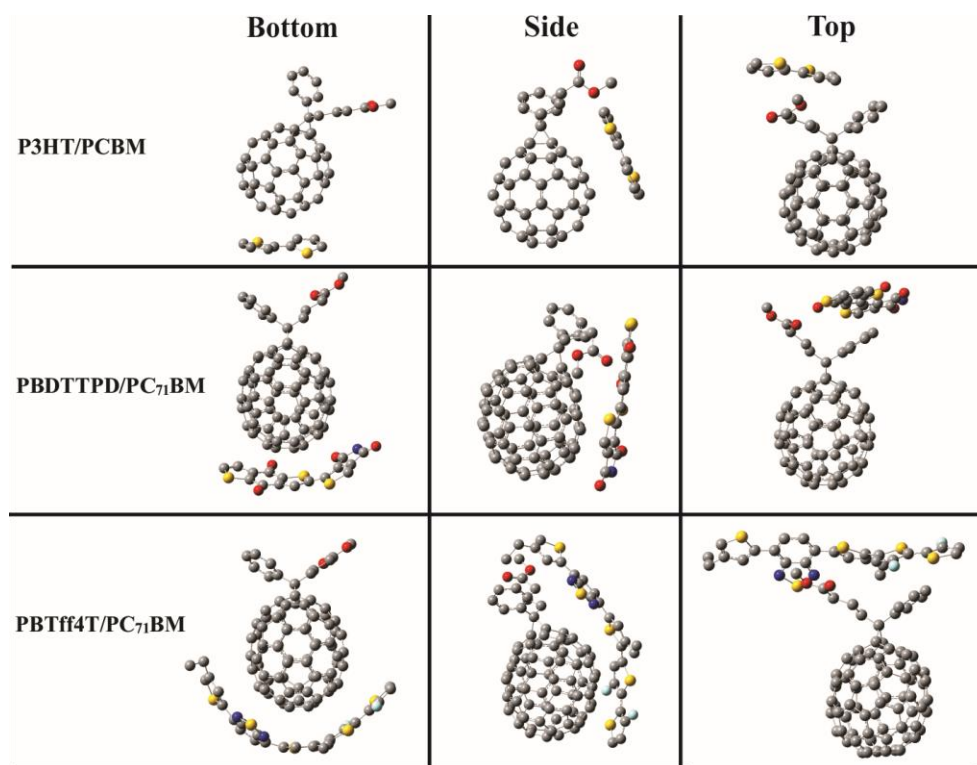


Figure 5.5: Representative examples of the B97D3 optimized geometries of three types of configurations for three different monomer/fullerene combinations. For clarity, hydrogen atoms are not shown.

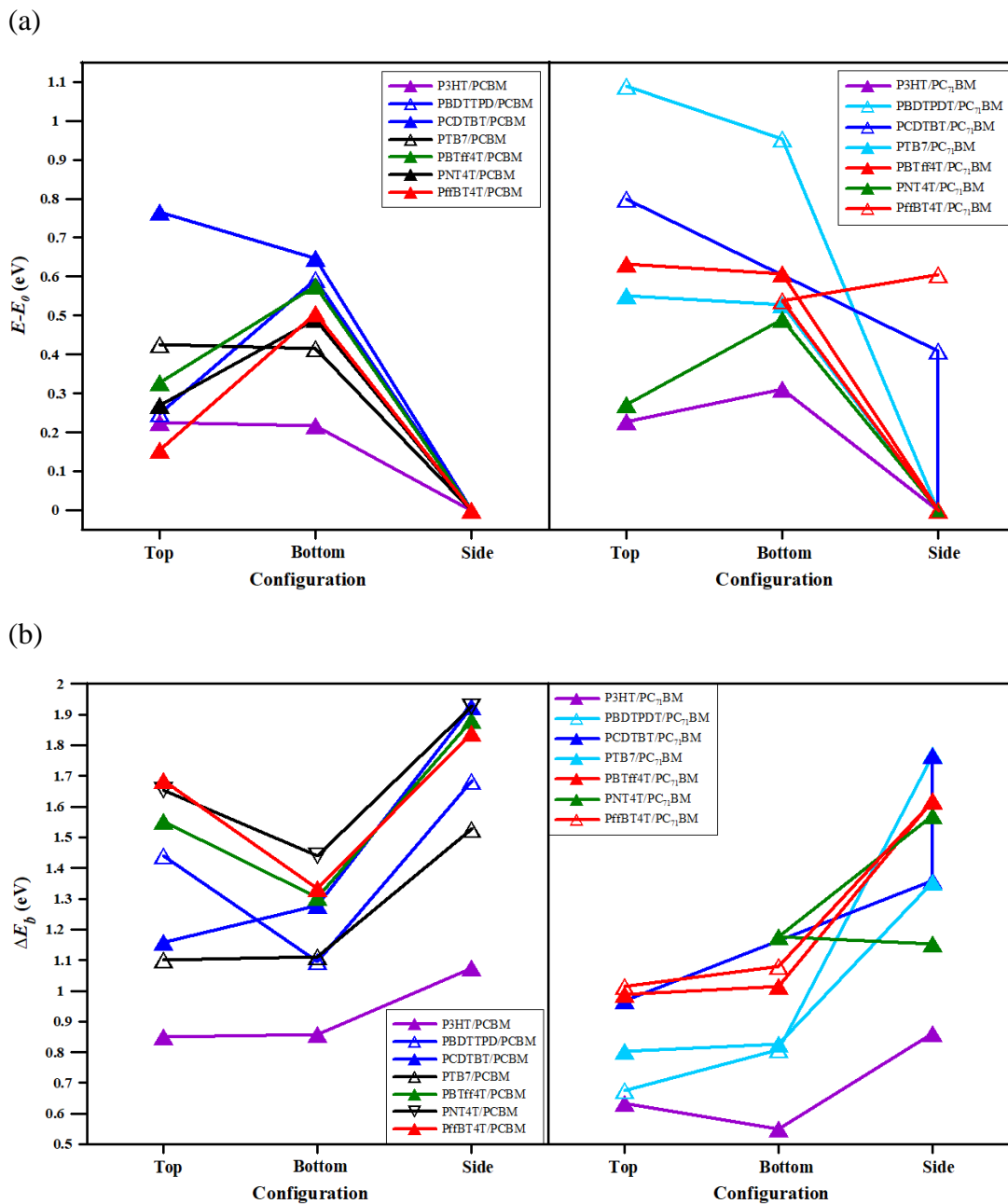


Figure 5.6: The relative conformational and binding energies for the three types of configurations of monomers/fullerene pairs optimized at the B97D3 method.

## 5.4.2 Electronic Properties of the Interacting Monomers and Fullerenes at the Interface

Using configurations with the lowest energy as discussed above, in this subsection, we investigate the (possible) correlations between their electronic structures and the experimental PCEs. That is, we look for quantities (see subsection 5.3.2), which either increase or decrease with increasing values of PCEs.

In Figure 5.7, we display the frontier energy levels of all heterogeneous pairs. It is well known [24] that a small  $\Delta\epsilon_{LUMO}$  is essential for high efficiency OSC. Hence, the pairs in Figure 5.7 are ordered according to decreasing  $\Delta\epsilon_{LUMO}$ 's. Figure 5.7 shows that, as monomer changes (from P3HT to PNT4T) with both types of fullerenes,  $\Delta\epsilon_{LUMO}$  decreases with increasing  $\Delta\epsilon_{HOMO}$ , decreasing  $\Delta\epsilon_{HD-LA}$ , and increasing PCEs. This trend is true for all pairs except for the case of PNT4T/fullerene. One possible explanation for this deviation is to notice that PNT4T monomer has the longest chain-length (20.72 Å). It is possible that the above relations between the various offsets and PCE break down somewhat when monomer's chain length exceeds 20 Å. Another explanation could be that, in the case of PNT4T/fullerene pairs, their corresponding solar cell efficiency has not reached its maximum and can be further improved upon.

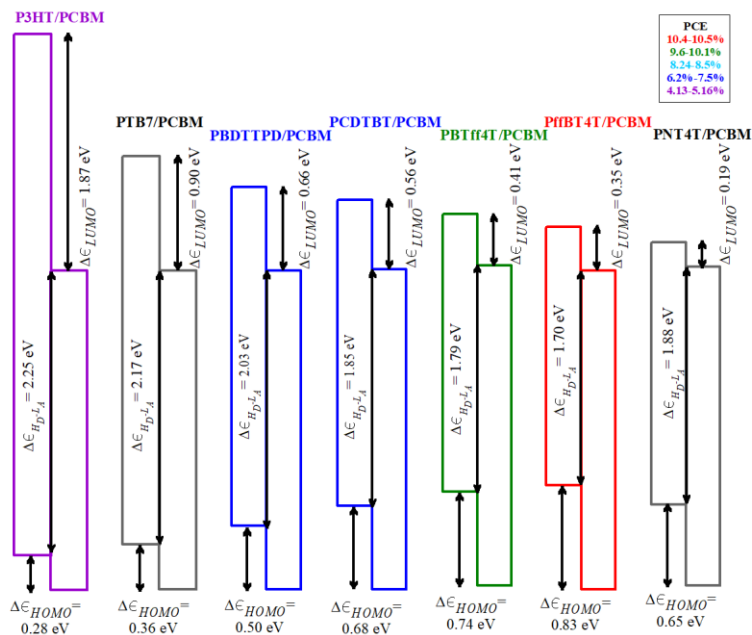
In subsection 5.3.2, we noted that maximizing the  $V_{OC}(\propto \Delta\epsilon_{HD-LA} - 0.3)$  relative to the  $E_g$  of the polymer enhances the PCE of OSC. Hence, first we confirm that the experimentally determined PCEs and the calculated interfacial band gaps,  $\Delta\epsilon_{HD-LA}$ 's, (as shown on Figure 5.7) are correlated. In Figure 5.8, the calculated  $\Delta\epsilon_{HD-LA} - 0.3$  are

plotted against the experimental PCEs. In the (a) part of the Figure 5.8, we employ the respective HOMO and LUMO eigenvalues that are obtained using the interacting (B97D3) monomer and fullerene geometries in the SP B3LYP computations. For comparison purposes, in Figure 5.8 (b) we employ the respective HOMO and LUMO eigenvalues that are obtained using the isolated B3LYP geometry optimized results for monomers and fullerenes. The results displayed in Figure 5.8 indicate that, in both cases, there is an approximate inversely linear relationship between  $\Delta\epsilon_{H_D-L_A} - 0.3$  and PCE, that is, higher efficiencies are found for monomer/fullerene pairs with smaller  $\Delta\epsilon_{H_D-L_A} - 0.3$ .

PCE values are typically not available in the initial material assessment. Instead, it is more useful to display the electronic structure properties as a function of the monomer  $E_g$ 's since low  $E_g$ 's are required for OSCs with high PCEs and  $E_g$ 's can be readily obtained from experimental and computational studies. Figures 5.9 and 5.10 display HOMO and LUMO offsets ( $\Delta\epsilon_{LUMO}$ 's and  $\Delta\epsilon_{HOMO}$ 's), and  $\Delta\epsilon_{H_D-L_A} - 0.3$  versus the monomer  $E_g$ 's. These results show that, not surprising, LUMO and HOMO offsets, and the interfacial band gaps of the combinations correlate well with the monomer  $E_g$ 's. For example, monomers with low  $E_g$ 's give low  $\Delta\epsilon_{LUMO}$  and high  $\Delta\epsilon_{HOMO}$ . It is also clear from Figure 5.9 (from its color scheme) that monomers with low  $E_g$ 's correspond to high PCEs. There is more scatter in HOMO offset data points in comparison to LUMO offset points that vary nearly linearly with  $E_g$ . Similarly, Figure 5.10 shows that there is an approximate linear relationship between  $\Delta\epsilon_{H_D-L_A} - 0.3$  and  $E_g$ , in a good agreement with the experimental result that states  $V_{OC}$  increases with increasing  $E_g$ . [2] As stated above large  $V_{OC}$  is a desirable property of OSC but not at an expense of a large  $E_g$  of polymers. The polymer

is the main recipient of the solar photons and its  $E_g$  should be relatively small for maximum absorption. Hence, it is the ratio of  $(\Delta\epsilon_{HD-LA} - 0.3)/E_g$  that should be maximized for highly efficient solar cells (not the quantity  $\Delta\epsilon_{HD-LA} - 0.3$ ). Figure 5.11 clearly shows that this is the case, confirming that maximizing the  $V_{OC} \propto \Delta\epsilon_{HD-LA} - 0.3$  enhances the PCE of OSC.

(a)



(b)

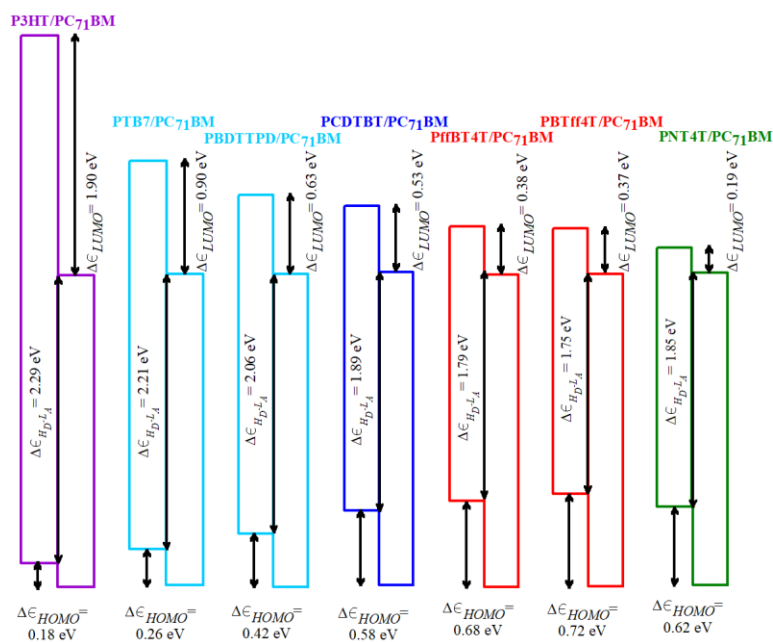


Figure 5.7: The energy levels of the interacting (a) monomer and PCBM and (b) monomer and PC<sub>71</sub>BM pairs (obtained using the B97D3 optimized geometries in SP B3LYP calculations).

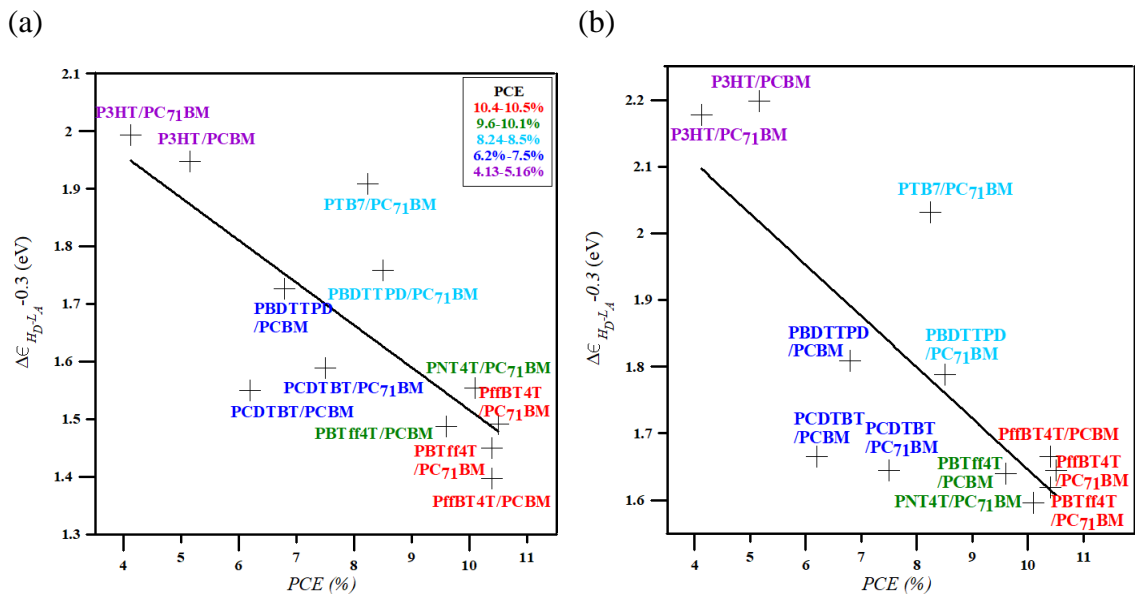


Figure 5.8:  $V_{OC} \propto \Delta\epsilon_{H_D-L_A} - 0.3$  of (a) the interacting monomers and fullerenes (obtained using the B97D3 optimized geometries in SP B3LYP calculations) and the (b) isolated monomers and fullerenes at the B3LYP method, versus the (experimentally determined) PCE.

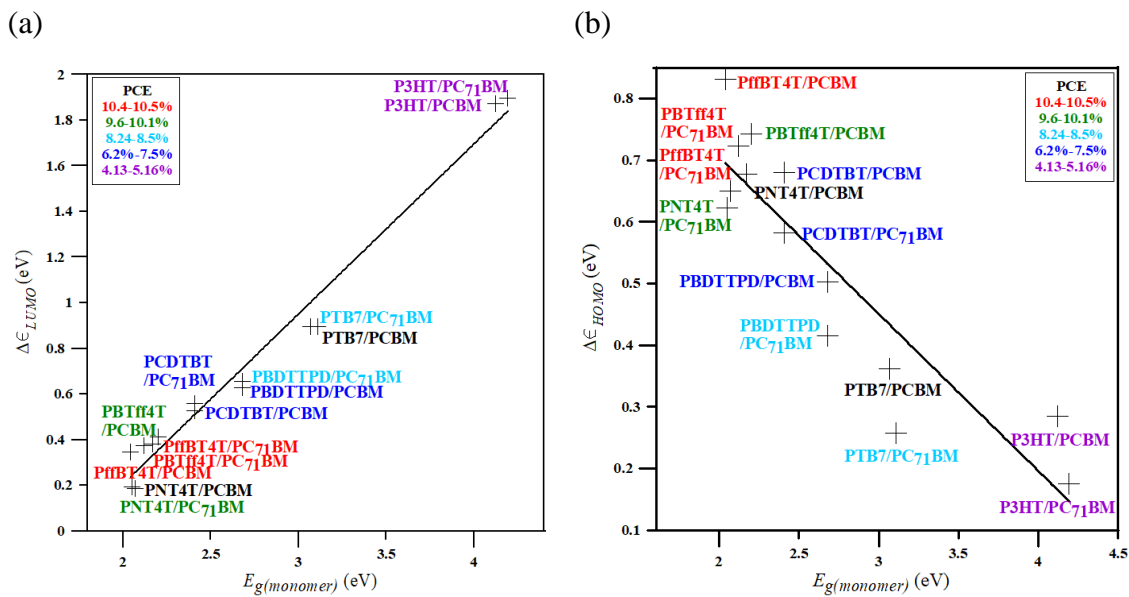


Figure 5.9: (a) LUMO offsets and (b) HOMO offsets of the interacting monomers and fullerenes (obtained using the B97D3 optimized geometries in SP B3LYP calculations) versus the respective monomer's  $E_g$ .

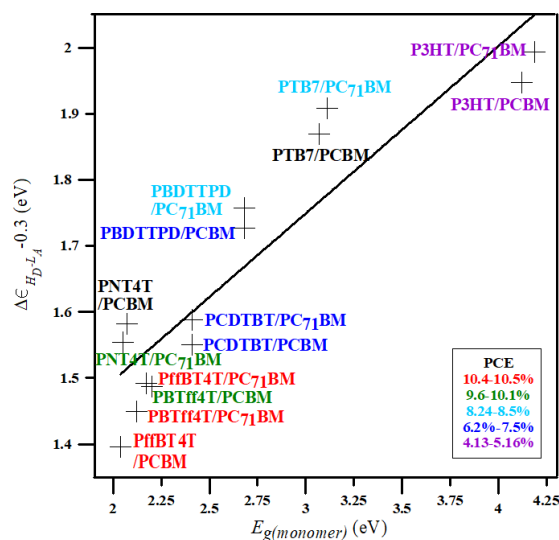


Figure 5.10:  $\Delta\epsilon_{H_D-L_A} - 0.3$  of the interacting monomers and fullerenes (obtained using the B97D3 optimized geometries in SP B3LYP calculations) versus the respective monomer's  $E_g$ .

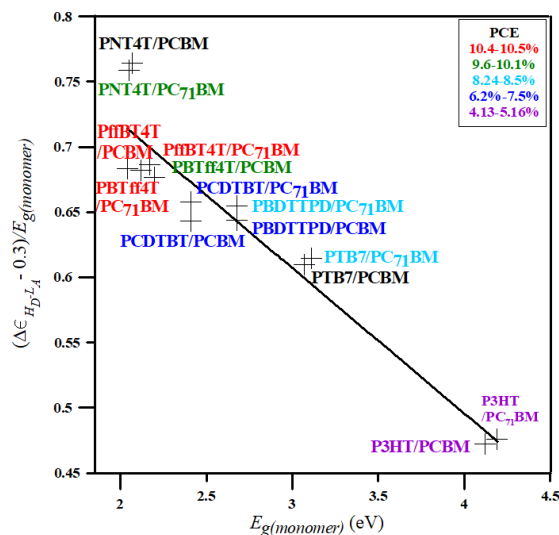


Figure 5.11:  $(\Delta\epsilon_{H_D-L_A} - 0.3)/E_g(\text{monomer})$  of the interacting monomers and fullerenes (obtained using the B97D3 optimized geometries in SP B3LYP calculations) versus the respective monomer's  $E_g$ .

### 5.4.3 Electronic Properties of the Isolated Monomers and Fullerenes

Since the electronic property trends of the subsection 5.4.2 that used the B97D3 geometries of the interacting monomers and fullerenes in SP B3LYP computations clearly show a good agreement with experimental trends, it would be helpful to check if similar results (but with less computations) can be obtained for gas phase monomers and fullerenes. Hence, in this subsection, we consider the energetic offsets (such as  $\Delta\epsilon_{LUMO}$ ,  $\Delta\epsilon_{HOMO}$ , and  $\Delta\epsilon_{H_D-L_A} - 0.3$ ) for the isolated monomers and fullerenes as obtained with B3LYP method and identify their correlations with PCE and monomer's  $E_g$ . The results of  $\Delta\epsilon_{H_D-L_A} - 0.3$  of the isolated monomers and fullerenes versus the experimentally determined PCEs were already mentioned in subsection 5.4.2 and displayed in Figure 5.8 (b). Similar situation is observed in all cases (see Figures 5.8 (a) and (b), and C5 and C6 in Appendix C). Hence it can be said that the promising materials with optimal properties (such as the lowest  $\Delta\epsilon_{LUMO}$ , the highest  $\Delta\epsilon_{HOMO}$ , and the highest  $(\Delta\epsilon_{H_D-L_A} - 0.3)/E_g$ ) can be identified with just B3LYP gas phase computations.

### 5.4.4 Binding Energies of Homogeneous and Heterogeneous Pairs

We showed in the previous subsections (5.4.2 and 5.4.3) that certain electronic properties of monomer/fullerene pairs correlate well with experimentally determined PCEs. What

about their binding energies? We investigate the trends in (B97D3)  $\Delta E_b$  of both heterogeneous and homogenous pairs (see Table C1 in Appendix C and Figure 5.12). Since the stability of the pairs (which is also important to the device performance) can be estimated from the strength of the binding interactions, it is expected that the highest  $\Delta E_b$ 's correspond to combinations with highest PCE. We have found that, in general, the homogenous pairs (such as Pff4TBT/Pff4TBT, PBTff4T/PBTff4T, and PNT4T/PNT4T) with the highest PCE exhibited the highest  $\Delta E_b$ . A closer look reveals that when monomer's chain length,  $L_{monomer}$ , is taken into account,  $\Delta E_b/L_{monomer}$  levels off for homogeneous pairs with the highest PCE (see Table C1 in Appendix C). The results of monomer/PCBM and monomer/PC<sub>71</sub>BM (see Figure 5.12) indicate that  $\Delta E_b$  levels off as PCE reaches values close to 10%.  $\Delta E_b$  for pairs containing PCBM is somewhat larger than  $\Delta E_b$  for pairs containing PC<sub>71</sub>BM.

In addition, we consider the structural parameters of the pairs such as the chain length of isolated monomers ( $L_{monomer}$ ) and the minimal intermolecular distance ( $d_{min}$ ) between monomers and fullerenes in each pair (see Table C1 in Appendix C). The  $\Delta E_b$  of heterogeneous pairs is examined versus  $L_{monomer}$  (see Figure 5.13 (a)). The results indicate that  $\Delta E_b$  increases somewhat with increasing  $L_{monomer}$ . This relatively small effect of the  $L_{monomer}$  on  $\Delta E_b$  is possibly due to the fact that the length of the fullerenes that are interacting with the monomers is approximately the same for all monomers irrespective of monomers' lengths (see for example Figure 5.13 (b)). The approximate trend that the higher PCEs are obtained for pairs with higher  $\Delta E_b$  and larger  $L_{monomer}$  still holds in most (not all) cases. The latter result is also reflected in the correlations involving

the  $d_{min}$ 's. The  $d_{min}$  of monomer/PCBM pairs is slightly smaller than  $d_{min}$  of monomer/PC<sub>71</sub>BM pairs which is consistent with the larger  $\Delta E_b$  for monomers/PCBM relative to monomers/PC<sub>71</sub>BM pairs. The shortest  $d_{min}$  is found for heterogeneous pairs (Pff4TBT/, PBTff4T/, and PNT4T/fullerene) with highest PCE (see Table C1 in Appendix C).

It should be noted that (see Figure 5.12 and Table C1 in Appendix C), for some cases the monomer/monomer  $\Delta E_b$ 's are lower or are comparable to the monomer/fullerene  $\Delta E_b$ 's, while for other cases monomer/monomer pairs exhibit the highest  $\Delta E_b$ 's compared to the monomer/fullerene pairs. The fullerene/fullerene  $\Delta E_b$ 's are also quite different for PCBM (1.8 eV) and PC<sub>71</sub>BM (1.3 eV). In summary, for the systems with high PCE, the binding energies are highest for the monomer/monomer pairs (greater than 2.0 eV), followed by comparable values (1.8 eV) of monomer/fullerene and fullerene/fullerene pairs for PCBM combinations, and followed by the values of monomer/fullerene (1.6 eV) and fullerene/fullerene (1.3 eV) pairs for PC<sub>71</sub>BM combinations. This implies that combinations containing PC<sub>71</sub>BM are less stable and more likely to separate into two phases than those containing PCBM. That is, heterogeneous mixtures containing PCBM are potentially more miscible relative to the one containing PC<sub>71</sub>BM. It is known that the absorption of PCBM is less than that of PC<sub>71</sub>BM, which in some cases can decrease its PCE. However Ma et al. [26] reported a higher PCE for PCBM with some conjugated polymers due to an improved morphology and miscibility compared to PC<sub>71</sub>BM. This indicates that factors such as the stability of the pairs can play important roles in increasing the PCEs of OSC.

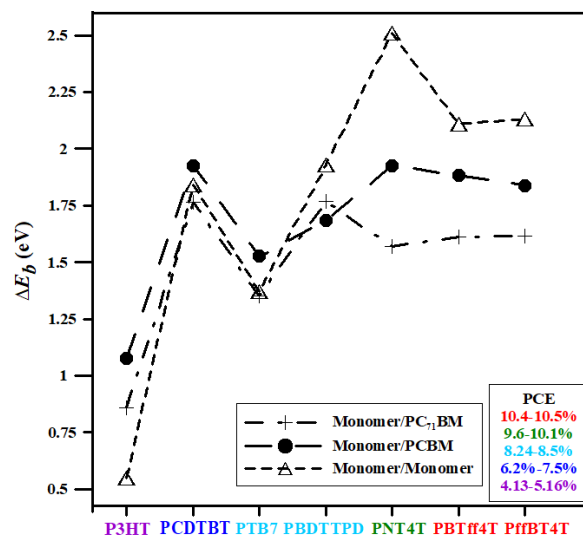


Figure 5.12: Binding energies of heterogeneous and homogenous pairs obtained with the B97D3 D-DFT method.

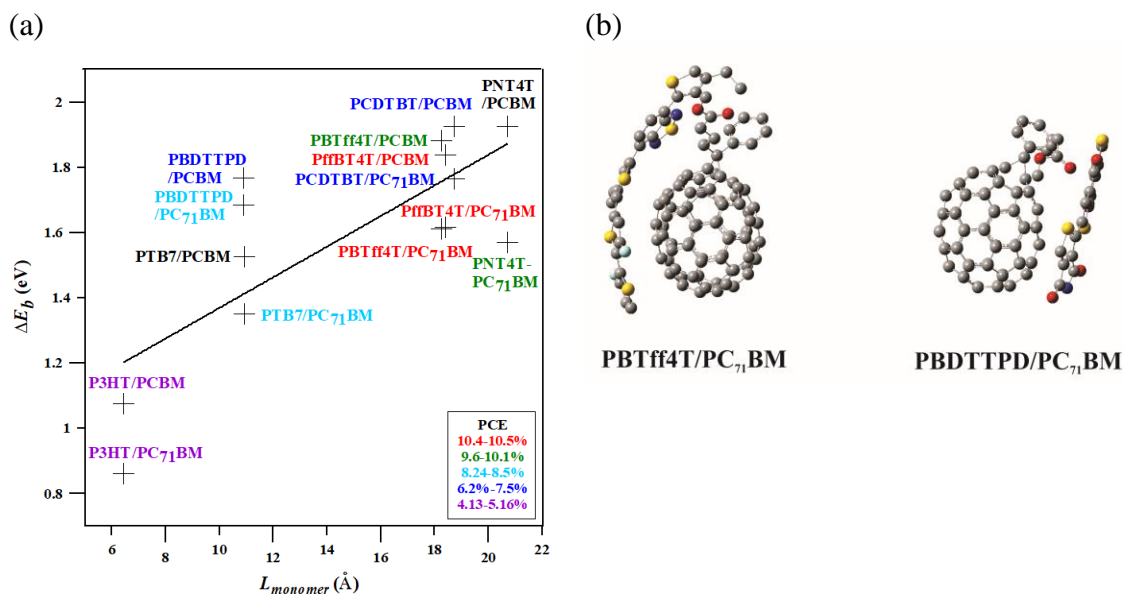


Figure 5.13: (a) Binding energy of monomer/fullerene pairs versus the isolated monomer's chain length. (b) A corresponding example of two pairs optimized at the B97D3 method with different  $L_{monomer}$  but similar  $\Delta E_b$ . For clarity, hydrogen atoms are not shown.

Based on the above results, we note that there is a strong correlation of experimental PCE with a homogenous  $\Delta E_b$  of monomer/monomer pairs and a heterogeneous quantity such as  $(\Delta\epsilon_{H_D-L_A} - 0.3)/E_g(\text{monomer})$  of monomer/fullerene pairs. Thus, both quantities are displayed in Figure 5.14. The results show a nearly linear relationship (with very little scatter of data points) between the two parameters with homogeneous pair  $\Delta E_b$  increases with increasing  $(\Delta\epsilon_{H_D-L_A} - 0.3)/E_g(\text{monomer})$ . This correlation sums up the importance of the stability of monomers pairs in addition to optimization of energetic offsets at the interface of monomer/fullerene pairs when improving the performance of OSCs.

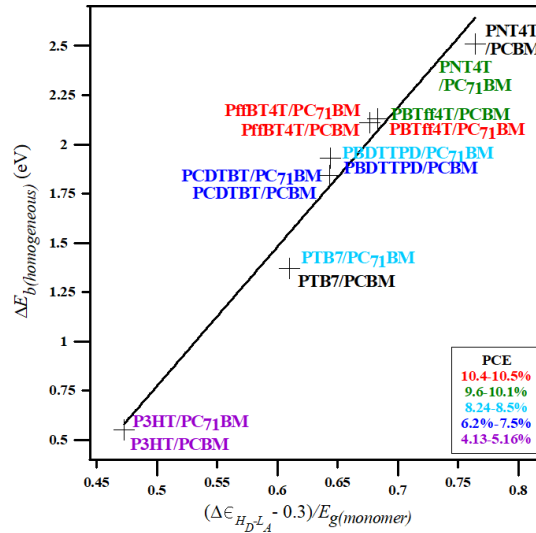


Figure 5.14: The binding energy of homogenous pairs optimized at the B97D3 method versus  $(\Delta\epsilon_{H_D-L_A} - 0.3)/E_g(\text{monomer})$  of heterogenous pairs (obtained using the B97D3 optimized geometries in SP B3LYP calculation).

## 5.4.5 Further Verification of our Conclusions

In the previous subsections 5.4.2, 5.4.3 and 5.4.4, our results indicate that the PNT4T/fullerene, PBTff4T/fullerene, and Pff4TBT/fullerene, which exhibited the highest PCEs, display some common interfacial and electronic properties that might be considered important for an optimal performance of OSC. As a further test, it would be useful to determine if these properties can be found in other OSC polymers with high PCEs. For this reason, we (randomly) select six other monomers of polymers used in OSCs with various PCEs as our test sample (this set does not include pairings corresponding to OSCs with the highest PCEs known). This sample includes PTTTPD with 1.44% [27], PCPDTPD with 3.1% [27], EH-DFBT with 3.37% [28], PDPP2FT with 6.5% [29], PDPPTPT with 7.3% [30], and PNNT-12HD with 8.2% [31]. We perform the B97D3 method on the monomer/monomer pairs and the B3LYP method on the gas phase monomers and fullerenes to obtain the interfacial and electronic quantities as described in subsection 5.3.2. The results of these computations show that similar trends are obtained as in previous subsections for the  $\Delta E_b$  of the homogeneous pairs and the  $\Delta\epsilon_{LUMO}$  and  $(\Delta\epsilon_{H_D-L_A} - 0.3)/E_{g(monomer)}$  of isolated monomers and fullerenes (see Figure 5.15). The HOMO offsets for this set are broadly spread out and do not exhibit clear trends. The results displayed in Figure 5.15 also show that the computed quantities of monomer/fullerene pairs correlate well with the experimental determined PCEs. In particular, the highest homogeneous  $\Delta E_b$ , the lowest  $\Delta\epsilon_{LUMO}$ , and the highest  $(\Delta\epsilon_{H_D-L_A} - 0.3)/E_{g(monomer)}$  are found unambiguously for pairs containing PNNT with the highest PCE. These findings confirm our general conclusions given in subsections 5.4.2-5.4.4. As an aid in identifying

the best polymers for highly BHJ OSCs we recommend a computational approach that is described in Appendix C.

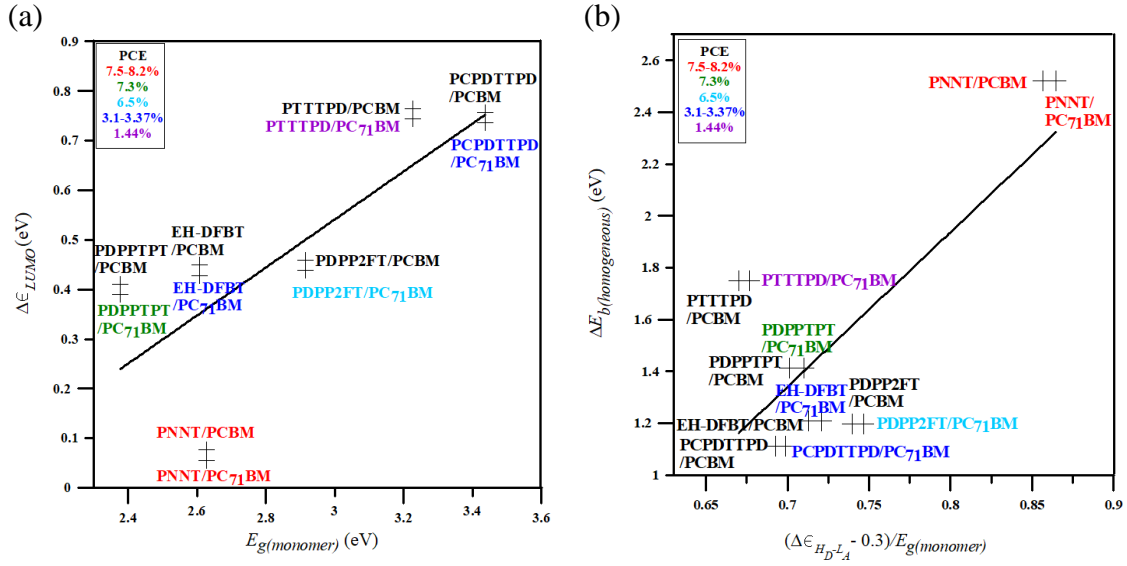


Figure 5.15: (a) LUMO offsets of the gas phase monomers and fullerenes versus the respective monomer's  $E_g$ , and (b) the binding energy of homogenous pairs optimized at the B97D3 method versus  $(\Delta\epsilon_{H_D-L_A} - 0.3)/E_{g(mononer)}$  of heterogenous pairs including the gas phase monomers and fullerenes. The gas phase monomers and fullerenes are optimized at the B3LYP method.

## 5.5 Conclusions

In this work, we have analyzed the conformations, electronic structures, and binding energies at the interfacial region of various homogeneous and heterogeneous pairings of monomers and fullerenes using the dispersion-corrected B97D3 and the hybrid B3LYP DFT methods. We have found that both methods can be used to obtain similar electronic

properties and correlations for gas phase and interacting monomers and fullerenes. We also determined the most stable configurations of monomer/monomer, monomer/fullerene, and fullerene/fullerene pairs. We have found that the preferred configuration for the fourteen heterogeneous pairings occurs when the monomer is located on the side of fullerene. Based on the original set of fourteen combinations, we have determined the following common interfacial factors that lead to achieving the highest experimental PCE (over 10%) for Pff4TBT/, PBTff4T/, and PNT4T/fullerene pairs in OSCs:

1. having the lowest LUMO offset,  $\Delta\epsilon_{LUMO}$  (close to 0.2 eV), the highest HOMO offset,  $\Delta\epsilon_{HOMO}$  (close to 0.7 eV), and the highest ratio  $(\Delta\epsilon_{HD-LA} - 0.3)/E_{g(monomer)}$  (in the range of 0.68 to 0.8);
2. having the highest or relatively high  $\Delta E_b$  (above 2 eV) for the homogeneous monomer pairs which preferably should be comparable to  $\Delta E_b$  for fullerene/fullerene and monomer/fullerene pairs for better miscibility;
3. having the optimal structural/interfacial properties such as the long  $L_{monomer}$  of isolated monomers (of the order of 20 Å), and the lowest  $d_{min}$  (3 Å) of monomer/fullerene pairs.

This study shows that the high-performance OSCs containing mixture of polymers and fullerenes have similar (common) interfacial and electronic properties that can be used to predict the best materials for the future, more efficient OSCs.

## Acknowledgments

We would like to thank the following for making this research possible: WestGrid ([www.westgrid.ca](http://www.westgrid.ca)), SHARCNET ([www.sharcnet.ca](http://www.sharcnet.ca)), ACENET ([www.ace-net.ca](http://www.ace-net.ca)), and Compute Canada *Calcul Canada* ([www.computecanada.ca](http://www.computecanada.ca)) for providing the computational facilities. ACENET is the regional high performance computing consortium for universities in Atlantic Canada, and it is funded by the Canada Foundation for Innovation (CFI), the Atlantic Canada Opportunities Agency (ACOA), and the provinces of Newfoundland and Labrador, Nova Scotia, and New Brunswick. SHARCNET ([www.sharcnet.ca](http://www.sharcnet.ca)) is a consortium of 18 colleges, universities and research institutes operating a network of high-performance computer clusters across south western, central and northern Ontario. We would also like to thank King Abdulaziz University in Saudi Arabia and the Saudi Cultural Bureau in Canada for the full scholarship given to S.A.A.

# Bibliography

- [1] K.A. Mazzi, C.K. Luscombe, *The Future of Organic Photovoltaics*, Chemical Society Reviews 44 (2015) 78-90.
- [2] J.F. Yan, B.R. Saunders, *Third-Generation Solar Cells: A Review and Comparison of Polymer: Fullerene, Hybrid Polymer and Perovskite Solar Cells*, RSC Advances 4 (2014) 43286-43314.
- [3] W.S. Yang, J.H. Noh, N.J. Jeon, Y.C. Kim, S. Ryu, J. Seo, S.I. Seok, *High-Performance Photovoltaic Perovskite Layers Fabricated through Intramolecular Exchange*, Science 348 (2015) 1234-1237.
- [4] Y.J. Jeon, S. Lee, R. Kang, J.E. Kim, J.S. Yeo, S.H. Lee, S.S. Kim, J.M. Yun, D.Y. Kim, *Planar Heterojunction Perovskite Solar Cells with Superior Reproducibility*, Scientific Reports 4 (2014).
- [5] J.B. Huang, X.G. Yu, J.S. Xie, D.K. Xu, Z.G. Tang, C. Cui, D.R. Yang, *Ambient Engineering for High-Performance Organic Inorganic Perovskite Hybrid Solar Cells*, ACS Applied Materials & Interfaces 8 (2016) 21505-21511.
- [6] M.D. Irwin, B. Buchholz, A.W. Hains, R.P.H. Chang, T.J. Marks, *P-Type Semiconducting Nickel Oxide as an Efficiency-Enhancing Anode Interfacial Layer in Polymer Bulk-Heterojunction Solar Cells*, Proceedings of the National Academy of Sciences of the United States of America 105 (2008) 2783-2787.
- [7] H.Y. Wang, X. Wang, P. Fan, X. Yang, J.S. Yu, *Enhanced Power Conversion Efficiency of P3HT: PC71BM Bulk Heterojunction Polymer Solar Cells by Doping a High-Mobility Small Organic Molecule*, International Journal of Photoenergy 2015 (2015).
- [8] S. Beaupre, M. Leclerc, *PCDTBT: En Route for Low Cost Plastic Solar Cells*, Journal of Materials Chemistry A 1 (2013) 11097-11105.
- [9] C. Cabanetos, A. El Labban, J.A. Bartelt, J.D. Douglas, W.R. Mateker, J.M.J. Frechet, M.D. McGehee, P.M. Beaujuge, *Linear Side Chains in Benzo 1,2-B:4,5-B' Dithiophene-Thieno 3,4-C Pyrrole-4,6-Dione Polymers Direct Self-Assembly and Solar Cell Performance*, Journal of the American Chemical Society 135 (2013) 4656-4659.
- [10] Z.C. He, C.M. Zhong, S.J. Su, M. Xu, H.B. Wu, Y. Cao, *Enhanced Power-Conversion Efficiency in Polymer Solar Cells Using an Inverted Device Structure*, Nature Photonics 6 (2012) 591-595.
- [11] Y.H. Liu, J.B. Zhao, Z.K. Li, C. Mu, W. Ma, H.W. Hu, K. Jiang, H.R. Lin, H. Ade, H. Yan, *Aggregation and Morphology Control Enables Multiple Cases of High-Efficiency Polymer Solar Cells*, Nature Communications 5 (2014) 5293.
- [12] X. Chen, F.Q. Bai, H.T. Wang, H.X. Zhang, Y.A. Tang, *The Impact of Molecular Stacking Interactions on the Electronic Structure and Charge Transport Properties in Distyrylbenzene (DSB-) Based D-A Complexes: A Theoretical Study*, RSC Advances 5 (2015) 47681-47691.
- [13] N.K. Elumalai, A. Uddin, *Open Circuit Voltage of Organic Solar Cells: An in-Depth Review*, Energy & Environmental Science 9 (2016) 391-410.
- [14] G. Boschetto, H.T. Xue, J. Dzedzic, M. Krompiec, C.K. Skylaris, *Effect of Polymerization Statistics on the Electronic Properties of Copolymers for Organic Photovoltaics*, Journal of Physical Chemistry C 121 (2017) 2529-2538.

- [15] T.L.D. Tam, T.T. Lin, *Tuning Energy Levels and Film Morphology in Benzodithiophene-Thienopyrrolodione Copolymers Via Nitrogen Substitutions*, *Macromolecules* 49 (2016) 1648-1654.
- [16] N. Van den Brande, G. Van Lier, F. Da Pieve, G. Van Assche, B. Van Mele, F. De Proft, P. Geerlings, *A Time Dependent DFT Study of the Efficiency of Polymers for Organic Photovoltaics at the Interface with PCBM*, *RSC Advances* 4 (2014) 52658-52667.
- [17] S.A. Ayoub, J.B. Lagowski, *Optimizing the Performance of Multilayered Organic Polymer Devices Using Computational Dimer Approach-A Case Study*, *Journal of Physical Chemistry C* 120 (2016) 496-507.
- [18] S. Grimme, *Semiempirical GGA-Type Density Functional Constructed with a Long-Range Dispersion Correction*, *Journal of Computational Chemistry* 27 (2006) 1787-1799.
- [19] A.D. Becke, *Density-Functional Thermochemistry .3. The Role of Exact Exchange*, *Journal of Chemical Physics* 98 (1993) 5648-5652.
- [20] C.T. Lee, W.T. Yang, R.G. Parr, *Development of the Colle-Salvetti Correlation-Energy Formula into a Functional of the Electron-Density*, *Physical Review B* 37 (1988) 785-789.
- [21] A.D. Becke, *Density-Functional Thermochemistry .3. The Role of Exact Exchange*, *J. Chem. Phys.* 98 (1993) 5648-5652.
- [22] M.J. Eslamibidgoli, J.B. Lagowski, *The Effect of Side-Chain Length on the Solid-State Structure and Optoelectronic Properties of Fluorene-Alt-Benzothiadiazole Based Conjugated Polymers-A DFT Study*, *Journal of Physical Chemistry A* 116 (2012) 10597-10606.
- [23] G.C. Arthur J. Nozik, Matthew C Beard, *Advanced Concepts in Photovoltaics* (The Royal Society of Chemistry, 2014).
- [24] M.C. Scharber, N.S. Sariciftci, *Efficiency of Bulk-Heterojunction Organic Solar Cells*, *Progress in Polymer Science* 38 (2013) 1929-1940.
- [25] C.Y. Chang, C.E. Wu, S.Y. Chen, C.H. Cui, Y.J. Cheng, C.S. Hsu, Y.L. Wang, Y.F. Li, *Enhanced Performance and Stability of a Polymer Solar Cell by Incorporation of Vertically Aligned, Cross-Linked Fullerene Nanorods*, *Angewandte Chemie-International Edition* 50 (2011) 9386-9390.
- [26] Z.F. Ma, E.G. Wang, K. Vandewal, M.R. Andersson, F.L. Zhang, *Enhance Performance of Organic Solar Cells Based on an Isoindigo-Based Copolymer by Balancing Absorption and Miscibility of Electron Acceptor*, *Applied Physics Letters* 99 (2011).
- [27] X.G. Guo, H. Xin, F.S. Kim, A.D.T. Liyanage, S.A. Jenekhe, M.D. Watson, *Thieno 3,4-C Pyrrole-4,6-Dione-Based Donor-Acceptor Conjugated Polymers for Solar Cells*, *Macromolecules* 44 (2011) 269-277.
- [28] Y.X. Li, J.Y. Zou, H.L. Yip, C.Z. Li, Y. Zhang, C.C. Chueh, J. Intemann, Y.X. Xu, P.W. Liang, Y. Chen, A.K.Y. Jen, *Side-Chain Effect on Cyclopentadithiophene/Fluorobenzothiadiazole-Based Low Band Gap Polymers and Their Applications for Polymer Solar Cells*, *Macromolecules* 46 (2013) 5497-5503.
- [29] A.T. Yiu, P.M. Beaujuge, O.P. Lee, C.H. Woo, M.F. Toney, J.M.J. Frechet, *Side-Chain Tunability of Furan-Containing Low-Band-Gap Polymers Provides Control of Structural Order in Efficient Solar Cells*, *Journal of the American Chemical Society* 134 (2012) 2180-2185.

- [30] K.H. Hendriks, G.H.L. Heintges, V.S. Gevaerts, M.M. Wienk, R.A.J. Janssen, *High-Molecular-Weight Regular Alternating Diketopyrrolopyrrole-Based Terpolymers for Efficient Organic Solar Cells*, *Angewandte Chemie-International Edition* 52 (2013) 8341-8344.
- [31] I. Osaka, T. Kakara, N. Takemura, T. Koganezawa, K. Takimiya, *Naphthodithiophene-Naphthobisthiadiazole Copolymers for Solar Cells: Alkylation Drives the Polymer Backbone Flat and Promotes Efficiency*, *Journal of the American Chemical Society* 135 (2013) 8834-8837.

# Chapter 6

## 6 A DFT Investigation of Conjugated Polymers and Fullerenes Interactions - Side Chain Effect

Sarah A. Ayoub and Jolanta B. Lagowski, (in preparation).

### 6.1 Abstract

Considerable experimental research has been conducted on the influence of polymer alkyl side chains on the performance of polymer/fullerene organic solar cells. However, a clear picture of the effect of alkyl side chains on the polymer/fullerene interfaces is not yet known. Using the dispersion-corrected density functional theory, we investigate the influence of alkyl side chains on the binding energies and electronic structures of various molecular pairings of fullerenes and monomers (e.g. a pair of PC<sub>71</sub>BM and a copolymer based on thieno[3,4-b]thiophene/benzodithiophene (PTB7) [1], PCBM and a copolymer based on 2,7-carbazole/dithienyl-2,1,3-benzothiazole (PCDTBT) [2], and PC<sub>71</sub>BM and a copolymer based on difluorobenzothiadizole/quarterthiophene (PffBT4T-2OD) [3]).

Depending on the sizes, types, and branched positions of alkyl side chains, the results indicate different trends of binding energies and interfacial properties that are correlated with the efficiencies of organic solar cells. This work provides deeper insights into the role of side chains in monomer/fullerene interactions. We identify favorable side chain arrangements that could be used to optimize the device performance of organic solar cells.

## 6.2 Introduction

Organic solar cells (OSCs) have attracted tremendous attention in the past decade due to their superior advantages over inorganic solar cells, such as the flexibility, non-toxic, and low cost of materials. [4] The interface between polymers and fullerenes in the active layer is critical to the operation of bulk-heterojunction OSCs. It is widely accepted that the processes of exciton dissociation, charge separation, and charge recombination are controlled by the polymer/fullerene interfaces. [5] Even though a huge effort was made on synthesizing hundreds of materials for OSCs to increase the power conversion efficiency (PCE), which currently reached above 10 % [3], no clear strategy is known for optimizing the polymer/fullerene interfaces. Many systems that include some promising materials' properties (such as the strong absorption and high hole mobility) yield low or moderate PCEs. [6-9] The potential problem of not obtaining the expected high PCEs for these systems is the fact that it is still poorly understood how the polymer/fullerene interactions and arrangements can influence the charge separation and transport in OSCs. However, it is difficult to anticipate experimentally how the intermolecular interaction of

polymer/fullerene will affect the device performance. Hence, some new insight and intermolecular factors that will affect the performance of OSCs are needed.

Recently, it has been recognized that the alkyl side chains attached to solution-processed OSC polymers are critical not only for controlling the solubility but also for the polymer/fullerene interaction and device performance. It has been reported that alkyl side chains can exert a considerable influence on the properties of low band gap (LBG) copolymers and can lead to higher PCEs in OSCs. [1, 10] The role of side chains is apparent on the  $\pi - \pi$  stacking and lamellar distances between polymers. Both factors are crucial for the charge transport and thus the device performance. [11, 12] Alkyl side chains can be of different types. They can be linear or branched. They can have different lengths or sizes, and they can be located at different positions along the backbones of the polymers. It is believed that the OSC efficiency depends strongly on the length of alkyl side chains (i.e. the number of carbon atoms). For example, the poly(3-hexylthiophene) (P3HT), which includes six C atoms on the side chains, have been found to have superior properties as an OSC material relative to poly(3-butylthiophene) (P3BT) and poly(3-pentylthiophene) (P3PT) which include four C and five C atoms on the side chains respectively. [13] Cabanetos et al. [10] showed also that the substitutions of linear side chains in TPD units of (PBDTPD) copolymers, which are based on benzo[1,2-b:4,5-b']dithiophene-thieno[3,4-c]pyrrole-4,6-dione, can highly affect the polymers self-assembling properties and OSC efficiency. For example, devices fabricated from PBDTPD with n-heptyl (C7)-substituted TPD motifs achieved a higher PCE of about 8.5% compared to those fabricated with n-hexyl (C6)- and n-octyl (C8)-substituted TPD

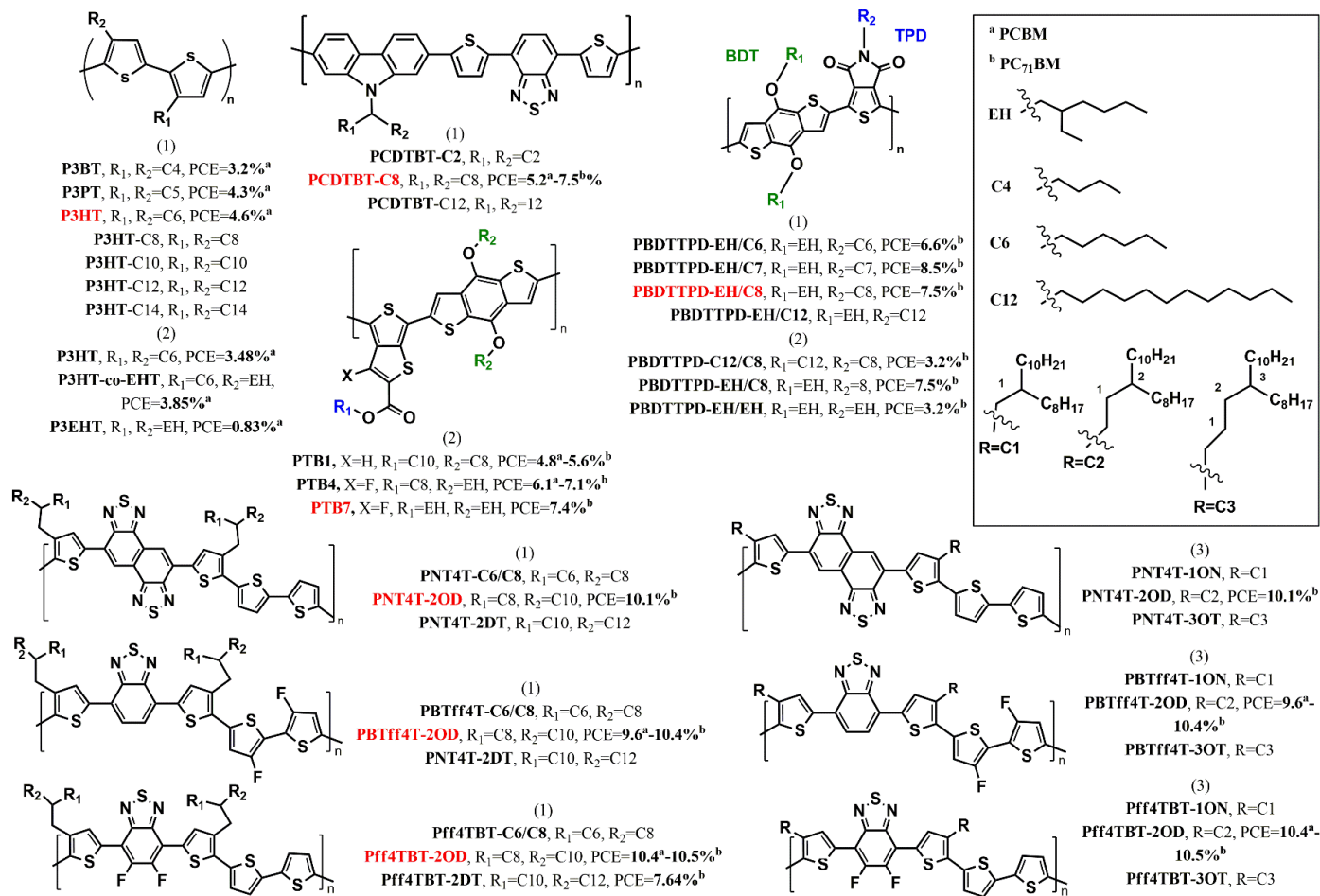
motifs which reached PCEs of about 6.6% and 7.5% respectively. However, it remains unclear how the addition/reduction of one or two carbon atoms on the alkyl side chains can affect the polymer/fullerene interactions and improve PCEs. Moreover, it has been reported that as the length of side chains in conjugated polymers increases, the open-circuit voltage  $V_{OC}$ , which is proportional to the interfacial energy gap ( $\epsilon_{HOMO(polymer)} - \epsilon_{LUMO(fullerene)}$ , where polymer is a donor and fullerene is an acceptor), also increases when the conjugated bone is kept constant. [13, 14] The reason for the higher  $V_{OC}$ 's (whether it is due to the lowering of  $\epsilon_{HOMO(polymer)}$ 's or because of the influence of interfacial interactions) is not generally explained in literature. However, some other studies showed no consistent trend between the side chain length and  $V_{OC}$ . [15, 16]

In addition, the type of side chains, the linear and branched, can play an important role in determining the efficiency of OSCs. It has been suggested that OSC materials should be designed with linear side chains attached to the electron-accepting motifs and branched side chains attached to the electron-donating motifs of polymers. [5, 17] This will make the acceptor units more accessible to the fullerenes and will lead to a favorable polymer/fullerene interactions. For example, the work of Cabanetos et al. [10] reported that a high PCE of 8.5 % was reached when the branched alkyl-substituted BDT (donor) motifs were combined with linear alkyl-substituted TPD (acceptor) motifs, however, when the branched side chains were replaced by linear ones in BDT units, a major change was induced in polymer self assembly that correlated with a huge drop in the PCE of OSC. Other studies also showed that the branched alkyl side chains (such as 2-ethylhexyl) in LBG polymers are significant for achieving the highest PCEs. [18, 19] For example, a remarkable PCE was achieved of about 8.24-9.2% with all-branched alkyl side chains on

the acceptor and donor units of PTB7 copolymers which are based on thieno[3,4-b]thiophene/benzodithiophene. [20] The branching position of alkyl side chains is another important factor that improves the polymer properties and device performance. In particular, the group of Liu et al. achieved a record PCE of above 10 % when the second-position branched alkyl-side-chains was used on quaterthiophene-based polymers (e.g. Pff4TBT-2OD). [3]

These studies confirm that the experimental studies do not provide a comprehensive picture on the effect of side chains on OSC device performance due to either not having enough data or changing too many parameters at the same time. In addition, theoretical studies of the role of alkyl side chains on polymer/fullerene interactions is still lacking. In our previous work [21], we employed the dispersion-corrected density functional theory (D-DFT) to investigate the electronic properties and the interfacial interactions of various promising monomers/fullerenes combinations. Our results exhibited optimal properties' trends that lead us to determine general guidelines that can be used to select the best polymers when designing OSCs with high efficiencies. In the present work, we focus on the effect of alkyl side chains using the same type of monomers and fullerenes as in the previous work (see Scheme 6.1). Our aim is threefold: (1) to examine the role of different lengths, types, and branching positions of side chains on the binding energies of various pairings of monomers and fullerenes, (2) to determine the effect of alkyl side chains on the electronic properties of monomers and fullerenes, and (3) to assess whether the trends we obtained in previous work of the electronic properties and the interfacial interactions of various pairings of monomers and fullerenes without side chains are consistent with the trends when side chains are added. This computational study

identifies new trends in alkyl side chains and determines the favorable monomer/fullerene interactions for the device performance. This study is also useful for designing successful polymers for achieving highly efficient OSCs.



Scheme 6.1: OSC polymers and their PCEs as reported in literature, wherein alkyl side chains are varied by the (1) length, (2) type, and (3) branching positions of alkyl groups.

## 6.2 Computational Details

### 6.2.1 Computational Approach

All combinations evaluated in this work were fully optimized at the B97-D3 [22] and B3LYP-D3 [23, 24] methods with the 6-31G(d) basis set as implemented in Gaussian 09. [25] Previous work showed that both D-DFT methods provide good performance and consistent trends in describing the interfacial interactions of monomers and fullerenes. Because B3LYP/6-31G(d) is known to give electronic structure parameters that agree well with experimental data [26, 27], the isolated monomers and fullerenes were optimized using the B3LYP to obtain the HOMO ( $\epsilon_{HOMO}$ ) and LUMO ( $\epsilon_{LUMO}$ ) eigenvalues and bandgaps ( $E_g$ 's) in the gas phase. The electronic structure parameters of interacting monomers and fullerenes were also determined from the single point B3LYP/6-31G(d) computations that used the optimized geometries of B97-D3 and B3LYP-D3 methods. Previous work showed that the latter approach gives very accurate and reliable results compared to experimental data of monomers and fullerenes. Since both D-DFT methods provide similar trends, in the following sections, we display only the B97-D3 results, the B3LYP-D3 results are given in Appendix D Tables.

## 6.2.2 The Preferred Configurations of Monomers and Fullerenes Pairings

Heterogenous and homogenous pairings are two types of interactions that were considered in this work to simulate the interfacial interactions within polymers and between polymers and fullerenes. Heterogenous pairing consists of one monomer and one fullerene (such as, for example, P3HT/PCBM), and homogenous pairing consists of two monomers of the same type (such as, for example, P3HT/P3HT). All the configurations of monomers and fullerenes pairings were selected based on the most stable conformations that correspond to the lowest total energy and highest binding energy (previous work determined these configurations[21]). The co-facial  $\pi$ -stacking (with the favorable relative orientations of monomers) were the preferred conformations for homogeneous pairs. Monomers in heterogenous pairs were located on the sides of fullerenes in their preferred configurations (monomers located on top and bottom of fullerenes give rise to less stable conformations).

Consideration was also given to the initial configurations (prior to optimizations) of two heterogenous pairings that included monomers of the same type and two different types of fullerenes (e.g. P3HT/PCBM and P3HT/PC<sub>71</sub>BM). For example, in order to have a valid comparison between the two pairings, P3HT was placed with the same orientation relative to both types of fullerenes PCBM and PC<sub>71</sub>BM (see the optimized geometries of both pairings in Figure 6.1 (a) and (b)). When the side chains are present in heterogenous pairs, the preferred configuration is when the side chains are wrapped around or directed

toward the fullerene (as displayed in Figure 6.1 (a) and (b)). Configurations that have side chains directed away from fullerenes (as displayed in Figure 6.1 (c)) are the least stable.

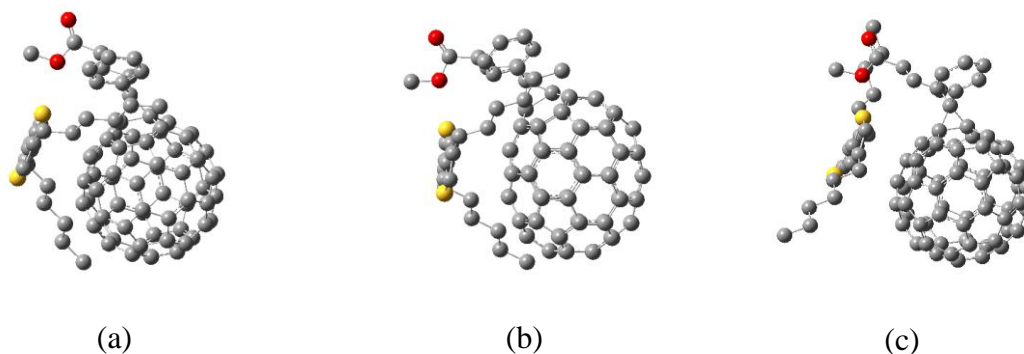


Figure 6.1: Illustrations of the preferred configurations of (a) P3HT/PC<sub>71</sub>BM and (b) P3HT/PCBM. They also illustrate the side chains of monomers wrapping around fullerenes whereas (c) illustrates the least stable configuration where the side chains are directed away from fullerene.

## 6.2.3 Side Chain Studies

In the first part of this work, we compare the binding energies of pairs that include the seven different types of most promising/popular monomers in literature (as marked in red in the Scheme 6.1 and discussed in section 6.3.1). The purpose of this first comparison is to examine the correlation of the binding energies with the experimentally determined PCEs (and to see if the results are consistent with previous work that contain no/short side chains).

In the second part of this work, we compare the binding energies of pairs that include the same type of monomers but with different alkyl side chains (as discussed in sections 6.3.2, 6.3.3, and 6.3.4). In this comparison, we considered three forms of alkyl

side chains that differ by: (1) length, (2) type, and (3) branching position of side chains. Based on these forms, monomers are divided into three categories, which are displayed in Scheme 6.1:

- (1) P3HT, PCDTBT, PBDTTPD, PNT4T, Pff4TBT, and PBTff4T. The size of side chains is defined by the number of carbon atoms ( $n_c$ ). The  $n_c$  is varied in P3AT from C4 to C12, in PCDTBT from C2 to C12, in PBDTTBT from C6 to C12, and in PNT4T, Pff4TBT, and PBTff4T from C6/C8 to C10/C12;
- (2) P3HT, PBDTTPD, and PTB. For each monomer, three types of side chains were considered: all-linear, linear-and-branched, and all-branched side chains. The type of side chains is defined by the number of branches ( $n_B$ ), hence  $n_B$  is varied from 0 to 2;
- (3) PNT4T, Pff4TBT, and PBTff4T. The alkyl side chains in each monomer are branched at three different branching positions ( $P_B$ 's) which are 1, 2, and 3.

To evaluate the effect of alkyl groups on the above categories of monomers, the binding energies of homogenous and heterogenous pairs were calculated as a function of  $n_c$ ,  $n_B$ , and  $P_B$  of alkyl side chains. This evaluation will help us to understand as to why certain side chains (such as C6, EH/C8, and  $P_B=2$  in P3HT, PBDTTPD, and Pff4TBT respectively) are optimal for the monomer/fullerene interactions, (and give high PCEs). We note that some monomers with side chains that were included in our study had no corresponding PCEs (see Scheme 6.1). They were added to our computational study to provide a more complete picture of the role of side chains in the interfacial interactions between monomers and fullerenes.

## 6.2.4 Computed Parameters

The strength of interfacial interactions of homogenous and heterogenous pairings including monomers with various forms of alkyl side chains is evaluated by determining the binding energies ( $\Delta E_b$ ) which are defined by,

$$\Delta E_b = \sum_{i=1}^2 E_i - E_{pair} \quad (6.1)$$

where  $E_{pair}$  is the total energy of monomer/monomer or monomer/fullerene pair, and  $E_1$  and  $E_2$  are the total energies of individual monomers or monomers and fullerenes respectively.

To examine the effect of side chains on the electronic structures, the electronic parameters ( $\epsilon_{HOMO}$ ,  $\epsilon_{LUMO}$ , and  $E_g$ ) were also calculated for the individual gas phase monomers and fullerenes as well as the interacting monomers and fullerenes. We determined in previous work the optimal electronic-properties trends for optimizing the PCE of OSCs (such as lowest  $\Delta\epsilon_{LUMO}$  and highest ratio  $(\Delta\epsilon_{HD-LA} - 0.3)/E_{g(monomer)}$ ) where  $(\Delta\epsilon_{HD-LA} = \epsilon_{HOMO_{Acceptor}} - \epsilon_{LUMO_{Donor}}$ . [21] In this work, we calculated these energetic offsets with varying side chains to search for trends that can correlate with the device performance.

## 6.3 Results and Discussion

### 6.3.1 Various Pairs with High PCEs

In this subsection, we examine the  $\Delta E_b$ 's of various heterogenous and homogenous pairs that include seven different types of promising monomers (which are marked in red in Scheme 6.1). These monomers have different types of side chains: P3HT (all-linear), PCDTBT (all-linear), PBDTTPD (linear-and-branched), PTB7 (all-branched), PNT4T (all-branched), Pff4TBT (all-branched), and PBTff4T (all-branched). As can be seen from Figure 6.2 (a), similar to the short side chains results in previous work [21], the  $\Delta E_b$ 's of pairs involving smaller fullerenes are larger than those involving larger fullerenes. However, unlike short side chains results, the inclusion of side chains reduces the  $\Delta E_b$ 's of homogenous pairs relative to heterogenous pairs. This order of  $\Delta E_b$ 's for homogenous and heterogenous pairs is obtained for most pairs involving the same type of monomers with different alkyl side chains (see subsections 6.3.2, 6.3.3, and 6.3.3). That is, for the three different types of pairings and various side chains, similar trends of  $\Delta E_b$ 's are obtained. Moreover, pairs involving PNT4T exhibit the highest  $\Delta E_b$  whereas pairs involving P3HT exhibit the lowest  $\Delta E_b$  among all combinations. In all cases, monomers with short and long side chains with the highest PCEs are found with the largest  $\Delta E_b$ 's. We note here that PNT4T has the longest isolated chain-length ( $L_{monomer}$ ) while P3HT has the shortest  $L_{monomer}$  among monomers studied. This indicates that  $\Delta E_b$  might depend on  $L_{monomer}$ . In Figure 6.3, we plot the  $\Delta E_b$  of monomer/fullerene pairs versus the respective isolated  $L_{monomer}$ . The results of both pairings containing PCBM and PC<sub>71</sub>BM show that

as  $L_{monomer}$  increases, the  $\Delta E_b$  slightly increases. In previous work [21], we noted that some pairs with different  $L_{monomer}$ 's of monomers with short/no side chains exhibited comparable  $\Delta E_b$ 's. Hence, with the exception of P3HT, the results of Figure 6.3 and previous work that did not include side chains show that  $\Delta E_b$ 's of monomer/fullerene do not strongly depend on the  $L_{monomer}$ 's because the length of the fullerene that interacts with the monomer is approximately the same for all monomers. To further study the dependence of  $\Delta E_b$ 's on chain lengths, we consider both lengths of monomers and fullerenes. Figure 6.2 (b) illustrates  $\Delta E_b$ 's per average chain lengths ( $L_{avg}$ 's defined as the sum of lengths of monomers and fullerenes divided by 2). The results confirm again the  $\Delta E_b$ 's trends as given in Figure 6.2 (a) for the three types of pairings (monomer/monomer, monomer/PC<sub>71</sub>BM, and monomer/PCBM). This indicates that the  $\Delta E_b$ 's of homogenous pairs must be less than those of heterogenous pairs to obtain optimal monomer/fullerene contacts (without being interfered with the monomer/monomer interactions).

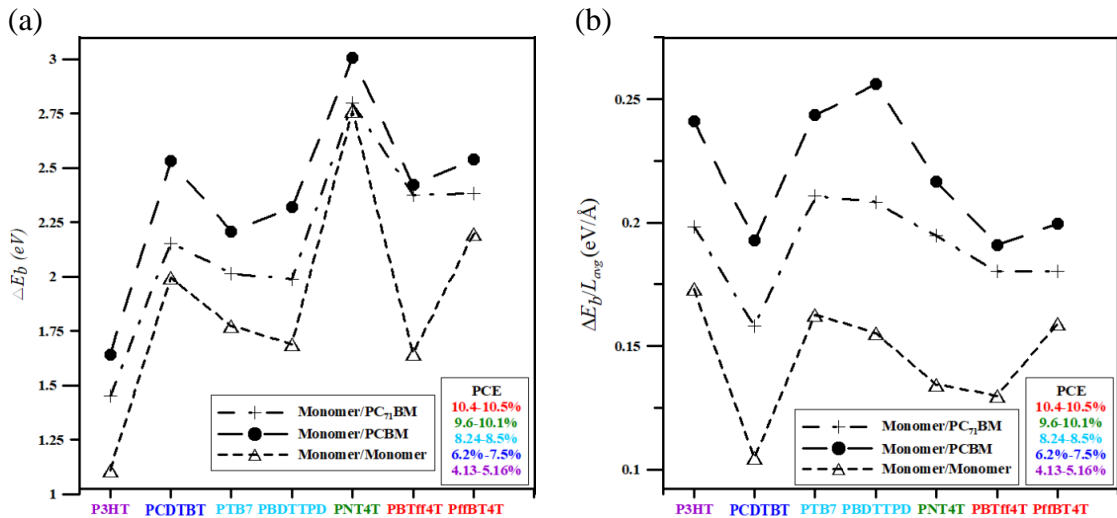


Figure 6.2: B97D3 (a) total binding energies and (b) binding energies per average chain lengths of homogenous and heterogenous pairs.

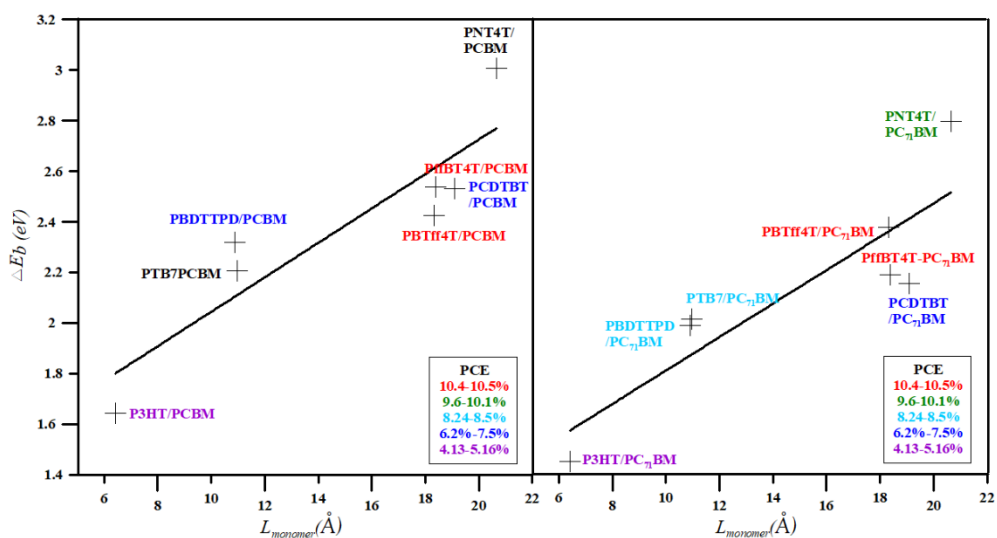


Figure 6.3: B97-D3 binding energies of monomer/PCBM and monomer/PC<sub>71</sub>BM pairs versus the isolated monomers' chain lengths.

### 6.3.2 Varying the Length of Side Chains

In this subsection, we calculate the  $\Delta E_b$ 's of homogenous and heterogenous pairs containing various lengths of side chains in monomers (of the same type) (see Figure 6.4 and Table D1 in Appendix D). Similar to the previous subsection, the results show that most monomer/monomer pairs exhibit the lowest  $\Delta E_b$ 's while monomer/PCBM pairs exhibit the highest  $\Delta E_b$ 's. The  $\Delta E_b$ 's of monomer/PC<sub>71</sub>BM give intermediate values. The results also show that, as expected,  $\Delta E_b$ 's are greatly dependent on the sizes of side chains. In particular,  $\Delta E_b$  is generally increased with increasing  $n_c$  in side chains. However, depending on the type of monomers, there is an optimal value of  $\Delta E_b$  for each type of pairing, meaning that with increasing  $n_c$ ,  $\Delta E_b$ 's are reduced or become stationary above the optimal value.

For pairs containing P3HT monomers, Figure 6.4 (a) show that as  $n_c$  in side chains increases from C4 to C8,  $\Delta E_b$ 's of homogenous and heterogenous pairs increases. For  $n_c$  larger than C8,  $\Delta E_b$  increases for homogenous pairs while it remains the same for monomer/PCBM and monomer/PC<sub>71</sub>BM pairs. The optimized geometries of monomer/fullerene show that for  $n_c$ 's up to C8, side chains are interacting with fullerenes, while for  $n_c$ 's larger than C8, side chains are exceeding the size of fullerenes (see examples of P3HT/PCBM pairs in Figure 6.5 (a-d) and (e-g) respectively). Hence,  $\Delta E_b$ 's of P3HT/fullerene pairs level off due to the excessive length of side chains that are no longer involved in the interaction. However, the optimized geometries of homogenous pairs show that the linear relationship between  $\Delta E_b$  and  $n_c$  is maintained due to the interaction between side chains (see example of P3HT-C14/P3HT-C14 in Figure 6.5 (h)). The  $\Delta E_b$ 's results of P3HT also show that they are correlated with experimental PCEs. For example, as monomer changes from P3BT (with C4 side chains) to P3HT (with C6 side chains),  $\Delta E_b$  of pairs containing the respective monomers with PCBM increases from approximately 1.5 to 1.6 eV with increasing the corresponding PCE from 3.2 to 4.6 % respectively (see Figure 6.4 (a)).

For pairs containing PCDTBT monomers, the increase in  $\Delta E_b$  due to increasing  $n_c$  (up to C8) is clearly seen for all heterogenous and homogenous pairs (see Figure 6.4 (b)). However,  $\Delta E_b$ 's of heterogenous pairs containing PCDTBT-C12 are larger than those containing PCDTBT-C8 while  $\Delta E_b$ 's of homogenous pairs remain the same for both C8 and C12 side chains. The latter result indicates that side chains are not involved in monomer/monomer interaction, hence increasing  $n_c$  larger than C8 will not affect the  $\Delta E_b$ 's

of homogenous pairs (see the optimized geometries of C8 and C12 side chains in PCDTBT/PCDTBT pairs in Figure 6.6 (a-b)). Figure 6.6 (c-d) also illustrates the difference between both side chains in the optimized geometries of PCDTBT/PC<sub>71</sub>BM pairs, confirming that the increase in  $\Delta E_b$  is due to C12 side chains that are interacting with more length of fullerenes compared to C8 side chains. Although PCDTBT with 2-octyl side chains are known to be the optimal side chains in literature, however, our computational results show that PCDTBT with C12 side chains can be good candidate for enhancing the PCE of OSCs.

For pairs containing PBDTTPD monomers, there are two types of side chains attached to each monomer: linear side chain (which can be varied into different lengths) on the TBD unit and branched side chain (which is kept constant) on the BDT unit. As can be seen from Figure 6.4 (c), as  $n_c$  increases from C6 to C12,  $\Delta E_b$  increases for homogenous and heterogenous pairs. However, the change in  $\Delta E_b$ 's is very small for  $n_c$  larger than C7 side chains, indicating that the optimal  $\Delta E_b$  is possibly reached at C7 or C8. The optimized geometries of monomer/fullerene pairs (see examples of PBDTTPD/PC<sub>71</sub>BM in Figure 6.7 (a-d)) show that C7 and C8 side chains are interacting with the full lengths of fullerenes whereas C6 side chains are interacting with less length of PC<sub>71</sub>BM and C12 side chains are exceeding the length of PC<sub>71</sub>BM. This indicates that C6 and C12 are the least favorable side chains for the optimal monomer/fullerene interactions. The optimized geometries of monomer/monomer pairs (see examples of PBDTTPD/PBDTTPD in Figure 6.7 (e-h)) show that the branched EH side chains of the BDT motifs are attractive to the linear side chains of TPD motifs of the other monomers, hence the larger  $n_c$  in linear side chains the

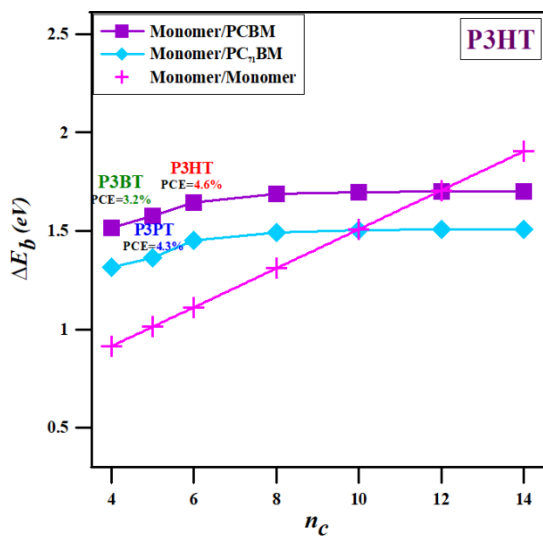
higher the  $\Delta E_b$  of a given PBDTTPD/PBDTTPD pair. More importantly, Figure 6.4 (c) show that the experimental PCEs of pairs containing PC<sub>71</sub>BM and PBDTTPD with 2EH/C6 and 2EH/C7 are correlated well with the values of  $\Delta E_b$ 's. However, although the PCE of devices containing PC<sub>71</sub>BM combined with PBDTTPD-2EH/C7 is higher than those containing PBDTTPD-2EH/C8, the similarities between both pairs in the  $\Delta E_b$ 's and structural properties are in good agreement with the similar optical properties and overall device performance that were reported for PBDTTPD with 2EH/C7 and 2EH/C8 side chains. [10] Our results also indicate that even though pairs containing PBDTTPD with EH/C12 side chains exhibit the highest  $\Delta E_b$ , however, EH/C12 are not recommended for OSC materials because they lead to unfavorable monomer/fullerene interaction.

For PNT4T, PBTff4T, and Pff4TBT monomers, the alkyl side chains can be branched into two different lengths (e.g. C6/C8). The results of pairs containing PNT4T, PBTff4T, and Pff4TBT monomers (see Figure 6.4 (d)) show that as  $n_c$  increases from C6/C8 to C8/C10,  $\Delta E_b$  increases for all heterogenous pairs while it slightly decreases for homogenous pairs. However,  $\Delta E_b$ 's are reduced for all monomer/monomer and monomer/fullerene pairs with increasing  $n_c$  from C8/C10 to C10/C12. Figure 6.8 illustrates examples of the optimized geometries of heterogenous and homogenous pairs with varying  $n_c$  from C6/C8 to C10/C12 side chains. The optimized geometries of monomer/fullerene pairs show that C6/C8 side chains interact with the least area of fullerenes, C8/C10 side chains interact most fully with fullerenes, and C10/C12 side chains exceed the diameter of fullerenes (see Figure 6.8 (a-f)). These interfacial/structural properties explain as to why the pairs containing C10/C12 side chains exhibit lowest  $\Delta E_b$ 's, C6/C8 side chains exhibit

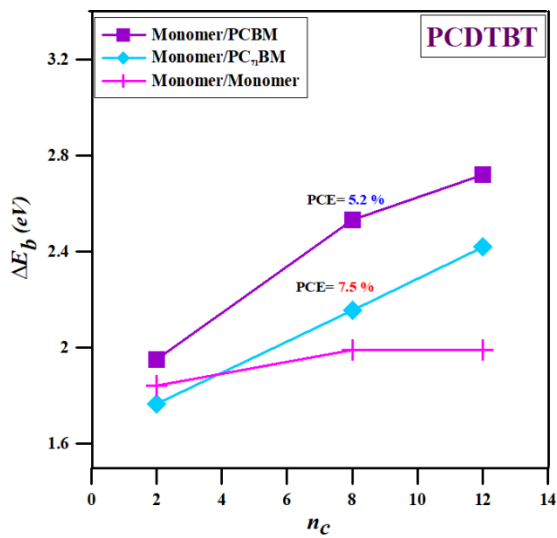
intermediate  $\Delta E_b$ 's, and C8/C10 side chains exhibit highest  $\Delta E_b$ 's. The optimized geometries of monomer/monomer pairs show that C6/C8 side chains tend to be more distant from the side chains of the other monomer in a given pair (see Figure 6.8 (g)), while C10/C12 side chains tend to be very close to each other (see Figure 6.8 (i)). However, C8/C10 side chains of monomer/monomer pairs, which exhibit highest  $\Delta E_b$ 's, tend to be not too close and not too distant from the side chains of the other monomer in a given pair (see Figure 6.8 (h)). Therefore, the most favorable side chains in homogenous and heterogenous pairs are C8/C10 due to their optimal  $\Delta E_b$ 's and interfacial properties. These results are in very good agreement with Liu et al. work which showed that devices containing Pff4TBT-2OD/PC<sub>71</sub>BM (with C8/C10) exhibited higher PCE than those containing Pff4TBT-2DT/PC<sub>71</sub>BM (with C10/C12). They also found that unnecessarily long alkyl chains lead to weaker stacking of polymers and hence several other detrimental effects. [3]

As mentioned in the previous subsection, it is preferable (for optimal device performance) for homogenous pairs with side chains to have lower  $\Delta E_b$ 's than for heterogenous pairs with side chains. Hence, we note that homogenous and heterogenous pairs with side chains lengths for which this is not the case (such as P3HT with  $n_c$  above C8, PCDTBT with  $n_c$ =C2, Pff4TBT with  $n_c$ =C6/C8, and PNT4T with  $n_c$ =C6/C8 side chains), correspond to OSCs with low PCEs.

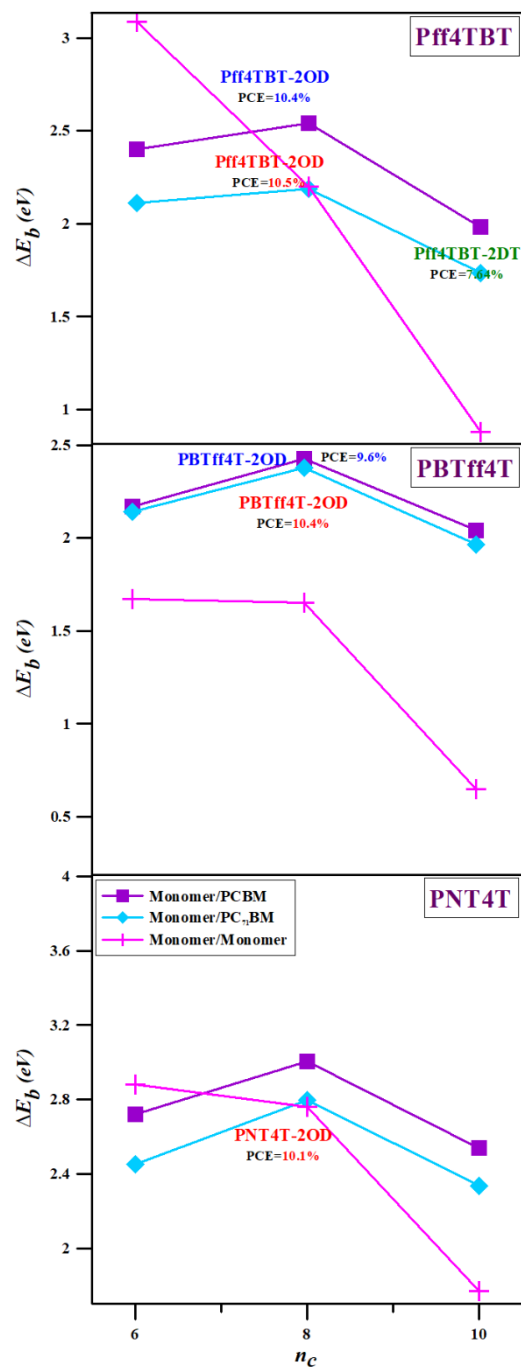
(a)



(b)



(d)



(c)

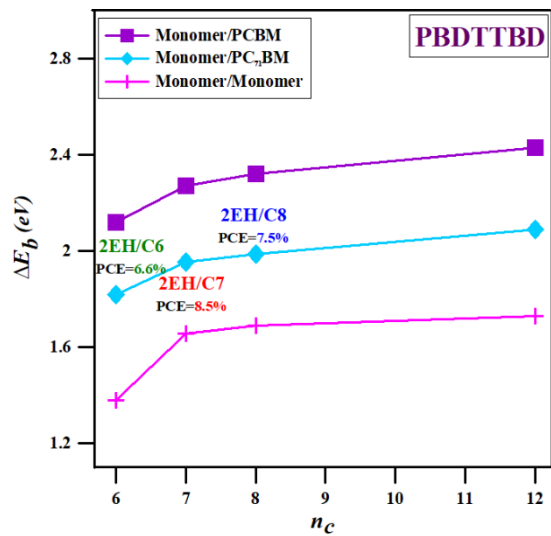


Figure 6.4: Binding energies of homogenous and heterogenous pairs versus the length of side chains in (a) P3HT, (b) PCDTBT, (c) the TPD motif of PBDTTPD, and (e) Pff4TBT, PBTff4T, and PNT4T. Monomers with highest experimental PCEs are colored in red.

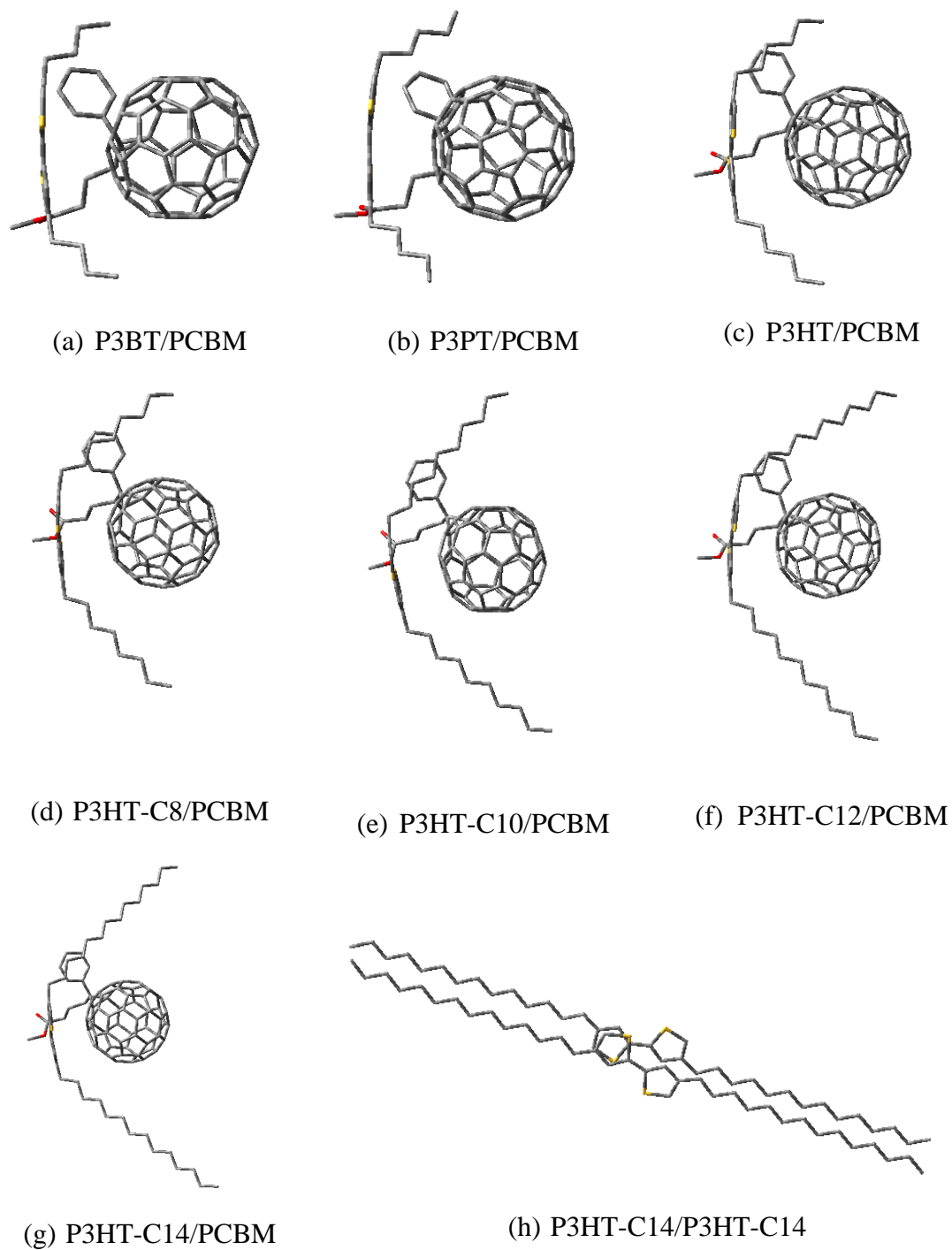
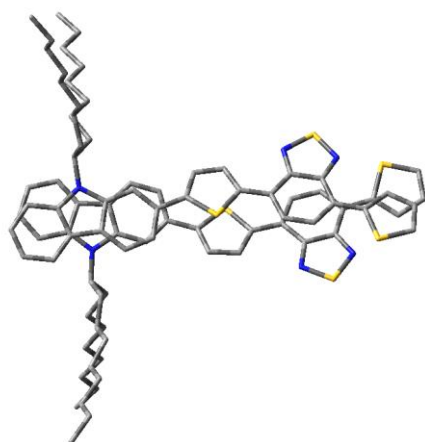
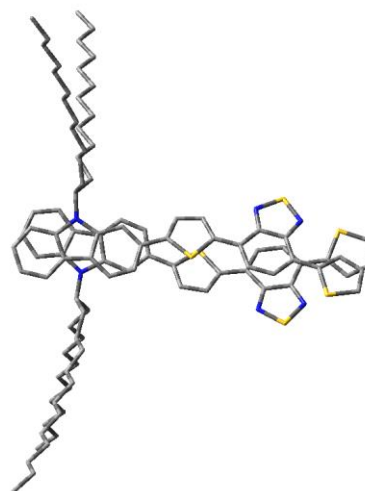


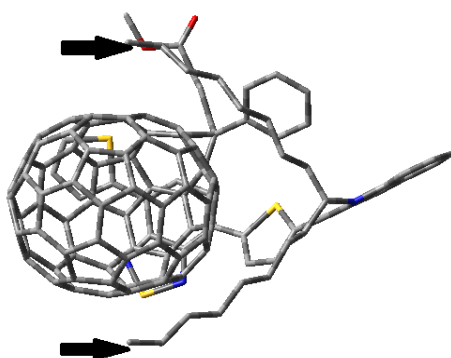
Figure 6.5: The optimized geometries of heterogeneous pairs containing P3HT with (a) C4, (b) C5, (c) C6, (d) C8, (e) C10, (f) C12, and (g) C14 side chains, and (h) the homogenous P3HT-C14/P3HT-C14 pair.



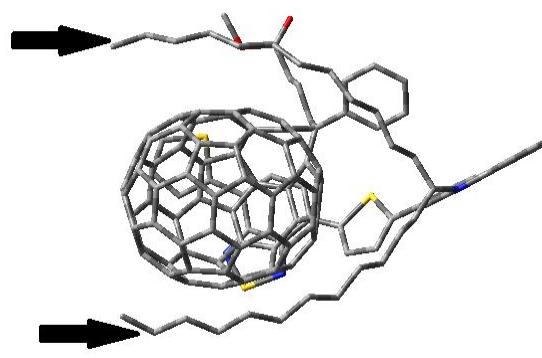
(a) PCDTBT-C8/PCDTBT-C8



(b) PCDTBT-C12/PCDTBT-C12



(c) PCDTBT-C8/PC<sub>71</sub>BM



(d) PCDTBT-C12/PC<sub>71</sub>BM

Figure 6.6: The optimized geometries of (a-b) homogenous and (c-d) heterogenous pairs containing PCDTBT with C8 and C12 side chains.

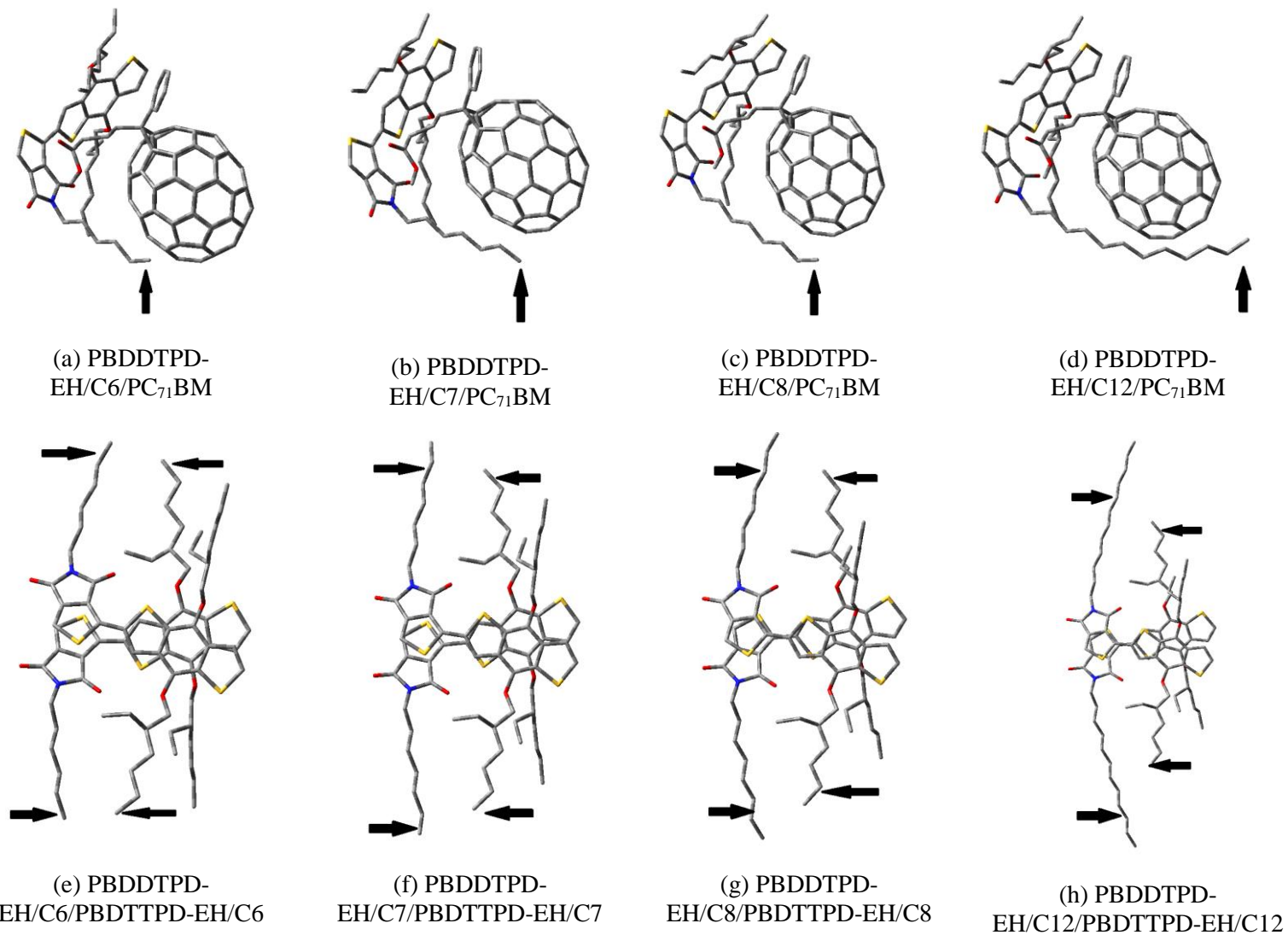


Figure 6.7: The optimized geometries of pairs containing PBDDTPD with C6, C7, C8, and C12 side chains.

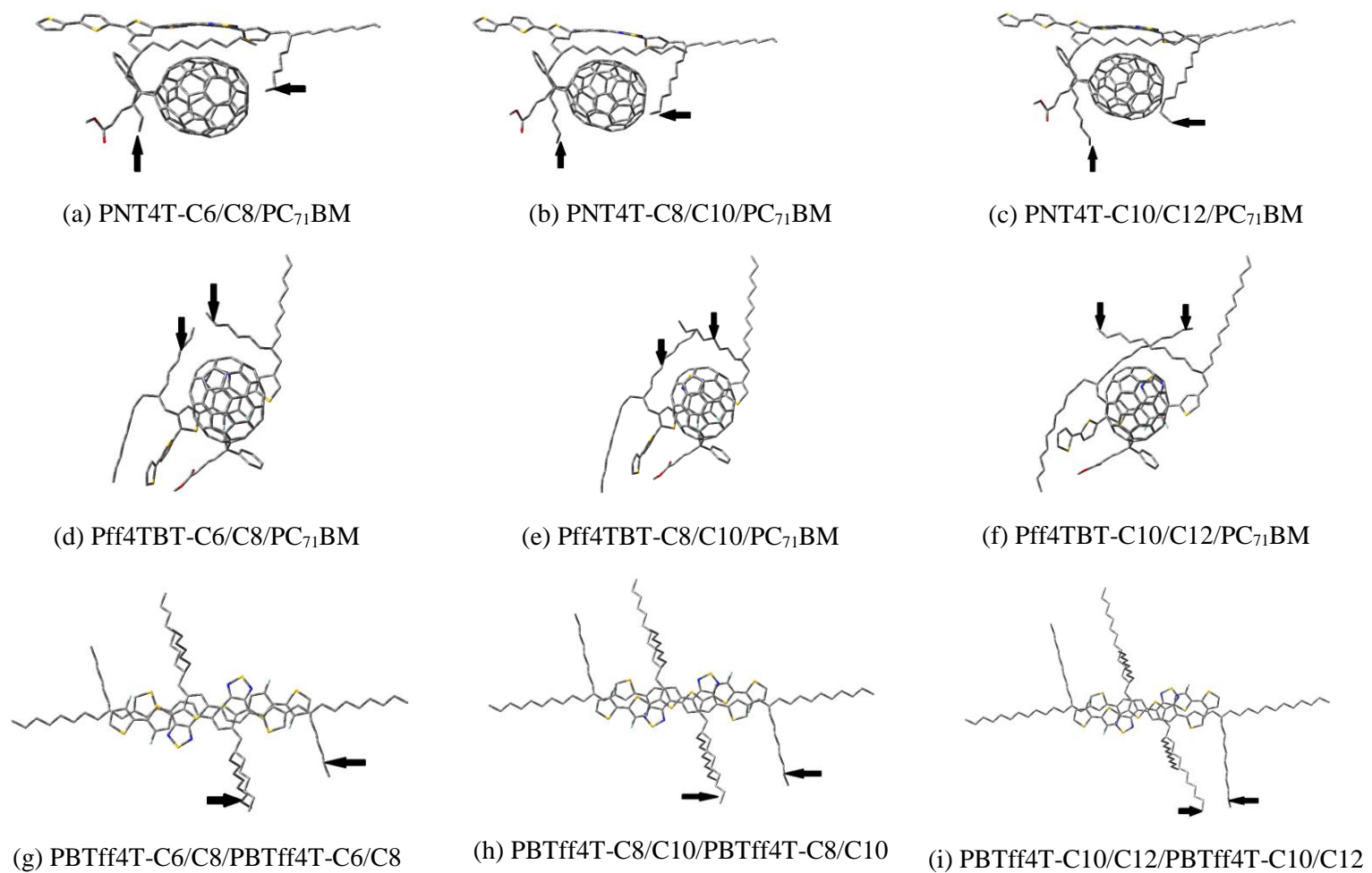


Figure 6.8: The optimized geometries of (a-f) the heterogenous and (g-i) homogenous pairs containing PNT4T, PBTff4T, and Pff4TBT with C6/C8, C8/C10, and C10/C12 side chains.

### 6.3.3 Varying the Type of Side Chains

To examine the effect of varying the type of side chains on monomer/fullerene interactions, we calculate the binding energies of homogenous and heterogenous pairs including monomers of the same type with all-linear ( $n_B=0$ ), linear-and-branched ( $n_B=1$ ), and all-branched ( $n_B=2$ ) side chains (see Figure 6.9 and Table D2 in Appendix D). Similar to the previous subsection 6.3.2, the results show that  $\Delta E_b$ 's are significantly affected by varying the type of side chains. Different trends in  $\Delta E_b$  are observed when length and type of side chains are varied. The results of Figure 6.9 reveal that the  $\Delta E_b$ 's are generally decreased with increasing the number of branches ( $n_B$ ) within monomers of the same type. This means that all-linear side chains lead to highest values of  $\Delta E_b$ , linear-and-branched side chains lead to intermediate values of  $\Delta E_b$ , and all-branched side chains lead to lowest values of  $\Delta E_b$ . This trend in  $\Delta E_b$  is consistent for the majority of heterogenous and homogeneous pairs involving P3HT, PBDTTPD, and PTB7 monomers.

For pairs including P3HT monomers, three P3HT derivatives are considered by varying the type of side chains from all-linear ( $n_B=0$ ) in P3HT to linear-and-branched ( $n_B=1$ ) in P3HT-*co*-EHT, and to all-branched ( $n_B=2$ ) in P3EHT. As we noted above, the  $\Delta E_b$  of most pairs decreases with increasing  $n_B$  (see results in Figure 6.9 (a)). For example, as the homogenous pair changes from P3HT/P3HT to P3EHT/P3EHT,  $\Delta E_b$  decreases from 1.1 to 0.9 eV with increasing  $n_B$  from 0 to 2, respectively. The optimized geometries of P3HT/fullerenes illustrate that increasing the number of branched side chains places the monomers away from the sides of fullerenes (see examples of P3HT/PCBM in Figure 6.10). Hence, all-branched side chains lead to the least favorable P3EHT/fullerene

interactions while all-linear side chains lead to the optimal P3HT/fullerene interactions. This result is in good agreement with literature which shows that the hexyl side chains are the optimal side chains for P3HTs. [13, 28] One notable exception in the results is the pairing of P3HT-*co*-EHT and PCBM which exhibits somewhat higher  $\Delta E_b$  compared to P3HT/PCBM. This is possibly due to the interaction between this monomer and the side group of the fullerene (see Figure 6.10 (b)). It can be said that the  $\Delta E_b$ 's of pairs that include P3HT and PCBM correlate well with the experimental PCEs as reported by Burkhart et al. [29] (see Figure 6.9 (a)). These results imply that the higher the  $\Delta E_b$  corresponds to the higher PCE when type of side chains is varied for a monomer such as P3HT.

For pairs including PBDTTPD, the relationship between  $\Delta E_b$  and  $n_B$  is illustrated in Figure 6.9 (b) for varying the type of side chains (from all-linear to all-branched). Unlike P3HT, branched side chains do not move the PBDTTPD away from the sides of fullerenes (see optimized geometries in Figure 6.11 (g-i)). As shown in Figure 6.11, due to the steric interactions, the optimized geometries of gas phase and interacting PBDTTPD show that linear side chains tend to be more attractive and branched side chains tend to be more repulsive. For example, in a pairing of PC<sub>71</sub>BM and PBDTTPD, all-linear side chains (C12/C8) are attracted to fullerene, in the half linear half branched side chains monomer the (C8) linear side chain of acceptor (TPD) motif is attracted to fullerene while the (EH) branched side chain of donor (BDT) motif is repulsed by fullerene, and all-branched side chains (2EH/EH) are mostly more away from fullerene. As mentioned in the Introduction, it has been suggested in literature that high performing OSC materials should be designed

with the acceptor unit of polymer being more sterically accessible and the donor unit being more sterically hindered. [5] This condition is clearly fulfilled with the linear-and-branched side chains of PBDTTPD, hence (EH/C8) are the favorable side chains and the resulting monomer/fullerene interaction is the optimal one for higher PCEs. In contrast, all-linear side chains (C12/C8) do not satisfy the condition for high performing OSC materials because C12 linear side chains of donor (BDT) motif are interfering with the interaction between fullerene and acceptor (TPD) motif (see again the optimized geometries in Figure 6.11 (g)). In this case, the highest  $\Delta E_b$  of pairs that contain PBDTTPD with C12/C8 side chains do not indicate highest PCE because the increase in  $\Delta E_b$  is mainly due to the strong interaction of all-linear side chains and structural arrangement of monomer versus fullerene must also be considered. In addition, the presence of C12/C8 side chains lowers the  $\Delta E_b$  of PBDTTPD/fullerene relative to PBDTTPD/PBDTTPD, hence, making the interactions between PBDTTPD and fullerenes less favorable. These results also explain as to why the all-linear side chains in the donor and acceptor motifs of PBDTTPD resulted in a dramatic drop of PCE of about 3%. [10] The low experimental PCE value for pairs involving PBDTTPD with all-branched side chains (2EH/EH) are also correlated well with the lowest  $\Delta E_b$ 's. Therefore, our results, which are in good agreement with literature, indicate that the optimal arrangement of the monomer/fullerene with the relatively high value of  $\Delta E_b$  are significant factors to consider when choosing the favorable acceptor-donor polymers in combination with fullerenes in OSCs.

For pairs containing PTB monomers, the results of varying the type of side chains confirm again that increasing the branched side chains generally decreases the  $\Delta E_b$  of

homogenous and heterogenous pairs (see Figure 6.9 (c)). Figure 6.12 (a-c) illustrates the optimized geometries of PTB monomers in gas phase with various types of side chains. For the homogenous pairs, the optimized geometries show that the all-linear side chains of one PTB1 are attracted toward the all-linear side chains of the other PTB1 in a given pair, whereas the linear side chains of the acceptor motif of one PTB4 are more distant from the branched side chains of the donor motif of the other monomer (see Figure 6.12 (d-f)). This indicates that, for a given PTB/PTB pair, the linear side chains of one monomer are more attracted and the branched side chains of one monomer are more repulsed by the respective side chains of the other monomer. Therefore, as expected, the PTB7/PTB7 with all-branched side chains exhibit the lowest  $\Delta E_b$  among other pairs. For the heterogenous pairs, the optimized geometries show that no interference was found by (any type) of side chains that could make monomers' acceptor units less accessible to fullerenes (see again Figure 6.12 (g-i)). This is mainly because the side chains of a PTB monomer tend to move away from each other. This result agrees with Graham et al. [5] who stated that PTB are exceptional from the donor-acceptor polymers because of the ester group that is making the side chains more distant from the conjugated backbone, hence, even with the all-branched side chains of PTB7, acceptor unit remains relatively accessible to fullerene. The optimized geometries show also that the C8/C10 linear side chains of PTB1 are exceeding the lengths of fullerene (see Figure 6.12 (h)). The excessive length of linear side chains in PTB1 lead to unfavorable interaction with lower  $\Delta E_b$ 's of PTB1/fullerene relative to the  $\Delta E_b$  of PTB1/PTB, and thus lower PCE. In addition, the all-branched side chains of PTB7, which are interacting with the least lengths of fullerene and hence lead to lowest  $\Delta E_b$ , are also unfavorable for the monomer/fullerene interaction. Although highest PCE was found

by PTB7/PC<sub>71</sub>BM pair, the low stability of pairs containing PTB7 agree with the reports that state that PTB7 suffers from certain limitations and it is sensitive to the choice of fullerene, meaning that PCEs are very low when PTB7 is combined with PCBM. [3, 5] In contrast, the optimized geometries of pairs containing PTB4 indicate that linear-and-branched side chains are the optimal ones because the C8 linear side chains of acceptor motif are interacting well with the full length of fullerene (see Figure 6.12 (h)). The relatively high  $\Delta E_b$  of pairs containing PTB4 with favorable interfacial properties correlate well with the PCE of PTB4/PCBM pair of about 6.1-7.1% which is considered to be relatively high. Therefore, PTB4 with different types of fullerenes can be a good candidate for improving the performance of OSCs.

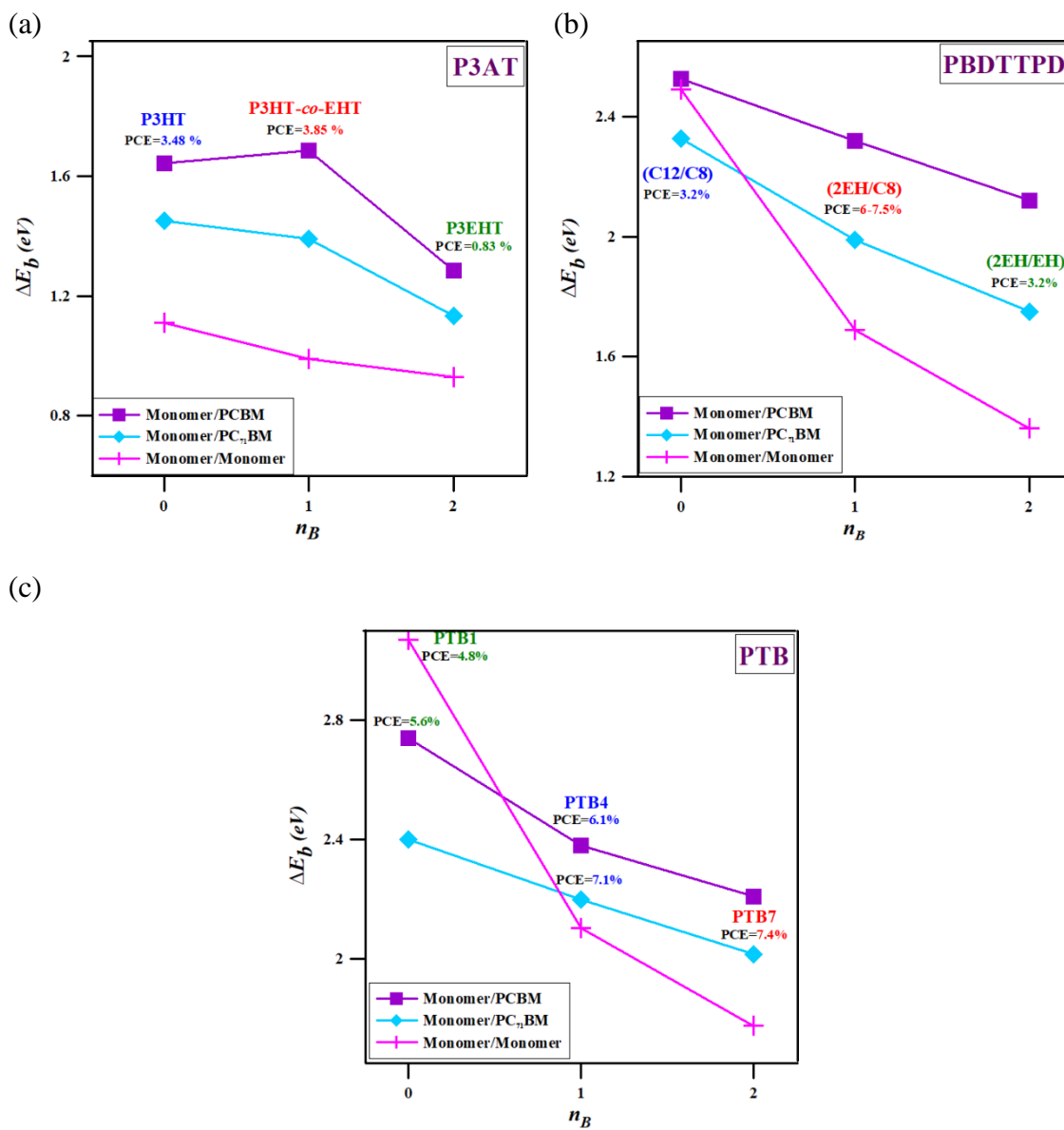
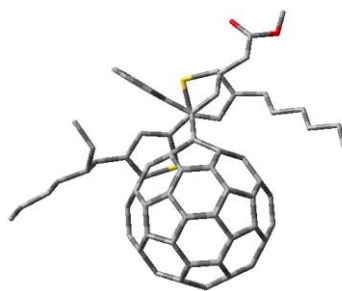


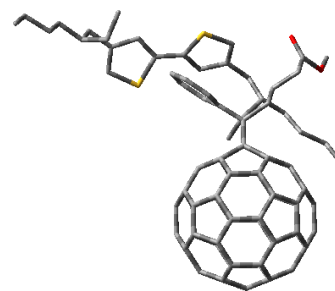
Figure 6.9: Binding energies of heterogenous and homogenous pairs containing (a) P3HT, (b) PBDTTPD, and (c) PTB7 versus  $n_B=0$  (all-linear),  $n_B=1$  (linear-and-branched), and  $n_B=2$  (all-branched) side chains.



(a) P3HT/PCBM



(b) P3HT-*co*-EHT/PCBM



(c) P3EHT/PCBM

Figure 6.10: The optimized geometries of heterogenous pairs containing P3HT with varying the number of branches in side chains from  $n_B=0$  to 2.

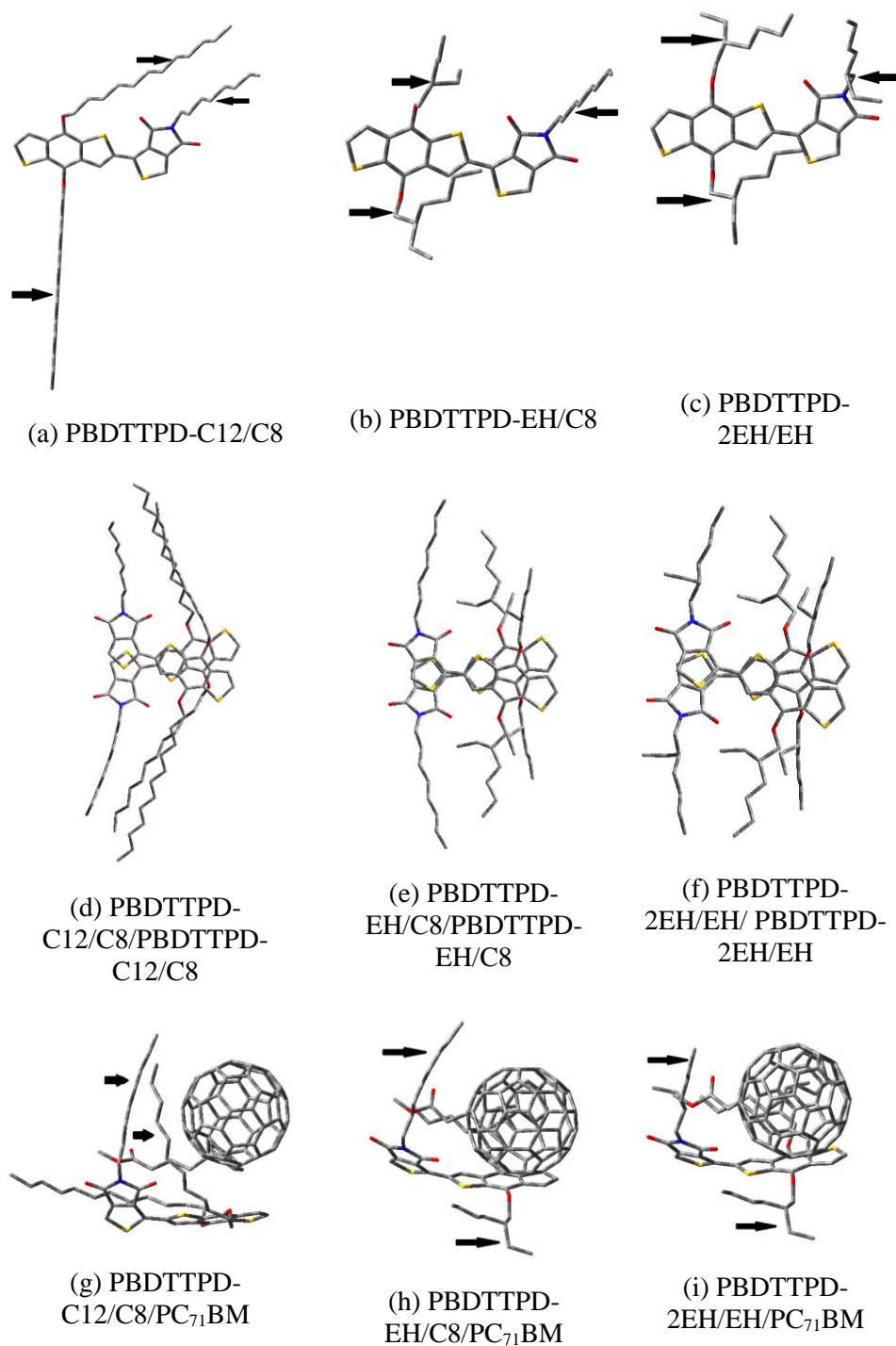


Figure 6.11: The optimized geometries of (a-c) the gas phase PBDTTPD and (d-f) homogenous and (g-i) heterogenous pairs containing PBDTTPD with C12/C8, EH/C8, and 2EH/EH side chains.

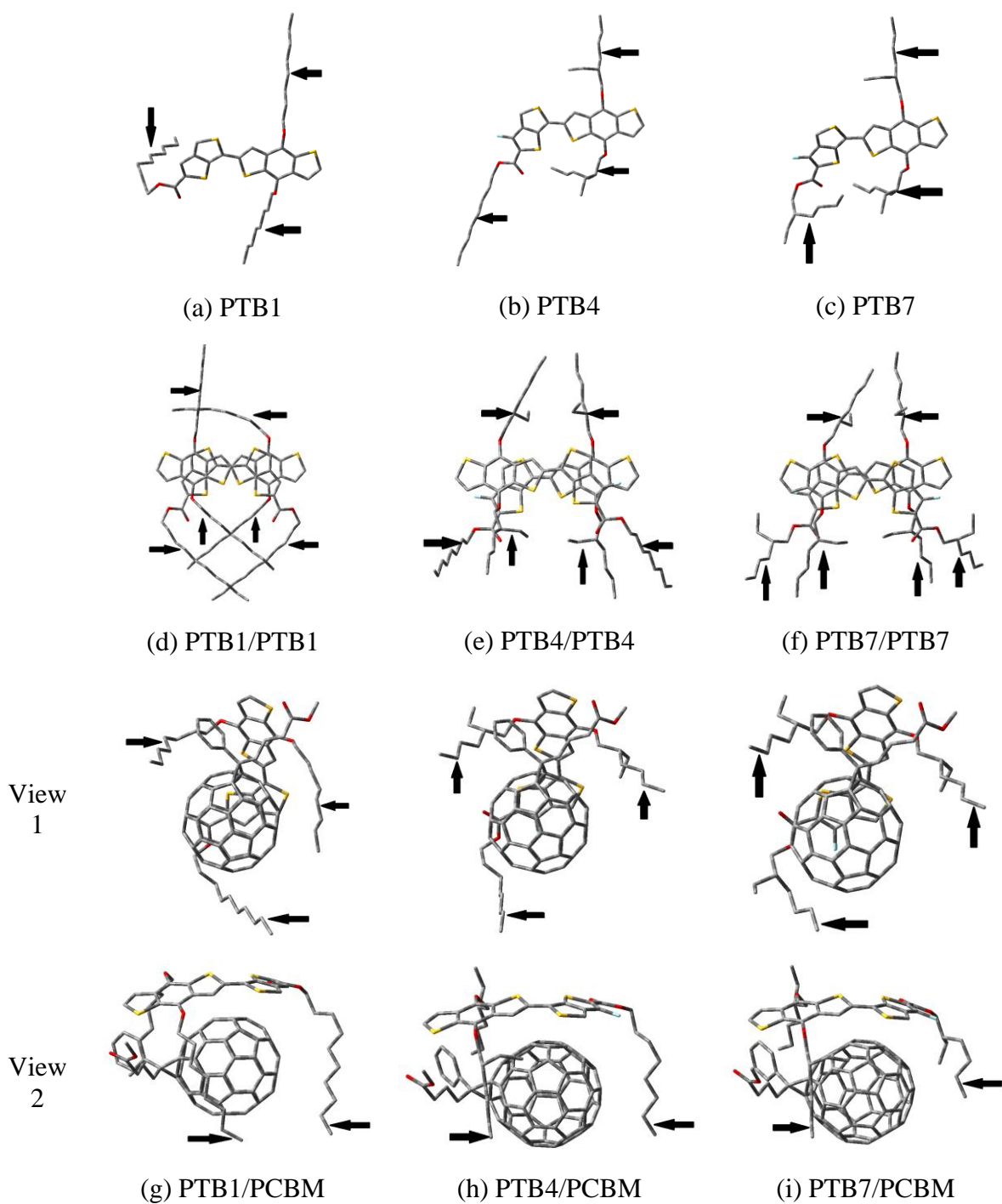


Figure 6.12: The optimized geometries of (a) the gas phase PTB and (b) homogenous and (c) heterogenous pairs containing PTB with C10/C8, EH/C8, and 2EH/EH side chains.

### 6.3.4 Branching Positions of Branched Side Chains

In this subsection, we consider three monomers with branched side chains only. We set the length of their side chains to C8/C10. The side chains of each monomer are branched at different branching positions ( $P_B$ 's): 1, 2, and 3. It was found recently that devices including these three polymers with  $P_B=2$  gave the highest PCEs that range from 9.6 to 10.5 %. [3] To understand why this particular branching position is favorable for monomer/fullerene interfaces, we calculate the  $\Delta E_b$ 's of heterogenous and homogenous pairs containing PNT4T, PBTff4T, and Pff4TBT with varying the  $P_B$  of side chains (see Figure 6.13 and Table D3 in Appendix D). The results for most of heterogenous pairs (see Figure 6.13) show that as  $P_B$  changes from 1 to 3, the  $\Delta E_b$  increases from 1 to 2, and then decreases from 2 to 3. For example, when monomer changes from Pff4TBT-1ON to Pff4TBT-2OD, and then to Pff4TBT-3OT, the  $\Delta E_b$  of Pff4TBT/PCBM increases from 2.1 to 2.5 and then decreases to 2.2 eV respectively. In most cases, the highest  $\Delta E_b$ 's were found for pairs including PNT4T-2OD, PBTff4T-2OD, and Pff4TBT-2OD (i.e. with  $P_B=2$ ). Moreover, the optimized geometries of monomer/fullerene pairs (see examples in Figure 6.14 (a-c)) show that  $P_B=2$  tends to bring side chains closer to fullerenes relative to side chains with  $P_B=1$  or 3. Another notable feature of monomers with  $P_B=2$  is that side chains that are not interacting with fullerenes are aligned more or less along the monomer backbone whereas those with  $P_B=1$  or 3 are structurally oriented in random directions or away from monomers (see Figure 6.14 (d-f)). These observations indicate that our results are in very good agreement with experimental findings in that position 2 is the best branching position of side chains for branched monomers. [3]

In contrast to the results of heterogenous pairs, the branched side chains in homogenous pairs behave differently as a function of the branching positions (see Table D3 in Appendix D). The results of homogenous pairs show that  $\Delta E_b$ 's are reduced for monomers with  $P_B=2$  side chains. This reduction can be understood when optimized geometries (see examples of PNT4T/PNT4T in Figure 6.14 (g-i)) are considered. It seems that  $P_B=2$  branching position tends to make the branched side chains of one monomer more distant from those of other monomer and hence increasing the interaction between the backbones of monomers (see Figure 6.14 (h)). Stronger interaction between the backbones is preferable for enhancing the charge transport. The  $\Delta E_b$ 's of pairs containing monomers with  $P_B=1$  and 3 are higher due to the larger interactions between the side chains of the monomers (see Figure 6.14 (g) and (i)). This increases the possibility that these side chains will interfere with the monomers' backbones interactions and hence decrease the PCEs. Moreover, unlike  $P_B=1$  and 3,  $P_B=2$  branching position tends to lower the  $\Delta E_b$ 's of homogenous pairs, leading to most favorable monomer/fullerene interactions. Therefore, in addition to the highest  $\Delta E_b$ 's and PCEs of monomer-2OD/fullerene pairs due to  $P_B=2$ , the second branching position leads to the most favorable monomer/monomer interfaces and hence optimizing the overall device performance.

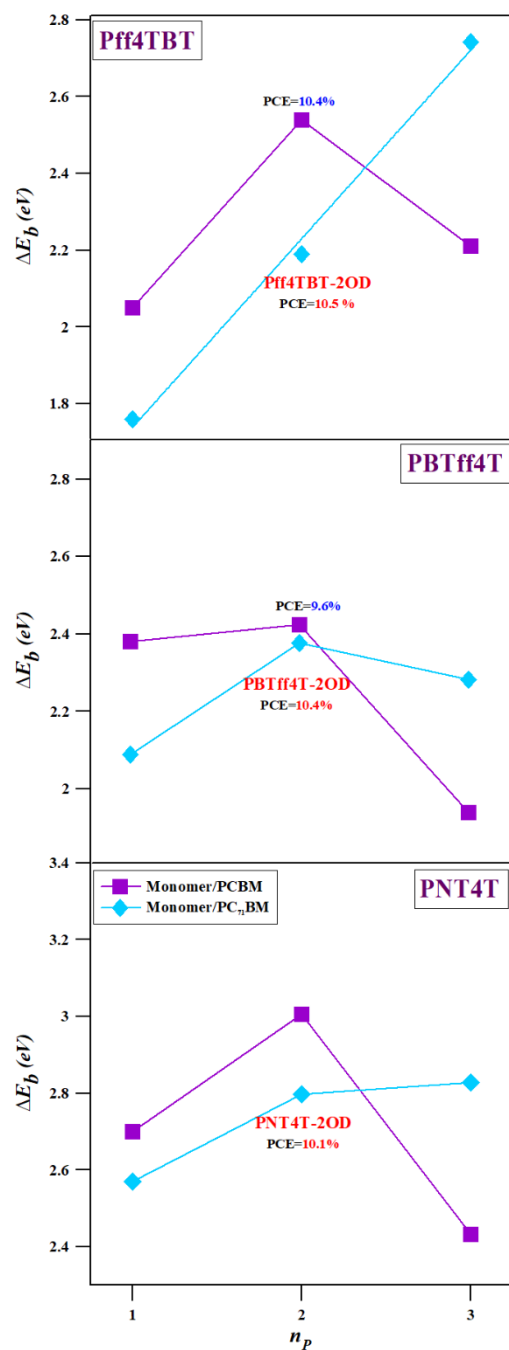


Figure 6.13: Binding energies of heterogenous pairs containing Pff4TBT, PBTff4T, and PNT4T with varying the branching position of branched side chains from  $P_B=1$  to 3.

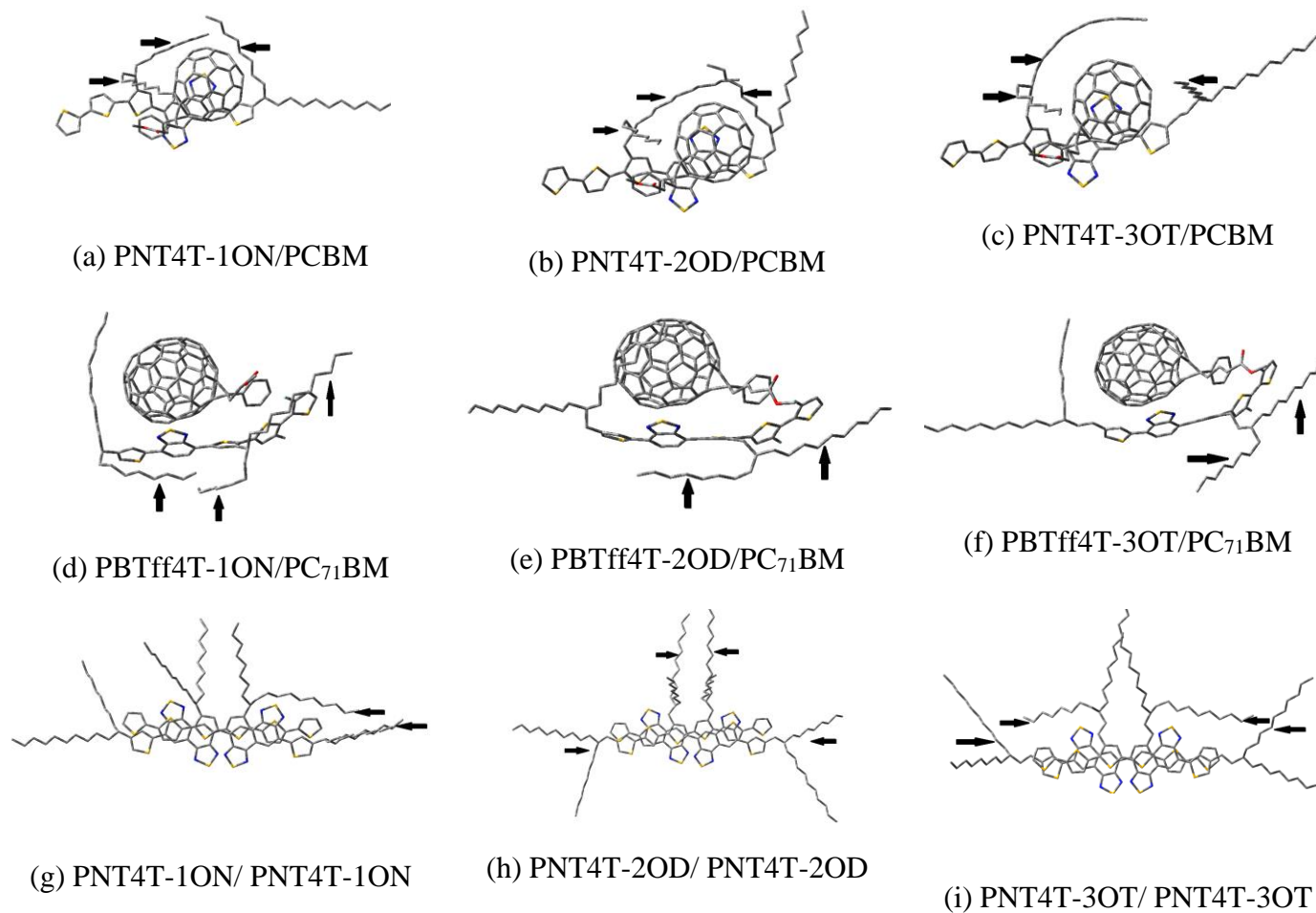


Figure 6.14: The optimized geometries of (a-f) heterogenous pairs containing PNT4T and PBTff4T, and (g-i) homogenous pairs containing PNT4T with various branching positions of side chains,  $P_B=1$  (1ON),  $P_B=2$  (2OD), and  $P_B=3$  (3OT).

## 6.3.5 Energy Levels of Monomers with Side Chains

In previous subsections, we showed that the side chains of monomers play an important role in monomer/fullerene interactions. In particular, we obtained different trends of  $\Delta E_b$ 's depending on the length, type, and branching position of side chains. What about the trends of electronic properties? It is known that the knowledge of energy levels of polymers and fullerenes is essential for the device performance of OSCs. However, side chains are generally shortened or replaced by hydrogen atoms in computational studies due to the negligible effect of side chains on the electronic structures of conjugated materials. In our previous work [21], we determined that low monomer's  $E_g$  (of the order of 2 eV), the lowest  $\Delta\epsilon_{LUMO}$ , and the highest  $(\Delta\epsilon_{H_D-L_A} - 0.3)/E_{g(monomer)}$  are the optimal electronic properties that can lead to achieving the highest experimental PCE in polymer/fullerene OSCs. It is worthwhile to determine if similar trends can be obtained when various lengths, types, and branching positions of side chains are used in monomers. Hence, in this subsection, we compare electronic structures of monomers with short/no side chains (referred to as without side chains) as obtained in previous work with those of different types and lengths of side chains (referred to as with side chains and marked in red in Scheme 6.1). We also calculate the SP B3LYP energy levels using B97-D3 and B3LYP-D3 optimized geometries of interacting monomers with both types of fullerenes and with various lengths, types, and branching positions of side chains (see Figure 6.17 for the B97-D3 results). In addition, we calculate the electronic offsets using the B97-D3 and B3LYP-

D3 interacting monomers and fullerenes as well as the B3LYP isolated monomers and fullerenes (see Table D4, D5, and D6 in Appendix D).

Figure 6.15 illustrates the energy levels of gas phase monomers with side chains and compares them to those without side chains as obtained in previous work. The results show that the side chains slightly increase the energy levels of short and medium-sized monomers (such as P3HT, PTB7, and PBDTTPD) relative to the energy levels of those without side chains. Also, HOMO levels of most long-sized monomers (such as PNT4T, PBTff4T, and Pff4TBT) with side chains are decreased slightly while LUMO levels remain the same compared to the HOMOs and LUMOs of those without side chains. Hence, the monomer energy levels are nearly independent of the presence or absence of side chains. In all cases, (with and without side chains), as the monomer length increases from P3HT to PNT4T, HOMO level increases and LUMO level decreases.

The results displayed in Figure 6.16 show that the energy levels of each monomer are not largely affected by varying the length, type, or branching position of the side chains. In some cases, slight changes were obtained in the HOMO and/or LUMO levels due to included in the geometries of interacting monomers. For example, for the various lengths and branching positions of side chains in Pff4TBT, monomers interacting with larger fullerenes exhibit slightly higher energy levels relative to those interacting with smaller fullerenes. In addition, unlike the binding energy results, the electronic offsets (calculated in Table D4, D5, and D6 in Appendix D) show no significant changes for different side chains. In fact, the electronic offsets between the majority of monomers and fullerenes are almost identical for the various lengths, types, and branching positions of side chains.

Based on the above results, it is expected that the electronic property trends that we obtained in a previous work, can be reproduced with monomers with different side chains. To confirm this, we reproduced a plot from the previous work for the ratio of  $(\Delta\epsilon_{H-L} - 0.3)/E_{g(monomer)}$  of gas phase monomers with side chains (that are marked in red in Scheme 6.1) and fullerenes versus  $E_{g(monomer)}$  (see Figure 6.17). The results show that maximizing this ratio is important for increasing PCE, confirming that both short and long side chains exhibit similar electronic properties trend for various monomers and fullerenes. This indicates that accurate electronic property trends can be obtained computationally for various monomer/fullerene pairs, regardless of the length and type of side chains.

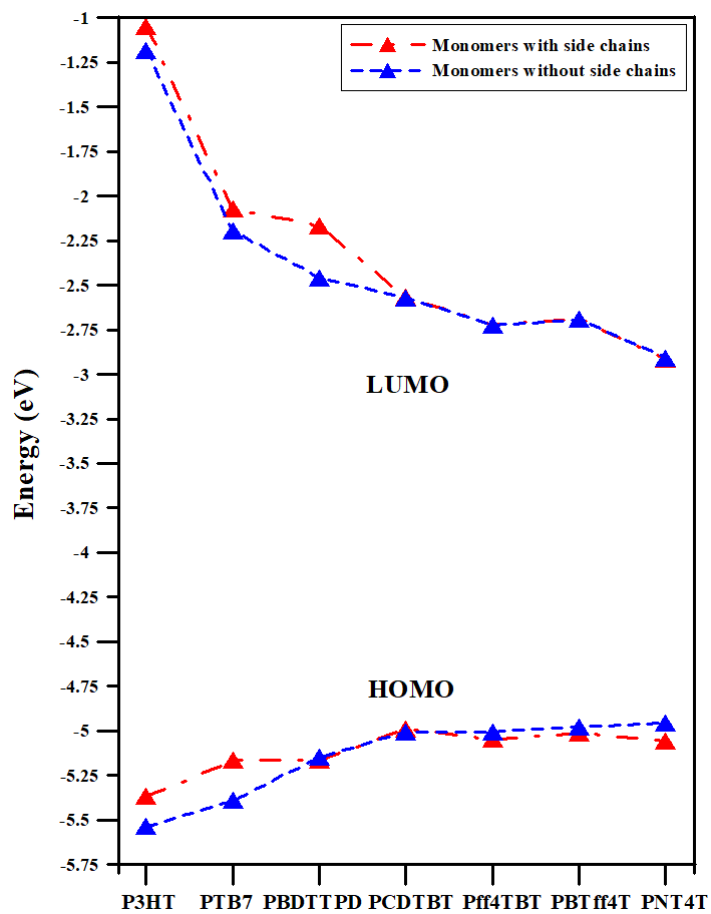
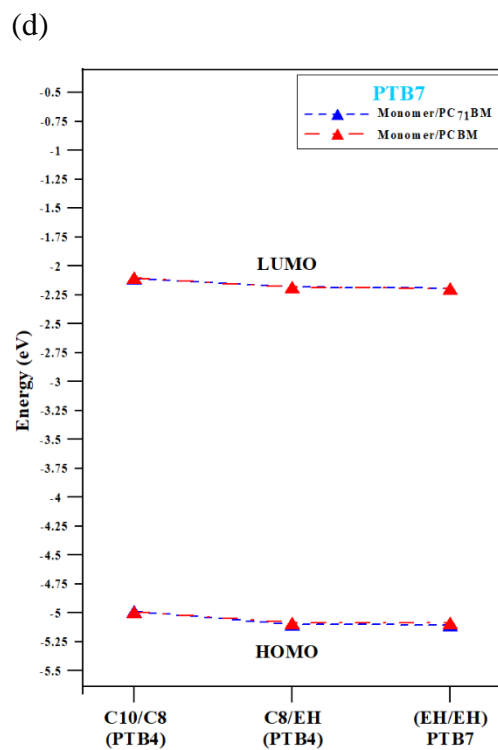
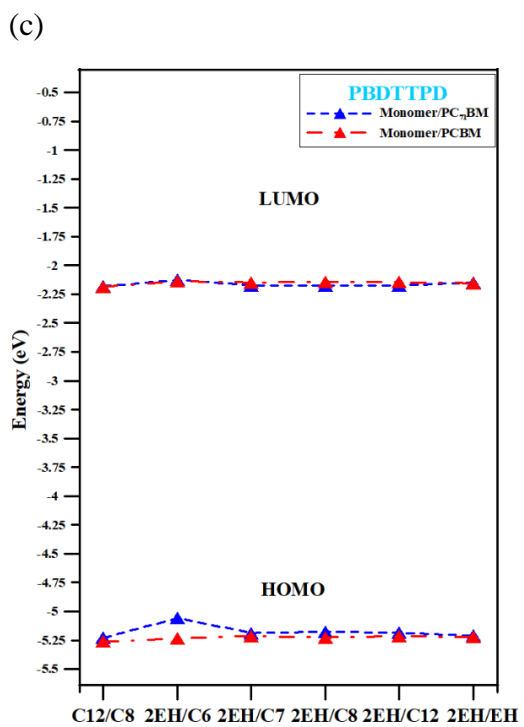
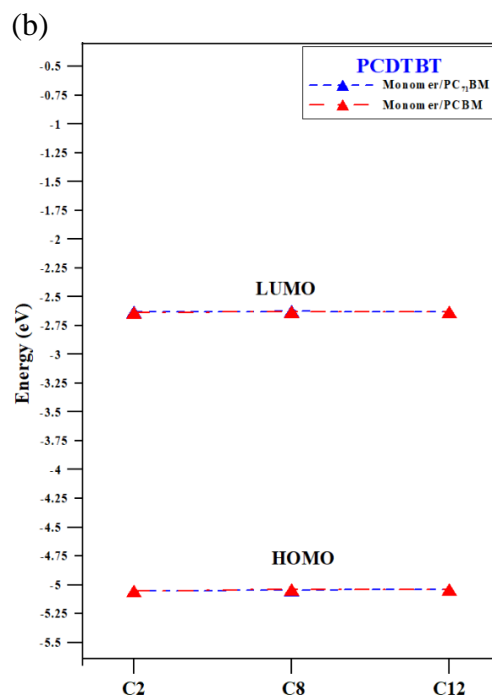
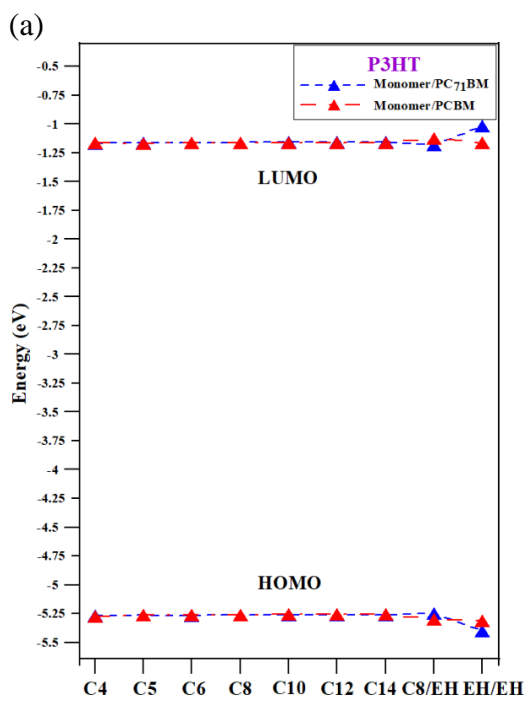


Figure 6.15: Energy levels of gas phase monomers with and without side chains calculated at the B3LYP method.



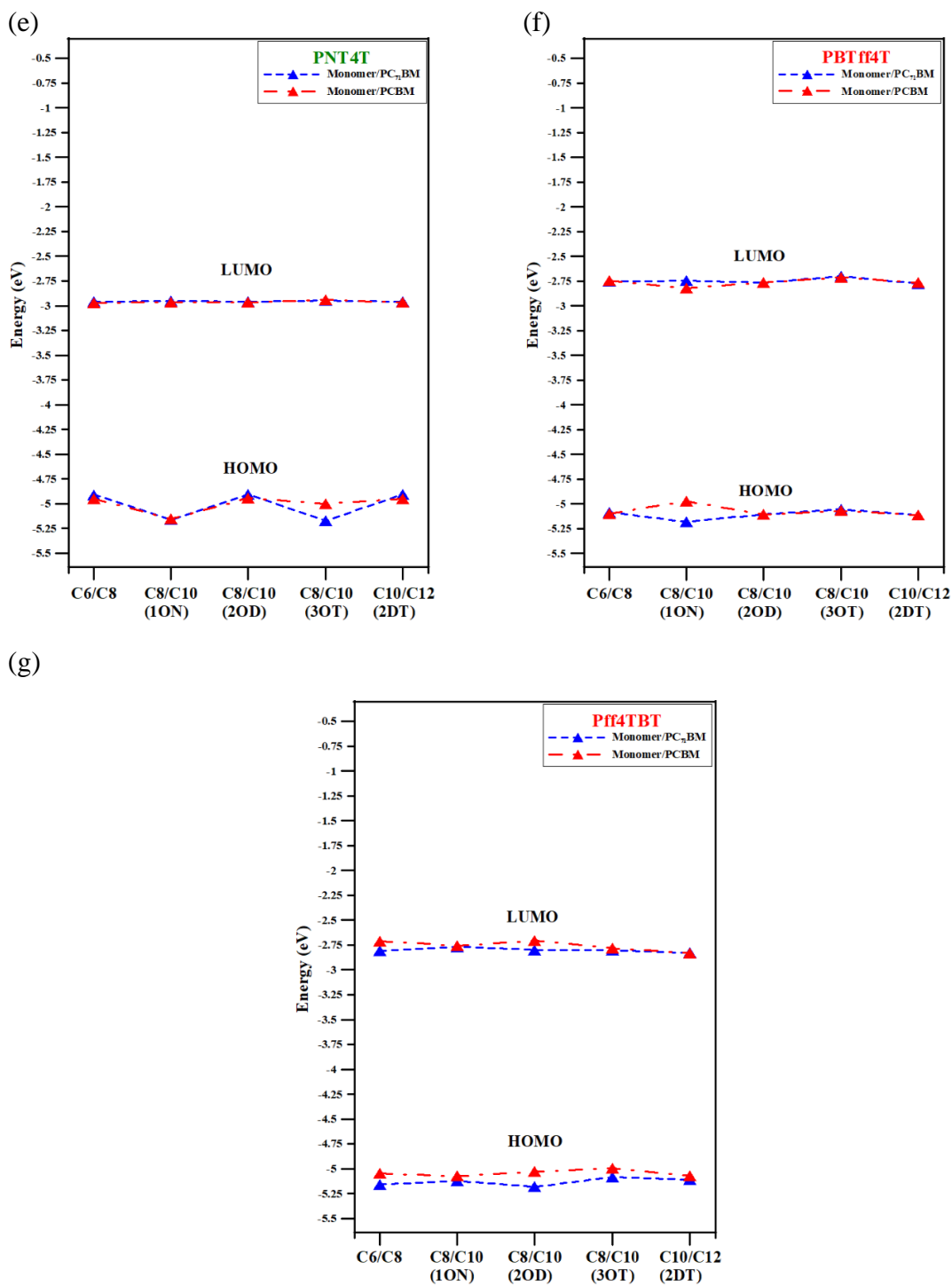


Figure 6.16: The energy levels of interacting (a) P3HT, (b) PCDTBT, (c) PBDTTPD, (d) PTB7, (e) PNT4T, (f) PBTff4T, and (g) Pff4TBT with various side chains, and with two types of fullerenes, calculated at the SP B3LYP using the B97-D3 optimized geometries.

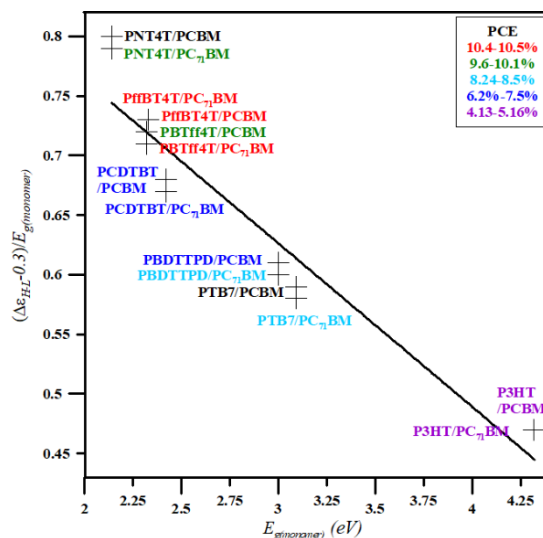


Figure 6.17: A reproduced figure from the previous work of the ratio  $(\Delta\epsilon_{HD-LA} - 0.3)/E_{g(mon)}$  using gas phase monomers with side chains (marked in red in Scheme 6.1) and fullerenes (optimized at the B3LYP method), versus the respective monomers'  $E_g$ 's.

## 6.4 Conclusions

In this work, we have investigated the role of length, type, and branching positions of side chains on the binding energies of various homogenous and heterogenous pairings of monomers and fullerenes using the dispersion corrected B97-D3 and B3LYP-D3 methods. We have found that the  $\Delta E_b$ 's are correlated with the monomer's chain lengths and corresponding experimental PCEs. We have also found that the alkyl side chains play a major role on the  $\Delta E_b$ 's and the structural arrangements of the combinations. In particular, we have determined the following  $\Delta E_b$ 's trends that are, for most cases, in good agreement with the experimental PCEs:

- 1- For monomers (such as P3HT, PCDTBT, PBDTTPD, PBTff4T, Pff4TBT, and PNT4T) with various lengths of side chains in a given pair, the length of side-chains is linearly correlated with  $\Delta E_b$ 's, however, there is an optimal value for the  $\Delta E_b$ ;
- 2- For monomers (such P3HT, PBDTTPD, and PTB7) with various types of side chains in a given pair, the number of branched side-chains is inversely correlated with  $\Delta E_b$ 's;
- 3- For monomers (PBTff4T, Pff4TBT, and PNT4T) with various branching positions of branched side chains in a given heterogenous pair: in most cases,  $\Delta E_b$  peaked at branching position  $P_B=2$ .

In addition to the  $\Delta E_b$ 's trends, we have found that the structural properties of monomer/fullerene and monomer/monomer interactions are important in determining the optimal side chains arrangement for improved PCEs of OSCs. The excessive length of side chains that exceed the dimension of the fullerenes are particularly not favorable for the monomer/fullerene interactions. In general, alkyl side chains that interact with the full length of fullerenes lead to the optimal  $\Delta E_b$ 's, and PCEs. Our results also agree with experimental studies that favor the linear-and-branched side chains in acceptor-donor monomers. Finally, no significant changes were found in electronic properties of monomer/fullerene combinations when monomer side chains were varied. This study provides important insight for selecting the proper polymer side chains to enhance the PCEs of OSCs.

# Bibliography

- [1] K.A. Mazzi, C.K. Luscombe, *The Future of Organic Photovoltaics*, Chemical Society Reviews 44 (2015) 78-90.
- [2] K.R. Graham, C. Cabanetos, J.P. Jahnke, M.N. Idso, A. El Labban, G.O.N. Ndjawa, T. Heumueller, K. Vandewal, A. Salleo, B.F. Chmelka, A. Amassian, P.M. Beaujuge, M.D. McGehee, *Importance of the Donor:Fullerene Intermolecular Arrangement for High-Efficiency Organic Photovoltaics*, Journal of the American Chemical Society 136 (2014) 9608-9618.
- [3] Y.H. Liu, J.B. Zhao, Z.K. Li, C. Mu, W. Ma, H.W. Hu, K. Jiang, H.R. Lin, H. Ade, H. Yan, *Aggregation and Morphology Control Enables Multiple Cases of High-Efficiency Polymer Solar Cells*, Nature Communications 5 (2014) 5293.
- [4] B. Carsten, J.M. Szarko, H.J. Son, W. Wang, L.Y. Lu, F. He, B.S. Rolczynski, S.J. Lou, L.X. Chen, L.P. Yu, *Examining the Effect of the Dipole Moment on Charge Separation in Donor-Acceptor Polymers for Organic Photovoltaic Applications*, Journal of the American Chemical Society 133 (2011) 20468-20475.
- [5] B. Carsten, J.M. Szarko, L.Y. Lu, H.J. Son, F. He, Y.Y. Botros, L.X. Chen, L.P. Yu, *Mediating Solar Cell Performance by Controlling the Internal Dipole Change in Organic Photovoltaic Polymers*, Macromolecules 45 (2012) 6390-6395.
- [6] Y.X. Li, J.Y. Zou, H.L. Yip, C.Z. Li, Y. Zhang, C.C. Chueh, J. Intemann, Y.X. Xu, P.W. Liang, Y. Chen, A.K.Y. Jen, *Side-Chain Effect on Cyclopentadithiophene/Fluorobenzothiadiazole-Based Low Band Gap Polymers and Their Applications for Polymer Solar Cells*, Macromolecules 46 (2013) 5497-5503.
- [7] X.G. Guo, N.J. Zhou, S.J. Lou, J.W. Hennek, R.P. Ortiz, M.R. Butler, P.L.T. Boudreault, J. Strzalka, P.O. Morin, M. Leclerc, J.T.L. Navarrete, M.A. Ratner, L.X. Chen, R.P.H. Chang, A. Facchetti, T.J. Marks, *Bithiopheneimide-Dithienosilole/Dithienogermole Copolymers for Efficient Solar Cells: Information from Structure-Property-Device Performance Correlations and Comparison to Thieno 3,4-C Pyrrole-4,6-Dione Analogues*, Journal of the American Chemical Society 134 (2012) 18427-18439.
- [8] C. Cabanetos, A. El Labban, J.A. Bartelt, J.D. Douglas, W.R. Mateker, J.M.J. Frechet, M.D. McGehee, P.M. Beaujuge, *Linear Side Chains in Benzo 1,2-B:4,5-B' Dithiophene-Thieno 3,4-C Pyrrole-4,6-Dione Polymers Direct Self-Assembly and Solar Cell Performance*, Journal of the American Chemical Society 135 (2013) 4656-4659.
- [9] Y.Y. Liang, D.Q. Feng, Y. Wu, S.T. Tsai, G. Li, C. Ray, L.P. Yu, *Highly Efficient Solar Cell Polymers Developed Via Fine-Tuning of Structural and Electronic Properties*, Journal of the American Chemical Society 131 (2009) 7792-7799.
- [10] C. Piliago, T.W. Holcombe, J.D. Douglas, C.H. Woo, P.M. Beaujuge, J.M.J. Frechet, *Synthetic Control of Structural Order in N-Alkylthieno 3,4-C Pyrrole-4,6-Dione-Based Polymers for Efficient Solar Cells*, Journal of the American Chemical Society 132 (2010) 7595-7597.

- [11] P.M. Beaujuge, H.N. Tsao, M.R. Hansen, C.M. Amb, C. Risko, J. Subbiah, K.R. Choudhury, A. Mavrinskiy, W. Pisula, J.L. Bredas, F. So, K. Mullen, J.R. Reynolds, *Synthetic Principles Directing Charge Transport in Low-Band-Gap Dithienosilole-Benzothiadiazole Copolymers*, *Journal of the American Chemical Society* 134 (2012) 8944-8957.
- [12] A. Gadisa, W.D. Oosterbaan, K. Vandewal, J.C. Bolsee, S. Bertho, J. D'Haen, L. Lutsen, D. Vanderzande, J.V. Manca, *Effect of Alkyl Side-Chain Length on Photovoltaic Properties of Poly(3-Alkylthiophene)/PCBM Bulk Heterojunctions*, *Advanced Functional Materials* 19 (2009) 3300-3306.
- [13] M. Al-Ibrahim, H.K. Roth, M. Schroedner, A. Konkin, U. Zhokhavets, G. Gobsch, P. Scharff, S. Sensfuss, *The Influence of the Optoelectronic Properties of Poly(3-Alkylthiophenes) on the Device Parameters in Flexible Polymer Solar Cells*, *Organic Electronics* 6 (2005) 65-77.
- [14] D.M. Stevens, J.C. Speros, M.A. Hillmyer, C.D. Frisbie, *Relationship between Diode Saturation Current and Open Circuit Voltage in Poly(3-Alkylthiophene) Solar Cells as a Function of Device Architecture, Processing Conditions, and Alkyl Side Chain Length*, *Journal of Physical Chemistry C* 115 (2011) 20806-20816.
- [15] L.H. Nguyen, H. Hoppe, T. Erb, S. Gunes, G. Gobsch, N.S. Sariciftci, *Effects of Annealing on the Nanomorphology and Performance of Poly(Alkylthiophene): Fullerene Bulk-Heterojunction Solar Cells*, *Advanced Functional Materials* 17 (2007) 1071-1078.
- [16] I. Constantinou, T.H. Lai, E.D. Klump, S. Goswami, K.S. Schanze, F. So, *Effect of Polymer Side Chains on Charge Generation and Disorder in Pbdtpd Solar Cells*, *ACS Applied Materials & Interfaces* 7 (2015) 26999-27005.
- [17] L.Q. Yang, H.X. Zhou, W. You, *Quantitatively Analyzing the Influence of Side Chains on Photovoltaic Properties of Polymer-Fullerene Solar Cells*, *Journal of Physical Chemistry C* 114 (2010) 16793-16800.
- [18] W.W. Li, R.P. Qin, Y. Zhou, M. Andersson, F.H. Li, C. Zhang, B.S. Li, Z.P. Liu, Z.S. Bo, F.L. Zhang, *Tailoring Side Chains of Low Band Gap Polymers for High Efficiency Polymer Solar Cells*, *Polymer* 51 (2010) 3031-3038.
- [19] Z.C. He, C.M. Zhong, S.J. Su, M. Xu, H.B. Wu, Y. Cao, *Enhanced Power-Conversion Efficiency in Polymer Solar Cells Using an Inverted Device Structure*, *Nature Photonics* 6 (2012) 591-595.
- [20] S.A. Ayoub, J.B. Lagowski, *Optimizing the Performance of the Bulk Heterojunction Organic Solar Cells – Some General Guidelines Obtained from the DFT Investigation*, *Materials and Design* (2018).
- [21] S. Grimme, *Semiempirical GGA-Type Density Functional Constructed with a Long-Range Dispersion Correction*, *Journal of Computational Chemistry* 27 (2006) 1787-1799.
- [22] A.D. Becke, *Density-Functional Thermochemistry .3. The Role of Exact Exchange*, *Journal of Chemical Physics* 98 (1993) 5648-5652.
- [23] C.T. Lee, W.T. Yang, R.G. Parr, *Development of the Colle-Salvetti Correlation-Energy Formula into a Functional of the Electron-Density*, *Physical Review B* 37 (1988) 785-789.
- [24] G.W.T. M. J. Frisch, H. B. Schlegel, G. E. Scuseria, M. A. Robb, J. R. Cheeseman, G. Scalmani, V. Barone, G. A. Petersson, H. Nakatsuji, X. Li, M. Caricato, A. Marenich, J. Bloino, B. G. Janesko, R. Gomperts, et al., (2016).

- [25] L. Ling, J.B. Lagowski, *Electronic Band Structure of Alternating Fluorene-Oxadiazole Conjugated Copolymer - A 1D Solid-State DFT Study*, *Journal of Molecular Structure-Theochem* 944 (2010) 146-155.
- [26] L. Ling, J.B. Lagowski, *DFT Study of Electronic Band Structure of Alternating Triphenylamine-Fluorene Copolymers*, *Polymer* 54 (2013) 2535-2543.
- [27] B. Friedel, C.R. McNeill, N.C. Greenham, *Influence of Alkyl Side-Chain Length on the Performance of Poly(3-Alkylthiophene)/Polyfluorene All-Polymer Solar Cells*, *Chemistry of Materials* 22 (2010) 3389-3398.
- [28] B. Burkhart, P.P. Khlyabich, B.C. Thompson, *Influence of the Ethylhexyl Side-Chain Content on the Open-Circuit Voltage in Rr-Poly(3-Hexylthiophene-Co-3-(2-Ethylhexyl)Thiophene) Copolymers*, *Macromolecules* 45 (2012) 3740-3748.

# Chapter 7

## 7 Summary and Future Work

In this thesis, I present the results of our exploration, using the dispersion-corrected DFT (D-DFT) method(s), on various homogenous and heterogenous pairings at the interfacial regions of multilayer OLEDs and bulk heterojunction OSCs. Combinations studied in this thesis involve OxFn and TPAFn (n=1-3) monomers (see Scheme 3.1) for multilayer OLEDs, and seven monomers (P3HT, PCDTBT, PBDTTPD, PTB7, Pff4TBT, PBTff4T) and two fullerenes (PCBM, PC71BM) (see Scheme 5.1) for BHJ OSCs. The correlations between our computational results (using the dimer and monomer/fullerene approaches with D-DFT methods) and experimental device performances yield new insights about the interfacial and electronic properties of organic materials at heterogenous junctions as well as useful information for future design of high-performing devices. These results also illustrate that the DFT methods are reliable approaches that can be used to investigate the properties of non-covalently bonded organic conjugated semiconducting molecular complexes.

In studying the heterojunction properties of non-covalently bonded pairs used in OLEDs and OSCs, we employ:

- B97-D method to geometry optimize pairings of OxFn and TPAFn (n=1-3) monomers with short and long side chains (Chapter 3);
- B97-D3, B3LYP-D3, PBE1PBE-D3, and  $\omega$ B97x-D methods to geometry optimize pairings of seven monomers (P3HT, PCDTBT, PBDTTPD, PTB7, PNT4T, Pff4TBT, PBTff4T) with short side chains and two fullerenes (PCBM, PC71BM) (Chapter 4);
- B97-D3 and B3LYP-D3 methods to geometry optimize pairings of seven monomers with short (Chapter 5) and long side chains and two fullerenes (Chapter 4 and 6);
- B3LYP method to geometry optimize isolated monomers and fullerenes to generate their gas phase HOMO and LUMO eigenvalues and energy gaps (Chapter 3, 4, 5, and 6);
- B3LYP method on the D-DFT optimized geometries of isolated and interacting monomers and fullerenes in single point calculations to obtain their electronic structures (Chapter 3, 4, 5, and 6);
- TD-DFT/B3LYP on the optimized isolated (D-DFT and B3LYP) and interacting D-DFT geometries of monomers to obtain their absorption spectra and maximum absorption wavelengths (Chapter 4).

The accuracies of the four D-DFT methods mentioned above were assessed in Chapter 4 by calculating the binding energies and electronic and optical parameters of monomer/fullerene pairs. Our results indicate that single point B3LYP calculations on D-DFT geometries should be performed in order to obtain accurate electronic and absorption

results. We select B97-D3 and B3LYP-D3 methods as the most favorable D-DFT methods for polymer and fullerene combinations because: 1- B97-D3 method is the least computationally intensive however its binding energy trend is similar to the B3LYP-D3 method which are also comparable to other D-DFT methods, 2- they yield (relative to experimental values) the most accurate electronic and absorption results, and 3- they provide consistent trends for the results of short and long side chain monomers. Therefore, we use both methods for further investigations in Chapter 5 and 6.

Common observations can be made about our results obtained in Chapter 3, 4, 5, and 6. we note that these observations are found for many different combinations, hence, we believe that they can be generalized to other organic systems in heterojunction devices as follows,

- The differences between energy levels of dimers or monomers and fullerenes (such as  $\Delta$ LUMO and  $\Delta$ HOMO offsets) display useful electronic-property trends that can be correlated well with the device performance;
- Structural properties of combinations such as monomers' chain lengths and orientations of compounds relative to each other are important factors in determining the device performance;
- The length and type of side chains are crucial in determining the magnitudes of binding energies;
- The length of side chains has a very small effect on the electronic structures of monomers.

In particular, we determined the interfacial factors that lead to the best device performance of OLEDs containing OxF3-TPAF2 pair in Chapter 3, and highest PCEs (over 10%) of OSCs containing PNT4T/, Pff4TBT/, and PBTff4T/fullerene pairs in Chapter 5. Pairings of OxF3 and TPAF2 monomers of copolymers exhibited the best device performance in OLED due to their best matching of monomers' chain lengths (without any additional monomer(s)) and between  $\Delta$ LUMO and  $\Delta$ HOMO, as well as their highest binding energy and closest intermolecular distance among all the combinations of OxFn and TPAFn (n=1-3) monomers. Combinations containing PNT4T, Pff4TBT, and PBTff4T monomers of copolymers exhibited highest PCEs in OSCs due to their lowest interfacial LUMO offset, largest ratio of  $V_{oc}$  (as determined by interfacial band gap) to monomer's energy gap, and relatively high binding energy which preferably should be comparable for all homogenous and heterogenous pairs for better miscibility. These optimal properties are found to be common characteristics not only between pairings including PNT4T, Pff4TBT, and PBTff4T monomers but also for other tested OSCs monomers with high PCEs.

In addition to the role of interfacial interactions of monomers and fullerenes, we demonstrate the role of alkyl side chains on binding energies and structural arrangements of OSC combinations. we find that the length, type, and branching positions of side chains play different roles in binding energies which correlate well with experimental PCEs. For example, binding energies of various pairs containing monomers (with different lengths, types, and branching positions of side chains): 1- have linear correlation with the number of carbon atoms along side chains, however, there is an optimal value for the binding energy, 2- have an inverse correlation with the number of branched side chains, and 3-

have a peak at the second-branching position of side chains, respectively. Moreover, we identify optimal side chain arrangement that leads to favorable intermolecular interactions (e.g. they should interact with the full length of the fullerenes without exceeding the dimension of them). Hence, the proper polymer's side chains can be selected using our computational strategy to enhance the PCEs of OSCs.

We find calculations of D-DFT binding energies useful for analyzing conformational structures and interfacial interactions of molecular combinations. For example, binding energy calculations can help us determine the most stable conformations (which are monomers located on the sides of fullerenes) for various of monomer/fullerene pairs. They are also useful to select favorable combinations for maximizing devices' efficiencies (as mentioned above). However, this is not always straightforward when the side chain effect is included in pairings of monomers and fullerenes. Therefore, we recommend not to use the highest or relatively high binding energies (alone) as an indicative factor for high device performance without considering other factors as well (such as optimal electronic and structural properties).

In the future we would like to investigate optical properties of pairings of monomer and fullerenes and the effect of the side chains on the absorptions using TD-DFT calculations. We plan to calculate maximum absorption wavelengths, excitation energies, and oscillator strengths of interacting monomers and fullerenes present in the interfacial region. We would like to see if these parameters are correlated with PCEs of OSCs to provide further guidance for selecting optimal OSC polymers. Because PC<sub>71</sub>BM OSCs have been used in literature more than PCBM [1] we aim to identify optical factors that

favor combinations involving PC<sub>71</sub>BM compared to those involving PCBM. In addition to the conjugated polymers and fullerenes, we would like to apply our computational strategy to other heterogenous systems such as those used in the hybrid organic-inorganic perovskite solar cells, which have recently achieved PCEs over 20%. [2] This new family of solar cells are based on methylammonium lead halide perovskite structures and pose remarkable advantages such as strong light absorption and long carrier diffusion length. However, the film absorption edge of perovskite is limited to 800 nm, thus finding other ways and formulating new material compositions are needed to further extend the absorption of perovskite-based solar cells. [3] Employing a layer of BHJ organic semiconductors on top of perovskite layer is considered a simple way to extend the photocurrent of the solar cell device beyond 800 nm. Recently, Gao et al. have reported such a hybrid solar cell with a PCE of 19.02%. [3] However, introducing more interactions in the perovskite/BHJ OSCs complicates things even further. For example, in this case, three heterogenous combinations should be considered (monomer/perovskite unit cell, perovskite unit cell/fullerene, and monomer/perovskite/fullerene). [1, 3] We believe that understanding intermolecular interactions in heterojunction systems will ultimately contribute to maximizing the PCEs of solar cells and expediate the process of producing renewable energy.

In summary, in this thesis new insights as related to the interfacial regions of organic heterojunction devices were obtained. Useful trends in interfacial, structural, and electronic properties and side chains effect were correlated with respective experimental efficiencies of OLEDs and OSCs. Due to the success of dimer and monomer/fullerene

approaches employed with D-DFT methods, we recommend using this simple computational strategy when designing new polymers in OSC experiments to push PCEs over 12%. We hope this thesis contributes in gaining an understanding over intermolecular interactions in organic heterojunction devices.

## Bibliography

- [1] J.F. Yan, B.R. Saunders, *Third-Generation Solar Cells: A Review and Comparison of Polymer: Fullerene, Hybrid Polymer and Perovskite Solar Cells*, RSC Advances 4 (2014) 43286-43314.
- [2] W.S. Yang, J.H. Noh, N.J. Jeon, Y.C. Kim, S. Ryu, J. Seo, S.I. Seok, *High-Performance Photovoltaic Perovskite Layers Fabricated through Intramolecular Exchange*, Science 348 (2015) 1234-1237.
- [3] K. Gao, Z.L. Zhu, B. Xu, S.B. Jo, Y.Y. Kan, X.B. Peng, A.K.Y. Jen, *Highly Efficient Porphyrin-Based OPV/Perovskite Hybrid Solar Cells with Extended Photoresponse and High Fill Factor*, Advanced Materials 29 (2017) 1703980.

# Appendices

## A. Supporting Information for Chapter 3: Optimizing the Performance of Multilayered Organic Polymer Devices Using Computational Dimer Approach – A Case Study

<b>Pair</b>	$\Delta E_e$ (OxFn-CA)	$\Delta E_h$ (TPAFn-ITO)	$\Delta HOMO$	$\Delta LUMO$	$\Delta E_g$
<b>OxF2-TPAF2</b>	0.11	0.36	0.57	0.52	0.05
<b>OxF2-TPAF3</b>	0.11	0.41	0.45	0.31	0.14
<b>OxF3-TPAF2</b>	0.32	0.36	0.52	0.47	0.05
<b>OxF3-TPAF3</b>	0.32	0.41	0.4	0.26	0.14

Table A1: Data obtained from Lu et al. [1] for the energy barrier of electron injection ( $\Delta E_e$ ), energy barrier of hole injection ( $\Delta E_h$ ), energy level offsets ( $\Delta LUMO$  and  $\Delta HOMO$ ), and energy gap difference ( $\Delta E_g$ ) for various pairings of OxFm-TPAFn (m,n=2-3).

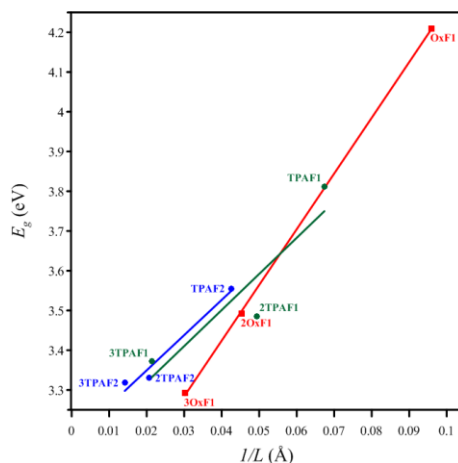


Figure A1: Calculated HOMO-LUMO gaps vs inverse chain length for nOxF1, nTPAF1, and nTPAF2, where n=1-3.

### A1. The Correlation Between the Chain Length Difference and Energy Gap Difference

The energy gap difference ( $\Delta E_g$ ), which is the difference between the HOMO-LUMO energy gaps of monomer 1 ( $E_g$ ) and monomer 2 ( $E'_g$ ) in a given dimer, can be expressed as the difference of their respective straight lines, that is,

$$\begin{aligned} \Delta E_g &= E_g - E'_g \\ &= \frac{m}{L} + b - \frac{m'}{L'} - b' \end{aligned} \tag{A1}$$

where  $m$  and  $m'$  are the slopes,  $b$  and  $b'$  are the intercepts of the straight lines,  $L$  and  $L'$  are the chain lengths that correspond to monomer 1 and 2, respectively. The chain lengths in

equation (A1) can be defined in terms of the chain length difference  $\Delta L = L_1 - L_2$  and the chain length average  $L_{avg} = \frac{L_1+L_2}{2}$ , as follows

$$L_1 = L_{avg} + \frac{\Delta L}{2} = L_{avg} \left(1 + \frac{\Delta L}{2L_{avg}}\right) \quad (\text{A2})$$

$$L_2 = L_{avg} - \frac{\Delta L}{2} = L_{avg} \left(1 - \frac{\Delta L}{2L_{avg}}\right) \quad (\text{A3})$$

To represent  $\Delta E_g$  as a function of  $\Delta L$  and  $L_{avg}$ , we substitute equations (A2) and (A3) into equation (A1) to obtain

$$\Delta E_g = \frac{m}{L_{avg} \left(1 + \frac{\Delta L}{2L_{avg}}\right)} - \frac{m'}{L_{avg} \left(1 - \frac{\Delta L}{2L_{avg}}\right)} + b - b' \quad (\text{A4})$$

By using the binomial expansion to first order in  $\Delta$  and defining the difference of the intercepts as  $\Delta b = b - b'$ , we obtain

$$\Delta E_g = \frac{m}{L_{avg}} \left(1 - \frac{\Delta L}{2L_{avg}}\right) - \frac{m'}{L_{avg}} \left(1 + \frac{\Delta L}{2L_{avg}}\right) + \Delta b + O(\Delta^2) \quad (\text{A5})$$

If we rearrange equation (S5), we obtain

$$\Delta E_g = \frac{\Delta m}{L_{avg}} + \Delta b - \frac{\Delta L}{L_{avg}^2} m_{avg} + O(\Delta^2) \quad (\text{A6})$$

where  $m_{avg} = \frac{m_1+m_2}{2}$  and  $\Delta m = m - m'$  are the average and the difference of the slopes.

The results of Table A2 show that  $\Delta b=0.04$  and  $\frac{\Delta m}{L_{avg}} \approx 0.1$  are smaller relative to  $\frac{\Delta L}{L_{avg}^2} m_{avg}$

that ranges between 0.1 to 0.6 eV for all the pairs of OxFn-TPAFm monomers (n,m=1-3).

Therefore,  $\Delta E_g$  can be approximated in equation (A6) to obtain

$$\Delta E_g = -\frac{\Delta L}{L_{avg}^2} m_{avg} + O(\Delta^2). \quad (\text{A7})$$

Table A2: Data obtained from Figure 3.6 in the manuscript for the first three terms in equation S6 for various pairings of OxFm-TPAFn (m,n=1-3).

<b>Pair</b>	$\Delta b$	$\frac{\Delta m}{L_{avg}}$	$\frac{\Delta L}{L_{avg}^2} m_{avg}$
<b>OxF1-TPAF1</b>		0.17	0.35
<b>OxF1-TPAF2</b>		0.13	0.54
<b>OxF1-TPAF3</b>		0.10	0.57
<b>OxF2-TPAF1</b>		0.13	0.20
<b>OxF2-TPAF2</b>	0.04	0.10	0.14
<b>OxF2-TPAF3</b>		0.09	0.25
<b>OxF3-TPAF1</b>		0.11	0.30
<b>OxF3-TPAF2</b>		0.09	0.05
<b>OxF3-TPAF3</b>		0.08	0.08

It is known from the literature that the use of B3LYP method produces better values of HOMO energies and energy gaps while it overestimates LUMO energies compared to experimental values. [2-4] The deviations of the electronic structure of OxFn and TPAFn monomers relative to the experimental values, as given in Table A.3, show that our results are consistent with the literature. In the experimental paper of Lu et al. work [1], the work functions of CA and ITO, which are used as cathode and anode, are -2.9 and -4.8 eV respectively. We notice a slight deviation of the calculated HOMO energies of TPAFn from the ITO work function while there are significantly larger deviations of their LUMO energies from the CA work function. This is expected for TPAFn since it is used as a hole transport layer to maximize the hole injection from the anode while blocking the electron flux from the emitting layer (OxFn) to reach the anode.

Table A3: The calculated and experimental values of the electronic structure data (in eV) of OxFn and TPAFn monomers with their deviations (the calculated data are obtained with B3LYP, see text for discussion). (LC stands for long side chains).

Monomer	Interacting Monomers (LC)			Isolated Monomers (vac.)			Expt. [1, 5, 6]			HOMO Deviations			LUMO Deviations			$E_g$ Deviations	
	HOMO	LUMO	$E_g$	HOMO	LUMO	$E_g$	HOMO	LUMO	$E_g$	(LC-vac.)	(LC-expt.)	With ITO*	(LC-vac.)	(LC-expt.)	With CA*	(LC-vac.)	(LC-expt.)
OxF1	-5.86	-1.17	4.21	-5.88	-1.58	4.31	-6.09	-2.93	3.16	0.02	0.23	1.06	0.41	1.76	1.25	0.1	1.05
OxF2	-5.37	-1.4	3.59	-5.45	-1.69	3.75	-5.73	-2.79	2.94	0.08	0.36	0.57	0.29	1.39	1.11	0.16	0.65
OxF3	-5.18	-1.51	3.36	-5.26	-1.71	3.55	-5.61	-2.58	3.03	0.08	0.43	0.38	0.2	1.07	1.08	0.19	0.33
TPAF1	-4.85	-1.65	3.68	-4.86	-1.05	3.82	-5.3	-2.3	3	0.01	0.45	0.05	0.6	0.65	1.73	0.14	0.68
TPAF2	-4.82	-1.79	3.42	-4.85	-1.30	3.55	-5.16	-2.27	2.89	0.03	0.34	0.02	0.49	0.48	1.5	0.13	0.53
TPAF3	-4.8	-1.82	3.29	-4.85	-1.41	3.44	-5.21	-2.32	2.89	0.05	0.41	0.02	0.41	0.5	1.39	0.15	0.4

\*For the ITO and CA electrodes, instead of energy levels, the workfunctions were used to calculate the corresponding HOMO and LUMO deviations.

Table A4: The HOMO and LUMO eigenvalues, and energy gaps of the interacting OxFn and TPAFn monomers with short and long side chains in both (a) heterogeneous and (b) homogenous pairs (all are computed with B3LYP).

Type of Side Chains			Ethyl (short side chains)			Octyl (long side chains)			
Pair	Monomer	Interacting with	HOMO (eV)	LUMO (eV)	$E_g$ (eV)	HOMO (eV)	LUMO (eV)	$E_g$ (eV)	
(a)	OxF1	TPAF1	-5.88	-1.65	4.23	-5.86	-1.66	4.2	
		TPAF2	-5.88	-1.66	4.21	-5.86	-1.65	4.21	
		TPAF3	-5.87	-1.66	4.21	-5.85	-1.64	4.21	
	OxF2	TPAF1	-5.4	-1.82	3.58	-5.36	-1.79	3.57	
		TPAF2	-5.42	-1.79	3.62	-5.41	-1.77	3.64	
		TPAF3	-5.39	-1.82	3.57	-5.35	-1.8	3.55	
	OxF3	TPAF1	-5.2	-1.85	3.35	-5.15	-1.83	3.32	
		TPAF2	-5.21	-1.84	3.37	-5.17	-1.81	3.36	
		TPAF3	-5.23	-1.82	3.41	-5.21	-1.81	3.4	
	TPAF1	OxF1	-4.83	-1.13	3.7	-4.84	-1.15	3.69	
		OxF2	-4.85	-1.11	3.74	-4.87	-1.16	3.71	
		OxF3	-4.82	-1.07	3.75	-4.85	-1.2	3.65	
	TPAF2	OxF1	-4.8	-1.41	3.39	-4.82	-1.35	3.47	
		OxF2	-4.79	-1.37	3.42	-4.8	-1.4	3.4	
		OxF3	-4.82	-1.44	3.39	-4.84	-1.46	3.38	
	TPAF3	OxF1	-4.82	-1.5	3.31	-4.81	-1.53	3.28	
		OxF2	-4.82	-1.54	3.28	-4.81	-1.53	3.28	
		OxF3	-4.82	-1.5	3.32	-4.77	-1.46	3.31	
		OxF1	1	-5.88	-1.65	4.23	-5.85	-1.63	4.22

(b)		2	-5.87	-1.66	4.21	-5.85	-1.64	4.21
	<b>OxF2</b>	1	-5.41	-1.82	3.59	-5.37	-1.79	3.58
		2	-5.4	-1.8	3.6	-5.37	-1.79	3.58
	<b>OxF3</b>	1	-5.22	-1.83	3.39	-5.18	-1.81	3.37
		2	-5.22	-1.83	3.39	-5.18	-1.8	3.38
	<b>TPAF1</b>	1	-4.82	-1.15	3.67	-4.81	-1.13	3.68
		2	-4.85	-1.15	3.7	-4.86	-1.13	3.73
	<b>TPAF2</b>	1	-4.82	-1.43	3.39	-4.82	-1.44	3.45
		2	-4.82	-1.42	3.39	-4.77	-1.48	3.3
	<b>TPAF3</b>	1	-4.82	-1.53	3.28	-4.76	-1.48	3.28
		2	-4.81	-1.54	3.27	-4.82	-1.5	3.33

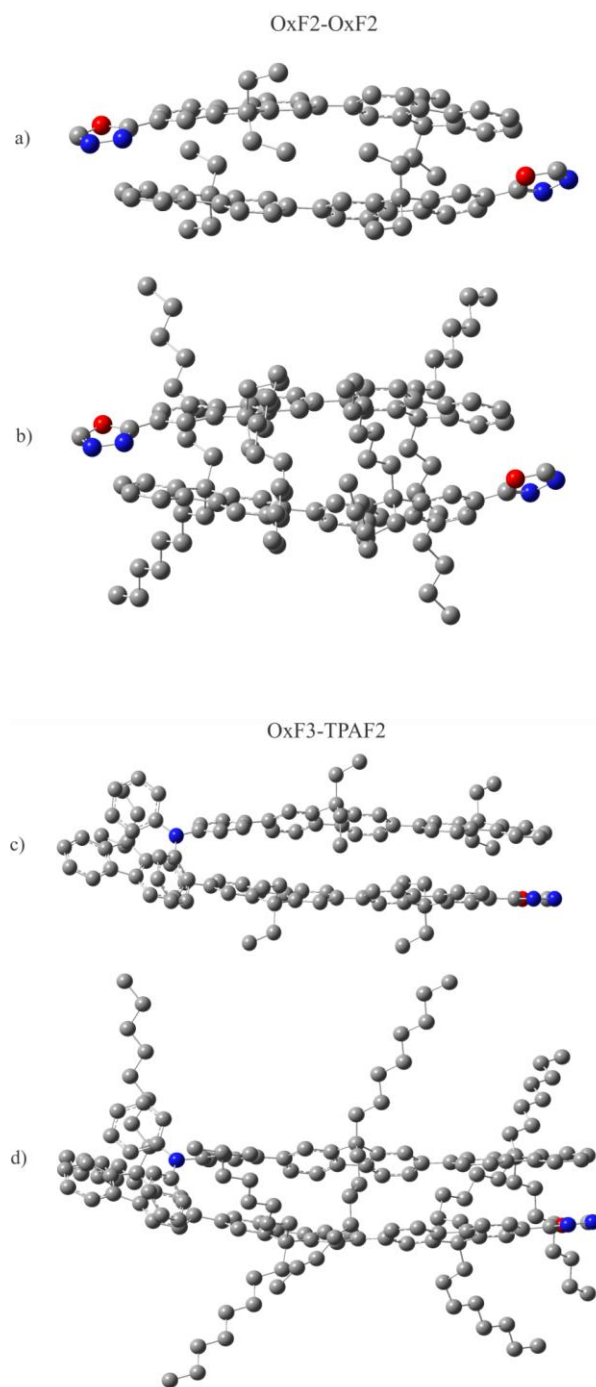


Figure A2: Illustration of the role of side chains with the use of optimized structures of OxF2-OxF2 and OxF3-TPAF2 pairs with (a,c) short and (b,d) long side chains.

		$L_{shift}(\text{\AA})$	$d(\text{\AA})$	$\Delta E_b/L_{avg}(\text{eV/\AA})$
<b>(a) Short Side Chains</b>	<b>OxF1-OxF1</b>	0.86	3.6	0.091
	<b>OxF2-OxF2</b>	1.91	4.0	0.081
	<b>OxF3-OxF3</b>	2.42	4.4	0.082
	<b>TPAF1-TPAF1</b>	1.5	4.5	0.089
	<b>TPAF2-TPAF2</b>	1.42	4.8	0.081
	<b>TPAF3-TPAF3</b>	2.93	4.5	0.068
<b>(b) Long Side Chains</b>	<b>OxF1-OxF1</b>	3.84	3.6	0.092
	<b>OxF2-OxF2</b>	2.67	3.9	0.133
	<b>OxF3-OxF3</b>	2.17	4.3	0.118
	<b>TPAF1-TPAF1</b>	0.5	4.5	0.099
	<b>TPAF2-TPAF2</b>	2.4	6.7 (4.0)	0.134
	<b>TPAF3-TPAF3</b>	0.39	5.2 (4.2)	0.100

Table A5: Length shift ( $L_{shift}$ ), intermolecular distance ( $d$ ), and binding energy per average chain length ( $\Delta E_b/L_{avg}$ ) for OxFn-OxFn and TPAFn-TPAFn (n=1-3) with (a) short and (b) long side chains. In some case, the average perpendicular distance ( $d_{\perp}$ ) is given in brackets for the significantly shifted monomers (with large  $L_{shift}$ , see Figure 3.9).

# Bibliography

- [1] J.P. Lu, Y.N. Jin, J.F. Ding, Y. Tao, M. Day, *High-Efficiency Multilayer Polymeric Blue Light-Emitting Diodes Using Boronate Esters as Cross-Linking Linkages*, Journal of Materials Chemistry 16 (2006) 593-601.
- [2] L. Ling, J.B. Lagowski, *DFT Study of Electronic Band Structure of Alternating Triphenylamine-Fluorene Copolymers*, Polymer 54 (2013) 2535-2543.
- [3] E.F. Oliveira, F.C. Lavarda, *Effect of the Length of Alkyl Side Chains in the Electronic Structure of Conjugated Polymers*, Materials Research 17 (2014) 1369-1374.
- [4] L. Ling, J.B. Lagowski, *Electronic Band Structure of Alternating Fluorene-Oxadiazole Conjugated Copolymer - A 1D Solid-State DFT Study*, Journal of Molecular Structure-Theochem 944 (2010) 146-155.
- [5] A.W. Hains, J. Liu, A.B.F. Martinson, M.D. Irwin, T.J. Marks, *Anode Interfacial Tuning Via Electron-Blocking/Hole-Transport Layers and Indium Tin Oxide Surface Treatment in Bulk-Heterojunction Organic Photovoltaic Cells*, Advanced Functional Materials 20 (2010) 595-606.
- [6] J.F. Ding, Y. Tao, M. Day, J. Roovers, M. D'Iorio, *Electrochemical and Fluorescent Properties of Alternating Copolymers of 9,9-Dioctylfluorene and Oxadiazole as Blue Electroluminescent and Electron Transport Materials*, Journal of Optics A: Pure and Applied Opti 4 (2002) S267-S272.

## B. Supporting Information for Chapter 4: Assessment of the Performance of Four Dispersion-Corrected DFT Methods Using Optoelectronic Properties and Binding Energies of Organic Monomer/Fullerene Pairs

### B1. Binding Energies and Electronic and Optical Parameters

Table B1: The binding energies of pairs including monomers with short and long side chains.

Monomer/Fullerene	$L_{monomer}$ (Å)	$N_h$	Monomers with Short Side Chains				$N_h$	Monomers with Long Side Chains	
			B97-D3	$\omega$ B97x-D	B3LYP-D3	PBE1PBE-D3		B97-D3	B3LYP-D3
P3HT/PCBM	6.43	84	1.08	1.00	1.03	0.95	96	1.64	1.58
PTB7/PCBM	10.94	98	1.53	1.37	1.41	1.31	124	2.21	2.30
PBDTTPD/PCBM	10.91	98	1.68	1.55	1.63	1.53	122	2.32	2.39
PBTff4T/PCBM	18.27	109	1.88	1.75	1.78	1.62	145	2.42	2.33
PffBT4T/PCBM	18.39	109	1.84	1.65	1.67	1.50	145	2.54	2.51
PCDTBT/PCBM	18.73	111	1.93	1.85	1.82	1.68	123	2.53	2.37
PNT4T/PCBM	20.72	114	1.93	1.77	1.77	1.61	150	3.01	2.83

P3HT/PC <sub>71</sub> BM	6.43	94	0.86	0.74	0.78	0.69	106	1.45	1.37
PTB7/PC <sub>71</sub> BM	10.94	108	1.35	1.14	1.21	1.07	134	2.21	2.11
PBDTTPD/PC <sub>71</sub> BM	10.91	108	1.77	1.63	1.72	1.56	132	2.32	1.99
PBTff4T/PC <sub>71</sub> BM	18.27	119	1.61	1.36	1.45	1.23	155	2.38	2.22
PffBT4T/PC <sub>71</sub> BM	18.39	119	1.62	1.46	1.50	1.32	155	2.19	2.09
PCDTBT/PC <sub>71</sub> BM	18.73	121	1.77	1.67	1.67	1.48	133	2.15	1.95
PNT4T/PC <sub>71</sub> BM	20.72	124	1.57	1.49	1.43	1.25	160	2.80	2.57

Table B2: The SP B3LYP electronic parameters ( $\epsilon_{HOMO}$ ,  $\epsilon_{LUMO}$ , and  $E_g$ ) obtained using the four D-DFT interacting monomers and fullerenes with short side chains.

Monomer/ Fullerene	$\omega$ B97x-D			PBE1PBE-D3			B3LYP-D3			B97-D3			Expt.		
	$\epsilon_{HOMO}$	$\epsilon_{LUMO}$	$E_g$												
<b>P3HT/PCB</b> M	-5.50	-1.15	4.35	-5.46	-1.19	4.26	-5.46	-1.25	4.22	-5.42	-1.30	4.12	-5.10	-3.00	2.10
<b>P3HT/PC<sub>71</sub></b> BM	-5.55	-1.10	4.45	-5.50	-1.15	4.35	-5.50	-1.20	4.30	-5.45	-1.26	4.19	[1]	[1]	[1]
<b>PBDTPD</b> /PCBM	-5.16	-2.35	2.81	-5.03	-2.68	2.36	-5.20	-2.43	2.77	-5.20	-2.52	2.68	-5.56	-3.75	1.81
<b>PBDTPD</b> /PC <sub>71</sub> BM	-5.16	-2.36	2.81	-5.14	-2.39	2.75	-5.22	-2.45	2.77	-5.21	-2.52	2.68	[2]	[2]	[2]
<b>PCDTBT/P</b> CBM	-5.13	-2.45	2.68	-5.03	-2.80	2.23	-5.08	-2.54	2.54	-5.02	-2.61	2.41	-5.45	-3.60	1.85
<b>PCDTBT/P</b> C <sub>71</sub> BM	-5.15	-2.43	2.72	-5.04	-2.81	2.23	-5.08	-2.54	2.54	-5.03	-2.61	2.41	[3]	[3]	[3]
<b>PTB7/PCB</b> M	-5.37	-2.09	3.27	-5.34	-2.12	3.22	-5.37	-2.18	3.19	-5.33	-2.27	3.07	-5.15	-3.31	1.84
<b>PTB7/PC<sub>71</sub></b> BM	-5.42	-2.05	3.36	-5.36	-2.10	3.27	-5.40	-2.15	3.25	-5.35	-2.25	3.11	[4]	[4]	[4]
<b>PBTff4T/P</b> CBM	-5.05	-2.55	2.50	-4.86	-2.90	1.97	-4.99	-2.64	2.35	-4.92	-2.73	2.20	-5.20	-3.57	1.63

<b>PBTff4T/P</b> C <sub>71</sub> BM	-5.05	-2.60	2.45	-4.85	-2.90	1.95	-4.99	-2.67	2.33	-4.90	-2.78	2.12	[5]	[5]	[5]
<b>PffBT4T/P</b> CBM	-5.03	-2.60	2.43	-4.83	-2.87	1.96	-4.94	-2.74	2.20	-4.87	-2.83	2.04	-5.34	-3.69	1.65
<b>PffBT4T/P</b> C <sub>71</sub> BM	-5.09	-2.59	2.50	-5.00	-2.63	2.37	-5.02	-2.70	2.32	-4.95	-2.78	2.17	[5]	[5]	[5]
<b>PNT4T/PC</b> BM	-5.19	-2.79	2.40	-5.09	-2.82	2.27	-5.10	-2.88	2.22	-5.02	-2.95	2.07	-5.24	-3.71	1.53
<b>PNT4T/PC</b> 7 <sub>1</sub> BM	-5.33	-2.77	2.57	-5.22	-2.80	2.42	-5.25	-2.86	2.38	-4.99	-2.95	2.05	[5]	[5]	[5]

Table B3: MADs of the SP B3LYP electronic parameters ( $\epsilon_{HOMO}$ ,  $\epsilon_{LUMO}$ , and  $E_g$ ) obtained using the D-DFT isolated and interacting fullerenes and monomers and with short and long side chains.

	Methods	MAD from B3LYP Gas Phase Values			MAD from Expt. Values		
		$\epsilon_{HOMO}$ (eV)	$\epsilon_{LUMO}$ (eV)	$E_g$ (eV)	$\epsilon_{HOMO}$ (eV)	$\epsilon_{LUMO}$ (eV)	$E_g$ (eV)
Fullerenes and Monomers with Short Side Chains	PBE1PBE-D3	0.02	0.05	0.04	0.36	1.11	0.83
	$\omega$ B97x-D	0.09	0.10	0.18	0.32	1.24	1.02
	B3LYP-D3	0.01	0.00	0.02	0.34	1.17	0.92
	B97-D3	0.05	0.07	0.12	0.36	1.11	0.82
Fullerenes and Monomers with Long Side Chains	B3LYP-D3	0.05	0.02	0.06	0.28	1.21	0.96
	B97-D3	0.05	0.07	0.08	0.31	1.14	0.86

Table B4: MADs in the four D-DFT electronic parameters ( $\epsilon_{HOMO}$ ,  $\epsilon_{LUMO}$ , and  $E_g$ ) from the experimental data.

Method	MAD from Experimental Values		
	$\epsilon_{HOMO}$ (eV)	$\epsilon_{LUMO}$ (eV)	$E_g$ (eV)
$\omega$ B97x-D	2.21	2.83	3.73
B3LYP-D3	0.34	1.17	0.92
B97-D3	0.96	0.74	0.33
PBE1PBE-D3	0.25	1.20	1.24

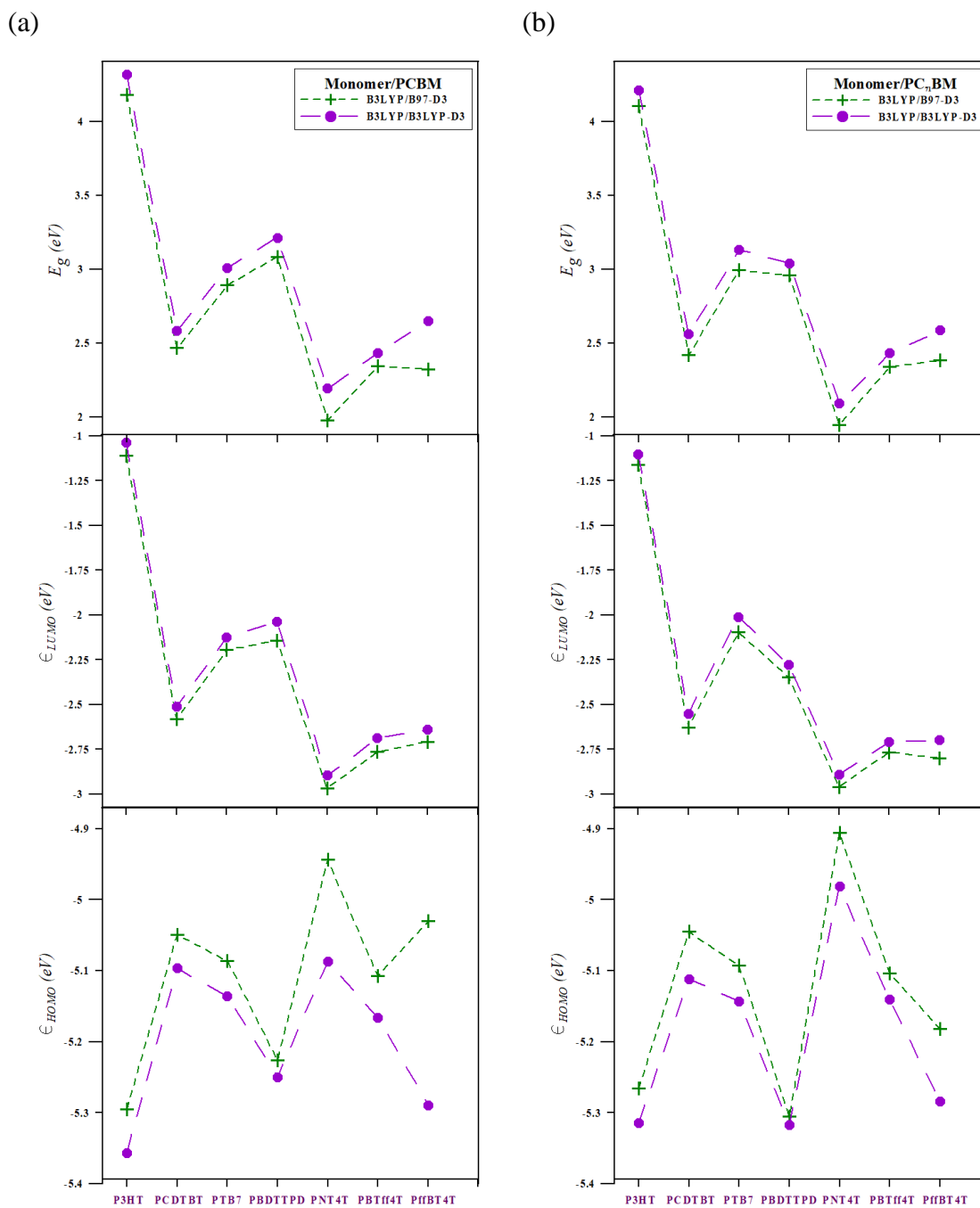


Figure B1: The SP B3LYP  $\epsilon_{HOMO}$ 's,  $\epsilon_{LUMO}$ 's, and  $E_g$ 's obtained using the selected D-DFT (B97-D3 and B3LYP-D3) optimized geometries of the interacting monomers with long side chains with (a) PCBM and (b) PC<sub>71</sub>BM.

Table B5: The electronic offsets of the interacting monomers (including short and long side chains) and fullerenes.

Monomer/Fullerene Combinations	SP B3LYP/B97-D3						SP B3LYP/B3LYP-D3					
	Short Side Chains			Long Side Chains			Short Side Chains			Long Side Chains		
	$\Delta\epsilon_{HOMO}$	$\Delta\epsilon_{LUMO}$	$\Delta E_g$									
P3HT/PCBM	0.28	1.87	1.59	0.44	2.01	1.57	0.24	1.88	1.65	0.39	2.02	1.63
P3HT/PC <sub>71</sub> BM	0.18	1.90	1.72	0.36	2.00	1.63	0.13	1.91	1.77	0.33	2.00	1.68
PBDTTPD/PCBM	0.50	0.66	0.15	0.45	1.01	0.55	0.45	0.66	0.21	0.43	1.07	0.64
PBDTTPD/PC <sub>71</sub> BM	0.42	0.63	0.21	0.46	0.99	0.53	0.42	0.65	0.23	0.44	1.01	0.57
PCDTBT/PCBM	0.68	0.56	0.12	0.64	0.51	0.13	0.62	0.59	0.03	0.59	0.61	0.02
PCDTBT/PC <sub>71</sub> BM	0.58	0.53	0.06	0.59	0.53	0.05	0.53	0.54	0.01	0.53	0.56	0.03
PTB7/PCBM	0.36	0.90	0.53	0.61	0.97	0.36	0.32	0.94	0.62	0.56	1.00	0.44
PTB7/PC <sub>71</sub> BM	0.26	0.90	0.64	0.52	0.95	0.44	0.22	0.94	0.72	0.49	0.97	0.49
PBTff4T/PCBM	0.74	0.41	0.33	0.60	0.41	0.20	0.68	0.45	0.22	0.54	0.44	0.09
PBTff4T/PC <sub>71</sub> BM	0.72	0.37	0.35	0.50	0.37	0.13	0.64	0.43	0.21	0.46	0.36	0.11
PffBT4T/PCBM	0.83	0.35	0.48	0.65	0.44	0.21	0.76	0.39	0.37	0.38	0.46	0.08
PffBT4T/PC <sub>71</sub> BM	0.68	0.38	0.30	0.40	0.32	0.08	0.62	0.40	0.22	0.32	0.37	0.05
PNT4T/PCBM	0.65	0.19	0.46	0.75	0.19	0.56	0.56	0.22	0.35	0.61	0.23	0.38
PNT4T/PC <sub>71</sub> BM	0.62	0.19	0.43	0.71	0.18	0.53	0.38	0.23	0.15	0.64	0.19	0.45

Table B6: The maximum absorption wavelengths (in nm) of the isolated monomer with short and long side chains (SC), and the MAD from the B3LYP gas phase and the experimental values.

TD-DFT combined with	P3HT	PCDTBT	PBDTTPD	PTB7	PNT4T	PBTff4T	PffBT4T	MAD from TD-B3LYP
$\omega$ B97x-D	271.78	422.39	394.88	335.52	446.26	429.76	428.09	
B3LYP/ $\omega$ B97x-D	289.83	540.13	526.03	409.15	610.01	557.07	566.62	41.43
PBE1PBE-D3	290.46	538.99	508.15	404.4	630.44	572.88	571.55	
B3LYP/PBE1PBE-D3	296.84	568.86	534.39	424.75	672.9	606.99	608.56	10.80
B3LYP-D3	301.04	576.44	533.61	426.83	688.31	614.43	620.88	
B3LYP/B3LYP-D3	301.04	576.44	533.61	426.83	688.31	614.43	620.88	3.91
B97-D3	324.9	759	698.27	568.33	979.67	843.83	866.26	
B3LYP/B97-D3	309.66	611.39	545.51	449.64	757.01	662	674.86	31.60
B3LYP (gas phase)	301.12	585.92	534.18	430.81	693.67	618.55	624.63	
B3LYP/B3LYP-D3 (Long SC)	305.97	585.13	454.59	447.55	666.27	586.98	574.61	16.73
B3LYP/B97-D3 (Long SC)	316.51	622.47	474.94	467.57	723.76	624.33	630.02	23.46
B3LYP (gas phase) (Long SC)	336.61	589.06	468.81	446.25	668.2	612.02	614.63	
Expt.	~550[7]	~560[8]	~625[9]	~680[10]	~700[5]	~700[5]	~700[5]	

Table B7: The maximum absorption wavelengths (in nm) of the interacting monomer with short and long side chains (SC), and the MAD from the experimental values.

TD-DFT combined with	Interacting Monomer/ Fullerene	P3HT	PCDTBT	PBDTTPD	PTB7	PNT4T	PBTff4T	PffBT4T	MAD from Expt.	MAD from Expt.*
B3LYP/ $\omega$ B97x-D	/PCBM	300.57	540.03	513.44	420.89	601.97	576.09	588.81	144.54	94.44
	/PC <sub>71</sub> BM	295.1	531.86	501.15	410.83	562.71	586.41	576.64		
B3LYP/PBE1PBE-D3	/PCBM	305.44	680.18	585.91	426.89	633.78	761.74	764.51	127.24	86.46
	/PC <sub>71</sub> BM	300.38	673.16	579.86	421.85	596.98	768.17	605.30		
B3LYP/B3LYP-D3	/PCBM	308.5	569.69	517.72	431.72	649.66	610.87	644.00	119.91	59.11
	/PC <sub>71</sub> BM	303.66	566.57	518.38	424.18	606.38	613.70	618.74		
B3LYP/B97-D3	/PCBM	314.67	601.02	534.63	449.46	697.33	650.53	688.65	95.78	27.31
	/PC <sub>71</sub> BM	310.63	596.75	533.75	444.47	704.69	669.26	658.23		
B3LYP/B3LYP-D3 (Long SC)	/PCBM	312.44	565.28	441.98	462.65	669.57	582.8	546.79	130.07	69.64
	/PC <sub>71</sub> BM	311.86	561.87	458.35	458.76	694.59	594.08	562.24		
B3LYP/B97-D3 (Long SC)	/PCBM	319.31	598.89	459.6	481.96	742.37	617.56	627.19	119.02	60.86
	/PC <sub>71</sub> BM	318.83	595.07	472.98	477.88	745.36	619.75	610.32		
Expt.		~550[7]	~560[8]	~625[9]	~680[10]	~700[5]	~700[5]	~700[5]		

In Figure B2, we show the TD-DFT/B3LYP absorption spectra of the longest D-DFT monomers (PCDTBT, PNT4T, PBTff4T, and Pff4TBT) since they exhibited the most accurate  $\lambda_{max}$ 's relative to the experimental values. For each monomer, four absorption spectra that correspond to the four D-DFT geometries are displayed. The results show that the computational and experimental spectra are in relatively good agreement. Each absorption spectrum exhibits a broad range from 400 to 800 nm and consists of two peaks. The second peak of the experimental absorption spectra for all monomers is associated with the lowest singlet excited-states. The results also show that the absorptions obtained using B97-D3 monomers are red shifted relative to the experimental spectra while those obtained using  $\omega$ B97xD3 are blue shifted. The absorption spectra obtained using B3LYP-D3 and PBE1PBE-D3 methods are very similar and are intermediate relative to those obtained with  $\omega$ B97x-D and B97-D3 method. The closest locations of  $\lambda_{max}$  to the experimental ones are found using B3LYP-D3 and PBE1PBE-D3 for PCDTBT and PNT4T, and using B97-D3 for PBTff4T and Pff4TBT. This indicates that B97-D3, B3LYP-D3, and PBE1PBE-D3 methods provide accurate results for the TD-DFT absorption calculation

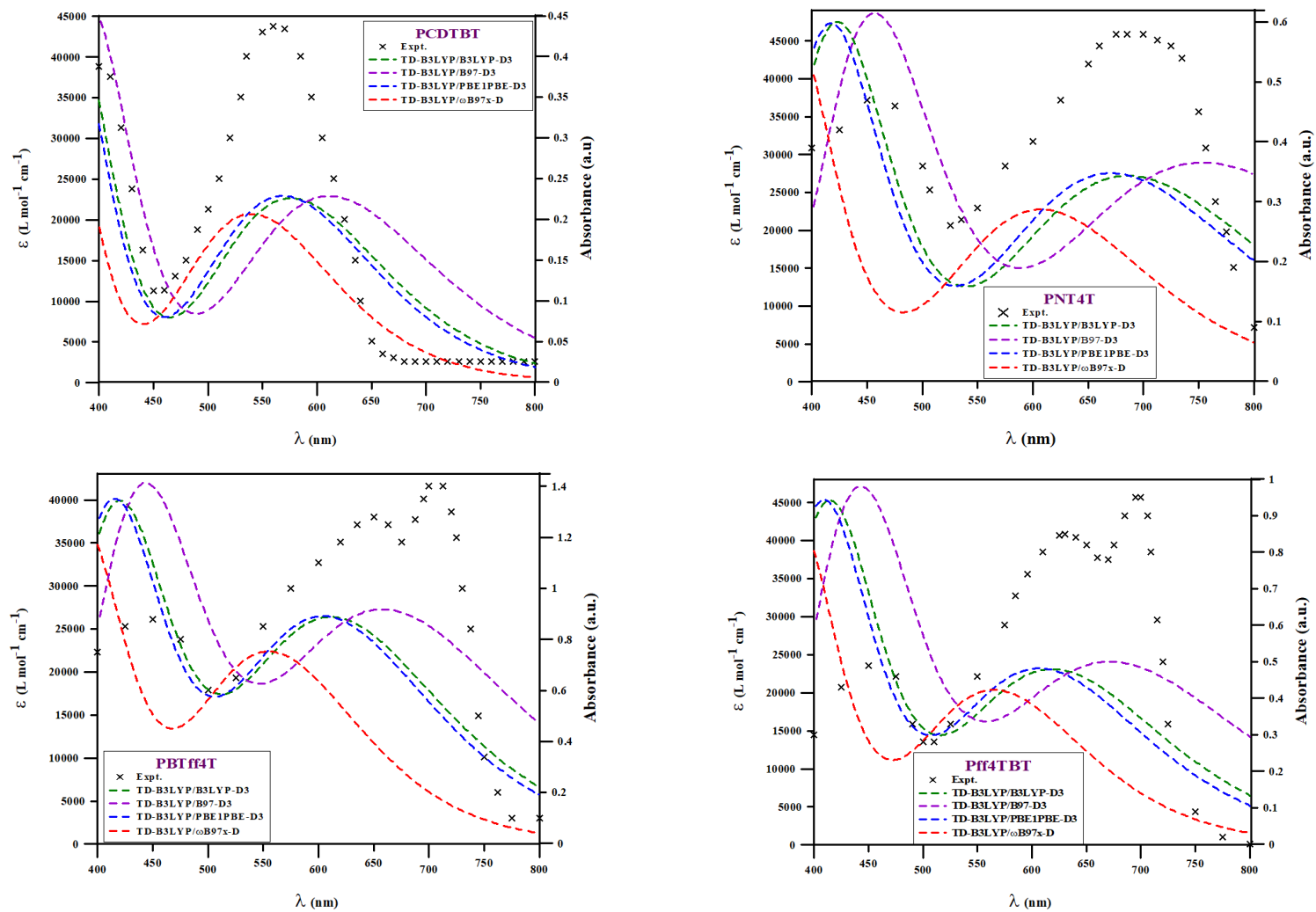


Figure B2: The absorption spectra of the isolated long chain-length monomers obtained at the TD-DFT/B3LYP using the four D-DFT geometries. The experimental data uses the right y-axis.

## B2. The Dependence of D-DFT Methods on the Monomers' Chain Lengths

In Figure B3, we illustrate the differences between the B97-D3 and PBE1PBE-D3 binding energies for monomer/PCBM and monomer/PC<sub>71</sub>BM pairs since PBE1PBE-D3 and B97-D3 give the smallest and the largest binding energies in Figure 4.1 in Chapter 4. The results indicate that there is a chain length dependence on the performance of D-DFT methods in the binding energy calculations. As the monomer changes from P3HT to PBTff4T in a given pair, the chain length increases from approximately 6 to 18 Å, and the differences between the B97-D3 and PBE1PBE-D3 binding energies increases from about 0.1 to 0.3 eV. In addition, the results show that for monomers' chain lengths above 18 Å, the differences level off between the binding energies obtained at B97-D3 and PBE1PBE-D3 methods. We conclude that the spread in the binding energy values as obtained from D-DFT methods is larger for longer monomers (>18 Å) and it tends to level off as the monomers get even longer.

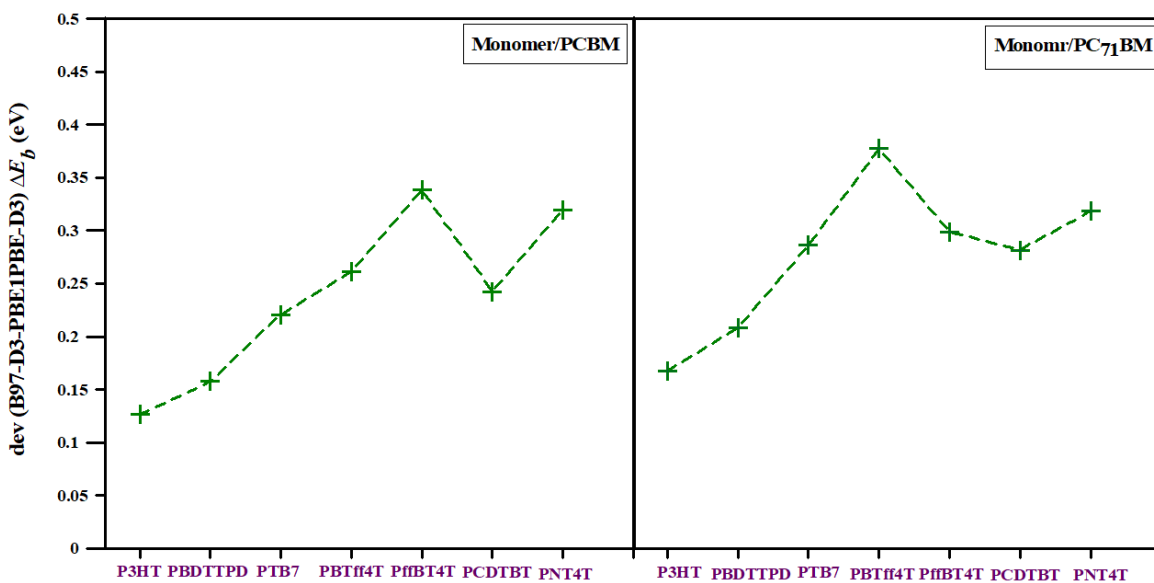


Figure B3: The differences between the B97-D3 and PBE1PBE-D3 binding energies for monomer/PCBM and monomer/PC<sub>71</sub>BM pairs. The monomers are ordered from the shortest to the longest along the x-axis.

Figure 4.2 in Chapter 4 shows that the calculated values of HOMO did not follow the general trend of the experimental data. In order to understand these discrepancies, we illustrate the deviations of  $\epsilon_{HOMO}$ 's of the SP B3LYP interacting monomers with PC<sub>71</sub>BM using the optimized geometries at the four D-DFT methods from the corresponding experimental data in Figure B4. The results show that, for most cases, the higher absolute deviations in  $\epsilon_{HOMO}$ 's are obtained for monomers with shorter chain lengths (such as P3HT) while the lower absolute deviations are obtained for monomers with longer chain lengths (such as PNT4T). This Figure indicates that the accuracy of D-DFT methods depends on the monomers' chain lengths. This result is also confirmed even more strongly even more strongly from other electronic parameters ( $\epsilon_{LUMO}$ 's and  $E_g$ 's in addition to  $\epsilon_{HOMO}$ 's, see Figure 4.2) that are deviated from the corresponding experimental data for SP B3LYP interacting monomers with both types of fullerenes using the B97-D3 optimized geometries (see Figure B5).

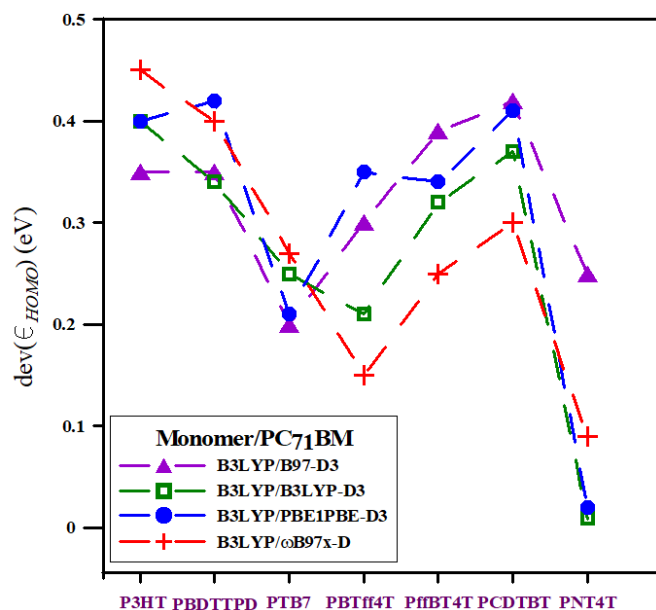


Figure B4: The absolute deviation in the HOMO energies from the corresponding experimental data for the interacting monomers with PC<sub>71</sub>BM. The monomers are ordered from the shortest to the longest along the x-axis.

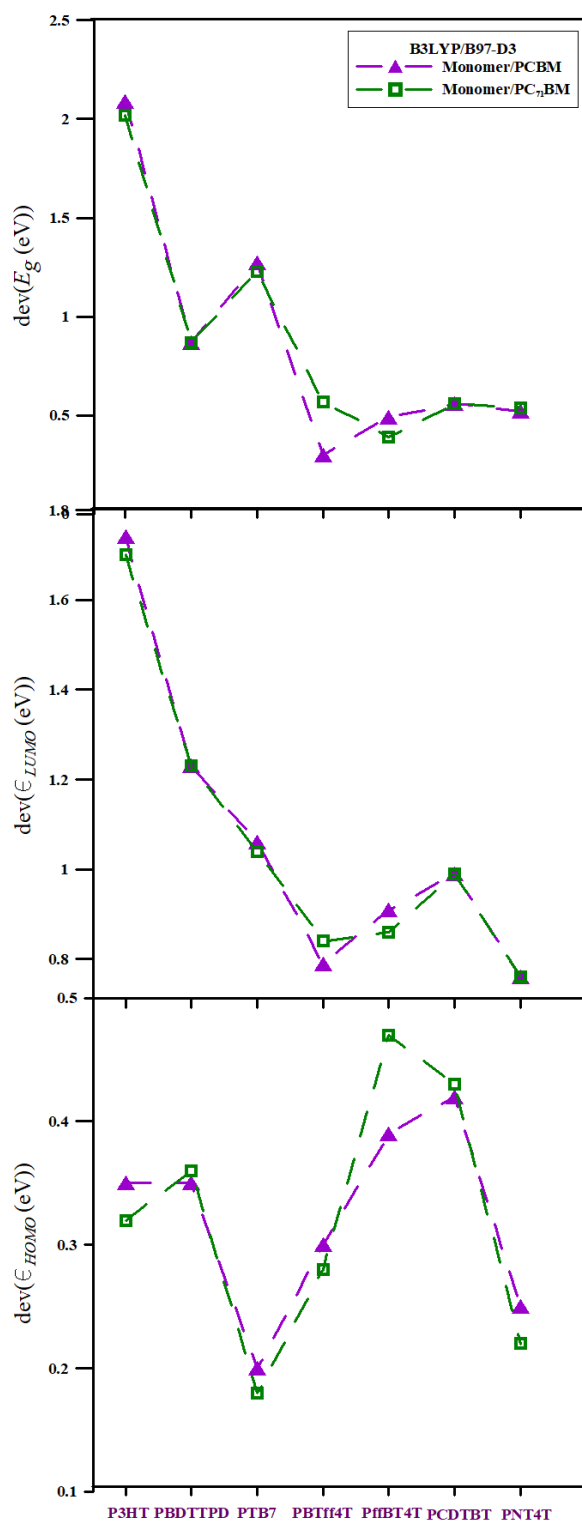


Figure B5: The absolute (B3LYP/B97-D3) deviations in the  $\epsilon_{HOMO}$ 's,  $\epsilon_{LUMO}$ 's, and  $E_g$ 's from the corresponding experimental data for the interacting monomers with PCBM and PC<sub>71</sub>BM.

# Bibliography

- [1] M.C. Scharber, D. Wuhlbacher, M. Koppe, P. Denk, C. Waldauf, A.J. Heeger, C.L. Brabec, *Design Rules for Donors in Bulk-Heterojunction Solar Cells - Towards 10 % Energy-Conversion Efficiency*, *Advanced Materials* 18 (2006) 789-794.
- [2] Y.P. Zou, A. Najari, P. Berrouard, S. Beaupre, B.R. Aich, Y. Tao, M. Leclerc, *A Thieno 3,4-C Pyrrole-4,6-Dione-Based Copolymer for Efficient Solar Cells*, *Journal of the American Chemical Society* 132 (2010) 5330-5331.
- [3] N. Blouin, A. Michaud, D. Gendron, S. Wakim, E. Blair, R. Neagu-Plesu, M. Belletete, G. Durocher, Y. Tao, M. Leclerc, *Toward a Rational Design of Poly(2,7-Carbazole) Derivatives for Solar Cells*, *Journal of the American Chemical Society* 130 (2008) 732-742.
- [4] C. Liu, C. Yi, K. Wang, Y.L. Yang, R.S. Bhatta, M. Tsige, S.Y. Xiao, X. Gong, *Single-Junction Polymer Solar Cells with over 10% Efficiency by a Novel Two-Dimensional Donor-Acceptor Conjugated Copolymer*, *ACS Applied Materials & Interfaces* 7 (2015) 4928-4935.
- [5] Y.H. Liu, J.B. Zhao, Z.K. Li, C. Mu, W. Ma, H.W. Hu, K. Jiang, H.R. Lin, H. Ade, H. Yan, *Aggregation and Morphology Control Enables Multiple Cases of High-Efficiency Polymer Solar Cells*, *Nature Communications* 5 (2014) 5293.
- [6] K. Tremel, S. Ludwigs, *In: P3HT Revisited: From Molecular Scale to Solar Cell Devices*, (Springer, 2014).
- [7] B. Giesecking, B. Jack, E. Preis, S. Jung, M. Forster, U. Scherf, C. Deibel, V. Dyakonov, *Excitation Dynamics in Low Band Gap Donor-Acceptor Copolymers and Blends*, *Advanced Energy Materials* 2 (2012) 1477-1482.
- [8] D.Q. Zhu, Q.Q. Zhu, C.T. Gu, D. Ouyang, M. Qiu, X.C. Bao, R.Q. Yang, *Alkoxy Side Chain Substituted Thieno 3,4-C Pyrrole-4,6-Dione to Enhance Photovoltaic Performance with Low Steric Hindrance and High Dipole Moment*, *Macromolecules* 49 (2016) 5788-5795.
- [9] V. Pranculis, A. Ruseckas, D.A. Vithanage, G.J. Hedley, I.D.W. Samuel, V. Gulbinas, *Influence of Blend Ratio and Processing Additive on Free Carrier Yield and Mobility in PTB7:PC71BM Photovoltaic Solar Cells*, *Journal of Physical Chemistry C* 120 (2016) 9588-9594.

## C. Supporting Information for Chapter 5: Optimizing the Performance of the Bulk Heterojunction Organic Solar Cells Based on DFT Simulations of their Interfacial Properties

### C1. The Conformational Analysis of Monomer and Monomer Pairings

For the optimal charge transport across the layer, it is best if conjugated polymers (and monomers), with the help of  $\pi$ - $\pi$  interactions, bring their backbones close together to form  $\pi$ -stacked clusters. For this reason, in this work, monomers in homogenous pairs were arranged in co-facial  $\pi$ -stacking configurations prior to geometrical optimizations. However, the two monomers in a pair can be differently oriented relative to each other (see for example PBDTTPD dimer in Figure C1), hence we consider four different orientations for each pair of monomers. In each dimer, one (top) monomer is kept fixed and the other (bottom) is allowed to move. As shown in Figure C1, in the first orientation, the monomers form a mirror (M) image of each other. Starting with the mirrored orientation, in the second one, the bottom monomer is rotated  $180^\circ$  in plane relative to the top monomer (MR), and, in the third one, the bottom monomer is rotated  $180^\circ$  out of plane relative to the top monomer (MO). Starting with the third orientation, in the fourth orientation, the bottom monomer is rotated  $180^\circ$  in plane relative to the top monomer (MOR). For each dimer, all four (initial) arrangements are then geometry optimized with the B97D3 method (as mentioned above) and the dimer with the orientation that has the lowest total energy ( $E_0$ ) (or the highest binding energy) is then used in further computations.

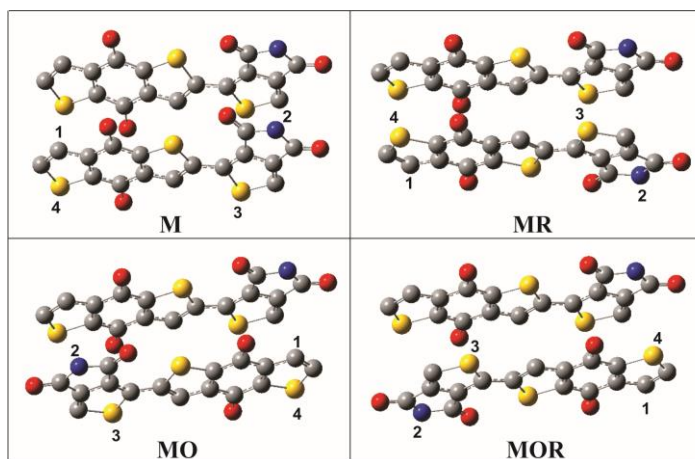


Figure C1: Example of four different orientations: M, MR, MO, and MOR (see text for description) of PBDTTPD/PBDDTPD pair prior to D-DFT/B97D3 optimizations. For clarity, hydrogen atoms are not shown.

The conformational analyses of the pairs that involve interactions between monomers and fullerenes, and between fullerenes themselves are more difficult to carry out in a straightforward way since, due to the near spherical shape of fullerenes, identifying the most stable conformations for these pairs is quite challenging. Therefore, a (in-house) code was developed that allowed us to quickly search many possible arrangements/orientations of a given monomer relative to the fullerene or a given fullerene relative to another fullerene for all combinations. This search required a submission of numerous jobs. Each job required that the molecules be placed in different positions relative to each other for a given combination and then to carry out geometry optimizations and so on until the most stable conformation was found.

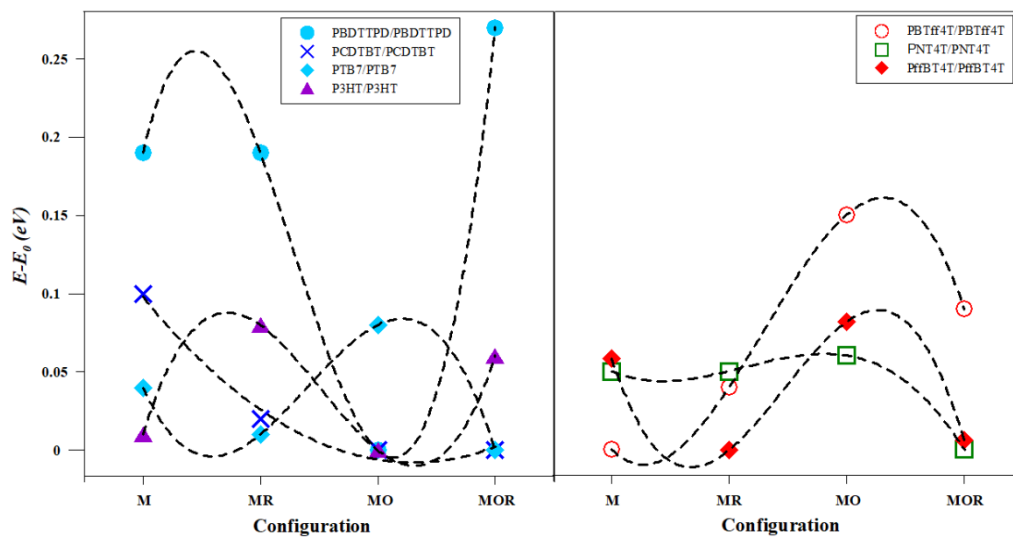
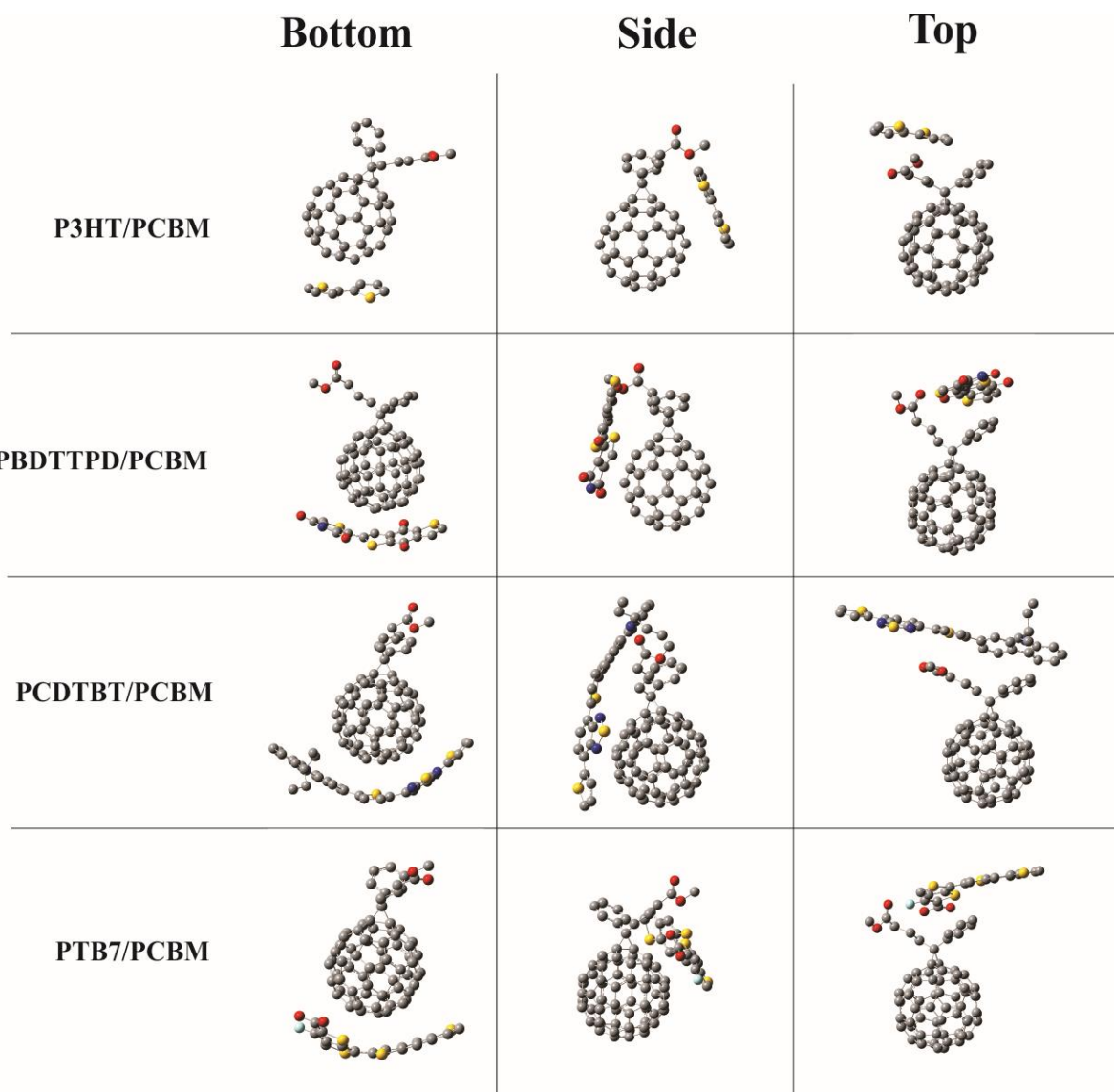


Figure C2: The relative conformational energy versus the configurations of homogenous monomer/monomer pairs optimized using the B97D3 method.



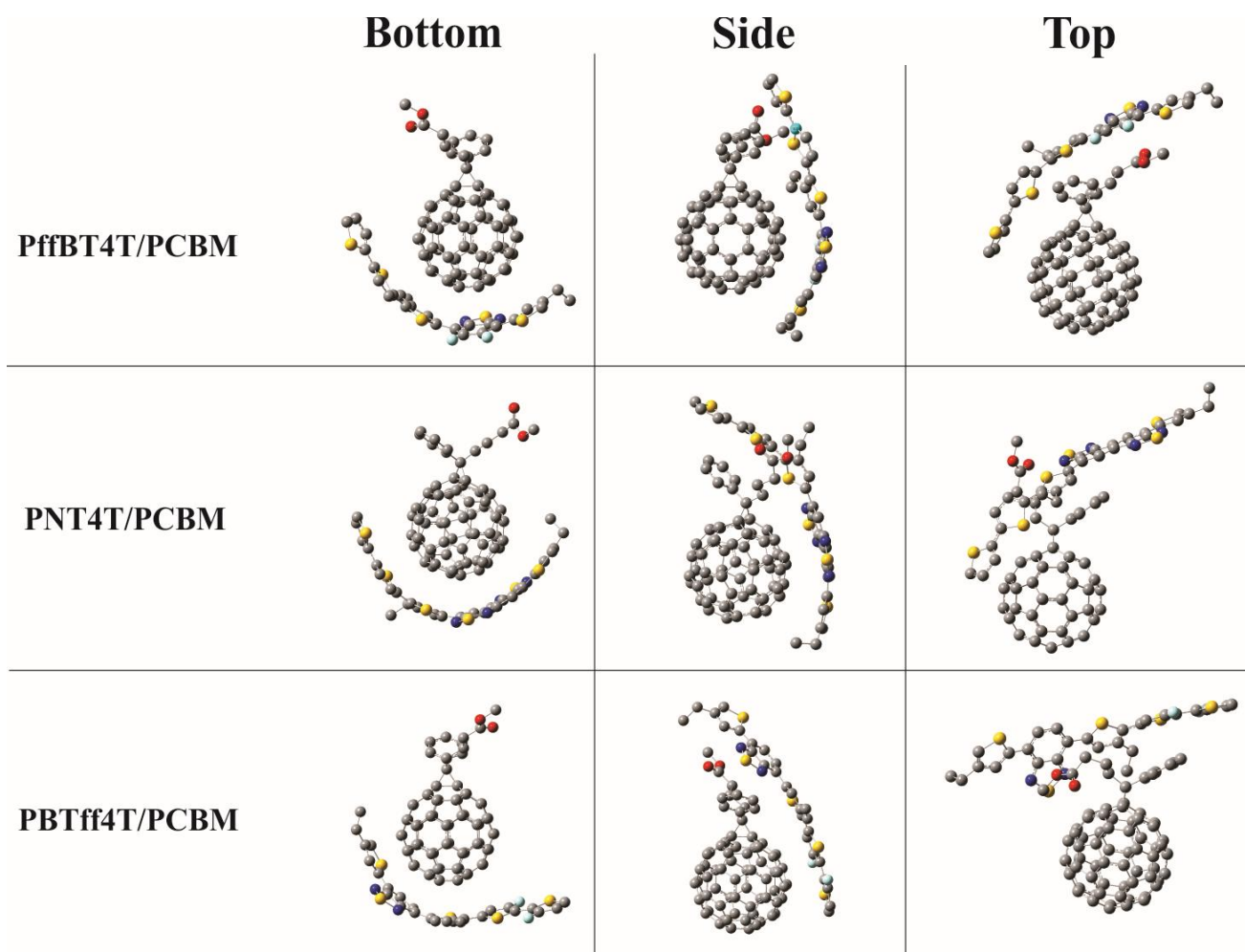
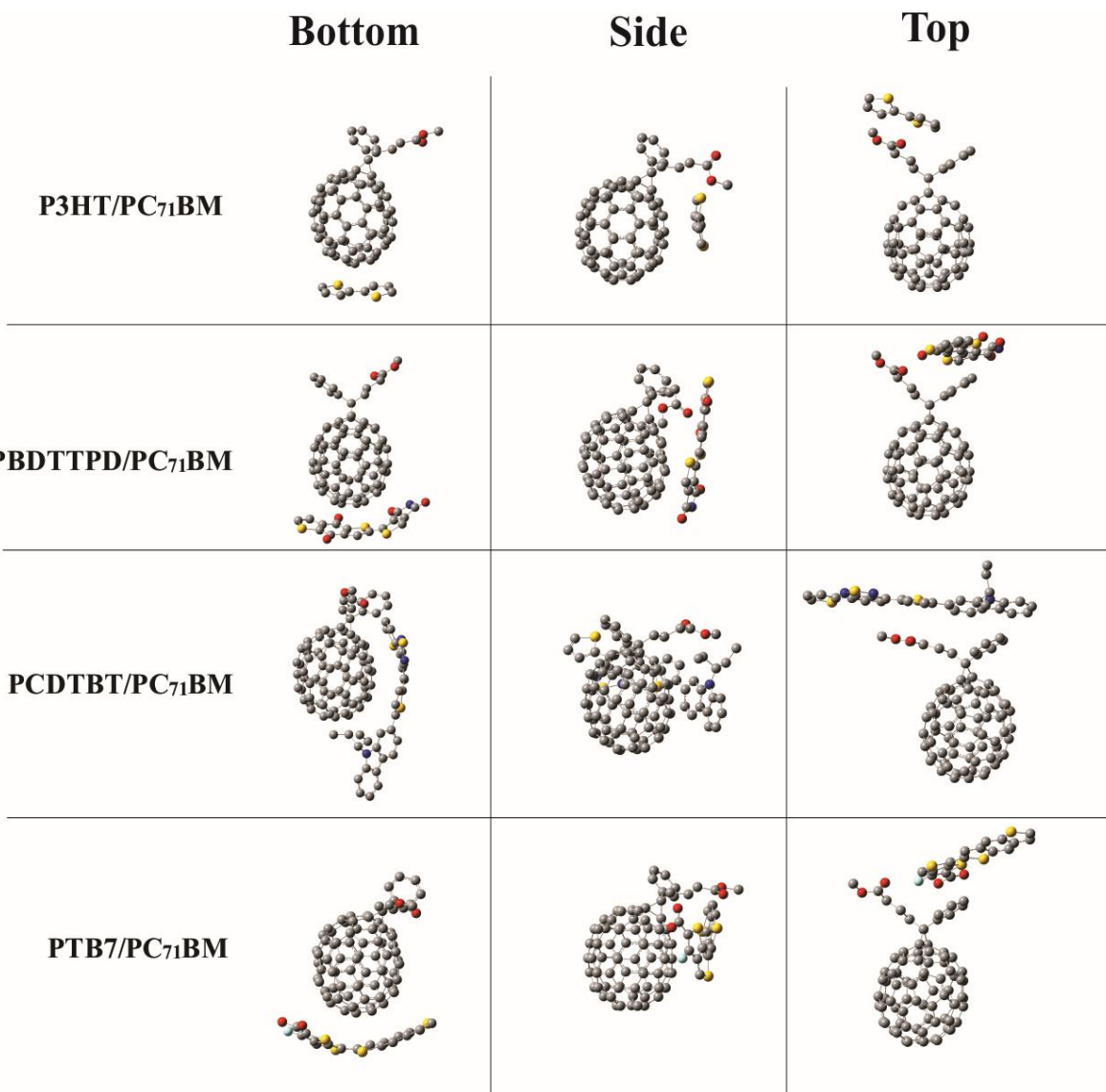


Figure C3: The three types of configurations for seven monomer/PCBM pairs optimized at the B97D3 method.



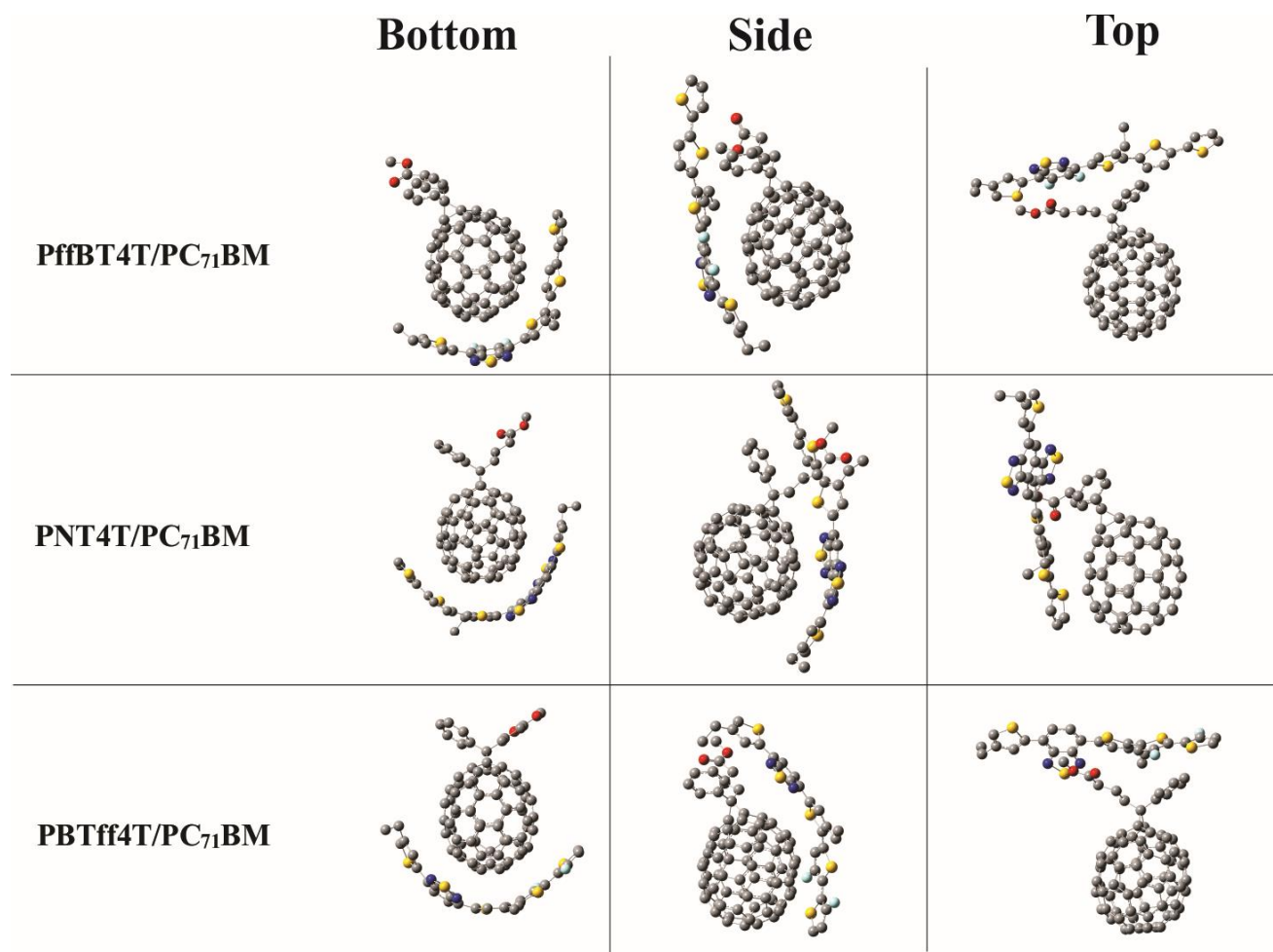


Figure C4: The three types of configurations for seven monomer/PC<sub>71</sub>BM pairs optimized at the B97D3 method.

Table C1: The most stable conformations of homogenous pairs with their (maximum) binding energies and the chain lengths of isolated monomers, the binding energies and minimal intermolecular distance of heterogenous pairs, and the experimental determined PCEs are given. The last row gives  $\Delta E_b$ 's of the fullerenes.

Monomer/ Monomer	Most Stable Conformat ion	$\Delta E_{b(\max)}$ (eV)	$L_{\text{monomer}}$ (Å)	$\Delta E_{b(\max)}$ / $L_{\text{monomer}}$ (eV)	Monomer/ PCBM	$\Delta E_b$ (eV)	$d_{\min}$ (Å)	PCE (%)	Monomer/ PC <sub>71</sub> BM	$\Delta E_b$ (eV)	$d_{\min}$ (Å)	PCE (%)
P3HT/ P3HT	MO	0.55	6.43	0.086	P3HT/PC BM	1.08	3.25	5.16 [6]	P3HT/ PC <sub>71</sub> BM	0.86	3.11	4.13 [7]
PCDTBT/ PCDTBT	MO	1.84	18.73	0.098	PCDTBT/ PCBM	1.93	3.09	5.2 [8]	PCDTBT/ PC <sub>71</sub> BM	1.77	3.20	7.5 [8]
PTB7/PTB7	MOR	1.37	10.94	0.125	PTB7/PC BM	1.53	3.10		PTB7/ PC <sub>71</sub> BM	1.35	3.20	8.24 [10]
PBDTTPD/ PBDTTPD	MO	1.93	10.91	0.177	PBDTTP D/ PCBM	1.68	3.11	6.8 [27]	PBDTTP D/ PC <sub>71</sub> BM	1.77	3.14	8.5 [9]
PNT4T/ PNT4T	MOR	2.51	20.72	0.121	PNT4T/P CBM	1.93	3.01		PNT4T/ PC <sub>71</sub> BM	1.57	3.06	10.1 [11]
PBTff4T/ PBTff4T	MR	2.11	18.27	0.115	PBTff4T/ PCBM	1.88	3.02	9.6 [11]	PBTff4T/ PC <sub>71</sub> BM	1.61	3.09	10.4 [11]
PffBT4T/ PffBT4T	MR	2.13	18.39	0.116	PffBT4T/ PCBM	1.84	3.00	10.4 [11]	PffBT4T/ PC <sub>71</sub> BM	1.62	3.03	10.5 [11]
PCBM/ PCBM	Side/Side (Same dir.)			1.81	PC <sub>71</sub> BM/ PC <sub>71</sub> BM	Side/Side (Opp. dir.)					1.29	

C2. The electronic properties of the isolated monomers and fullerenes calculated using the B3LYP method.

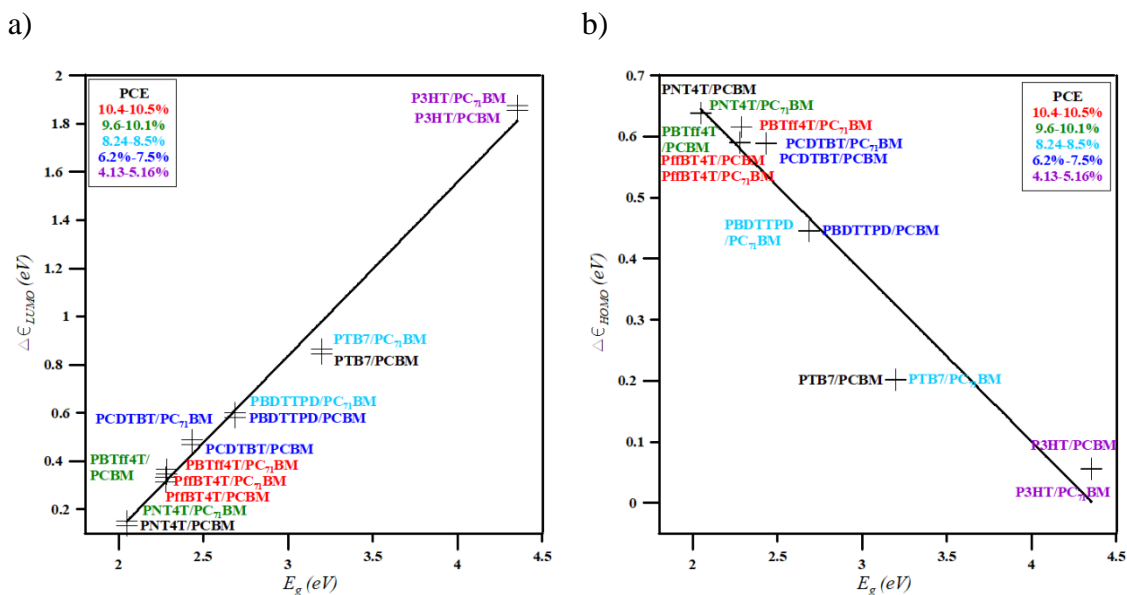


Figure C5: a) LUMO offsets and b) HOMO offsets of the gas phase monomer/fullerene pairs versus monomer's  $E_g$ .

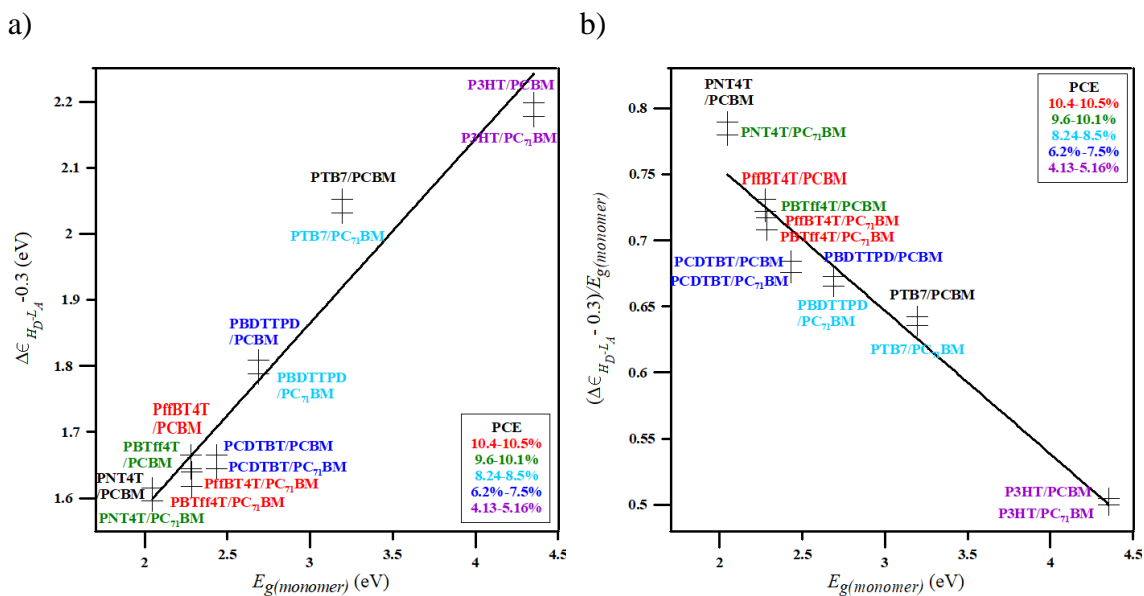


Figure C6: a)  $\Delta\epsilon_{\text{HD-LA}} - 0.3$  and b)  $(\Delta\epsilon_{\text{HD-LA}} - 0.3)/E_{g(\text{mon})}$  of the gas phase monomer/fullerene pairs versus monomer's  $E_g$ .

C3. The recommended computational approach for selecting the best polymers to be used in OSCs devices:

- 1- select number of polymers and fullerenes with the appropriate electronic structure (e.g. low  $E_g$ );
- 2- for the chosen homogenous monomer pairs, calculate their  $\Delta E_b$ 's using one of the dispersion corrected DFT such as the B97D3 method;
- 3- compute the gas phase  $E_g$ 's of the monomers, as well as interfacial quantities such as  $\Delta\epsilon_{LUMO}$ , and  $(\Delta\epsilon_{HD-LA}-0.3)/E_{g(monomer)}$  using the hybrid exchange-correlation DFT functional such as, for example, the B3LYP functional;
- 4- carry out experiments with the pairs with the lowest  $\Delta\epsilon_{LUMO}$ , highest homogenous  $\Delta E_b$ , and highest  $(\Delta\epsilon_{HD-LA}-0.3)/E_{g(monomer)}$ .

## Bibliography

- [1] M.D. Irwin, B. Buchholz, A.W. Hains, R.P.H. Chang, T.J. Marks, *P-Type Semiconducting Nickel Oxide as an Efficiency-Enhancing Anode Interfacial Layer in Polymer Bulk-Heterojunction Solar Cells*, Proceedings of the National Academy of Sciences of the United States of America 105 (2008) 2783-2787.
- [2] H.Y. Wang, X. Wang, P. Fan, X. Yang, J.S. Yu, *Enhanced Power Conversion Efficiency of P3HT: PC71BM Bulk Heterojunction Polymer Solar Cells by Doping a High-Mobility Small Organic Molecule*, International Journal of Photoenergy (2015).
- [3] S. Beaupre, M. Leclerc, *PCDTBT: En Route for Low Cost Plastic Solar Cells*, Journal of Materials Chemistry A 1 (2013) 11097-11105.
- [4] Z.C. He, C.M. Zhong, S.J. Su, M. Xu, H.B. Wu, Y. Cao, *Enhanced Power-Conversion Efficiency in Polymer Solar Cells Using an Inverted Device Structure*, Nature Photonics 6 (2012) 591-595.
- [5] C. Piliago, T.W. Holcombe, J.D. Douglas, C.H. Woo, P.M. Beaujuge, J.M.J. Frechet, *Synthetic Control of Structural Order in N-Alkylthieno 3,4-C Pyrrole-4,6-Dione-Based Polymers for Efficient Solar Cells*, Journal of the American Chemical Society 132 (2010) 7595-7597.
- [6] C. Cabanetos, A. El Labban, J.A. Bartelt, J.D. Douglas, W.R. Mateker, J.M.J. Frechet, M.D. McGehee, P.M. Beaujuge, *Linear Side Chains in Benzo 1,2-B:4,5-B' Dithiophene-Thieno 3,4-C Pyrrole-4,6-Dione Polymers Direct Self-Assembly and Solar Cell Performance*, Journal of the American Chemical Society 135 (2013) 4656-4659.
- [7] Y.H. Liu, J.B. Zhao, Z.K. Li, C. Mu, W. Ma, H.W. Hu, K. Jiang, H.R. Lin, H. Ade, H. Yan, *Aggregation and Morphology Control Enables Multiple Cases of High-Efficiency Polymer Solar Cells*, Nature Communications 5 (2014) 5293.

## D. Supporting Information for Chapter 6: A DFT Investigation of Conjugated Polymers and Fullerenes Interactions - Side Chain Effect

Table D1: The results of B97-D3 and B3LYP-D3 binding energies of homogenous and heterogenous pairs with varying the lengths of side chains, and corresponding experimental determined PCEs.

Monomer	$n_c$	monomer/ monomer	Monomer/PCBM			Monomer/PC <sub>71</sub> BM		
		$\Delta E_b$ (eV)	$\Delta E_b$ (eV)	$\Delta E_b$ (eV)	PCE (%)	$\Delta E_b$ (eV)	$\Delta E_b$ (eV)	PCE (%)
		B97-D3	B97-D3	B3LYP-D3		B97-D3	B3LYP-D3	
P3BT	4	0.91	1.52	1.47	3.2 [1]	1.31	1.23	
P3PT	5	1.01	1.57	1.52	4.3 [1]	1.36	1.28	
P3HT	6	1.11	1.64	1.58	4.6 [1]	1.45	1.37	
P3HT	8	1.31	1.69			1.49		
P3HT	10	1.51	1.70			1.50		
P3HT	12	1.71	1.70			1.51		
P3HT	14	1.90	1.70			1.51		
PCDTBT-C2	2	1.84	1.93	1.82		1.77	1.67	
PCDTBT-C8	8	1.99	2.24	2.11	5.2 [2]	2.15	1.95	7.5 [2]

PCDTBT-C12	12	1.99	2.72			2.42		
PBDTTPD-2EH/C6	6	1.38	2.12			1.82		6.6 [3]
PBDTTPD-2EH/C7	7	1.66	2.27	2.36		1.91	1.95	8.5 [3]
PBDTTPD-2EH/C8	8	1.69	2.32	2.39		1.92	1.99	7.5 [3]
PBDTTPD-2EH/C12	12	1.73	2.43			2.09		
PNT4T-C6/C8	6/8	2.88	2.72			2.45		
PNT4T-2OD	8/10	2.76	3.01	2.83		2.80	2.57	10.1 [4]
PNT4T-2DT	10/12	1.77	2.54	2.44		2.33	2.14	
PBTff4T-C6/C8	6/8	1.67	2.17			2.14		
PBTff4T-2OD	8/10	1.65	2.42	2.33	9.6 [4]	2.38	2.22	10.4 [4]
PBTff4T-2DT	10/12	0.65	2.04	1.92		1.97	2.11	
PffBT4T-C6/C8	6/8	3.09	2.40			2.11		
PffBT4T-2OD	8/10	2.20	2.54	2.51	10.4 [4]	2.19	1.89	10.5 [4]
PffBT4T-2DT	10/12	0.88	1.98	2.09		1.73	1.37	7.64 [5]

Table D2: The results of B97-D3 and B3LYP-D3 binding energies of homogenous and heterogenous pairs with varying the number of branched side chains, and corresponding experimental determined PCEs.

Monomer	$n_B$	monomer/ monomer	Monomer/PCBM			Monomer/PC <sub>71</sub> BM		
		$\Delta E_b$ (eV)	$\Delta E_b$ (eV)	$\Delta E_b$ (eV)	PCE (%)	$\Delta E_b$ (eV)	$\Delta E_b$ (eV)	PCE (%)
		B97-D3	B97-D3	B3LYP-D3		B97-D3	B3LYP-D3	
P3HT	0	1.11	1.64	1.58	3.48 [6]	1.45	1.37	
P3HT- <i>co</i> -EHT	1	0.99	1.69	1.68	3.85 [6]	1.39	1.47	
P3EHT	2	0.93	1.28	1.13	0.83 [6]	1.13	1.13	
PBDTPD-C12/C8	0	2.49	2.53	2.83		2.17	2.61	3.2[3]
PBDTPD-2EH/C8	1	1.69	2.32	2.39		1.99	1.99	6-7.5 [3, 7]
PBDTPD-2EH/EH	2	1.36	2.12			1.75		3.2
PTB1	0	3.07	2.74		4.8[8]	2.40		5.6[8]
PTB4	1	2.10	2.37	2.25	6.1[8]	2.20	1.99	7.1[8]
PTB7	2	1.77	2.22	2.30		2.01	2.11	7.4

Table D3: The results of B97-D3 and B3LYP-D3 binding energies of homogenous and heterogenous pairs with varying the branching positions of branched side chains, and the corresponding experimental determined PCEs.

Monomer/Monomer	$P_B$	monomer/ monomer	Monomer/PCBM			Monomer/PC <sub>71</sub> BM		
		$\Delta E_b$ (eV) B97-D3	$\Delta E_b$ (eV) B97-D3	$\Delta E_b$ (eV) B3LYP-D3	PCE (%) [4]	$\Delta E_b$ (eV) B97-D3	$\Delta E_b$ (eV) B3LYP-D3	PCE (%) [4]
PNT4T-1ON	1	3.22	2.70	2.56		2.57	2.30	
PNT4T-2OD	2	2.76	3.01	2.83		2.80	2.57	10.1
PNT4T-3OT	3	3.22	2.43	2.27		2.83	2.23	
PBTff4T-1ON	1	1.50	2.38	2.49		2.09	1.91	
PBTff4T-2OD	2	1.65	2.42	2.33	9.6	2.38	2.22	10.4
PBTff4T-3OT	3	2.36	1.94	2.18		2.28	2.11	
PffBT4T-1ON	1	2.81	2.05	1.88		1.76	1.92	
PffBT4T-2OD	2	2.20	2.54	2.51	10.4	2.19	2.09	10.5
PffBT4T-3OT	3	2.92	2.21	2.76			2.56	

Table D4: The electronic offsets of isolated monomers and fullerenes calculated at the B3LYP method.

Isolated Monomers	Electronic Offsets from PCBM				Electronic Offsets from PC <sub>71</sub> BM			
	$\Delta\epsilon_{HOMO}$	$\Delta\epsilon_{LUMO}$	$\Delta\epsilon_{H-L} - 0.3$	$\frac{\Delta\epsilon_{H-L} - 0.3}{E_g(monomer)}$	$\Delta\epsilon_{HOMO}$	$\Delta\epsilon_{LUMO}$	$\Delta\epsilon_{H-L} - 0.3$	$\frac{\Delta\epsilon_{H-L} - 0.3}{E_g(monomer)}$
P3BT	0.22	1.98	2.03	0.47	0.22	2.00	2.01	0.47
P3PT	0.23	1.98	2.02	0.47	0.23	2.00	2.00	0.47
P3HT	0.22	1.99	2.03	0.47	0.22	2.01	2.01	0.47
P3HT-co-EHT	0.23	1.96	2.02	0.47	0.23	1.98	2.00	0.47
P3EHT	0.27	1.91	1.98	0.47	0.27	1.93	1.96	0.47
PCDTBT-C2	0.59	0.47	1.66	0.68	0.59	0.49	1.64	0.68
PCDTBT-C8	0.60	0.47	1.65	0.68	0.60	0.49	1.63	0.67
PBDTPD-2EH/C7	0.40	0.86	1.85	0.61	0.40	0.88	1.83	0.61
PBDTPD-2EH/C8	0.43	0.87	1.82	0.61	0.43	0.89	1.80	0.60
PBDTPD-C12/C8	0.28	0.82	1.97	0.64	0.28	0.84	1.95	0.63
PTB4	0.43	1.01	1.82	0.58	0.43	1.03	1.80	0.58
PTB7	0.42	0.97	1.83	0.59	0.42	0.99	1.81	0.58
PNT4T-1ON	0.46	0.15	1.79	0.80	0.46	0.17	1.77	0.79
PNT4T-2OD	0.53	0.12	1.72	0.80	0.53	0.14	1.70	0.79

PNT4T-3OT	0.60	0.14	1.65	0.79	0.60	0.16	1.63	0.78
PNT4T-2DT	0.59	0.12	1.66	0.80	0.59	0.14	1.64	0.79
PBTff4T-1ON	0.52	0.39	1.73	0.72	0.52	0.41	1.71	0.71
PBTff4T-2OD	0.58	0.35	1.67	0.72	0.58	0.37	1.65	0.71
PBTff4T-3OT	0.59	0.39	1.66	0.71	0.59	0.41	1.64	0.70
PBTff4T-2DT	0.50	0.35	1.75	0.73	0.50	0.37	1.73	0.72
Pff4TBT-1ON	0.50	0.33	1.75	0.73	0.50	0.35	1.73	0.73
Pff4TBT-2OD	0.54	0.32	1.71	0.73	0.54	0.34	1.69	0.73
Pff4TBT-3OT	0.63	0.32	1.62	0.72	0.63	0.34	1.60	0.71
Pff4TBT-2DT	0.51	0.30	1.74	0.74	0.51	0.32	1.72	0.74

Table D5: The electronic offsets of interacting monomers and fullerenes calculated at the SP B3LYP method using the B97-D3 optimized geometries.

Interacting Monomers	Electronic Offsets from PCBM				Electronic Offsets from PC <sub>71</sub> BM			
	$\Delta\epsilon_{HOMO}$	$\Delta\epsilon_{LUMO}$	$\Delta\epsilon_{H-L} - 0.3$	$\frac{\Delta\epsilon_{H-L} - 0.3}{E_{g(monomer)}}$	$\Delta\epsilon_{HOMO}$	$\Delta\epsilon_{LUMO}$	$\Delta\epsilon_{H-L} - 0.3$	$\frac{\Delta\epsilon_{H-L} - 0.3}{E_{g(monomer)}}$
P3BT	0.43	2.00	1.80	2.03	0.36	1.99	1.81	2.03
P3PT	0.44	2.00	1.79	2.02	0.37	2.00	1.81	2.03
P3HT	0.44	2.01	1.79	2.02	0.36	2.00	1.81	2.03
P3HT-co-EHT	0.38	2.02	1.85	2.08	0.38	1.98	1.79	2.02
P3EHT	0.38	2.00	1.85	2.08	0.23	2.14	1.94	2.17
PCDTBT-C2	0.68	0.56	1.55	1.73	0.58	0.53	1.59	1.76
PCDTBT-C8	0.64	0.51	1.60	1.77	0.59	0.53	1.59	1.76
PBDTPD-2EH/C7	0.47	1.00	1.76	0.58	0.45	0.99	1.72	0.57
PBDTPD-2EH/C8	0.45	1.01	1.78	0.58	0.46	0.99	1.71	0.57
PBDTPD-C12/C8	0.42	0.96	1.81	0.59	0.38	0.95	1.80	0.59
PTB4	0.61	0.98	1.62	0.56	0.52	0.97	1.65	0.56
PTB7	0.61	0.97	1.62	0.56	0.52	0.95	1.66	0.57
PNT4T-1ON	0.55	0.19	1.69	0.78	0.45	0.18	1.73	0.78
PNT4T-2OD	0.75	0.19	1.49	0.75	0.71	0.18	1.47	0.76

PNT4T-3OT	0.70	0.22	1.54	0.75	0.43	0.18	1.75	0.78
PNT4T-2DT	0.75	0.19	1.49	0.75	0.71	0.18	1.47	0.76
PBTff4T-1ON	0.69	0.31	1.54	0.72	0.43	0.38	1.74	0.72
PBTff4T-2OD	0.60	0.41	1.64	0.70	0.50	0.37	1.67	0.71
PBTff4T-3OT	0.64	0.46	1.60	0.68	0.54	0.42	1.63	0.69
PBTff4T-2DT	0.59	0.40	1.65	0.70	0.50	0.36	1.68	0.72
Pff4TBT-1ON	0.61	0.41	1.63	0.70	0.48	0.35	1.70	0.72
Pff4TBT-2OD	0.65	0.44	1.59	0.68	0.40	0.32	1.77	0.74
Pff4TBT-3OT	0.67	0.35	1.56	0.71	0.51	0.32	1.66	0.73
Pff4TBT-2DT	0.59	0.30	1.64	0.73	0.47	0.29	1.69	0.74

Table D6: The electronic offsets of interacting monomers and fullerenes calculated at the SP B3LYP method using the B3LYP-D3 optimized geometries.

Interacting Monomers	Electronic Offsets from PCBM				Electronic Offsets from PC <sub>71</sub> BM			
	$\Delta\epsilon_{HOMO}$	$\Delta\epsilon_{LUMO}$	$\Delta\epsilon_{H-L} - 0.3$	$\frac{\Delta\epsilon_{H-L} - 0.3}{E_g(\text{monomer})}$	$\Delta\epsilon_{HOMO}$	$\Delta\epsilon_{LUMO}$	$\Delta\epsilon_{H-L} - 0.3$	$\frac{\Delta\epsilon_{H-L} - 0.3}{E_g(\text{monomer})}$
P3BT	0.38	2.02	1.89	0.45	0.32	2.00	1.91	0.45
P3PT	0.39	2.02	1.89	0.45	0.33	2.00	1.91	0.45
P3HT	0.39	2.02	1.88	0.45	0.33	2.00	1.91	0.45
P3HT- <i>co</i> -EHT	0.27	2.09	2.00	0.46	0.34	1.98	1.89	0.45
P3EHT	0.35	2.00	1.92	0.45	0.19	2.15	2.05	0.45
PCDTBT-C2	0.62	0.59	1.65	0.65	0.53	0.54	1.70	0.67
PCDTBT-C8	0.59	0.61	1.68	0.65	0.53	0.56	1.71	0.67
PBDTPD-2EH/C7	0.42	1.08	1.85	0.57	0.43	0.99	1.80	0.58
PBDTPD-2EH/C8	0.43	1.07	1.84	0.57	0.44	1.01	1.79	0.58
PBDTPD-C12/C8	0.42	1.00	1.85	0.59	0.38	0.98	1.86	0.59
PTB4	0.55	1.01	1.72	0.57	0.51	0.99	1.73	0.57
PTB7	0.56	1.00	1.71	0.57	0.49	0.97	1.75	0.58

PNT4T-1ON	0.34	0.18	1.93	0.80	0.41	0.22	1.83	0.78
PNT4T-2OD	0.61	0.23	1.66	0.76	0.64	0.19	1.60	0.77
PNT4T-3OT	0.56	0.26	1.72	0.76	0.55	0.26	1.69	0.75
PNT4T-2DT	0.61	0.22	1.66	0.76	0.63	0.19	1.61	0.77
PBTff4T-1ON	0.61	0.35	1.66	0.72	0.20	0.42	2.04	0.74
PBTff4T-2OD	0.54	0.44	1.74	0.70	0.46	0.36	1.77	0.73
PBTff4T-3OT	0.60	0.54	1.67	0.67	0.50	0.44	1.74	0.68
PBTff4T-2DT	0.51	0.45	1.76	0.70	0.46	0.35	1.78	0.73
Pff4TBT-1ON	0.49	0.43	1.79	0.71	0.41	0.33	1.82	0.74
Pff4TBT-2OD	0.38	0.46	1.89	0.71	0.32	0.37	1.92	0.74
Pff4TBT-3OT	0.33	0.45	1.93	0.72	0.41	0.37	1.82	0.73
Pff4TBT-2DT	0.34	0.47	1.93	0.72	0.30	0.37	1.93	0.74

# Bibliography

- [1] A. Gadisa, W.D. Oosterbaan, K. Vandewal, J.C. Bolsee, S. Bertho, J. D'Haen, L. Lutsen, D. Vanderzande, J.V. Manca, *Effect of Alkyl Side-Chain Length on Photovoltaic Properties of Poly(3-Alkylthiophene)/PCBM Bulk Heterojunctions*, *Advanced Functional Materials* 19 (2009) 3300-3306.
- [2] S. Beaupre, M. Leclerc, *PCDTBT: En Route for Low Cost Plastic Solar Cells*, *Journal of Materials Chemistry A* 1 (2013) 11097-11105.
- [3] C. Cabanetos, A. El Labban, J.A. Bartelt, J.D. Douglas, W.R. Mateker, J.M.J. Frechet, M.D. McGehee, P.M. Beaujuge, *Linear Side Chains in Benzo 1,2-B:4,5-B' Dithiophene-Thieno 3,4-C Pyrrole-4,6-Dione Polymers Direct Self-Assembly and Solar Cell Performance*, *Journal of the American Chemical Society* 135 (2013) 4656-4659.
- [4] Y.H. Liu, J.B. Zhao, Z.K. Li, C. Mu, W. Ma, H.W. Hu, K. Jiang, H.R. Lin, H. Ade, H. Yan, *Aggregation and Morphology Control Enables Multiple Cases of High-Efficiency Polymer Solar Cells*, *Nature Communications* 5 (2014) 5293.
- [5] Z.H. Chen, P. Cai, J.W. Chen, X.C. Liu, L.J. Zhang, L.F. Lan, J.B. Peng, Y.G. Ma, Y. Cao, *Low Band-Gap Conjugated Polymers with Strong Interchain Aggregation and Very High Hole Mobility Towards Highly Efficient Thick- Film Polymer Solar Cells*, *Advanced Materials* 26 (2014) 2586-2591.
- [6] B. Burkhart, P.P. Khlyabich, B.C. Thompson, *Influence of the Ethylhexyl Side-Chain Content on the Open-Circuit Voltage in Rr-Poly(3-Hexylthiophene-Co-3-(2-Ethylhexyl)Thiophene) Copolymers*, *Macromolecules* 45 (2012) 3740-3748.
- [7] K.R. Graham, C. Cabanetos, J.P. Jahnke, M.N. Idso, A. El Labban, G.O.N. Ndjawa, T. Heumueller, K. Vandewal, A. Salleo, B.F. Chmelka, A. Amassian, P.M. Beaujuge, M.D. McGehee, *Importance of the Donor:Fullerene Intermolecular Arrangement for High-Efficiency Organic Photovoltaics*, *Journal of the American Chemical Society* 136 (2014) 9608-9618.
- [8] J.M. Szarko, J.C. Guo, Y.Y. Liang, B. Lee, B.S. Rolczynski, J. Strzalka, T. Xu, S. Loser, T.J. Marks, L.P. Yu, L.X. Chen, *When Function Follows Form: Effects of Donor Copolymer Side Chains on Film Morphology and BHJ Solar Cell Performance*, *Advanced Materials* 22 (2010) 5468-5472.